Macromolecular Studies of the Dynamic Structure and Mechanical Properties of the Endothelial Surface Layer

by

Darina Danova-Okpetu

A dissertation submitted to Johns Hopkins University in conformity with the requirements for the degree of Doctor of Philosophy

Baltimore, Maryland

October, 2005

Abstract

The endothelial surface layer (ESL) is a micron-scale macromolecular lining of the luminal side of blood vessels, composed of proteoglycans, glycoproteins, polysaccharides and plasma proteins in dynamic equilibrium. Its physiological implications include blood flow and microvascular permeability regulation, and active participation in mechanotransduction, stress regulation, coagulation, inflammation and angiogenesis. The ESL dynamic structure and mechanical properties are primarily controlled by its composition and topology on macromolecular scales and are decisive for most ESL functions.

In this thesis, theoretical research on the glycocalyx was performed using computer simulation and modeling. A topological model was created containing three basic macromolecular elements: branched proteoglycans, linear polysaccharides, and plasma proteins, and studied using non-equilibrium MD simulations. The effects of composition and shear flow were investigated initially for permanently-bound ESL. Proteoglycans were not sufficient to efficiently screen the shear flow from the cell surface. ESL lacking plasma proteins was much less dense than the protein-containing ESL. Low to moderate shear flows had negligible effect on the glycocalyx structure. High shear flows provoked ESL thinning and pronounced stretching in the flow direction. Self-assembling ESL with associating proteins in equilibrium with the bulk was next investigated. The plasma protein distribution was found sensitive to the polysaccharide-protein interaction energy but not affected by shear flow. The protein diffusion in the bulk and in the ESL was evaluated and the average lifetimes of the polysaccharide-protein complexes were

estimated. The ESL dynamic structure and the protein distribution were observed for different total protein concentrations. For weak polysaccharide-protein interactions, the gradual decrease of total protein in the system resulted in drastic decrease of the ESL-associated amount. For strong interactions there was significant residual protein in the ESL even for negligibly low protein concentrations in the plasma.

Finally, a theoretical model of the self-assembling ESL was created based on established models for tethered and associating polymers. Equilibrium and steady-state ESL properties were calculated including height, osmotic pressure, deformation under flow, and the mean number of coils per chain in the ESL as a function of various physico-chemical parameters. The model predictions were found to be broadly consistent with the simulation results.

Thesis Committee:

James L. Harden, Ph.D.
Associate Professor of Physics, University of Ottawa (Advisor)
Adjunct Associate Research Engineer, JHU

Kathleen J. Stebe, Ph.D.
Professor of Chemical and Biomolecular Engineering, JHU (Departmental Advisor)

Aleksander S. Popel, Ph.D.
Professor of Biomedical Engineering, JHMI (Reader)

Richard J. Rivers, M.D., Ph.D.
Associate Professor of Anesthesiology and Critical Care Medicine, JHMI (Reader)

Acknowledgements

I would like to thank …

… my research advisor, Professor James Harden, for the privilege of working with him and for the fine and rare to find balance between academic guidance and freedom I was given, that allowed me to explore my research interests and at the same time count on advice, shared scientific insight and unbreakable spirit throughout my years of study.

… Professor Alexander Popel for introducing me to various aspects of the glycocalyx research, sharing his scientific expertise during numerous meetings at the JHMI and for the helpful suggestions related to this thesis.

… Professor Gary Grest from Sandia Laboratories for providing a million hours of computational time without which my research would have probably taken a lifetime.

… Dr. David Heine from Sandia Laboratories for walking me through the learning curve of LAMMPS.

… Professor Richard Rivers and Professor Kathleen Stebe for taking the time to read my work and participate in my defense committee.

… my husband, Baba A. Okpetu, for all the love, continuous support and active encouragement, and, on occasions, for being a prod behind my back.

… my father, Prof. Krasimir Danov, for being the most important teacher in my life, also my mother and grandparents for being there at all times.

… Zara, for the most unconditional support I have ever seen and the constant quiet understanding.

Contents

List of Figures

1. Introduction

1.1. The Endothelial Surface Layer – Definition and Background

The cardiovascular system is responsible for the transport of all essential substances throughout the body. Apart from its main constituent - the heart, it represents a dense mesh of vessels of several types and greatly varying sizes – arteries and arterioles bringing oxygenated blood to the tissues; veins and venules returning the blood rich in carbon dioxide from the tissues back to the heart and through the lungs, and the smallest vessels – the capillaries, where the actual absorption and exchange of various substances takes place (*Berne and Levy, 1993*).

One common feature for all blood vessels, whatever their size or type, is the vascular endothelium. It is a cellular layer situated on the surface of the inside vessel walls, forming a distinct boundary between the interstitial space and the blood flow. Apart from being just a physical barrier between blood and tissues, the vascular endothelium is actively involved in a range of vasculature functions, playing an important role in blood cell activation and migration in physiological and pathological conditions, fluid and solute exchange, hemostasis, coagulation, etc (*Risau, 1995*). The surface properties of the endothelium-plasma boundary are a crucial factor for all the processes mentioned above and thus for the optimal performance of the vascular endothelium in general.

The endothelium-plasma boundary is a system much more complex than simply adjoined endothelial cell membranes in contact with blood. The luminal side of the vascular endothelial cells is not directly exposed to the blood flow but is lined with a

thick extracellular layer referred to as glycocalyx or endothelial surface layer (*Pries et al, 2000*). It represents a highly hydrated matrix of various biomacromolecules, including ectodomains of membrane-bound glycoproteins and proteoglycans, polysaccharides, and associated plasma proteins. The presence of the endothelial surface layer significantly influences the overall properties of the cell surface and thus the glycocalyx plays a key role for the proper vasculature functioning in nearly every aspect. On the other hand, damage or degradation of the endothelial surface layer can result in various pathological states of the vascular system.

Extensive research efforts both experimental and theoretical have been concentrated on clarifying physiological impact of the endothelial surface layer and determining its exact composition and physical, mechanical, chemical and biological properties. This chapter aims to cover the latest development of the glycocalyx research and present an inclusive picture of the state-of-the-art knowledge on the subject. The following subchapters will respectively deal with: i) historical overview of the endothelial surface layer research and efforts in finding suitable experimental techniques for its visualization; ii) physiological implications – role in blood flow regulation, shear stress transduction, microcirculation permeability, etc.; iii) pathological states accompanied by glycocalyx dysfunction and partial degradation; iv) molecular composition with detailed structural information about each potential constituent; v) description of the efforts in theoretical modeling of the glycocalyx and prediction of its properties. The last part of this chapter will briefly go over possible alternative approaches in glycocalyx modeling not yet explored in the literature. Their possible advantages and applications will be discussed and the particular approach of the present work will be outlined.

1.2 Historical Overview

The concept of the extracellular layer present at the luminal surface of the vascular endothelium in one form or another has existed for many decades. One of the earliest and very indirect indications for its presence came from a study by Poiseuille of 1835, when it was inferred from flow measurements that blood cells moving along capillaries are separated from their walls by a layer of immobile plasma. The thickness of this plasma layer and its dependence upon the blood flow velocity were subject of investigations in later works without attaining consistent results.

Almost a century later, the first attempts to postulate the endothelial surface layer composition appeared. They were based on blood apparent viscosity and capillary permeability studies. In 1940, Danielli investigated microvascular permeability by comparing the appearance of edema in frogs under different conditions and came to the conclusion that the presence of serum is decisive for edema prevention, while solutions of other substances (gum acacia, ovalbumin, red cells from different species, etc.) even ones with osmotic pressure comparable to serum, did not show the same effect (*Danielli, 1940*). He thus came up with a hypothesis that plasma proteins are somehow adsorbed to the capillary walls forming an "endocapillary layer" that plays an important role in the microvascular permeability regulation. A later study (*Chambers and Zweifach, 1947*) confirmed the presence of adsorbed serum proteins, albumin in particular, on the vascular endothelium surface. The authors were again investigating microvascular permeability and edema in frogs in presence of various colloids. A part of their study was an attempt to visualize the layer proposed by Danielli but direct microscopic evidence was not

obtained. An indirect but more successful approach was the perfusion of Evans blue solution known for its affinity for plasma albumin. As a result, faint blue colored strands and sheets of translucent material were observed detaching from the inner walls of the frog's blood vessels. Those were not apparent when the blood vessel was rinsed by an alternative solution and becoming increasingly edematous. They were shown to reappear after subsequent perfusion with serum.

An alternative hypothesis as to the composition of the endothelial surface layer was developed a few years later by Copley. In 1953 and in later works, he introduced his hypothesis for the so-called "endo-endothelial layer", situated on the surface of endothelial cells but not spreading out all across the immobile plasmatic layer (Fig. 1.1).

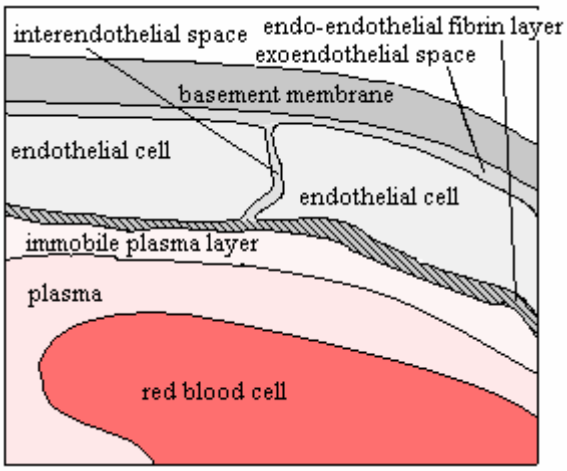

Fig. 1.1

Structure of the plasma - endothelium surface as postulated in the hypothesis of Copley. The endo-endothelial fibrin layer is situated at the endothelial cell surface and takes only a part of the immobile plasmatic zone as defined by Poiseuille (adapted from *Copley, 1962*)

The endo-endothelial layer was hypothesized to contain mainly fibrin with possibly associated plasma proteins and was believed to possess lubricant properties (*Copley and Scott Blair, 1958; Copley, 1974; Copley 1984*). The attention was drawn to the glycocalyx because of major discrepancies observed between the results of blood and plasma viscosity experiments in real blood vessels versus measurements in glass tubes as were mostly done at the time. The hypothesis itself resulted from an adherence study of artificial capillaries lined with various substances such as wax, silicone, fibrin etc, and the

comparison of the results to equivalent conditions in vivo. Their in-vivo experiments based on intravital microscopy observations of venules and arterioles with injected blue dye and graphite solutions provide another indirect attempt for visualization of the immobile plasma layer and a rough estimate of its thickness, reported to be in the micron range (*Copley and Staple, 1962*). Later studies attribute more importance to the endo-endothelial layer with respect to the initiation of thrombosis (*Copley, 1971*) based on rheological studies of viscous resistance, i.e. torque in response to shear, of plasma protein layers containing fibrinogen. The observed aggregation of proteins into polymolecular surface layers was considered to be the initiating step for thrombosis with the platelet aggregation and fibrin gelation as merely following stages.

During the same period of time, Michel and coauthors concentrated their efforts on additionally clarifying the role of the endothelial surface layer in the regulation of capillary permeability. Using vesicles labeled with ferritin and investigating their transport across capillary walls in frogs (*Michel, 1979*), it was found out that ferritin is effectively excluded from the proximity of the endothelial cell surface. Additional measurements of filtration and osmotic reflection coefficients of single capillaries (*Loudon et al, 1979, Mason et al, 1977*) gave way to the conclusion that the selectivity of the capillary pores is controlled mainly by the extracellular material that covers the surface of the endothelial cells and the gaps between them, rather than the size of the pores themselves. The glycocalyx is viewed as a three dimensional fiber network of membrane glycoproteins reinforced by adsorbed plasma proteins (*Curry and Michel, 1980*). With that said, other more recent works concerning the glycocalyx functions and structure will be mentioned in the next parts of this chapter.

As long as the concept for the glycocalyx has been around considerable efforts have been concentrated on achieving direct visual proof for its existence. Mainly for technical reasons and because of the fragile nature of the layer, the earliest of those attempts have proven unsuccessful and most of the later ones, highly inaccurate. For that reason a number of authors (*Florey et al, 1959; Stehbens and Florey, 1960; Stehbens, 1963*) disputed the existence of the endothelial surface layer up until the late 1960s, when Luft achieved the first successful glycocalyx visualization by electron microscopy (*Luft, 1966*). Using ruthenium red dye for staining in the presence of osmium tetroxide, the author was able to directly demonstrate for the first time the presence of an endocapillary layer with a thickness reported to be around 20nm. Based on the fact that the dye used had a high affinity for acid mucopolysaccharides, the author came to the conclusion that the glycocalyx consists of mainly charged carbohydrates (heparan sulfate, chondroitin sulfate, hyaluronan). This conclusion was later disputed by Copley on the grounds that the ruthenium red was not specific in binding only polysaccharides but binds fibrin as well.

In later studies, numerous attempts were made to further investigate the possibilities for microscopic visualization of the endothelial surface layer. Alternative cationic dyes were used for staining such as cationized ferritin, lanthanum chloride, tannic acid or uranyl acetate, and alcian blue (*Simionescu and Simionescu, 1986; Adamson and Clough, 1992; Haldenby et al., 1994*). Nevertheless, the results obtained about the thickness of the layer, reported usually to be up to hundred nanometers, were still in strong disagreement with indirect measurements implying thicknesses in the micron range. This discrepancy could be explained by a considerable collapse of the endothelial surface layer during

fixation and staining procedures, with a consequence that the microscopy experiments actually show only the small part of the layer that is directly bound to the cell membranes. During those experiments, however, other useful information about the endothelial surface layer was revealed. The chemical composition of the glycocalyx was further clarified. It was found to be a highly negatively charged structure mainly due to the presence of various charged polysaccharides. It was also confirmed that it contains external moieties of a variety of membrane components – plasma proteins such as albumin and fibrin, glycoproteins, proteoglycans with heparan sulfate and chondroitin sulfate side chains (*Buonassisi and Colburn, 1982*), sialoconjugates etc. A number of more specialized components were found as well such as various growth factors.

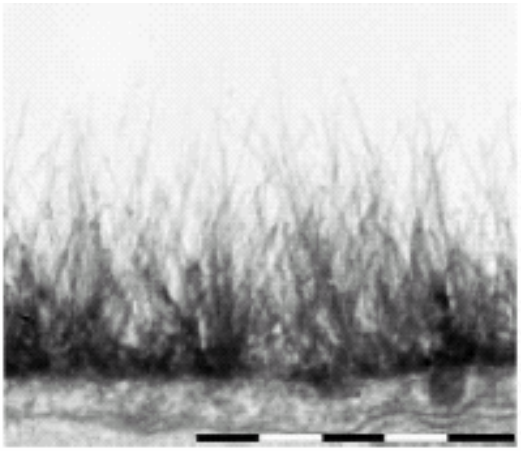

Fig. 1.2

Electron microscopy picture of the endothelial surface layer in rat myocardial capillary (*Vink et al, 2003)*

(*reprinted with permission of Lippincott, Williams & Wilkins*)

(bar = 0.5μm)

The most recent and successful observations of the endothelial surface layer (*van den Berg et al., 2003*) are shown on Fig 1.2. The visualization was performed by intravital microscopy; a new approach was used to stabilize the anionic carbohydrate structures by a modified version of Alcian blue in order to preserve the fragile layer as much as possible. The glycocalyx revealed by this method had a size of the order of half a micron, which is much more consistent with the previous indirect glycocalyx measurements.

1.3 Functions of the Endothelial Surface Layer

The presence of the endothelial surface layer is decisive for nearly every function of the vasculature. Being impenetrable for the blood flow, the glycocalyx provides protection for the vessel walls, helps regulate the effective vessel diameter and as a consequence plays a role in blood flow and hematocrit, as well as apparent blood viscosity regulation. Its macromolecular constituents subjected to the blood flow, are responsible for attenuation and redistribution of the shear stress that reaches the cell membrane. Thus the glycocalyx plays a major role in stress regulation, mechanotransduction and all the processes that occur in the endothelial cells as a response to shear stress variations.

The endothelial surface layer creates an additional obstacle for material transport as well. The mesh of macromolecules it represents acts like a molecular sieve, selectively allowing molecules to reach the endothelial cell surface. The glycocalyx is thus decisive for the regulation of the permeability of the blood vessel walls for various macromolecules.

The thickness of the endothelial surface layer is such that it effectively covers molecules constantly present on the cell surface and responsible for initiation of rolling and sticking of leukocytes, such as selectins and integrins. This fact, plus the layer's lubricant properties, does not allow the leukocytes rolling and sticking to the vessel wall in normal conditions; controlled shedding of the glycocalyx and exposing the molecules needed for initiation of inflammatory response reveals that the glycocalyx is also a major

player in inflammation processes. Last but not least, the endothelial surface layer has its role in lipid metabolism, coagulation and angiogenesis.

Blood flow regulation and microvascular resistance: since the presence of the endothelial surface layer reduces the functional size of the blood vessels (*Vink and Duling, 1996*), an effect which is most pronounced in the capillaries due to their small size, it is perhaps natural to expect that it would have an impact on the microvascular resistance to blood flow (*Pries et al, 1994; Pries et al 1997b*). Indeed, observations of blood flow in the microcirculation and measurements of the volume flow rates and pressure drops in capillary networks and glass tubes have shown a considerable difference in the resistance in the two cases, by up to a factor of two in magnitude. Other than the presence of the endothelial surface layer, explanations for this discrepancy could include for example irregularities in the blood vessel walls or particular properties of the flow in presence of white blood cells, but neither of those factors was shown to be enough to explain the extent to which the discrepancy occurs (*Pries et al, 1997a; Warnke and Skalak, 1990*). Using an enzyme (heparinase) known to cut off a major part of the endothelial surface layer, and comparing the blood flow and microvascular resistance in normal and glycocalyx-free capillaries, the authors showed a decrease in the flow resistance of about 20% as a consequence from the glycocalyx removal. Comparing their results with previous simulations of microcirculatory networks, an estimate of around 0.5 micron for the layer thickness was made, consistent with most findings. A similar effect of reduction of flow resistance was observed during hemodilution and saline perfusion (*Pries et al 1998*). That could also be connected to the glycocalyx, which contains adsorbed plasma proteins which can be washed away and thus affect the layer thickness.

The endothelial surface layer is also important for the regulation of the blood flow. That was demonstrated by a study by Vogel where cerebral blood flow in mice was investigated after treatment with heparinase (*Vogel et al, 2000*). The thickness of the layer was shown to be reduced in half by the enzyme treatment, which led to increase in the cerebral blood flow by about 15%. That increase was only transient and the blood flow went back to normal in about 5 minutes. On the contrary, in conditions of elevated concentration of carbon dioxide in the blood, the increase in the flow is not transient but remains for the duration of the experiment (15min). This is an indication of some type of positive feedback between the glycocalyx and the blood flow, allowing regulation of the blood flow according to the oxygen needs of the tissues. This phenomenon might partially account for the ability of muscles to vary the blood flow by up to 30 percent between rest and exercise.

Tube hematocrit and blood viscosity: It has long been known that the blood hematocrit and viscosity in the microcirculation are substantially different than in larger blood vessels. It was first demonstrated in 1929 in a study of colloidal stability of blood (*Fahraeus, 1929; Albrecht et al, 1979*; *Goldsmith et al, 1989*), that the hematocrit in capillary tubes of diameter smaller than 0.3mm is lower than the systemic hematocrit. The so called Fahraeus effect was found to depend on the capillary size and was explained by a redistribution of the red blood cells; they concentrate near the capillary axis, resulting in overall larger mean velocity of the red blood cells compared to the surrounding fluid. The decrease in the hematocrit results in a decrease in the blood viscosity as well.

It was postulated that the ratio of capillary versus systemic hematocrit would correspond to the ratio of the red cell and blood mean velocities. The proposed dependence could only explain reduction of the capillary versus systemic hematocrit of up to 50%, in disagreement with experimental measurements where the ratio between microcirculatory and systemic hematocrit was found to range from 0.2 to 0.5 (*Klitzman and Duling, 1979; Pries et al, 1986*). Explanations for this additional hemodilution include a network effect (*Pries et al, 1986*) or accounting for the presence of the endothelial surface layer (*Desjardins and Duling, 1990; Desjardins and Duling, 1987*).

According to the first possibility, successive bifurcations in vascular networks result in a non-homogeneous distribution of the red blood cells. At any bifurcation, the higher flow daughter vessel would have a higher hematocrit compared to the parent vessel and vice versa. The increase of the hematocrit in the higher flow vessel has to be less than the decrease in the slower flow vessel which would lead to a decrease in the average hematocrit along the network. Such a generalization of the classical Fahraeus effect can account for decrease in microcirculatory hematocrit beyond 50%.

The presence of a surface layer of slowly moving plasma in the capillaries can also lead to reduction of the capillary hematocrit. It was shown (*Desjardins and Duling, 1987*) that a layer of thickness about 1μm would lead to the capillary hematocrit being as low as 20% of the systemic hematocrit. The hypothesis that it is the glycocalyx that would be responsible for the plasma immobile layer was investigated by measuring the hematocrit after enzymatically removing the glycocalyx by heparinase (*Desjardins and Duling, 1990*); a two-fold increase in the hematocrit was observed, without additional increase in the red blood cell velocity. Similar results were obtained after treatment with oxidized

low-density lipoproteins (LDL) which are known to degrade the endothelial surface layer – the red blood cells velocity remained unchanged while the hematocrit increased by 2-2.5 times (*Constantinescu et al, 2001*). The effect on the microcirculatory hematocrit and blood viscosity of plasma protein concentration reduction, as another means of partially removing the glycocalyx, was also investigated (*Long et al, 2004*) to obtain results consistent to the previous works mentioned.

Mechanotransduction and stress regulation: The fact that the blood flow in immediate proximity to the vessel wall is largely hindered has two possible implications. First, the fluid shear stress reaching the endothelial cell surface is very small (compared to what it would have been without the glycocalyx). Thus the endothelial surface layer has a screening protective role for the endothelial cell membrane. Rather, the major part of the shear stress that actually reaches the endothelial cell is transmitted through the macromolecular constituents of the glycocalyx. In that aspect, the dynamic structure of the glycocalyx would play a crucial role as to how exactly the shear stress is being transmitted. On the other hand the topology of the endothelial surface attachment points of the membrane bound glycocalyx constituents would also be decisive as to where the shear stress is being applied. There are experimental observations showing that the glycocalyx is not just a random bushy structure, but there is some order and regularity to it (*Squire et al, 2001*). By the use of data processing by autocorrelation functions and Fourier transforms of electron microscopy images, an underlying three-dimensional meshwork was found in the glycocalyx structure. It has two characteristic lengthscales, one of them about 20nm, corresponding to the characteristic mesh size of the network and having implications for the permeability of the glycocalyx, and the other about

100nm is the average distance between clusters inside the network. The second lengthscale corresponds closely to the characteristic spacing in the sub-membrane cytoskeletal network of the endothelial cells and is speculated to reveal an immediate structural and functional connection between the glycocalyx and the cytoskeleton for the purpose of effective shear stress transmission.

Various other experimental data also confirms the importance of the endothelial surface layer in shear stress transmission and mechanotransduction. Increased secretion of glycocalyx constituents such as heparan sulfate and chondroitin sulfate is observed after prolonged exposure of endothelial cells to unphysiologically high shear stress (*Arisaka et al, 1995*). This might indicate some feedback mechanism for glycocalyx growth regulation depending on the shear stress applied to the endothelial cell surface. The presence of the glycocalyx was also proved crucial for the flow-induced endothelial nitric oxide production. Enzymatic treatments by hyaluronidase (*Mochizuki et al, 2003*), neuraminidase (*Hecker et al, 1993*) or heparinase (*Florian et al, 2003*) were used to degrade a substantial part of the endothelial surface layer. The subsequent flow-induced nitric oxide production was decreased down to 20% of the control in the case of hyaluronidase treatment, 64% of the control in the case of sialic acid removing enzyme and completely abolished for the heparinase. It was concluded that the endothelial surface layer acts as a shear-detecting mechanism in the nitric oxide production pathway. Shear-dependent albumin uptake was also shown to depend on the glycocalyx (*Ueda et al, 2004*). This study was based on exposure of endothelial cells to a wide range of shear stresses and subsequent measurement of the albumin uptake. A dual response was observed, with the albumin uptake increasing at low shear rates compared to static

conditions, and decreasing in high shear stress conditions. Increase of the overall glycocalyx thickness in higher shear rates was also observed, accompanied by increase in the glycocalyx negative charge – the effects were correspondingly 70% and 80% higher compared to static conditions. The influence of the endothelial surface layer charge was investigated by comparing those results to experiments performed with 'neutralized' glycocalyx, where the increase in albumin uptake exceeded by far the corresponding effect in the charged glycocalyx.

The connection between the glycocalyx and the endothelial cell cytoskeleton was more closely investigated recently (*Thi et al, 2004*). After high shear stress exposure of endothelial cells, the intracellular distributions of various cellular components known to be related to cytoskeletal response to shear, such as actin, vinculin, paxillin etc., were investigated using confocal microscopy. The same experiment was performed with endothelial cells with compromised glycocalyx. In the case of intact glycocalyx, a well pronounced reorganization of all the monitored cytoskeletal components was observed. In contrast, no reorganization was present in the case of damaged glycocalyx. Based on the results of the experiments and adapting Squire's 'lattice' view for the glycocalyx, a detailed explanation for the mechanism of shear transduction from the glycocalyx to the cytoskeleton is proposed, the so called 'bumper-car' mechanism. According to it, the actin fibers of the cytoskeleton are only loosely connected to the basal attachment sites and thus an initiation of a cytoskeletal response would require a threshold value of the applied torque which would only be reached at high enough values of the shear stress.

Cell adhesion and inflammatory response: The presence of the endothelial surface layer substantially alters the adhesive properties of the endothelial cell walls and therefore modulates the interactions between the vascular endothelium and various types of blood cells. Given that the microvascular entrapment of leukocytes is an indispensable part of the inflammatory response, the glycocalyx might also play its own role during inflammation as well.

Recent studies have shown that disruption of the glycocalyx leads to increased adhesion of platelets and leukocytes to the endothelial cell walls. After injection of oxidized low-density lipoproteins, the thickness of the glycocalyx was observed to transiently decrease by about 60%, which was accompanied by the appearance of platelets adhering to the vessel walls (*Vink et al, 2000*). The same experiment was repeated in the presence of superoxide dismutase, an enzyme blocking the effect of ox-LDL on the glycocalyx; no platelet adhesion was observed in that case. A similar study using ox-LDL was performed to investigate the adhesion of leukocytes (*Constantinescu et al, 2003*), where was shown that the addition of ox-LDL dramatically increased the leukocyte-endothelial cell adhesion. Furthermore, when fluorescent forms of known glycocalyx constituents such as heparan sulfate and heparin were added, they were observed to incorporate themselves onto the endothelial cell surface thus reconstructing the endothelial surface layer and as a result a decrease in the leukocyte-endothelium adhesion was observed.

An alternative study investigated the effect of glycocalyx removal by heparinase on leukocyte-endothelial cell adhesion (*Mulivor and Lipowsky, 2002*). The behavior of antibody coated, fluorescently labeled microspheres and white blood cells was compared

in the presence and absence of glycocalyx; also in the presence and absence of the adhesion stimulating chemo-attractant f-MLP. In the case of microspheres, both the chemo-attractant and the heparinase treatment resulted in a dramatic increase of the microsphere-endothelial cell adhesion. In the case of leukocytes, the adhesion was not strongly influenced by the heparinase treatment, and increased after the chemo-attractant addition. The addition of heparinase *after* the chemo-attractant resulted in decrease of the white blood cells adhesion to the vessel wall. The authors explained the results obtained by the possibility that the heparinase could remove from the endothelial cell wall not only the glycocalyx but also other molecular species crucial for leukocytes rolling and adhesion and stuck to the conclusion that the glycocalyx is indeed a barrier for adhesion and that its shedding during endothelial cell activation is an important part of the inflammation. It was confirmed in a later study (*Mulivor and Lipowsky, 2004*) where changes in the glycocalyx composition in response to inflammation and after ischemia and reperfusion were investigated. The results supported the idea that the glycocalyx structure comes from a dynamic equilibrium between shedding and endothelial cell biosynthesis of its constituents. Individual components of the endothelial surface layer such as heparan sulfate and chondroitin sulfate were shown to shed in response to reperfusion after ischemia or inflammation and accumulate on the endothelial cell wall during ischemia. The former was accompanied by increased labeled microsphere (prepared similarly to the previous mentioned study) and leukocyte adhesion. On the other hand, no shedding or accumulation of the core proteins of the membrane bound proteoglycans was observed. The observations indicate that in the absence of shear forces the endothelial surface layer might grow thicker than its normal physiological state.

Microvascular permeability: The exchange of macromolecules, solutes and water between the microcirculation and the surrounding interstitial tissues is another important aspect of vasculature function in which the glycocalyx is considered to play a significant role. In general the endothelium in the capillaries can either be continuous as in most cases or fenestrated as in intestines, stomach, kidneys, certain glands (*Rostgaard and Qvortrup, 1997*). Interestingly, while the permeability for small molecules differs depending on the type of capillaries, the macromolecular permeability is relatively independent on the presence of fenestrae (*Curry and Michel, 1999*). The macromolecular sieving properties of the capillary walls are therefore determined not by the size of the pores and overall properties of the intercellular clefts, which are different for continuous and fenestrated microvasculature, but by a structure common for all capillary types. After a set of experiments showing that ferritin is effectively excluded from the proximity of the endothelial cell walls it was suggested (*Michel and Curry, 1980*) that the endothelial surface layer might just be that common structure – a spatial fiber network providing additional resistance for solutes and water permeation and effective sieving for macromolecules. This hypothesis was further tested by investigating the response of the hydraulic conductivity after partial enzymatic digestion of the glycocalyx. When a relatively mild enzyme - pronase was used (*Adamson, 1990*) - it was concluded that the glycocalyx might contribute to about 60% of the capillary hydraulic resistance. After observing increased microvascular permeability in the case of removed glycocalyx, it was additionally verified that the condition of the intercellular clefts had remained unchanged. A similar study using two enzymes - pronase and heparinase for removing the glycocalyx compared the permeability in coronary arterioles for two anionic protein types of

different size – α-lactalbumin with molecular weight 14kDa and serum albumin with molecular weight 65kDa (*Huxley and Williams, 2000*). The permeability for both proteins was shown to increase several times, and the increase for the smaller protein was expectedly more pronounced. The glycocalyx became more permeable also after treatment with hyaluronidase (*Henry and Duling, 1999*). This treatment resulted in layer modification that allowed the subsequent penetration of Dextran-70 and Dextran-145, which are in normal conditions effectively screened away of the endothelial cell wall. At the same time, penetration of larger molecules such as Dextran-580 and Dextran-2000 did not show any change. Apparently, the treatment by hyaluronidase did mainly affect the porosity of the glycocalyx without considerably changing its thickness.

Angiogenesis, coagulation, lipid metabolism, etc: The glycocalyx incorporates a rich variety of molecular constituents with specific biological functions (*Schriver et al, 2002*). For example, cell surface heparan sulfate proteoglycans are shown to play an important role in lipid metabolism as they bind enzymes such as lipoprotein lipase and have high affinity for certain lipoproteins. This would lead to concentration of plasma lipoproteins close to the corresponding receptors and facilitation of their internalization. Heparan sulfate proteoglycans were also shown to bind antithrombin III (*Mertens et al, 1992*), a key element preventing the initiation of coagulation cascade; therefore the glycocalyx is actively involved in the cell surface anticoagulant properties. Angiogenetic factors such as growth factors and chemokines also have binding affinity to heparan sulfate. It was further demonstrated (*Brown et al, 1992*) that chronic stimulation of muscles results in shedding of the glycocalyx as a possible preparatory step for future capillary sprouting and angiogenesis.

1.4 Glycocalyx and Pathological States

Dysfunction and partial degradation of the endothelial surface layer were recently shown to accompany pathological conditions related to high risk of vascular damage, such as diabetes, hyperlipidemia or high cholesterol concentrations in blood.

Type 1 diabetes is usually characterized by increased systemic permeability leading to high atherosclerotic risk. Clinical studies have shown substantially decreased glycocalyx in diabetic patients that, possibly, contributes to that risk (*Vink et al., submitted*). The overall amount of glycocalyx was measured in healthy and diabetic mice and humans and it was observed that the glycocalyx in diabetic patients and mice was decreased by 30%. Diabetic patients were also shown to have elevated blood levels of hyaluronan. After an additional permeability experiment with dextran-40, a conclusion was drawn that hyaluronan was selectively lost from the glycocalyx due to the diabetes. Hyaluronan overproduction was also seen provoked by the reduced glycocalyx, the high glucose levels (*Yevdokimova, 2003*) or in a more complex way relating the two factors.

The presence of high concentrations of lipids in the blood was shown to be accompanied by damaged endothelial cell membrane permeability (*Constantinescu et at., submitted*). The glycocalyx thickness and overall state were compared for mice fed on normal and high-fat-high-cholesterol diets. It was demonstrated that diet-induced hyperlipidemia reduces the glycocalyx thickness in extents similar to heparinase treatment. Furthermore, its permeability for lipids is substantially increased leading to lipoprotein leakage into the subendothelium and, in the most severe cases, to uncontrolled accumulation of lipid vesicles inside the endothelial cells.

1.5 Composition of the Endothelial Surface Layer

The membrane of the endothelial cells is covered with macromolecules of different structure and enormous functional variety including cell adhesion molecules, e.g. integrins and selectins, enzymes, growth factors, glycolipids, proteoglycans, etc. Strictly speaking all of them are constituents of the endothelial surface layer. In this work though, the accent will be put on the overall dynamic structure, physical and mechanical properties of the glycocalyx and many of the molecular components mentioned above do not especially contribute to the properties in consideration. Thus they will only be shortly mentioned later in this part of the chapter, while chosen components suspected to be the essential ingredients of the endothelial surface layer structure will be extensively described.

Among the macromolecular types whose presence in the glycocalyx is absolutely required are heparan sulfate proteoglycans, charged polysaccharides such as hyaluronan, and adsorbed globular plasma proteins. Rich experimental evidence is available, mostly based on enzymatic treatment of the endothelial surface that removal of any of the constituents mentioned above would lead to visible collapse in the glycocalyx structure. Heparinase and hyaluronidase are shown to greatly reduce or entirely wipe out the endothelial surface layer (*Vogel et al, 2000; Pries et al, 1997a; Warnke and Skalak, 1990; Desjardins and Duling 1990*; *van den Berg et al., 2003; Henry and Duling, 1999*); partial degradation of the glycocalyx is also observed during hemodilution and saline perfusion experiments (*Pries et al., 1998; Long et al., 2004*).

Heparan sulfate proteoglycans: Proteoglycans are a major group of components participating in the glycocalyx. In general, a proteoglycan molecule consists of a core protein with one or more side glycosaminoglycan chains covalently attached through an O-glycosyl linkage. The glycosaminoglycan chains are extended macromolecules with characteristic repeating disaccharide units. One of these disaccharides is usually an amino-substitute of either D-glucosamine or galactosamine and the other is a D-glucuronic or iduronic acid residue. Both units can be sulfated which increments the charge and the heterogeneity of the chains. The most common types are heparan sulfate, chondroitin sulfate and hyaluronic acid.

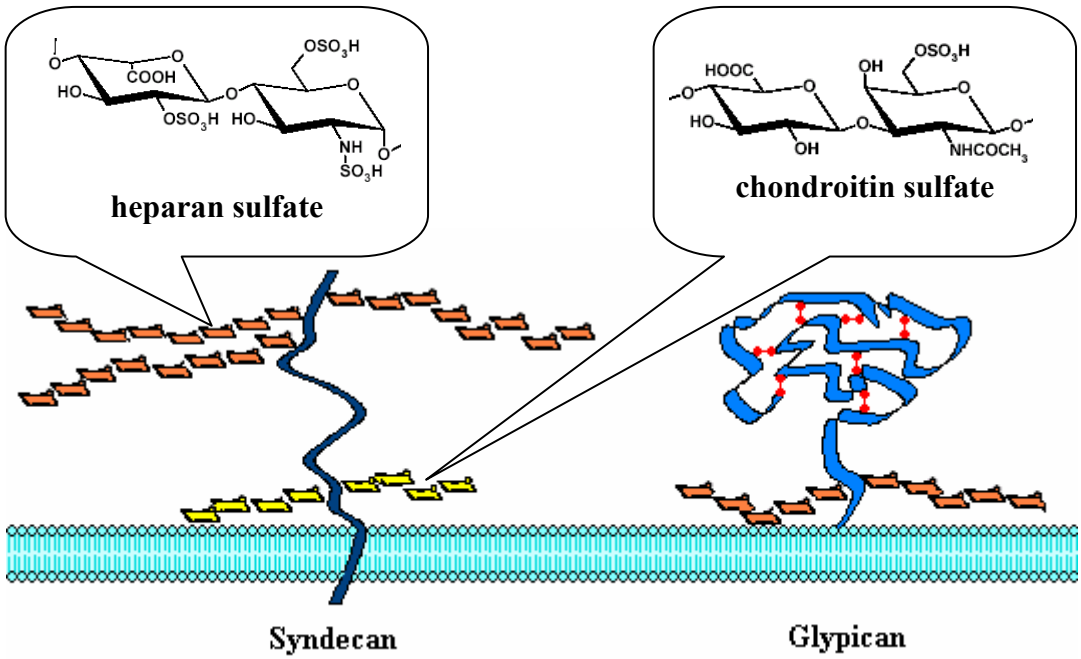

Fig. 1.3

Schematic representation of endothelial cell surface proteoglycans. A syndecan molecule contains up to three heparan sulfate side chains and some members (syndecan-1) – up to two chondroitin sulfate side chains situated very close to the membrane. The average glypican possesses up to two heparan sulfate chains, also situated close to the membrane and a compact globular protein core, held together by multiple disulfide bridges. The basic disaccharide repeats for the two types of side chains are also shown. (*Picture drawn not to scale*)

Among the proteoglycan groups present on the endothelial cell luminal surface, probably the most important are the syndecans and the glypicans (see Fig. 1.3). The **syndecan** family is a four-member group of transmembrane heparan-sulfate proteoglycans (*Bernfield et al, 1992*). They consist of a relatively short core protein (21-42kDa) and a varying number of longer heparan sulfate or chondroitin sulfate side chains (~160kDa) attached to the core at strictly determined sites. The intracellular region of the core protein has a highly preserved sequence; it is known to form dimers and to be associated to the endothelial cell actin cytoskeleton allowing the syndecan molecule to play an important role in various cell signaling pathways and mechanotransduction (*Zimmermann and David, 1999*). The extracellular domain has relatively high proline content therefore could be expected to have an extended structure. The number, fine structure and attachment sites of the side chains vary between the members of the group: for example syndecan-1 has up to three heparan sulfate and up to two chondroitin sulfate side chains, while syndecan-4 has strictly three heparan sulfate chains and no chondroitin sulfate. The heparan sulfate side chains structure is also presented on Fig.1.3. During molecule biosynthesis, the original disaccharide units undergo additional enzymatic deacetylation and sulfation (*Bernfield et al, 1992*), so there is much more sequence variability than shown in the figure (*Lindahl et al, 1998*). The fine-tuning of the heparan sulfate side chains depends on the location/source of the particular syndecan molecule and numerous other factors. It is closely related on its biological functions since it affects the molecule binding properties for various receptors (*Carey, 1997*). The sulfated disaccharide units are not homogeneously distributed along the chains. They tend to form highly charged regions of average length of 6 to 10 disaccharides. Those patches are

divided by longer non-sulfated regions with considerably less charge; their average length is in average between 16 and 20 disaccharide units (*Bernfield et al, 1999*). The boundaries between the two types of regions are usually not sharp but may include short mixed sequences of acetylated and sulfated units.

While there is extensive data available about the structure of the syndecan components, and their biological activity (*Carey, 1997; Beauvais and Rapraeger, 2004)*, there has been little quantitative research on their mechanical and macromolecular properties. In particular, the persistence length (as a measure of the chain stiffness) of neither the protein core nor the side chains is available from literature. What is known is that the core protein does not have a pronounced secondary structure but an extended conformation for which a roughly averaged persistence length is known to be around 5 amino acids or ~4nm (*Bright et al, 2001*). The heparan sulfate is expected to be less stiff than heparin due to considerably lower degree of charge. Data about the stiffness of the heparin chains is available – the persistence length was estimated to be around 20Å (*Khorramian and Stivala, 1986*).

The **glypican** family comprises six molecular types. As with the syndecan group, they consist of a core protein with two or three heparan sulfate chains attached very close to the endothelial cell membrane (see Fig.1.3). The core proteins of the different types have molecular weights ranging from 57 to 69kDa (*Stringer and Gallagher, 1997*) and are covalently bound to the endothelial cell membrane by so-called glycosyl phosphatidylinositol linkages. The core proteins contain 14 highly conserved cysteine residues which provide the possibility for a well pronounced secondary folding held together by multiple disulfide bridges. That results in a fairly compact globular

conformation of the glypican core proteins, which is also very similar between the different glypican types (*Fransson, 2003*). The side chain attachment site positions are also known to be conserved in all the glypicans (*Filmus and Selleck, 2001*). They are restricted within the first 50 amino-acids from the C-terminus (connected to the cell membrane). The length of the side chains of the glypicans is of the same order of magnitude as in syndecans. Its structure is also comparable – the sulfated versus nonsulfated blocks are present with the same functional variety.

Hyaluronic acid: The hyaluronic acid (or hyaluronan or hyaluronate) is a linear highly charged polysaccharide molecule composed of repeating disaccharide units of N-acetyl-glucosamine and D-glucuronic acid, linked together by glycosidic bonds (see Fig. 1.4). It has an enormous molecular weight of the order of 10^5-10^7Da and is known to be

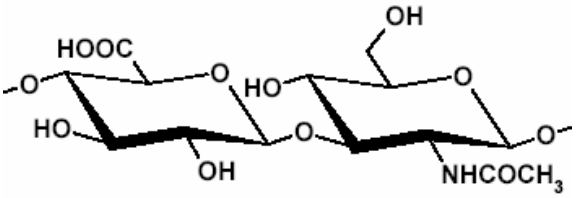

Fig 1.4.

Disaccharide monomeric repeat of hyaluronan.

present in the serum in very low concentrations of around 0.03μg/l (*Laurent and Frasier, 1992*). Its concentration on the endothelial cell surface as a part of the endothelial surface layer though is not known and is difficult to estimate, since it does not come from the plasma but is produced and shed by the cells and then immediately incorporated into the glycocalyx matrix (*Gouverneur et al., 2005*). Because of the charge of the molecule, its persistence length depends on the ionic strength of the surrounding solution (*Fouissac et al, 1992*) and is usually reported to be around 10 nm (*Balazs, 1958; Lapcik et al, 1998; Mendichi et al, 2003*). Persistence length of such order puts the hyaluronic acid into the group of worm-like or semiflexible polymers. Such a conclusion is consistent with

available electronic and atomic force microscopy pictures of hyaluronan (see Fig.1.5). According to some authors (*Cowman et al, 1998*) association between hyaluronan chains in solution is possible and even often observed.

Fig. 1.5

Tapping-mode atomic force microscopy of hyaluronan (*Cowman et al, 1998*). According to the authors, chains of hyaluronan in solution show the tendency to (self)associate.

(*reprinted with permission of Biophysical Journal*)

The hyaluronic acid is not permanently linked to the cell surface through a peptide core like the heparan sulfate. A number of endothelial cell surface receptors for it are known (*Turley et al, 2002; Toole et al, 2002*) including the integral proteins CD-44 and RHAMM, and the protein cores of certain proteoglycans such as versican. The exact mechanism of these interactions is generally not known.

There is no direct evidence concerning possible association of hyaluronan and heparan sulfate. There are indirect implications about the possibility of these two elements of the endothelial surface layer being somehow connected. The extensive destruction of the glycocalyx by heparinase, an enzyme unable to cut hyaluronan chains from the cell surface, implies that the hyaluronic acid chains may be attached to the cell surface through the side chains of the available proteoglycans, either directly or through a third party. This assumption will be used in the investigations later.

The adsorption of **plasma proteins** is apparently crucial for the overall thickness and appearance of the endothelial surface layer. Among the plasma constituents known to incorporate themselves into the glycocalyx are albumin, orosomucoid, fibrinogen, various heparan sulfate binding proteins and a number of enzymes.

The **albumin** is the most abundant serum protein. It is found circulating in the plasma at concentrations 35-50mg/ml. The albumin molecule has a molecular weight of around 66kDa and well pronounced globular geometry sustained by secondary and higher structures. It is responsible for the maintenance of proper oncotic pressure in the blood vessels. it is also a transporting unit for various substances such as hormones and fatty acids. When associated with the endothelial cell surface, albumin also regulates microvascular permeability. There is a group of several specific receptors for albumin (GP-group) known on the endothelial cell surface (*Vogel et al, 2001*). They bind albumin as an initiation of its transport across the endothelium. Other than that, there is evidence of albumin associating with hyaluronan (*Pigman et al, 1961; Bettelheim and Philpott, 1959*) which might be more relevant in explaining the albumin adsorption into the ESL.

The **orosomucoid** is another plasma constituent that binds to the glycocalyx and helps regulate the microvascular permeability (*Schnitzer and Pinney, 1992*). It is a highly sialylated anionic glycoprotein produced by the endothelial cells and in the liver (*Sorensson et al, 1999*), that augments the glycocalyx charge and modulates charged macromolecules penetration into the ESL without affecting the small molecules transport.

Fibrinogen was an early postulated part of the glycocalyx (*Copley, 1962*); later studies however show contradicting results - affinity for fibrinogen in endothelial cells (*Witte, 1983*) and blockage of the binding in presence of albumin (*Delvos et al., 1985*).

1.6 Modeling of the Endothelial Surface Layer

Compared to the various experimental studies of the endothelial surface layer, the efforts for its mathematical modeling are somewhat less extensive. The available models usually do not consider the detailed structure of the glycocalyx, but rather represent the layer as some form of continuous media with prescribed properties, or in terms of purely mechanical structural elements. The reasoning behind this simplification is the presumption that the biophysical and mechanical properties, which the models are attempting to recover, would not depend on the layer's detailed molecular topology and biological activity, but more on its averaged behavior as a continuous medium with assigned viscoelastic and transport properties.

The research works available from literature most often aim to describe the contribution of the endothelial surface layer to microvascular permeability, or the role of the glycocalyx in regulating the blood flow and viscosity and the transmission of shear stress across it. The earliest **modeling** attempts were concentrated on the influence of the glycocalyx on the **permeability** of the endothelial wall (*Curry and Michel, 1980*). The glycocalyx was essentially treated as a porous medium. Although it was explicitly admitted that the 'endo-endothelial layer' is made of fibers forming a three-dimensional network, that fact was only used to define the porosity of the medium as a function of unit lengths of fibers per unit volume. The nature and characteristics of the fibers were not clarified or used in any way. The so defined porosity ε was then used for calculation of volumetric flow J per unit area according to the Carman-Kozeny equation (Carman,

1937), used originally to describe fluid flow in a random arrangement of fibers of arbitrary geometry:

$$J = \Delta P \cdot \frac{A_P}{\Delta x} \cdot \frac{r_f^2}{4K\eta} \cdot \frac{\varepsilon^3}{(1-\varepsilon)^2} \tag{1.1}$$

where ΔP is the pressure drop, r_f is the fiber radius, η is the fluid viscosity; A_p is the area of porous regions per area of capillary wall; Δx is the average length of the porous channels; K is a constant which takes into account the channels geometry. In addition, the authors used previously derived expression for the diffusion coefficient in the case of diffusion of a molecule through a random fiber mesh and ended up with an expression for the permeability P_{D} of the 'fibrous membrane' already in terms of the fiber size parameters:

$$P_{\mathrm{D}} = \frac{A_P}{\Delta x} \cdot D_0 \exp\left(-\sqrt{\pi l}\,(a + r_f) - \pi l\left(2ar_f + a^2\right)\right) \tag{1.2}$$

where D_0 is the diffusion coefficient of the penetrating molecule in an aqueous solution; l is the fibers concentration in terms of fiber length per unit volume, and a is the radius of the diffusing molecule, which is assumed spherical for simplicity. An additional relation was obtained also for the osmotic reflection coefficient.

Using the derived expressions, the authors analyzed available experimental measurements of microvascular permeability for small molecules such as K^+. All the permeability values were found to give the same consistent value for the fiber mesh porosity ε. Using it to find the osmotic reflection coefficients for various substances gave results comparable to experimental ones. Then by using available molecular data to estimate the parameters needed, a value for the permeability of potassium was derived,

also within the range of values from the available experiments. One important limitation of such a model comes from the fact that the endothelial surface layer is much more than just a passive unchangeable barrier.

Later permeability models were mainly based on modifications of the Starling hypothesis, but the role of the glycocalyx was still restricted to a passive porous medium as described by the fiber mesh model of Curry and Michel. A more recent attempt to model the endothelial surface layer in a much more elaborate way (*Stace and Damiano, 2001*) included for the first time explicit representation of the ionic charges in the system and evaluation of the electrochemical equilibrium between the layer and the bulk. The endothelial surface layer was presented as a continuous medium in this model as well – it was an isotropic matrix with homogeneously distributed negative charges submerged in electrolyte solution. The diffusion within such a matrix was considered to be a result of forces provoked by two factors - concentration gradients and electric fields due to possible local non-homogeneity of the mobile counterion distribution:

$$\frac{\partial c^{\gamma}}{\partial t} = \nabla \cdot \left(D^{\gamma} \nabla c^{\gamma} - D^{\gamma} \frac{z^{\gamma} q}{kT} c^{\gamma} \mathbf{E} \right) \tag{1.3}$$

where c^{γ} is the concentration of the diffusing species; D^{γ} is the diffusion constant of the diffusing species; z^{γ} is the valence; $\mathbf{E}$ is the electric field; q is an elementary charge, and k and T are respectively the Boltzmann constant and the absolute temperature. The local electric field in turn was connected back to the charge concentration profiles by Gauss' law:

$$\nabla \cdot \mathbf{E} = \frac{\rho}{\varepsilon} \tag{1.4}$$

where ρ is the local charge density and ε is the surrounding medium permittivity.

The connection between the local charge density and the concentration profiles was given by:

$$\frac{\rho}{q} = \sum z_i c_i \qquad (1.5)$$

The boundary conditions imposed were zero concentration on the capillary center axis (due to symmetry) and on the capillary wall (due to the condition for global electroneutrality). The initial concentration profiles were chosen in the following way: the molecular tracers (i.e. the diffusing molecules) were assumed to have Gaussian distribution; the glycocalyx was assumed to have a box-like profile as a simplification; and the initial equilibrium electrolyte ion density profiles were obtained by solving the problem with the given glycocalyx and tracer profiles in the limit that the electrolyte ion fluxes were zero. After the initial distribution of anionic tracers was applied to the system, it was possible to numerically solve the system of equations above and estimate the diffusion of the tracers through the matrix with time. An example for the diffusion through a box-like glycocalyx profile (in the center) is shown on the Fig. 1.6.

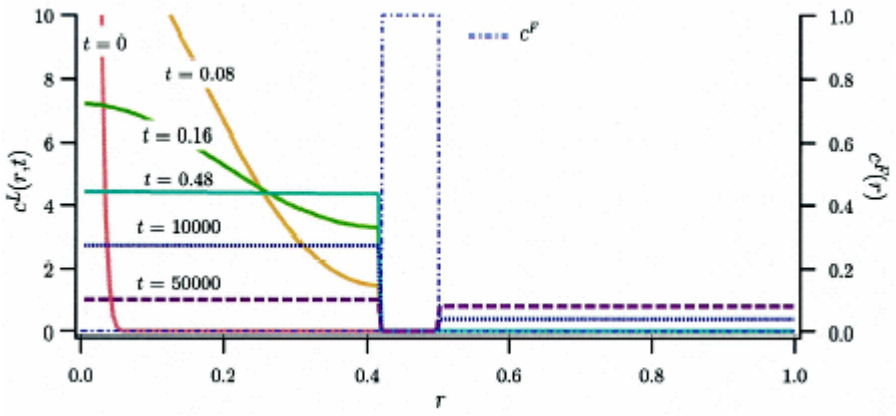

Fig 1.6:

Diffusion of charged molecules through box-shaped profile of glycocalyx (*Stace and Damiano, 2001*)
(*reprinted with permission from the Biophysical Journal*)

The parameters needed for the calculations were taken from experimental data. Then, results for the characteristic time of diffusion for various size dextrans were compared to those available in literature. As a result, the fixed-charge density estimations corresponding to the experimentally measured diffusion times turned out to be considerably different from what could be expected based on the glycocalyx composition. In order to further clarify these discrepancies, alternative experimental techniques were suggested based on the model results.

Other attempts to estimate the glycocalyx charge influence on its permeability were usually based on presenting the endothelial surface layer as a charged membrane in a Donnan-like equilibrium (*Fu et al, 2003; Chen and Fu, 2004*). The electrostatic potential and concentration distributions could then be obtained and the influence of a perturbation of the local electroneutrality due to the presence of negatively charged macromolecules close to the glycocalyx was investigated. It was demonstrated that the charges of both the glycocalyx and the diffusing molecules are decisive for the capillary permeability and selectivity with the negative charge of the glycocalyx greatly restricted the permeability for other negatively charged solutes. On the other hand, when the luminal side solution contained large charged molecules that could not enter the layer due to steric hindrance, the effect of permeability restriction was shown to be substantially attenuated (*Fu et al, 2003*). In the subsequent modification of the model (*Chen and Fu, 2004*), the Starling hypothesis was incorporated. Thus it became valid in presence of osmotic pressure differences that were neglected in the initial study. This provided the possibility to investigate the microvessel permeability dependence on both the osmotic pressure and charges of diffusing molecule and glycocalyx.

A series of investigations is also available in literature that deals with **modeling** the role of the glycocalyx in **blood flow regulation**. In one of the earliest attempts (*Damiano et al, 1996*) the endothelial surface layer was approximated as a porous deformable medium lining the inner walls of a cylindrical tube. It was considered a mixture of two intrinsically incompressible phases, namely linearly elastic solid and Newtonian fluid. Pressure-driven flow of pure fluid and of fluid with presence of closely fitting pellets (representing red blood cells) was studies. Equations for both phases in the glycocalyx region and for the fluid in the lumen were defined. When the red blood cells were present, lubrication theory was used. As a result, fluid flow velocity inside and outside the glycocalyx were obtained together with solid displacement profiles. Additional estimates for the apparent blood viscosity and hematocrit were also evaluated. Using physiological data to fit the dimensionless parameters appearing in the problem, it was possible to estimate the hydraulic conductivity of the endothelial surface layer to be in the range of $10^{-8}\,\mathrm{cm}^4\left(\mathrm{dyn}\cdot\mathrm{s}\right)^{-1}$. In a following study (*Damiano, 1998*) the glycocalyx was still considered to be linearly elastic, but the representation of the red blood cells was elaborated - they were modeled as fluid-filled deformable membranes, very resistant to change in area but readily sheared. The shear elasticity of the red blood cells was not taken into account, just as the membrane bending modulus was considered negligible compared to the large pressure and shear stresses in the lubrication layer between the red cell membrane and the glycocalyx. Thus the model was confined to the case of the high fluid flow velocity limit. This representation made possible the construction of profiles of red cells under flow. The glycocalyx presence was shown to increase the red cell

deformation and membrane tension, as well as the pressure drop. The hydraulic conductivity of the layer was estimated to be of the same order as in the previous work.

An alternative to the linearly elastic approach to glycocalyx mechanics is the idea that the resistance of the glycocalyx to deformation might result from osmotic forces generated by the adsorbed plasma proteins (*Secomb et al, 1998*) rather than from elastic stress. The additional osmotic pressure in the layer is then balanced by increased tension in the chains of molecules composing the glycocalyx. The layer was also allowed to have varying hydraulic conductivity which would account for the diffuse boundary of the endothelial surface layer. This effect would correspond to a sigmoidally varying radial force on the red blood cell as it enters the layer. The red blood cells were described identically with the Damiano model with the same restriction on flow velocity. When experimental data was used for the free model parameters, the result for the hydraulic permeability of the glycocalyx was consistent with the previous modeling attempts. In order to be consistent with experimental data, this glycocalyx model would correspond to a very dilute macromolecular system. The additional fact that the endothelial surface layer is too fragile to survive most staining techniques of the time supports these results. A point was also made that a system so dilute is unlikely to resist considerable shear stresses based on purely mechanical linearly-elastic means which was considered as a supportive argument in favor of the osmotic approach used. When the bending and shear elasticity of the red cell membranes were also taken into account (*Secomb et al, 2001b*) the effect of flow velocity on the red blood cell profiles could be investigated. The obtained average gap width between the glycocalyx and the erythrocytes was very much consistent with experimental data.

The influence of possible non-uniformity in capillary cross section on red blood cell motion and shear stress transduction was also recently investigated (*Secomb et al, 2002*). Using very similar representation for the endothelial surface layer and the red blood cells as in the previous study (*Secomb et al, 2001b*), it was found that the presence of the glycocalyx reduces the shear stress (Fig. 1.7) and flow resistance fluctuations due to the capillary irregularities, thus reducing the fluctuations in the red cell profiles. It was also suggested that the layer might actually play a protective role for the red blood cells, preventing them from more pronounced deformation in much larger shear stresses characteristic for the blood vessels without glycocalyx.

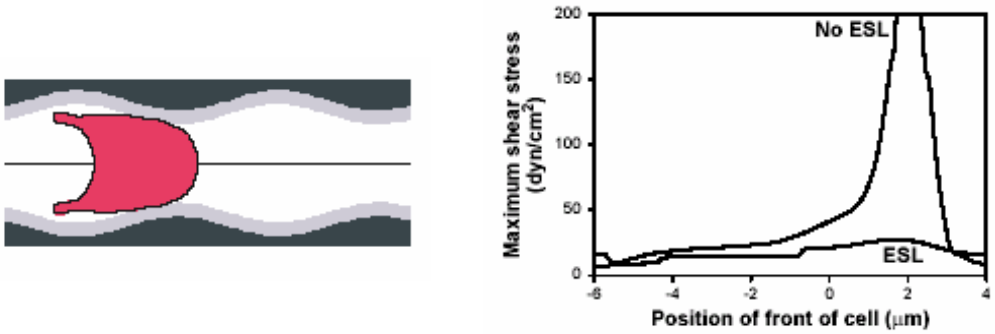

Fig. 1.7:

Left - red blood cell profile in a non-uniform capillary; **right** - shear stress variation with cell positioning with/without the presence of the glycocalyx. (*Secomb et al, 2002*)
(*Reproduced by permission from Taylor & Francis Group, LLC*)

All models that were mentioned so far were dealing with the glycocalyx using continuum approaches. Apparently, those would not be particularly useful in **modeling** the role of the endothelial surface layer in **shear stress transmission** and mechanotransduction. It is particularly in this domain of the glycocalyx function that the underlying molecular structure plays a crucial role. To address this issue, the fluid shear stress transmission was evaluated by modeling the glycocalyx in a more structured

manner (*Secomb et al., 2001a*), as a matrix of stiff strands with fluid shear stress imposed on the top of the layer. The response to flow resulted in intrinsic tension along the strands, which was balanced by the increased osmotic pressure in the layer. A modified Stokes equation was used to describe the two-dimensional flow through the matrix and the deformation of the strands via the matrix displacement field:

$$\mu\nabla^2\mathbf{u} = \nabla p + K\left(\mathbf{u} - \frac{\partial \mathbf{U}}{\partial t}\right) \tag{1.6}$$

where $\mathbf{u}$ is the fluid velocity; $\mathbf{U}$ is the matrix displacement; $p(x,y,t)$ is pressure; K is the hydraulic resistivity of the layer; μ is fluid viscosity; t_0 is the characteristic tension of the strands per unit area. The above expression with the continuity equation and an additional relation between the matrix shear stress and deformation:

$$\frac{\partial \tau_x}{\partial y} = t_0 \frac{\partial^2 U_x}{\partial y^2} = -K\left(u_x - \frac{\partial U_x}{\partial t}\right) \tag{1.7}$$

coming from mechanical equilibrium in x-direction, represent an analytically solvable system of equations in the case of steady uniform unidirectional flow. The fluid velocity, matrix displacement and shear stress contributions from the fluid and matrix were then evaluated. The numerical values for the parameters used were taken from previous theoretical investigations (*Damiano et al, 1996; Pries et al, 2000*) and physiological data and are as follows: $K \sim 10^8\,\mathrm{dyn\cdot s/cm^4}$; $t_0 = 20\mathrm{dyn/cm^2}$; layer thickness $1\mu\mathrm{m}$; imposed shear stress on the top of the layer $5\mathrm{dyn/cm^2}$; pressure gradient $2.5\cdot10^4\,\mathrm{dyn/cm^3}$. Using those values for the parameters, a characteristic flow penetration depth was calculated to be around $0.07\mu\mathrm{m}$. Thus, it was confirmed that almost the entire fluid flow and fluid

shear stress are effectively screened from the cell membrane. On the other hand, the matrix shear stress increases in depth into the layer toward the cell surface.

To model the endothelial layer disturbances that would result from a passage of a red blood cell above it, the solution was sought for the response of the top surface of the glycocalyx to a perturbation in the form of a sinusoidal traveling wave. Using a stream function approach and Fourier analysis, the slowest decaying mode is found providing an estimate of the extent of propagation of the disturbances into the glycocalyx. It is shown that fluctuations in both fluid and matrix shear stress that would normally accompany the passage of red blood cells in capillaries are substantially attenuated by the presence of the endothelial surface layer – a result consistent with the investigations described above (*Secomb et al, 2002*).

Because the major part of the shear stress reaching the cell surface is transported through the glycocalyx, the importance of the points where it is connected to the cell surface is once again underlined, since it is in exactly those points that the shear stress is applied on or through the cell membrane. That idea is developed in a series of research works in which the exact mechanism of the shear stress transmission through the membrane and the corresponding cytoskeletal response were hypothesized in the so called 'bumper-car' model (*Weinbaum et al, 2003; Thi et al 2004*). According to it, the core proteins of the membrane bound heparan sulfate proteoglycans constituting the glycocalyx were fairly rigid molecules, stretching out through the ESL (~400nm). The rest of the layer, directly connected to the protein cores, was considered to consist of much more flexible components and is still viewed generally as a porous medium the flow through which was described by a Brinkman-like equation. The Darcy permeability

of the layer is defined from solutions for Stokes flow through a hexagonal array of cylinders (according to the Squire hypothesis of hexagonal regularity of the endothelial surface layer). The protein core rigidity makes it possible to withstand shear stresses without considerable bending thus explaining the layer's stiffness under flow. On the other hand, when shear stresses are imposed on the layer cores (either by the fluid flow or concentrated through the rest of the glycocalyx network), that would result in the appearance of torques at the intracellular end of the core proteins. Since it is known that the transmembrane regions of the heparan sulfate proteoglycans are in topological proximity to molecules participating in the cytoskeletal response to shear stress, the hypothesis was made that it was the integrated torque produced by the protein cores that was one of the possible driving forces for the initiation of the shear stress response (Fig. 1.8).

Based on this hypothesis, the rigidity of the protein cores was estimated using a viscoelastic model for the timescales of recovery of the endothelial surface layer after compression due to passing of a white blood cell. The value for the rigidity obtained from

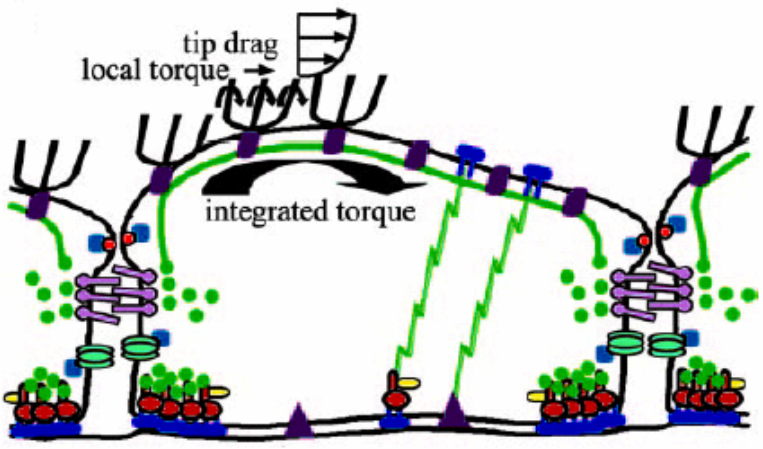

Fig. 1.8

'Bumper-car' model for shear stress transmission with the participation of the glycocalyx core proteins (*Thi et al, 2004*)
(*Reprinted with permission from National Academy of Sciences, Copyright 2004*)

the analysis $El \sim 7 \cdot 10^2 \,\mathrm{pN} \cdot \mathrm{nm}^2$ is about 20 times smaller than the corresponding value measured for actin filaments.

Another area of interest is the behavior of the endothelial surface layer under the influence of a passing white blood cell. Leukocytes greatly exceed the red blood cells both in size and stiffness and when they pass through the microcirculation the **glycocalyx** undergoes substantial **radial deformation**. After the leukocyte has passed, the endothelial surface layer would eventually restore its initial conformation and thickness. The timescale of this event was found to be of the order of a second (*Vink et al, 1999*). One of the first attempts for the theoretical modeling of the glycocalyx radial deformation was attempted recently using a similar electromechanical approach (*Damiano and Stace, 2002*) as the one previously described for modeling microvascular permeability (*Stace and Damiano, 2001*). The glycocalyx was again presented as a charged matrix in electrolyte solution. The diffusion of ions and the electrostatic equilibrium were modeled in the same way as previously with additional expression for the conservation of momentum including again contributions from both shear stress and the local electric field. Also as previously, the blood flow was neglected. The analysis provided an estimate for the glycocalyx characteristic recovery times, as well as the fixed charge density of the layer and the amount of stress that would be enough for it to compress. The value for the fixed charge density is more consistent with estimations based on glycocalyx structure than the previous model from the authors. It was estimated to be such that one fixed charge in the glycocalyx corresponds to around 100 charges coming from the blood. At the same time the stress needed for the layer deformation was in the same range as calculated from alternative theoretical investigations. The overall

conclusion was that the radial compression provokes additional gradients in the electro-chemical potential and leads to a redistribution of the mobile ions within the glycocalyx. The electrochemical potential gradient is considered to be dominant over the tension in the compressed state, and to lead to the glycocalyx restoration to its initial configuration. The main mechanism is therefore considered of electrostatic rather than elastic origin.

A subsequent study was concentrated on the deformation of the endothelial surface layer in the region behind a passing leukocyte (*Damiano and Stace, 2005*). In contrast to their previous work, the electrostatic contributions are not taken into account. Instead, the flow and deformation fields are analyzed respectively by Brinkman-like and linear elasticity theory equations. This study did not claim that the glycocalyx is linearly elastic as in previous models (*Damiano et al, 1996*). Rather, the use of linear elasticity relations simply provided a way to analyze the dependence of the shape, length and other characteristics of the wake region of the endothelial surface layer from its mechanical properties. Once those are estimated, it would always be possible to use them as parameters in a more sophisticated approach accounting for the electrostatics as well. From the analysis, an explicit expression for the characteristic length of the wake related to the layer unperturbed thickness and elastic modulus were obtained. In addition, a connection was made between the elastic modulus in this investigation and electrochemical properties of the glycocalyx that were in focus in the previous electromechanical approach. A value of $50\mu m$ was obtained for the characteristic lengthscale of the wake based on a layer of thickness $0.5\mu m$ and characteristic recovery time $1s$. The corresponding elastic modulus was predicted to be $200 dyn/cm^2$, which was consistent with previous data.

1.7 Possible Modeling Alternatives

The importance of the endothelial surface layer in numerous aspects of vascular function and its proven significance in understanding and dealing with diseases was made clear in the previous parts of this chapter. Those are perfectly adequate reasons for its recent re-discovery and the increasing efforts, both experimental and theoretical, to further clarify its structure, properties and mechanisms of interactions with its surroundings.

From theoretical and numerical points of view there is clearly room for improvement in the model description of the endothelial surface layer. Using the recently acquired knowledge of the likely molecular species important for glycocalyx function and having in mind the recent rapid development of computationally powerful machines, it is now possible to develop more detailed structural biomacromolecular models and use them for numerical experiments (simulations) to gain more insight into the glycocalyx behavior and composition in different conditions (e.g. in presence/absence of shear flow; during hemodilution or ischemia). Such studies could give results in macromolecular detail and at a scale impossible to achieve experimentally at this point. Using numerical experiments it is also possible to investigate the glycocalyx permeability for macromolecules of different sizes and properties, and to study the shear stress transmission through the layer again as a function on the glycocalyx composition and topology and varying physico-chemical parameters. In Chapter 2 of this thesis, such a macromolecular model of the glycocalyx is proposed, while in Chapters 3 and 4

computer simulations of this model are presented for different realization of the glycocalyx and for different physico-chemical conditions.

Since the endothelial surface layer is a polymeric structure in its nature, analytical models based on notions developed in polymer physics might provide another possible approach for further elaboration of glycocalyx properties. Polymers are known to have completely different mechanisms for responding to various external stimuli, and might therefore describe more successfully the glycocalyx behavior and capture details about it that previous models are unable to predict. An entire field of research has emerged in recent years for providing a scaling description of polymer chains in different settings. For instance, scaling theories of grafted polymer chains pioneered by Alexander and De Gennes (*De Gennes, 1976; Alexander, 1977; Rabin and Alexander, 1990, Barrat, 1992; Kuznetsov and Chen, 1998*) are potentially a powerful tool that may be used to describe the endothelial surface layer. Using this approach might be helpful for example in characterizing the possible glycocalyx deformation under flow or in compression.

Associative polymer theories (*Rubinstein and Dobryinin, 1997; Winnik and Yekta, 1997*) can also be successfully introduced for the glycocalyx theoretical description. They combine the specific nature of the macromolecular structures with the possibility of different types of association between the elements (which is what must occur in the glycocalyx), resulting in a system with distinct rheological and mechanical behavior. Recently, it was experimentally shown that associative polymers absorbing on surfaces are able to self-assemble into multiple layer types similar to the presumed glycocalyx topology (*Huang and Santore, 2002*). Thus, this might be an appropriate way to model the dynamic equilibrium between the endothelial surface layer and its surroundings and

the influence of the glycocalyx structure and thickness on factors like the plasma composition and applied shear flow. In Chapter 5 of this thesis, a simple scaling model of the glycocalyx is proposed that incorporates aspects of the theories of grafted polymers and associating polymers. This model is used to study the behavior of the glycocalyx in conditions qualitatively similar to those studies by simulation in Chapters 3 and 4. Chapter 6 concludes this thesis with a discussion o the model and the simulations and connection between the results of these studies and available experimental results.

2. Numerical Experiments – Simulation Methods and Topology Model

2.1. Coarse-Graining Approach and Macromolecular Systems

Virtually every system can be numerically described in many various levels of detail, from accounting for electron orbits and energy levels to continuum approaches. The corresponding information that can be obtained depends on the level of detail chosen, characterized by appropriate lengthscales and corresponding timescales, which can vary by many orders of magnitude. For example, if the glycocalyx is described at the atomistic level of detail, the type of information available would include the lengths and types of bonds between the atoms, very intimate molecular conformations of the monomeric units of its different constituents, etc. It may also be possible to observe, if present, the exact secondary and tertiary structures of the protein and the higher order arrangements of glycan components of the layer; to predict characteristic binding domains for different molecular types; and to observe the conformational changes accompanying a binding event or the detailed conformational change from local shear stress application. If such information was desired, the simulations would require a very high level of detail in the glycocalyx description and modeling.

Such an approach, though able to give a deep insight into the exact atomic structure and properties of the endothelial surface layer, would require an immense amount of computational time and resources for a system as large as the glycocalyx (a representative system would consist of billions of elements). On the other hand, the characteristic time step of the simulation has to be consistent with the level of detail,

which in the atomistic representation corresponds to time steps of order 10^{-12}s, as required to properly describe atomic trajectories. However, the characteristic time scales for macroscopic behavior is larger by many orders of magnitude. As a result, even if such a simulation was attempted, the timescales which would be achievable would not be anywhere nearly long enough to obtain useful statistically-averaged information about the macroscopic properties of the glycocalyx. From that point of view, imposing such level of detail would be an unreasonable way to explore biophysically relevant properties of the endothelial surface layer such as the overall thickness profile of the layer, the average positions of the ends of the different constituents or the overall rearrangement of the glycocalyx in response to shear flow or the shear stress transduction.

Choosing to study the glycocalyx on a larger scale can greatly reduce the degrees of freedom in the system and thus the amount of computational resources required for its analysis, so that it could become possible to perform the simulations needed for timescales characteristic for the particular properties of interest. However, realistic large scale models of the glycocalyx cannot entirely neglect the smaller scale properties of its constituents. So, general information about appropriate microscopic properties is still required from alternative sources. It would be then incorporated into the model in the form of additional parameters. Such an approach to building larger scale models from microscopic information is known as coarse-graining. This approach has already been successfully used in investigating linear polymer brush properties under shear flow (*Grest, 1999*), self-assembly of block copolymers (*Srinivas et al, 2004; Srinivas and Klein, 2004*), polymer melts (*Padding and Briels, 2002*) etc.

Based on the coarse-graining methodology, a simplified macromolecular description of the various glycocalyx components has been developed in this thesis research that mimics the overall molecular topology of the glycocalyx and the generic macromolecular properties of its constituents. The following two sections present the topological model for the glycocalyx and the computer simulation methods used to study this model under a variety of physical conditions.

2.2. Glycocalyx Topology Model

Based on the extensive amount of data available about the glycocalyx constituents and their possible interactions and relative arrangement, a coarse-grain macromolecular model for the layer composition and topology was developed as follows.

Two distinct sub-layers are assumed to comprise the overall structure of the endothelial surface layer. The **inner sub-layer** consists of a number of identical molecules built following the average structure of a syndecan molecule (Fig. 2.1). Since

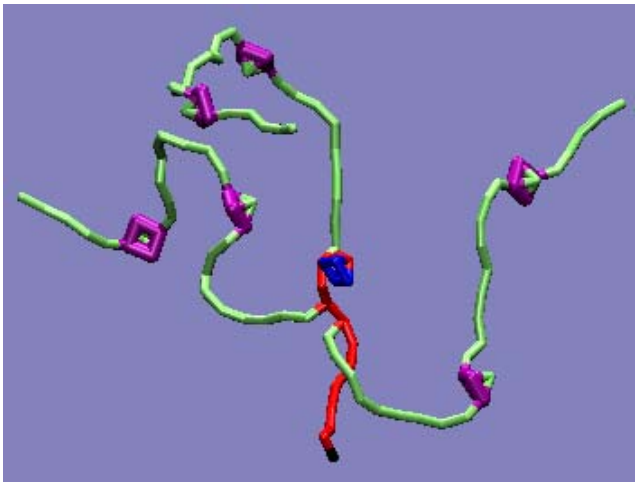

Fig. 2.1:

Model of an average heparan sulfate proteoglycan molecule. The different bead types are as follows: ***red*** – core protein; ***black*** – anchoring point; ***blue*** – protein active end; ***green*** – heparan/chondroitin sulfate side chain; ***purple*** – active sites on the side chains

the different members of the syndecan family do not drastically differ in their macromolecular composition and structure on the lengthscales of interest, the inner sub-layer's compositional variety was limited to only one molecular type. Another important proteoglycan group on the endothelial cell surface, the glypican family, has a distinctly different topology including pronounced secondary structure of its protein core and different arrangement of the side chains, but in this particular investigation those differences are neglected.

The model for the anchored proteoglycan molecule consists of a relatively short central chain representing the core protein, and three identical longer side chains representing the heparan sulfate or chondroitin sulfate branches of the proteoglycan. The central chain has special bead types at both ends. One of them is meant to play the role of an anchor when the corresponding molecule is grafted on a surface. The other binding domain signifies the hydrophobic sequence in the end of the extracellular region of most syndecans which is hypothesized to have signaling properties. The side chains have a fixed number of evenly spaced active sites which provide possibility for association with the other constituents of the modeled endothelial surface layer.

We now take a closer look into how the **active sites** of the model proteoglycan molecules are built. These are not assumed to be simply single-bead spherically symmetric binding elements. If they were modeled in such a simplistic manner, there would not be a robust way to achieve selectivity of the binding (see the lower left panel of Fig. 2.2). As the glycocalyx is a biologically active system, it is natural to expect that the binding of its elements would be on a specific, one-on-one basis. Therefore, a selective, "ligand-receptor" type of binding in the model would be a desirable feature. One of the possible ways to decrease the promiscuity of binding is to create more complex geometry of the active sites. This approach was used successfully in the investigation of the association of coiled-coil protein elements into bundles using coarse-grained simulation methods (*Zhou and Karplus, 1999*). The method involved modeling of amphiphilic alpha helices by simple bead spring representations that utilized complex dihedral potentials to maintain the helical geometry (*Guo and Thilumalai, 1996*). Recently, this approach has been employed in simulations of the association of proteins

with end terminal amphiphilic helical elements into regular hydrogel networks (*Heine et al, unpublished*), In these latter studies, protein hydrogel crosslinks were formed by trimeric helical bundles, as shown in the top panel of Fig. 2.2.

In the present case, there is no experimental information available about the possible geometry of the active binding sites on the various glycocalyx constituents. However, for our purposes there is no particular need for such detailed local information. Rather, the aim here was to create a geometric configuration for the active site which would be as simple as possible, so as to not affect the overall behavior of the endothelial surface layer as modeled, and at the same time would provide specific binding between its constituents. The chosen pyramidal configuration can be seen in Fig. 2.1 and in the lower

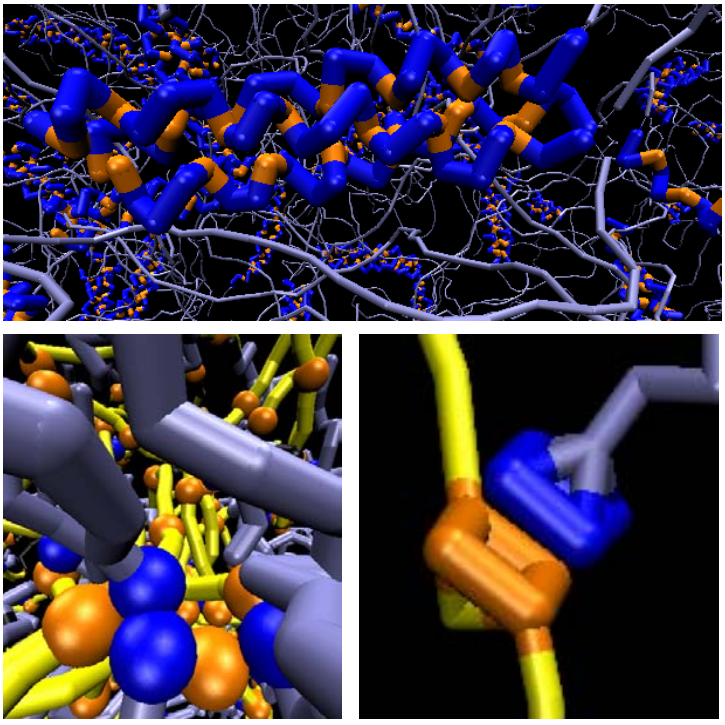

Fig. 2.2

Various possible binding site geometries and corresponding cluster topologies:

Top: triple bundle of helical binding domain in a protein hydrogel:
orange – hydrophobic active beads; ***blue*** – hydrophilic beads

Left: irregular cluster of single bead active sites (spheres in ***blue*** and ***orange***);

Right: regular double pyramid associate

right panel of Fig 2.2. Even though it is rather mechanistic and has little in common with any known binding site topology, it has proved convenient because of its small size and rigid, compact form, strongly constraining its binding configuration as shown in the

figure. A characteristic feature of such binding site geometry is its high sensitivity to the energy of interaction; as a relatively weak attractive interaction between corresponding ligand and receptor beads is amplified in a synergistic way for properly aligned complexes.

The **secondary sub-layer** of the modeled glycocalyx is composed of two major constituents. The first molecular type is represented by extended linear semiflexible chains that model the polysaccharide constituents of the endothelial surface layer, such as hyaluronic acid (Fig. 2.3). The molecules of this type have active end sites designed for association with the active domains of the proteoglycan side chains; they also have evenly spaced active domains of a different type along each chain. Those are designed for association with the third constituent of the model which will be described next. The active domains of this molecular type are also designed with pyramidal binding structures.

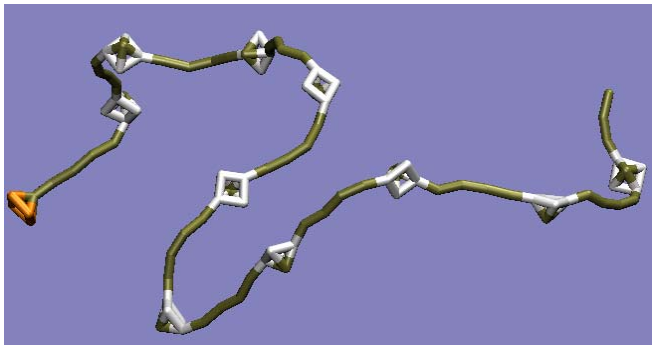

Fig. 2.3

Model of an extended glycan molecule (ex. hyaluronan): ***orange*** – active end domain; ***olive*** – regular non-active beads; ***white*** – active beads along the chains for serum protein association

The third and final constituent of the presented glycocalyx topology model is a molecular type meant to denote an averaged structure of plasma proteins (Fig. 2.4). They are modeled as identical short, flexible linear chains with pyramidal active domains at both ends. Sufficient flexibility is required in order to achieve a coil-like equilibrium conformation for these linear chains that mimics the relatively compact structures of soluble plasma proteins. One of the active domains of each chain end will be used for

possible association to the hyaluronan active sites, while the other is reserved for possible association between the serum proteins themselves. A full representation of the endothelial surface layer topology model - one syndecan molecule with its associated polysaccharide and plasma protein molecular species attached is shown in Fig. 2.5.

The association between the active sites of the different constituents can be modeled

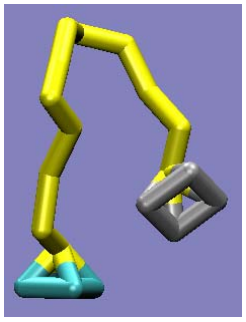

Fig. 2.4

Model of a coil-like plasma protein molecule
silver – active domain for association with glycan chains; ***yellow*** – regular non-active beads; ***cyan*** – active domain for association to other globular protein molecules

as either covalently bound or dynamically associating and dissociating via attractive inter-particle Lenard-Jones (or other) potentials. Each approach can be used to obtain certain insight into the glycocalyx dynamical structure and properties.

The first approach, using covalent bonds to build the endothelial surface layer, is a good starting point for exploring the differences between conformations of the glycocalyx resulting from its partial enzymatic degradation. In this way, it would be possible to observe how the thickness and the overall appearance of the layer will change after removing the serum protein molecular type from its composition. In terms of available experimental data, such studies could be compared to results from hemodilution experiments, in which the plasma proteins may be washed away from the glycocalyx leaving behind the rest of the constituents (*Pries et al, 1998; Long et al, 2004*). Moreover, the conformation of the layer after further removing its glycan components might be compared with the results of experimental hyaluronidase treatment of glycocalyx (*Mochizuki et al, 2003; Henry and Duling, 1999*). Finally, studies of

glycocalyx layers stripped down to the glycoprotein could be compared with the results of experimental heparinase digestion of the glycocalyx (*Vogel et al, 2000; Desjardins and Duling, 1990; Florian et al, 2003*).

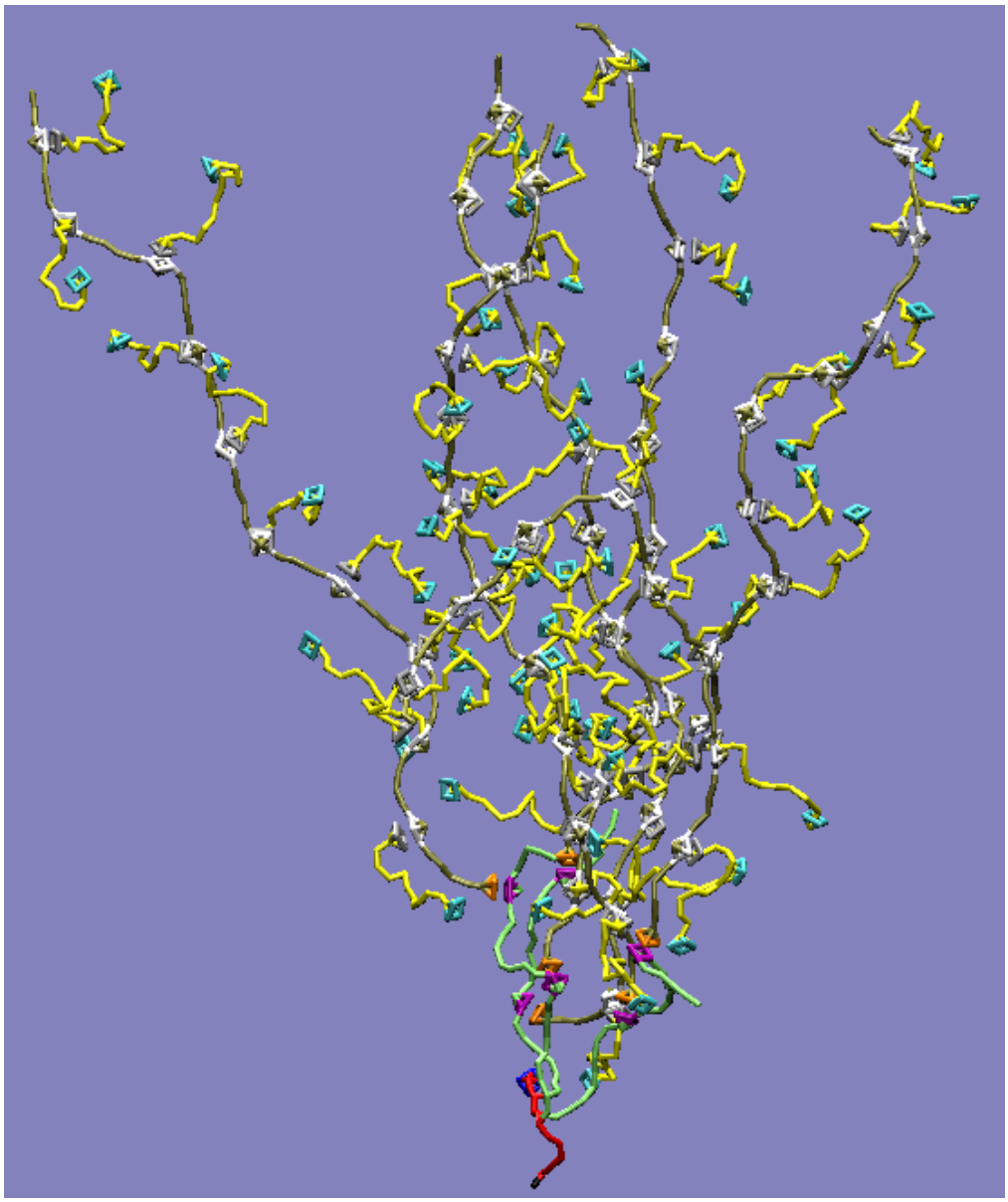

Fig. 2.5

Endothelial surface layer topology: the different building elements with their relative positions and binding partners are shown on an exemplary syndecan molecule with the hierarchy of other molecular species attached according to the assumptions of the model. Note that the bonds between the elements are permanent in this example.

2.3. Numerical Experiments Setup

Using the topology model defined in the previous section of this chapter, it is possible to define and conduct a large array of numerical experiments. In principle, a variety of numerical simulation techniques, including Brownian Dynamics, Monte Carlo, and Molecular Dynamics, could be used to study our model for the glycocalyx.

We have chosen to use Molecular Dynamics (MD) simulation methods in this work. They are generally based on evolving in time the system in consideration by solving Newton's equations of motions for all of the system elements at each time step. The method can be successfully applied for systems both in equilibrium and in steady state conditions (for example – macromolecules in shear flow). The major alternative of Molecular Dynamics is the Monte Carlo (MC) simulation method which is based on biased sampling of the energy space by random displacement of several degrees of freedom in a system and further trial of the move during which it is accepted or rejected based on Boltzmann weight. The MC method is not considered appropriate for using in non-equilibrium cases due to its purely stochastic nature because of which velocity of the beads in the system is undefined and dissipative processes cannot be observed. As for the other available alternative, the Brownian Dynamics includes ad-hoc modeling of the solvent hydrodynamic properties such as viscosity and damping, while the solvent is taken to be a continuous medium. Such an approach can also result in a non-realistic description of the hydrodynamic interactions, especially in systems containing macromolecules.

Our MD simulations were performed using a parallel processor enabled code, namely LAMMPS, developed by Sandia National Laboratories. The bonds and angles between the different types of monomer units in the glycocalyx building elements were described using a coarse-grain bead and spring model. In the spirit of the coarse-grained approach, the beads as defined do not correspond directly to monomer units in the constituent molecules, but to whole blocks of monomers. The glycocalyx as modeled was immersed in a solvent solution consisting of explicitly added single beads (each of them again corresponding to a block of real solvent molecules). The overall bead density in the system, mainly defined by the presence of the solvent beads, should correspond to fluid state at normal pressure and room temperature. The use of explicit solvent in these simulations allows for more realistic studies of molecular transport and the response of the glycocalyx elements to flow conditions.

The entire system is confined to a simulation box which is periodic in two of the dimensions. In the third dimension, namely on the top and bottom, walls are introduced. They are represented by Lenard-Jones potentials acting on all beads, preventing them from passing through and getting out of the box. The lower wall also serves as a grafting surface for the syndecan molecular elements of the glycocalyx via their terminal anchoring beads. The attachment of the anchor beads to the walls is achieved by imposing zero initial velocity and zero force on the respective bead type at all times.

Whenever flow is to be imposed on the system, it is achieved by moving the two walls in the opposite directions. Moreover, the anchor beads are also set in motion with an appropriate constant velocity, in order to keep them grafted to the moving walls. The initial velocity is set to the desired value and the force at each moment is again imposed

to be zero. Since the walls are molecularly smooth, attempting to create fluid flow simply by moving the wall would result in solvent slip near the wall and thereby hinder the establishment of the desired hydrodynamic flow profiles in the bulk solvent. In order to avoid this effect, short linear chains are additionally grafted on the upper wall of the simulation box. They have no reference to the endothelial surface layer model – their only purpose is to insure that there will be no slip at the wall and the shear stress would be passed on to the bulk resulting in proper hydrodynamic fluid flow profiles.

Harmonic spring potentials are used to model the bonds and angles between the monomer units of chain molecules:

$$E(x = r, \theta) = K_x (x - x_0)^2 \tag{2.1}$$

where E is the energy of interaction; r is the distance between the two consecutive beads in a molecule forming a bond; θ is the angle between three consecutive beads in a molecule; K_x characterizes the strength of the interaction; x_0 is the equilibrium bond length or the equilibrium angle. In the case of bonds, the force constant should be chosen large enough to ensure a narrow enough distribution of bond lengths. The angle force constant is the parameter regulating the respective molecule type stiffness. Since specific geometry is required for the pyramid structure of the active domains, special angle types will be used to describe the angles within the active domains and the force constants of those will be such that they are extremely stiff and holding at all times the exact geometrical shape desired.

The non-bonded interactions, including those responsible for the dynamic association and dissociation when applicable, will all be described by standard Lenard-Jones potentials with an imposed cut-off distance:

$$E(r)=\begin{cases}4\varepsilon\left(\left(\frac{\sigma}{r}\right)^{12}-\left(\frac{\sigma}{r}\right)^{6}\right) & r<r_{\text{cutoff}}\\ 0 & r>r_{\text{cutoff}}\end{cases} \tag{2.2}$$

where E is the energy of interaction; ε gives the interaction strength; σ is the unit of length, and r is the distance between the non-bonded beads. Changing the force constant and the cutoff distance enables fine regulation of the non-bonded interactions. This in turn provides the ability to control the distribution of the associating elements between their two possible states (associated and dissociated) and thus regulate the relative population of macromolecular elements between the glycocalyx and the bulk solvent phase. Since the chosen geometry for the active domains is found to be quite sensitive to both the interaction energy and cutoff distance, by tuning those properly it is possible to get the desired one-on-one, "ligand-receptor" type of association.

All simulations were performed at room temperature and in isothermal conditions, provided by the use of a Langevin thermostat. As with previous simulation studies of polymer brushes under flow (*Grest, 1999*), the thermostat was coupled exclusively to the flow in the vorticity direction (y-direction), thereby inhibiting the screening of hydrodynamic interactions between molecular elements and minimizing the perturbation of the hydrodynamic flow profiles in the flow-gradient (x - z) plane

Since the non-bonded interactions are modeled by Lenard-Jones potentials, it is clear that the possible effects of the electric charges in the system are entirely neglected. This might seem as an extreme approximation since the glycocalyx is known to be a highly charged structure and its charge is considered to be an important part of its microcirculation permeability regulatory function. However, when it comes to its dynamical structure and mechanical properties, the presence of charge in the model is not

of crucial importance. Rough estimates indicate that the concentration of ions in the blood exceeds by two orders of magnitude the concentration of ions in the glycocalyx (*Stace and Damiano, 2002)*. Thus, any long range interactions between the charged units are effectively screened out, while the remaining short range interactions can be successfully captured using appropriate Lenard-Jones potentials. For the case of grafted polyelectrolyte layers, theoretical evidence indicates that in the regime of low charge density or relatively high electrolyte concentrations compared to the brush charges, the chain conformations and overall layer behavior can be qualitatively explained using neutral grafted polymer notions (*Harden et al, 2001; Harden et al, 1997*). Thus, not taking into account the charges in the system is justified in this initial investigation, although the possibility of improvement in future studies has to be acknowledged.

Several series of simulations have been performed for this thesis research. In the first series, described in Chapter 3, fully covalently bound layers are explored. At first, the different molecular constituents are sequentially included into the layer and the effect of each one on the layer properties (thickness, density of the different components, etc.) is analyzed. The conformations of the chains of the different constituents within the layer are also characterized. Parallels are then drawn between the conformations of the partial layers and the results from partial enzymatic degradation of the endothelial surface layer, and the results are compared to available experimental data for selectively degraded glycocalyx. Next, each of the layers constructed in the first part is subjected to flows with range of shear rates and the response in the layer conformation is observed. It is then possible to estimate the glycocalyx permeability to shear flow, changes in end to end

distances, chains orientations, ends distributions and other features for the different components as a function of the applied shear flow and glycocalyx constitution.

In the next series of simulations, presented in Chapter 4, the plasma protein constituents of the full endothelial surface layer are allowed to dissociate. As a result, a dynamic equilibrium distribution of these mobile elements is established between the glycocalyx and the bulk phase. This equilibrium distribution is explored as a function of the energy of interaction between the associating elements and their chosen geometry, and the dependence of this distribution on shear flow velocity is also investigated. The molecular permeability of the glycocalyx for the plasma proteins is also characterized by tracking these molecules, and analyzing their pathways and diffusion through the layer or in the bulk. Finally, the possible effect on the endothelial surface layer from protein concentration reduction in plasma is explored. By varying the concentration of plasma proteins in the bulk, their new equilibrium distributions between the glycocalyx and the bulk phase are obtained. The distribution dependence on various factors such as the bulk concentration and the energy of interaction between the plasma protein and the extended glycan chains to which it associates. The effect on overall layer thickness and density is also determined.

In Chapter 5 a simple decorated polymer brush model for the glycocalyx is presented and analyzed. Predictions of this model for the properties of the glycocalyx under quiescent and flow conditions are then compared qualitatively to the simulation results from Chapters 3 and 4. Finally, in Chapter 6 the successes and shortcomings of the model and its analysis are discussed and directions for future research are proposed.

3. Molecular Dynamics Simulations of Covalently Bound Glycocalyx

3.1. Specifications and Parameter Values

Using the Molecular Dynamics method and the topology model described in the previous chapter, computer simulations were performed on three chosen configurations of the endothelial surface, in quiescent conditions (Section 3.2) and in the presence of shear flow (Section 3.3). The first configuration consists of proteoglycan molecules only, grafted randomly but relatively uniformly on the bottom wall of the simulation box. The second configuration consists of the proteoglycan molecules in their original grafted positions, with a given number of polysaccharide chains attached to their binding sites. The third configuration consists of the same molecular assembly as the second one with a certain number of globular protein molecules attached to the binding sites of the polysaccharide chains. The bonds between the associating elements have been made irreversible at this point to study the effects of glycocalyx topology on layer properties.

All the parameters used to define the system in the subsequent numerical experiments are made dimensionless using corresponding scaling values. All length-dimension variables such as bond lengths, box size, etc. have been non-dimensionalized using the single bead size σ as a characteristic lengthscale. The energy variables are non-dimensionalized by the thermal energy kT as a characteristic energy scale, with the temperature being room temperature $T \sim 300\text{K}$ (also used in these simulations for scaling of the temperature). Time has been approximately non-dimensionalized by the characteristic time τ needed for a single bead to diffuse its own size in quiescent

conditions. All the remaining composite parameters are non-dimensionalized by proper linear combinations of the characteristic energy, time and length.

In dimensionless units as defined, the simulation box dimensions $\left(L_{\mathrm{x}}, L_{\mathrm{y}}, L_{\mathrm{z}}\right)$ were chosen to be $44.72 \times 44.72 \times 100$. The first two dimensions were defined such that the base of the box is a square in which it is possible to fit 10 proteoglycan molecules so that their dimensionless grafting density is $\sigma = 0.005$ again normalized by a single bead area. The third dimension was chosen such that there was ample space for the whole layer without the box being filled by it or the glycocalyx being compressed by the upper wall. At the same time, it is important that the box height does not exceed substantially the glycocalyx thickness, because this would lead to simulation of more solvent molecules than necessary, resulting in a major increase in the computational resources needed with no additional information obtained.

The molecular types present in the three layers have the following specifications. The core proteins of the proteoglycans consist of 17 beads, the first of which is the anchor bead for grafting to the wall and the last 5 of which are grouped into an active domain, which results in an expected conformation as if the core protein length was actually 13 beads. The places of attachment for the three side chains to the protein cores were chosen to be at bead 8, 9 and 11 starting from the anchoring point, which roughly corresponds to the relative positioning of the heparan sulfate chains on an average syndecan molecule. The side chains were chosen to be identical, with length of 33 beads each and two evenly spaced active domains along the chains. Similarly to the protein core, because of the concentration and compact positioning of the beads in the active domains, the 33-bead side chain is expected to behave roughly as a 25-bead long chain with single-bead active

sites. The number of active domains corresponds to approximate fraction of 0.07 of active domains or to 9-bead spacers between two neighboring active domains. The glycan molecules were made to be 98 beads long with 10 active domains along each chain and one at the end. That corresponds to effective chain length of 54 beads with single-bead binding domains or to 4-bead spacers between neighboring active domains. The plasma protein type has chain length of 20 beads of which the first 5 and the last 5 are grouped into binding domains, resulting in a compact molecule with effective size of 12 beads.

The amount of the different constituents in this set of simulations is the following. The first layer consists of 10 proteoglycan molecules; the second layer consists of 10 proteoglycans and 60 polysaccharide (hyaluronan) chains permanently attached to the 60 available binding domains of the proteoglycan side chains. The third layer consists of the 10 proteoglycans and 60 hyaluronan molecules comprising the second layer, with 600 globular protein molecules permanently attached to the 600 available binding domains of the polysaccharide chains. In all simulations, there are also 50 chains of 10 beads each, grafted to the top surface for shear stress transfer into the bulk and a very large number of solvent single bead molecules. The overall bead density of the simulation box is chosen to be 0.7 which corresponds to about 140000 total beads in the box. Even in the case when the fully-grown endothelial surface layer is simulated, the percentage of solvent in the box is still predominant – around 86% of the beads in the box are solvent. For comparison, the solvent percentage is 95% when the plasma proteins are removed and 99% in the syndecan-only layer. That is the major reason for regulating the size of the simulation box to be such that computational resources are not wasted on performing simulations on a box in which a considerable amount of space is filled by solvents only.

The coefficients for the bonds and angles potentials as well as non-bonded interaction potentials are chosen as follows. All bond lengths are given the same equilibrium value 1.0 and the same force constant 500.0. A force constant of this magnitude would give a narrow distribution of bonds with minimal values around 0.8 and maximal 1.2. The angle equilibrium values are 180° for all chains, 90° for the branching points, and 60°, 90° or 135° for the angles that maintain the pyramid structure of the binding domains. The angle coefficients for the various molecular types are in the range from the highly flexible chain limit of 0.2 for the branching points, 0.5 for the globular protein molecules and the grafted short chains on the top of the box, 0.8 for the core protein, 2.0 for the side chains to the semiflexible limit of 5.0 for the hyaluronan chains (those values of the angular stiffness coefficients correspond to a range of persistence lengths from 1-2 beads for the globular proteins, 3-4 beads for the core proteoglycan protein, ~6 beads for the heparan sulfate side chains and ~8 beads for the hyaluronan). On the other hand, the angle coefficients for the binding domains are chosen to be extremely high (50.0) to insure stiffness of the structures, while the coefficients for the angles connecting the chains to the binding domains are modeled so that they do not substantially affect the overall stiffness of the chain. More precisely, the values for the different chain types connecting binding domains are made to be half the value of the regular angle coefficients of the corresponding regular chains, namely 0.25 for the grafted short chains and plasma proteins, 0.4 for the proteoglycan cores, 1.0 for the proteoglycan side chains and 2.5 for the polysaccharide molecules.

Since all the elements in the layer are permanently bound, the non-bonding interactions between all atom types are made "neutral" with $\varepsilon = 1.0$ and

$r_{\text{cutoff}} = 2^{1/6} = 1.122462$. Such choice of parameters would correspond to repulsion between the particles once the distance between them becomes less than the chosen cutoff and no interaction whatsoever then the distance exceeds that value. The only exceptions in the non-bonding interaction parameter choices concern the anchoring bead type interactions. In order to keep those beads grafted, there should not be any force acting on them at any time. That is achieved by assuming that for the non-bonded interactions between a bead of the anchoring type and any other bead, the strength of interaction is zero, given by $\varepsilon = 0.0$.

The simulations were run with a time step of 0.005 and at dimensionless temperature $\widetilde{T} = 1.0$, corresponding roughly to room temperature. The time step was chosen so that it does not lead to instabilities in the calculations and at the same time is large enough to avoid waste of computational time.

The initial coordinate files used to start the simulations were built only considering the connectivity of the endothelial surface layer and without taking into account the chains stiffnesses, homogeneity of the beads distributions etc. Thus, at the starting point the configuration of the molecules in the simulation box is quite far from equilibrium. On average about 20 to 40 million time steps were required to reach the equilibrium state of the glycocalyx and the surrounding solvent; corresponding to a dimensionless equilibration time of 100000 to 200000. Among the different components, the fastest to equilibrate are the solvent beads, and the slowest are the polysaccharide chains because of their large size. The systems were checked for equilibrium based on a complete set of measurable parameters (layer thickness, homogeneity of the solvent density, ends

distributions etc); once they reach constant values, with acceptable thermal fluctuations, the system is considered in equilibrium.

Once in equilibrium, the systems are simulated for another 20 million steps in order to gain enough data for proper analysis and statistic averaging. Coordinate files from these equilibrated quiescent endothelial surface layer configurations were subsequently used to initialize MD simulations of these layers under applied shear flows. For these shear studies, linear velocity profiles in the z-direction in the simulation box were obtained by moving the beads attached to the walls in opposite directions with constant predetermined velocities, as explained previously. Two values for the dimensionless wall velocity were investigated, namely $v = 0.01$ and $v = 0.1$. All other simulation parameters were identical to those utilized in the quiescent studies. The average time needed to reach steady state in the presence of solvent flow ranged from 20 million steps for the smaller systems (PG-only layer) to 40 million steps for the full ESL layer. After the steady state was reached, each system was again run for additional 20 million steps to gain enough data for analysis.

Output data from the simulation procedures include coordinates for each bead in the system dumped, velocity profiles as a function of the $z-$coordinate based on averaging over all beads, and density distributions per component also as a function of the $z-$coordinate. The data is collected into files every given number of steps – for the coordinate file the data is dumped every 100000 steps and for the density and velocity files the interval is 50000 steps. Various FORTRAN codes were used to extract the information needed from the raw data.

3.2. Effect of Layer Composition

Simulation snapshots of the conformations from the three investigated structures of the endothelial surface layer at equilibrium are shown in Fig. 3.1. They provide qualitative insight into the particular role of each constituent in the overall layer conformation and may perhaps be compared to available experimental results on glycocalyx enzymatic or hemodilution degradation. The overall impression from the snapshots is that the proteoglycans do not contribute substantially to the layer thickness

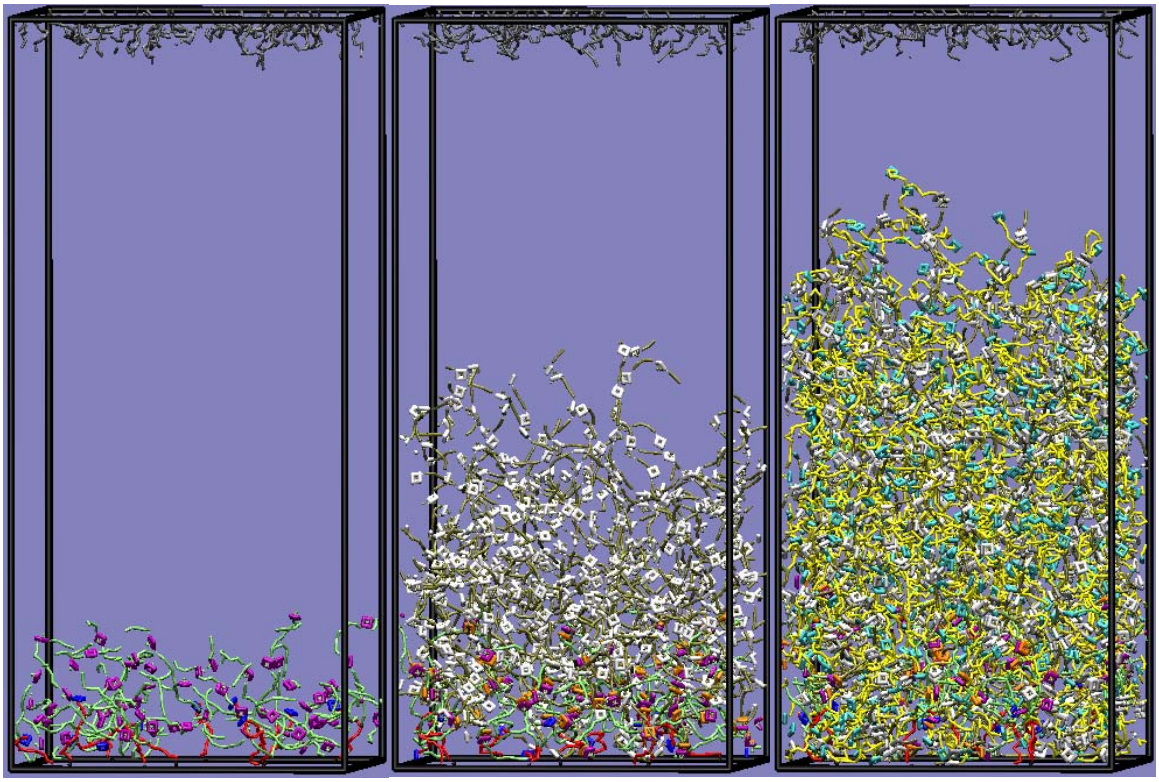

Fig. 3.1

Quiescent equilibrium conformations of the endothelial surface layer as a function of its composition: **left** – proteoglycans only; **center** – proteoglycans with associated hyaluronan; **right** – proteoglycans, hyaluronan and associated plasma proteins. Colors of the different bead types are as defined in chapter 2. Solvent beads are not drawn for clarity.

or its density. Rather, it is the polysaccharide chains that provide most of the glycocalyx thickness, due to their comparably higher stiffness to the remaining elements, and it is the plasma proteins that contribute most to the glycocalyx density (and therefore to the osmotic pressure).

More detailed analysis of the three layer structures is possible through evaluation of relevant physical properties of the layer and its constituents such as density profiles, and the free end distributions and end-to-end distances of the various macromolecular components of the glycocalyx.

Figure 3.2 shows several types of density profiles. These are calculated by slicing the simulation box into a given number (in this case it is 100) of intervals in the $z-$direction (the density is not dependent on the remaining two coordinates) and directly counting the number of beads of each type inside the intervals. Note that these densities are not normalized on the plots and that the overall bead density (including solvent beads) everywhere is fixed at $\rho = 0.7$. The three layers are denoted respectively PG-only for the proteoglycan layer; PG+HA for the proteoglycan with attached polysaccharide (hyaluronan) version of the glycocalyx and full ESL for a layer containing all the components including the associated plasma proteins. In the top portion of Fig. 3.2, the overall density of the three layers is plotted against the $z-$coordinate of the simulation box. The PG-only configuration only reaches an average dimensionless height of 10-12 and its density is more than an order of magnitude less than the overall bead density. That corresponds to a very diffuse structure, which as will be seen in later investigations, is by no means effective in preventing shear flow from reaching the cell surface. The density of the PG+HA configuration exceeds that of the first layer by a factor of 2. Moreover, the

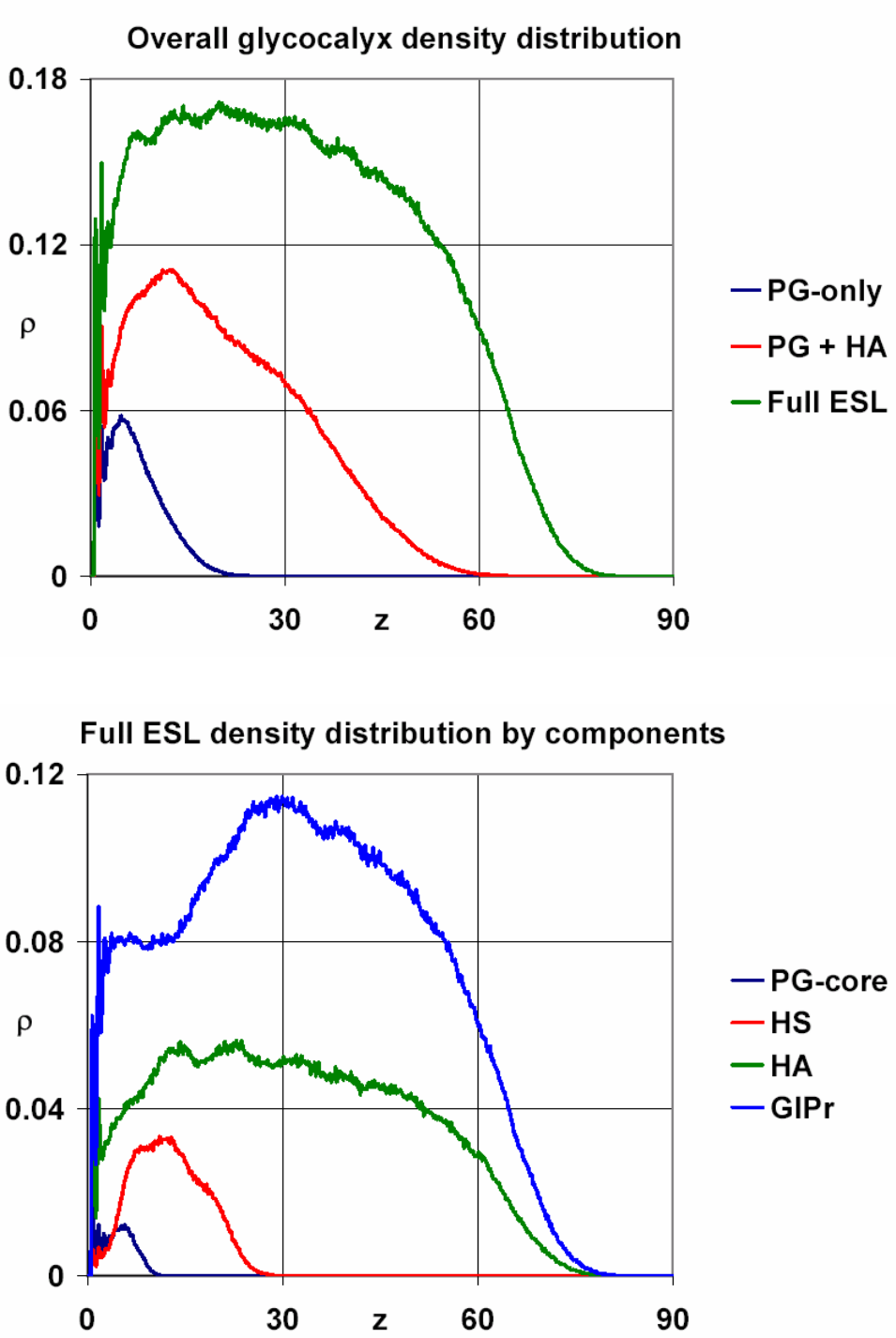

Fig 3.2

Density distribution in the equilibrated glycocalyx layers:
top – overall layer density for the three layer conformations;
bottom – contribution of the glycocalyx components to the overall layer density

height of the PG+HA is essentially double that of the PG-only layer. Similar ratios between the density and height of PG+HA and the full ESL are also observed.

The bottom plot of Fig. 3.2 shows the relative contribution of the different constituents in the full ESL layer to the total density. The following abbreviations are adopted here: PG-core signifies the core protein of the proteoglycan molecular type; HS (heparan sulfate) is the denotation of the proteoglycan side chains; HA stands for the polysaccharide chains with the hyaluronic acid as a main representative and GlPr is the generic plasma protein structural species.

The observations from the snapshots of the layers are confirmed by the density profiles. The proteoglycans, especially their core protein parts play an insignificant role in the overall glycocalyx density – their density is close to an order of magnitude smaller than the density of the elements associated on top. The extended glycan chains effectively determine the overall height of the layer. The associated proteins also influence somewhat the extent of stretching of the HA chains due to the increased osmotic pressure resulting from their presence in the layer, but their main role seems to be to increase the glycocalyx density and thereby decrease its permeability to shear flow. Figure 3.3 shows dimensionless osmotic pressure profiles $\Pi_{os}(z)$ for the PG, PG +HA and full ESL layers. These osmotic pressure profiles were calculated from the dimensionless density profiles ρ(z) using the mean-field relationship between osmotic pressure and dimensionless density for a semi-dilute polymer solution in good solvent conditions *(Rubinstein and Colby, 2004)* with subsequent non-dimensionalization:

$$\Pi_{os} = \frac{\pi_{os}\sigma^3}{kT} = \rho^2 \tag{3.1}$$

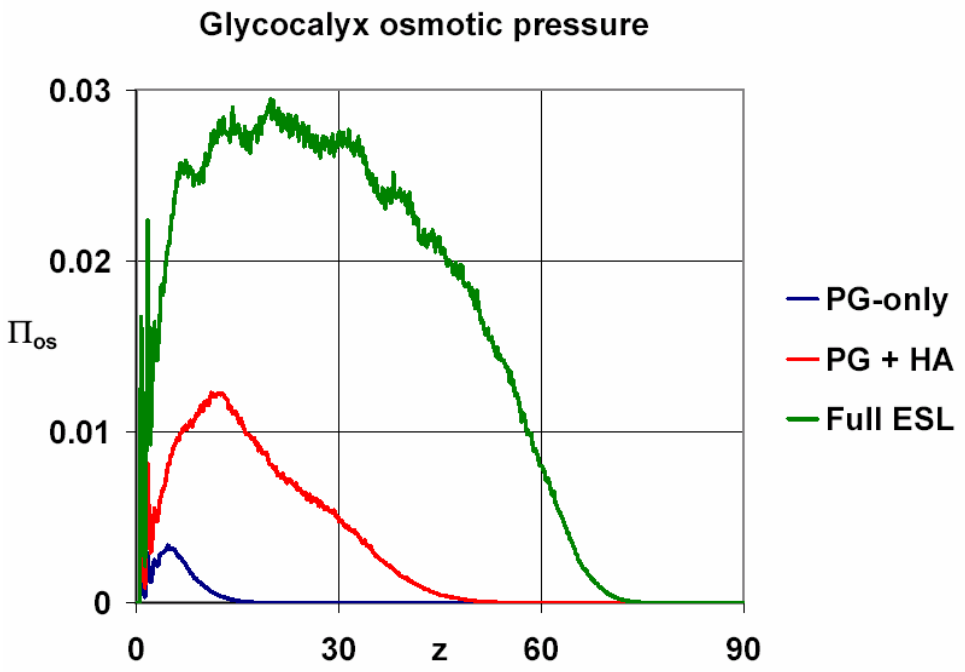

Fig. 3.3

Osmotic pressure of the endothelial surface layer as a function of the layer composition.

where ρ is the bead density; π_{os} and Π_{os} - dimensional/dimensionless osmotic pressure and σ is the single bead size.

Since the dimensionless osmotic pressure is proportional to the square of the bead density, the effect from the endothelial layer build-up on it is even more pronounced compared to the effect on the bead density. In fact, the osmotic pressure increases by about an order of magnitude from the PG-only to the full ESL configuration with the main increase due to the addition of the globular plasma protein species. That confirms again that the presence of the outer-layer components, the polysaccharide chains and especially the plasma proteins is decisive for the glycocalyx properties such as permeability for various molecules and the shear flow (hydraulic permeability).

In the next Figure 3.4 density profiles for individual glycocalyx components are presented as a function of layer type. The response of all the molecular types seems to be similar - as the glycocalyx is built-up by the addition of components ($PG \rightarrow PG + HA \rightarrow PG + HA + GlPr$), all chain types tend to stretch further away from the grafting wall. Such behavior seems logical if the effects of osmotic pressure are taken into consideration. As additional components are included, the glycocalyx density increases, resulting in a considerable increase of the osmotic pressure inside the layer (Fig. 3.3). This elevated osmotic pressure naturally provides additional normal force acting on the chains, resulting in incremental chain extension. Ultimately it is the balance of osmotic forces and internal chain tension that determines the equilibrium chain extension of the macromolecular elements of the glycocalyx.

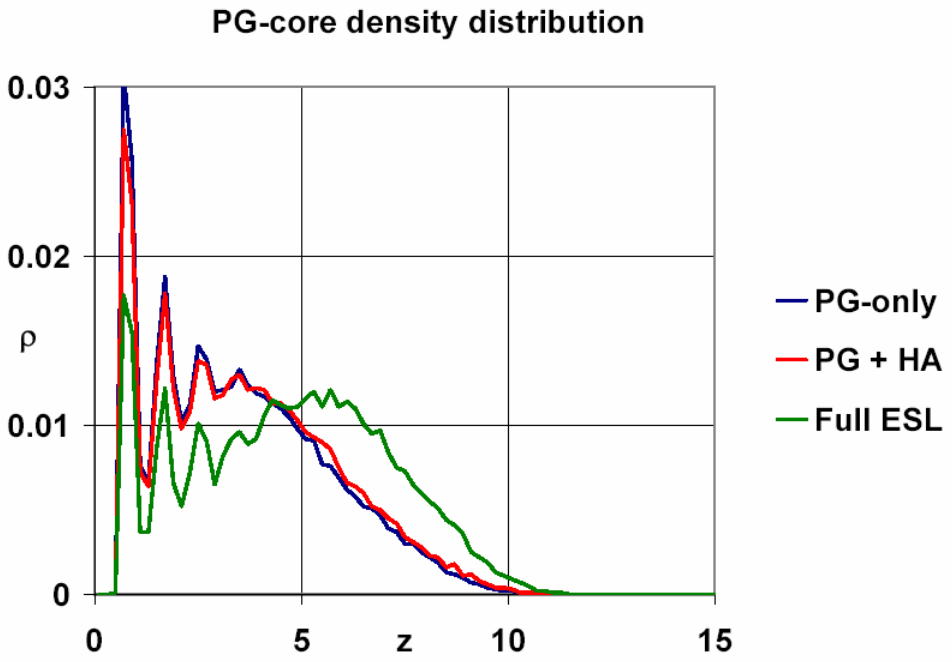

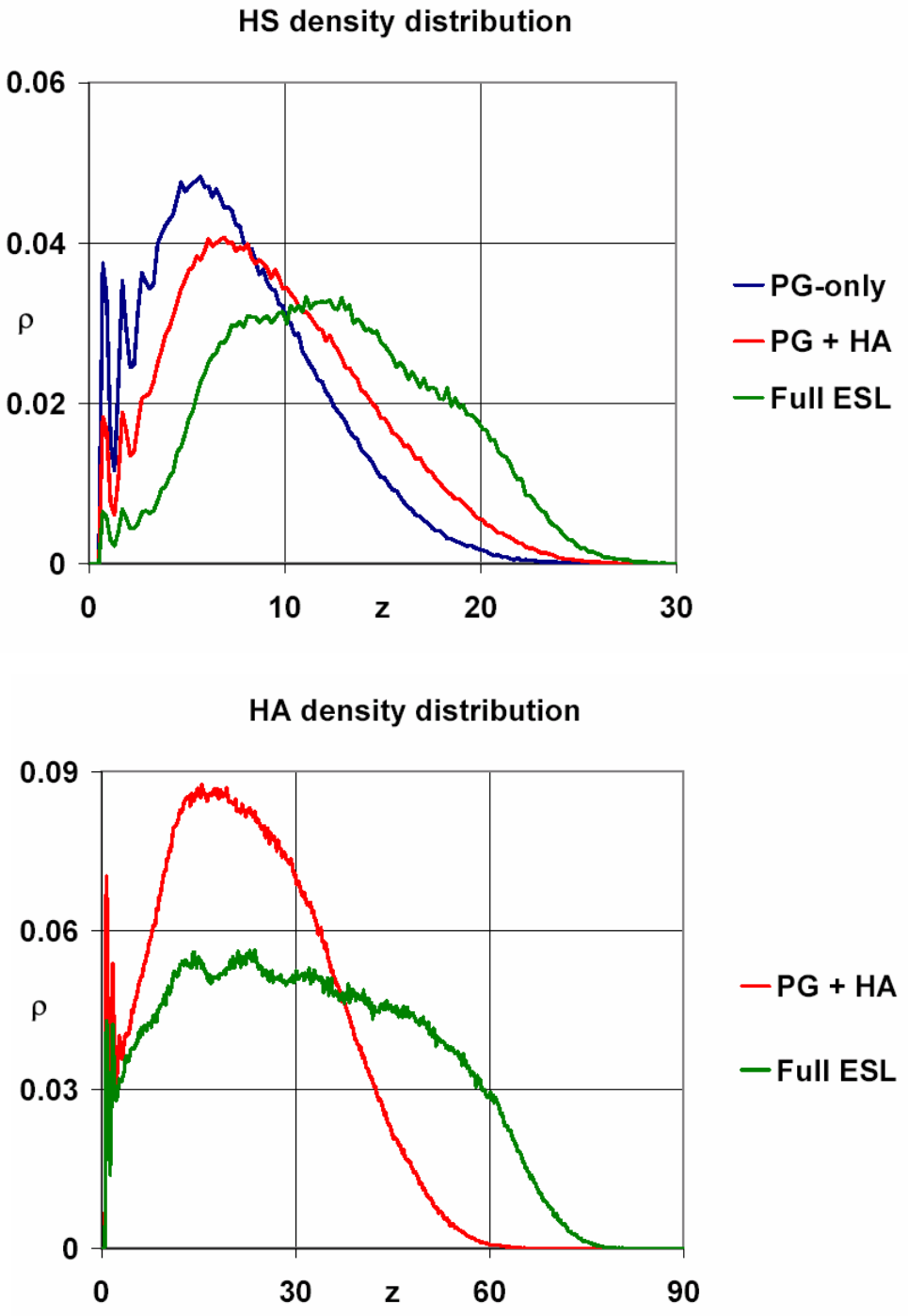

Fig. 3.4

Density profiles dependence on layer composition by component: **from top to bottom** (including plot on previous page) – proteoglycan core, heparan sulfate and polysaccharide density profiles.

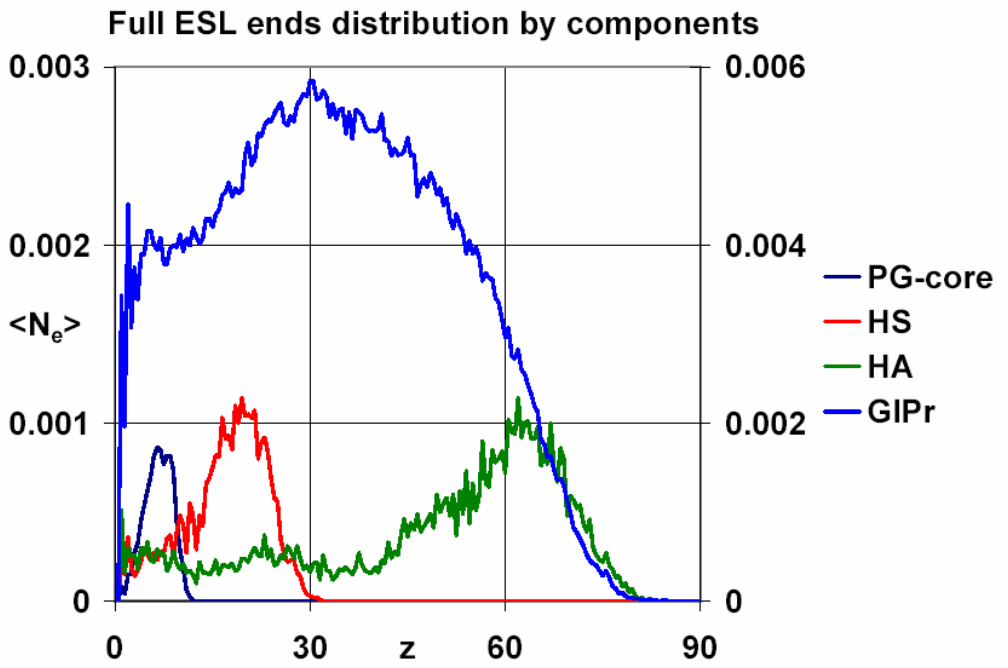

Fig. 3.5.

Free end distributions of the components of the equilibrated full endothelial surface layer. Note: the secondary axis is for the plasma protein end distribution due to the big difference in overall number of ends of GlPr versus the other components.

Figure 3.5 shows the chain end distributions of each molecular species in a full ELS layer. As with the density distributions, the simulation box was divided into a number of intervals (in this case 200) in the $z-$direction, and the number of chain ends for each molecular type was counted in each interval. The fine interval partition was chosen to minimize the noise level in the end profiles without introducing artifacts due to the small size of certain glycocalyx component molecules (e.g. syndecan protein cores). The number of ends per slice was then normalized by the slice volume, so that $\langle N_e \rangle$ from all the plots has the meaning of number of molecule ends per unit volume. Note that the second vertical axis on the right is used exclusively for the end density of the plasma protein types.

The free ends distributions on Fig 3.5 indicate the degree of stretching in the conformations of the layer components. The proteoglycan core proteins are shown as only partially stretched, with a considerable portion of the ends situated close to the grafting surface (at a distance of about 5 beads from the grafting surface). The globular plasma proteins ends distribution generally follows closely the hyaluronan density, which is to be expected since the globular proteins are short and grafted to the polysaccharide chains. The side chains of the proteoglycans and the hyaluronan molecules are the most stretched components, with a small fraction of the molecular ends being buried in the layer and most of them extended to a degree described by a relatively narrow peak (according to the positioning of those peaks the predominant chain ends for the heparan sulfate side chain are situated at around 20 bead and for the polysaccharide chains at around 60 beads from the grafting surface). We have to note that the amount of stretching of these glycan molecules, which are not directly attached to the grafting surface, is not as directly related to the free end distributions as in the case of the proteoglycan core proteins. This is due to the fact that the positions of the grafting points of the side chains and hyaluronan chains have a distribution of their own. More quantitative information about the stretching can be obtained from the end-to-end distances estimation, as will be discussed in the next section on the influence of shear flow on the layer conformation. Nevertheless, the outward shift of the glycan free end distributions in response to the addition of components in the layer does provide at least qualitative information about chain stretching in the layer.

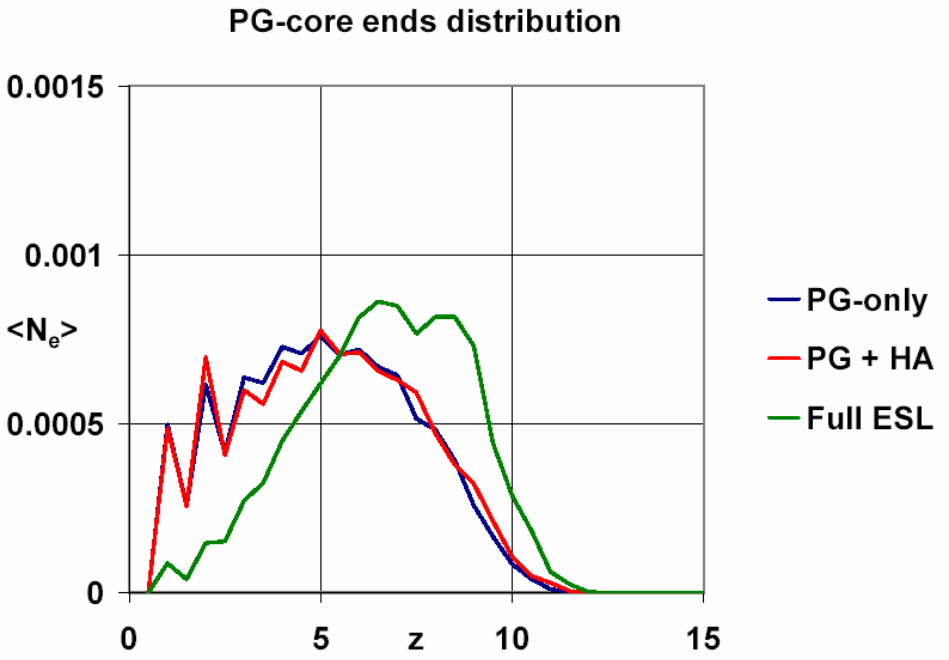
PG-core ends distribution
0.0015
0.001
<Ne>
0.0005
0
0
5
z
10
15
PG-only
PG + HA
Full ESL

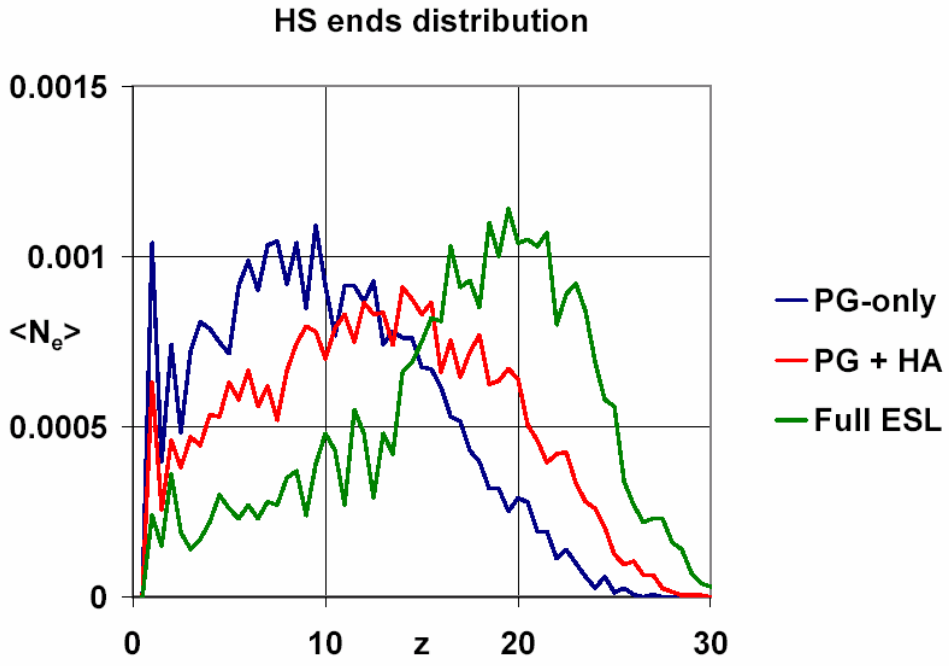
HS ends distribution
0.0015
0.001
<Ne>
0.0005
0
0
10
z
20
30
PG-only
PG + HA
Full ESL

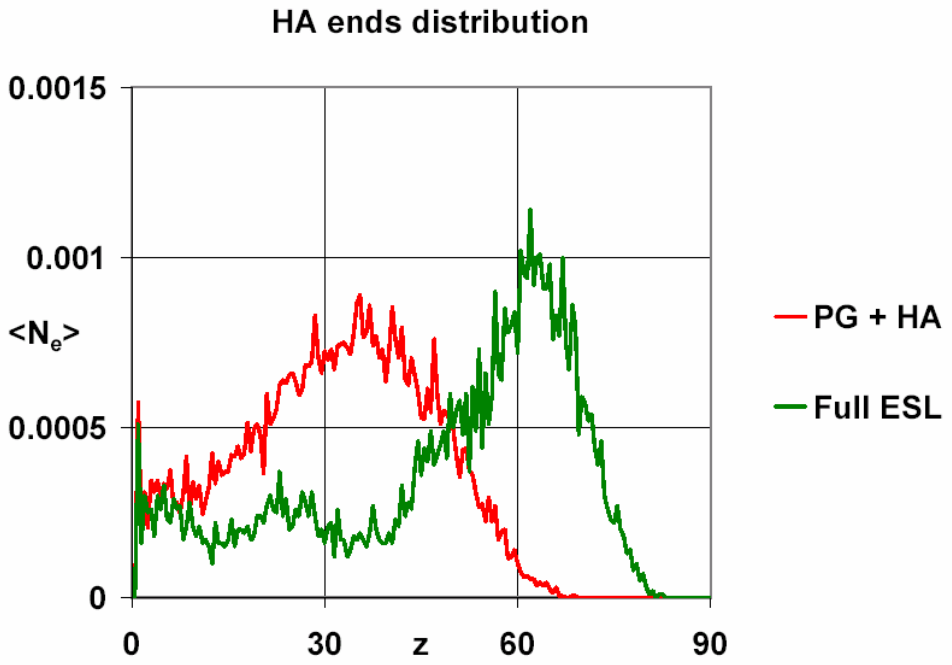

Fig. 3.6

Glycocalyx component end distribution dependence on layer composition: from top to bottom (including previous page) – PG-core, heparan sulfate and HA ends distributions.

The free end distributions of the separate components show similar trends as the density distributions as the glycocalyx is built up with additional components, as shown on Fig. 3.6. This effect is most pronounced in the case when the plasma proteins are attached to the layer, which further confirms the importance of the osmotic forces for the glycocalyx equilibrium conformation. Among the glycocalyx components, the hyaluronan ends distribution is shifted to the greatest extent by the addition of the plasma proteins. This is also an intuitive and logical result, given the chosen topology model for the endothelial surface layer.

3.3 Effect of Shear Flow

Simulation snapshots for the three glycocalyx layers in the quiescent case (left) and sheared (middle and right) by the two velocities, $v = 0.01$ and $v = 0.1$, are shown in Fig. 3.7. From these snapshots, a qualitative idea about the response of the layers to the shear flow can be obtained. More specifically the dependence of the glycocalyx thickness and component chain orientations on the applied shear flow can be seen. Overall, it is clear that the lower applied shear flow does not considerably change the layer structure (compare left and middle layer configurations on each level in Fig. 3.7). On the contrary, when stronger shear flow is imposed on the system, there is visible decrease in the layer thicknesses for the case of the decorated glycocalyx structures (PG+HA and full ESL) and pronounced chain tilting in the flow direction in all cases (compare the left and middle configurations to the right ones in Fig. 3.7 top and bottom).

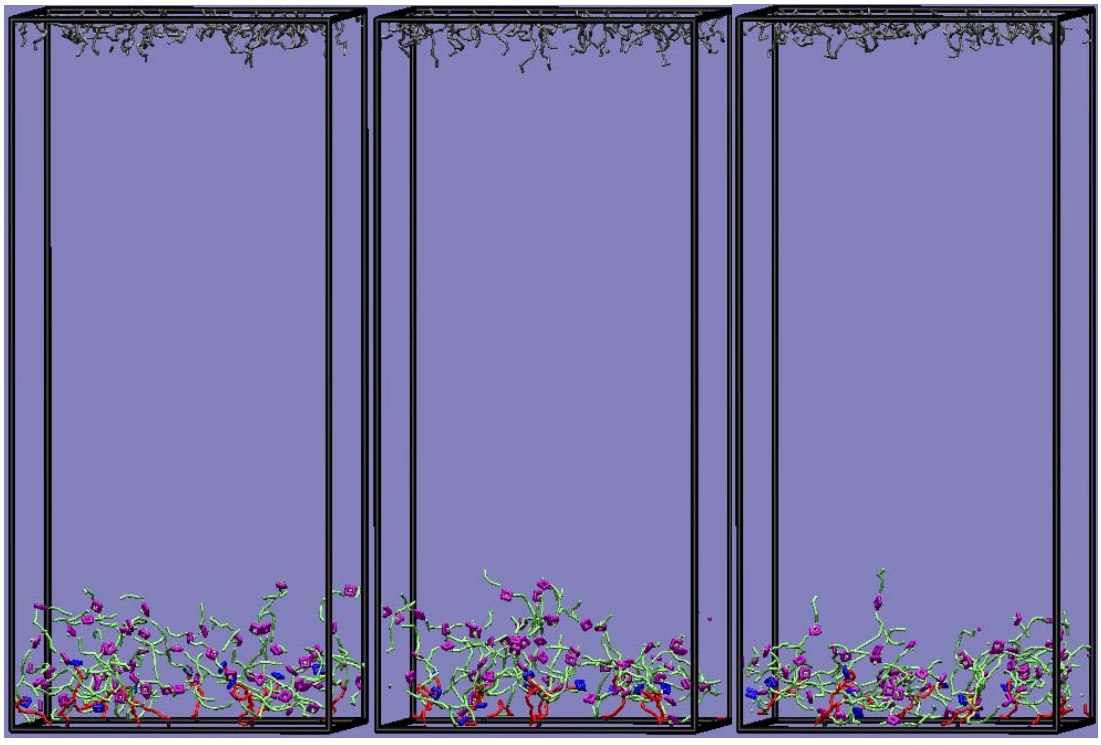

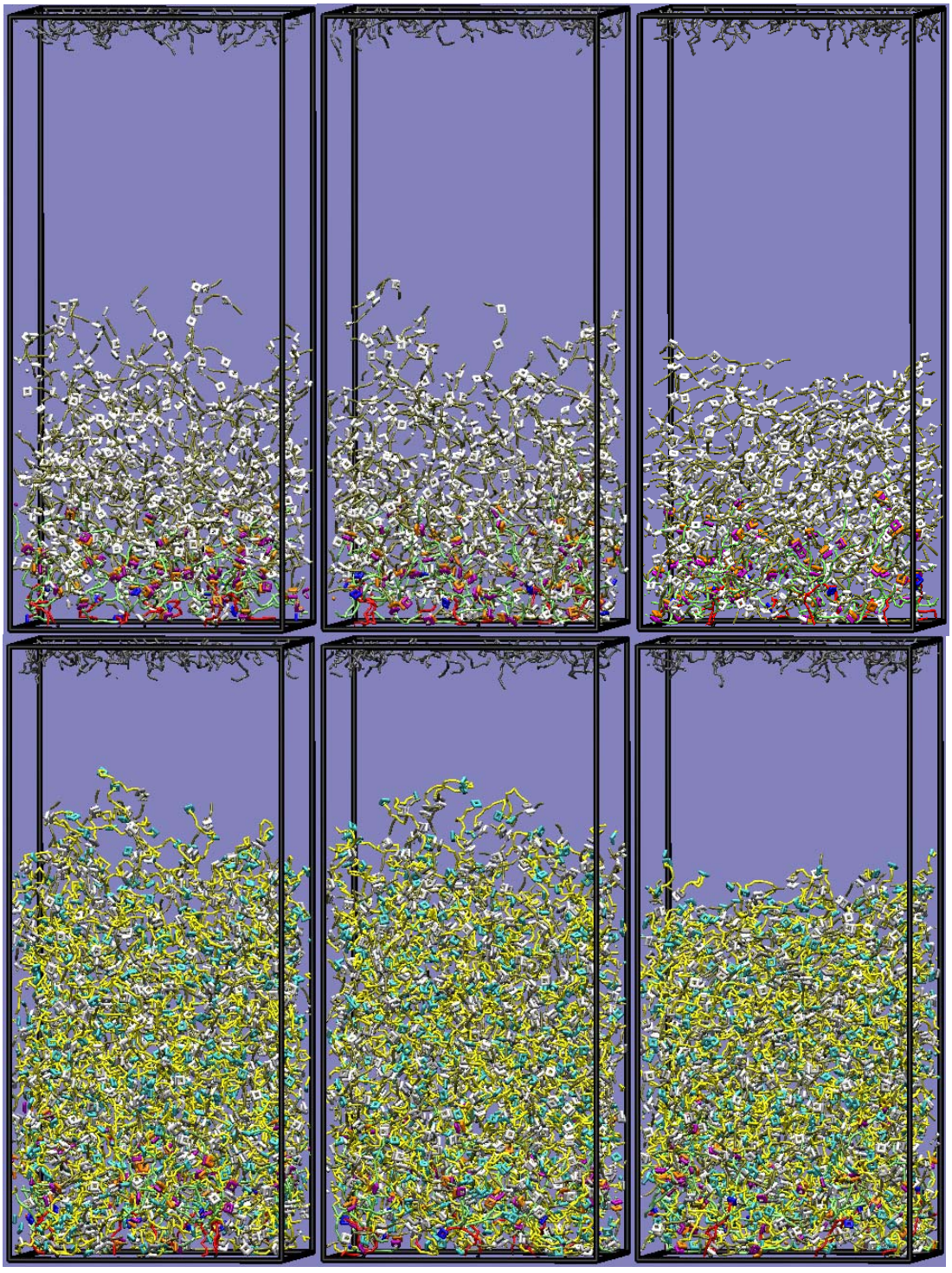

Fig. 3.7

Glycocalyx under shear flow: **left to right** - quiescent case, $v = 0.01$; $v = 0.1$; **top to bottom** (including previous page)– PG-only, PG+HA, full ESL

As in the case of layers in quiescent conditions, the layer density and end distributions were analyzed for the different velocities. In addition, it was also possible to construct solvent velocity profiles for comparison with density profiles. Such a comparison serves to verify that the hydrodynamic interactions in the system are captured correctly, and may be used to estimate the extent of flow penetration into the different glycocalyx layers.

In Fig. 3.8 the overall densities of the three layers are shown for the case of strong shear flow imposed on them. On the same plot the fluid flow velocity profiles relative to the bottom surface flow velocity are also plotted. Since the velocities of the bottom and top wall were chosen to be 0.1 and -0.1, respectively, the relative velocity of the fluid on

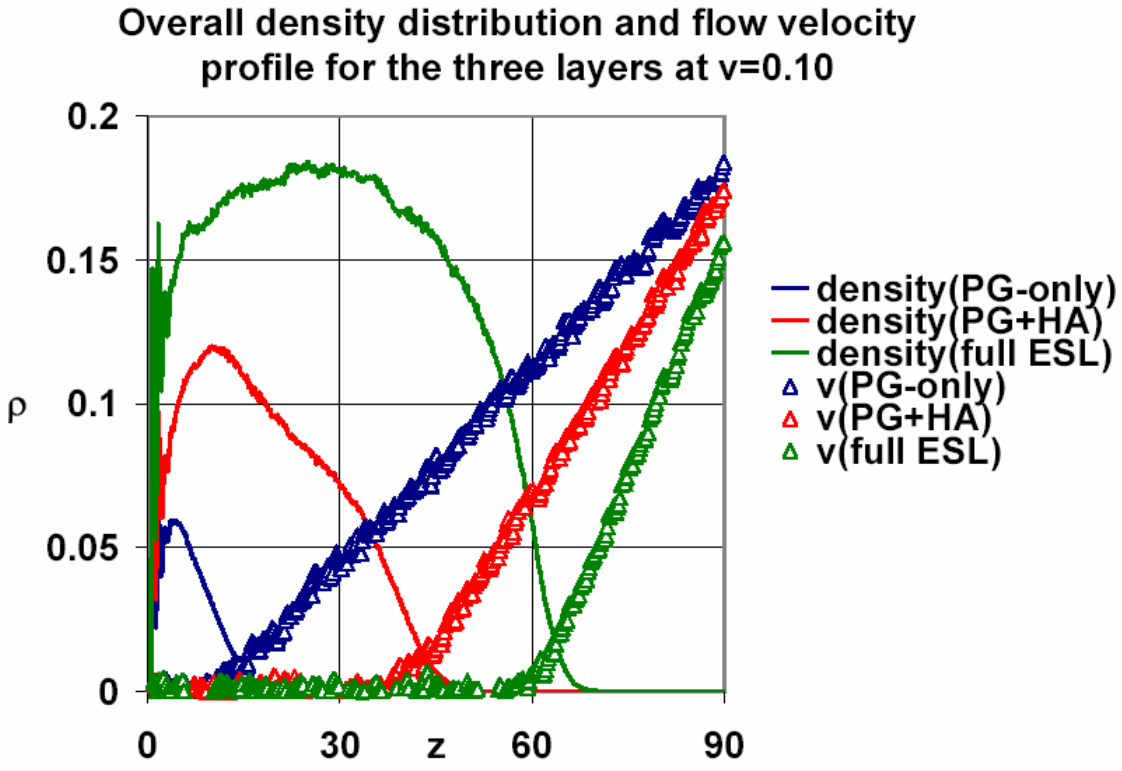

Fig. 3.8

Density distribution and flow profile dependence on the endothelial layer configuration.

the top wall would be 0.2, consistent that seen on the plot. The pronounced linearity of the three velocity profiles outside of the glycocalyx layer provides confirmation that the hydrodynamic interactions in the system were modeled correctly.

The ratios of the different layer densities and thicknesses are very similar to what was observed in the corresponding quiescent cases – both the layer thickness and density seems to double with the addition of each new component. Moreover, the extent of velocity penetration into the layers is consistent with the layer density profiles as well. The penetration depth of the PG-only layer is calculated to be around 10, while for the PG+HA and full ESL layer it is about 5-7. If the value of the penetration depth is compared with the overall layer thickness, it can be clearly seen that a glycocalyx layer consisting only of proteoglycan molecules is not particularly successful in screening the fluid flow away from the grafting surface. The composite PG+HA and the full ESL layers, however, are able to effectively attenuate the fluid flow close to the surface, even when the layer actually takes a majority of the space inside the simulation box (as in the case of the full ESL). Due to the fixed box size, the attenuated flow of solvent in the composite glycocalyx layers and its expanded thickness relative to a bare PG-based glycocalyx layer leads to an increase by a factor of 2-3 of the velocity gradient experienced by the glycocalyx. This implies a doubling or tripling of the shear stress imposed on the full endothelial layer surface relative to the base PG layer. This effect has possible physiological implications for the shear stress transduction – the thickness of the layer can be used as a means of controlling the amount of shear stress applied on the endothelial surface layer and therefore the amount of shear stress that reaches the cell surface through the intricately interconnected components of the glycocalyx.

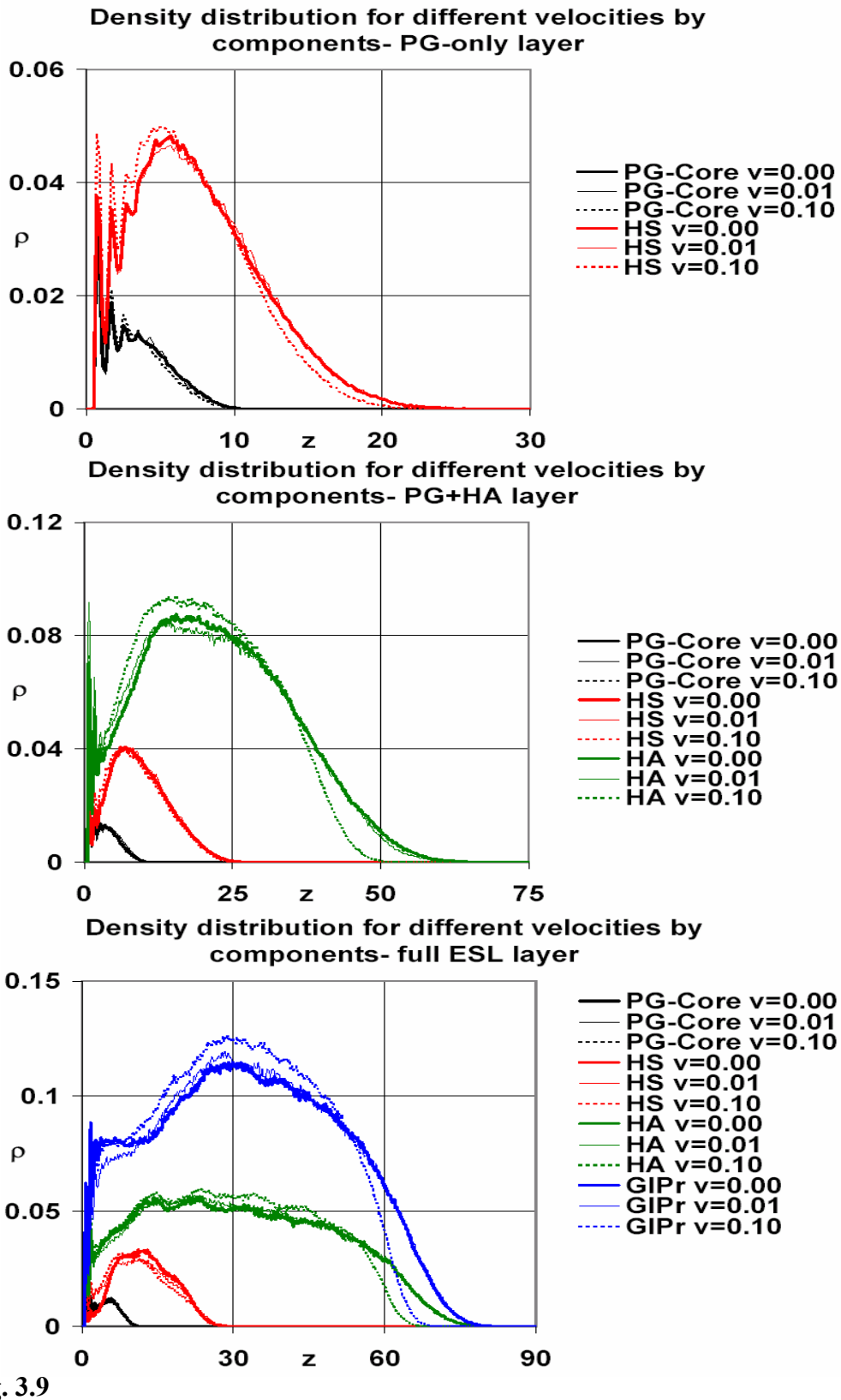

Fig. 3.9

Density profiles per component: **top to bottom** – PG-only, PG+HA, full ESL

In Fig. 3.9 the density profiles of the components of each layer are shown for several shear flow rates. The behavior of the different chain types is similar for the three simulated layers. The density of the core proteins of the proteoglycans does not visibly respond even at the higher shear rate, presumably due to their short length and relatively high flexibility. The remaining components do not show detectable changes in their densities at the lower shear rate. However at the higher shear rate, there is slight shrinkage of some component layers, especially the proteoglycan side chains and hyaluronan layers. This layer compression is dependent on the bending stiffness of the layer components. If one compares the effect of the strong shear flow on the PG-side chains to that of the polysaccharide chains, it is clear that the stiffer polysaccharide chains tend to respond more to the shear flow. (However, the response of the plasma proteins simply follows the polysaccharide chains to which they are attached.) If the effect of the strong shear on the hyaluronan chains is compared with and without the attached plasma proteins, the overall impression is that once the short protein chains are attached, the response to the flow becomes more localized to the outer part of the glycocalyx while in the case of the PG+HA configuration the response in the density is seen throughout the whole layer. Logically, with the shrinking of the density profiles at the high shear rates, there is a slight accompanying effect of increased average density of the three layer configurations. Strictly speaking this increase would result in slightly decreased endothelial surface layer permeability. However the effect is sufficiently weak (based on the density differences) that it should have little physiological importance except possible on permeability regulation of large solute molecules.

Finally, we note here that while it is possible to construct velocity profiles for the lower velocity as well, the effects of this flow on layer density profiles is negligible and the actual velocity profiles are obscured by the noise levels in the simulation.

In the same manner as for the quiescent case, we will next construct a plot for the dimensionless osmotic pressure (see Fig. 3.10), defined as previously in (3.1). Due to the quadratic dependence of the osmotic pressure from the overall layer bead density it is apparent that the influence of the shear velocity on the osmotic pressure will be very much similar to the density dependence. This is exactly what can be observed from the plots on Fig. 3.10 – the osmotic pressure of all three layers does not visibly change for the lower attempter shear rate while higher shear flows provoke slight increase of the average osmotic pressure accompanying the decrease in the glycocalyx thickness.

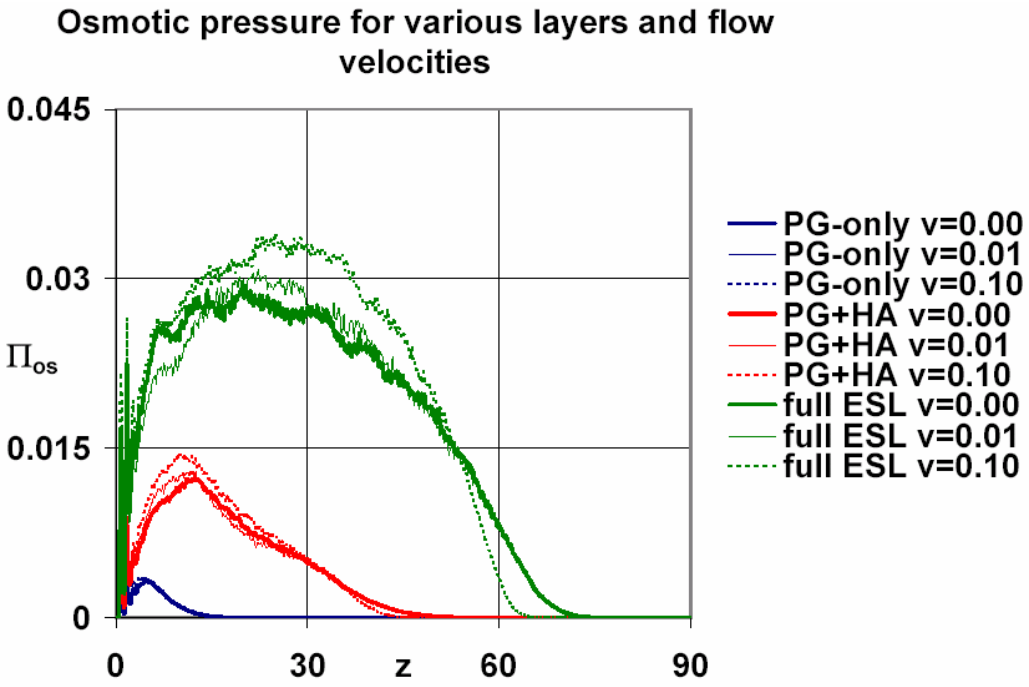

Fig. 3.10

Dimensionless osmotic pressure of the three conformations of the endothelial surface layer at the three velocities simulated.

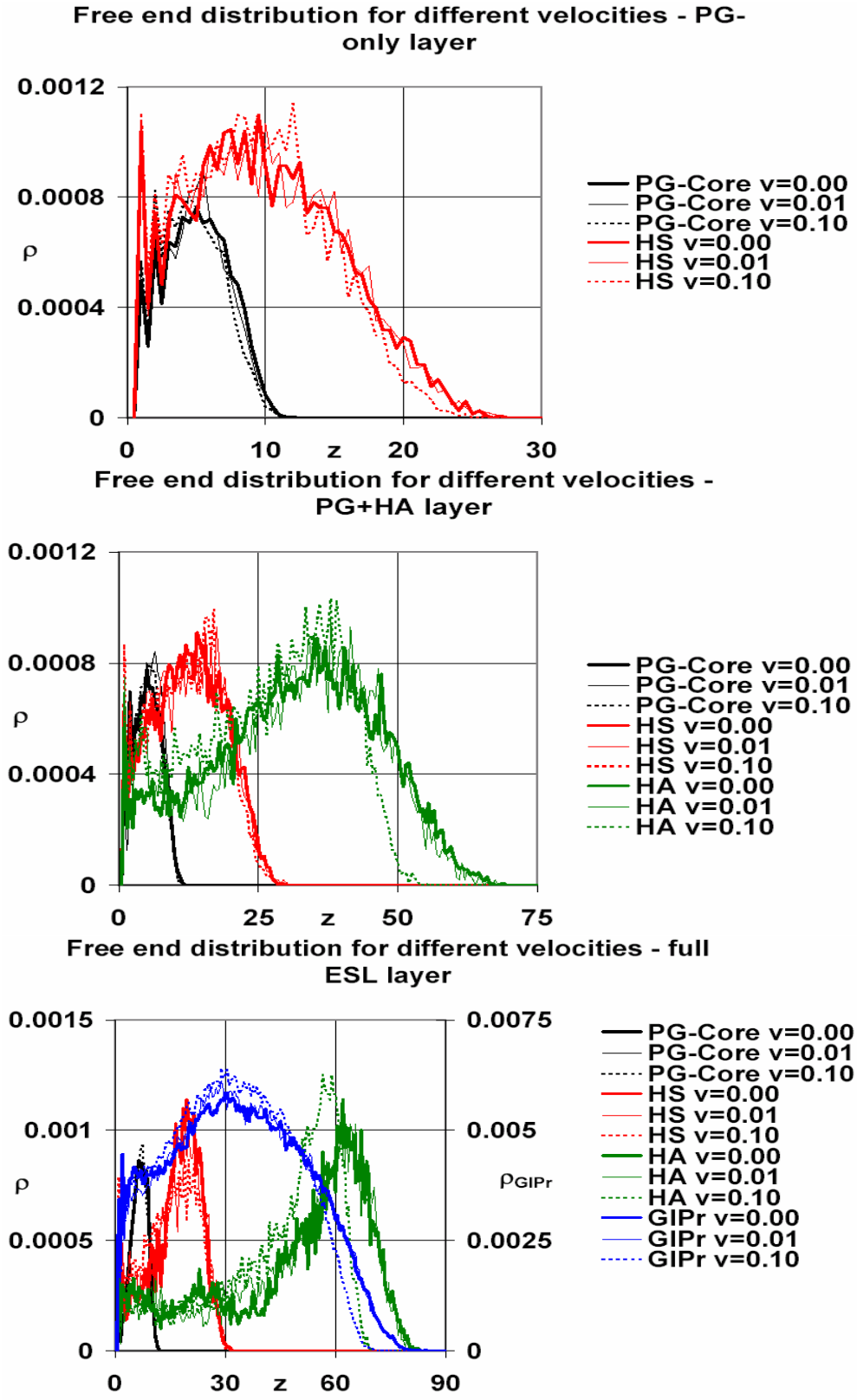

Fig. 3.11

Ends distributions by component – dependence on shear flow velocity.

In Fig. 3.11, the free end distributions of the components in each of the three layers are shown as a function of the applied shear rate. The end distribution profiles were constructed in an identical way to the analysis in quiescent conditions. Generally, the same dependences are observed as in the density profiles analysis – the lower shear rate does not affect any of the components in any of the glycocalyx configurations and the higher shear rate reduces the overall layer thickness and the vertical extension of some of the chain types, mainly depending on the corresponding chain stiffness. Because of the substantially smaller signal-to-noise ratio in the free end distribution profiles compared to the corresponding densities (due to the lower number of ends available for averaging), the weakest effects that were possible to distinguish in the density distributions, such as the dependence on the velocity of the proteoglycan side chains, are now comparable to the noise present in the data and thus undetectable.

From the data available, it can also be concluded that even in the cases when the free end distribution indicates a decrease of layer thickness in response to flow, the ratio of ends buried in the bulk of the glycocalyx to those situated near the free surface does not change in flow conditions, i.e. the shear flow does not provoke a redistribution of the chain ends within the layer bulk. The majority of the ends, especially in the component with the greatest stiffness, are still close to the layer surface, corresponding to fairly extended conformations.

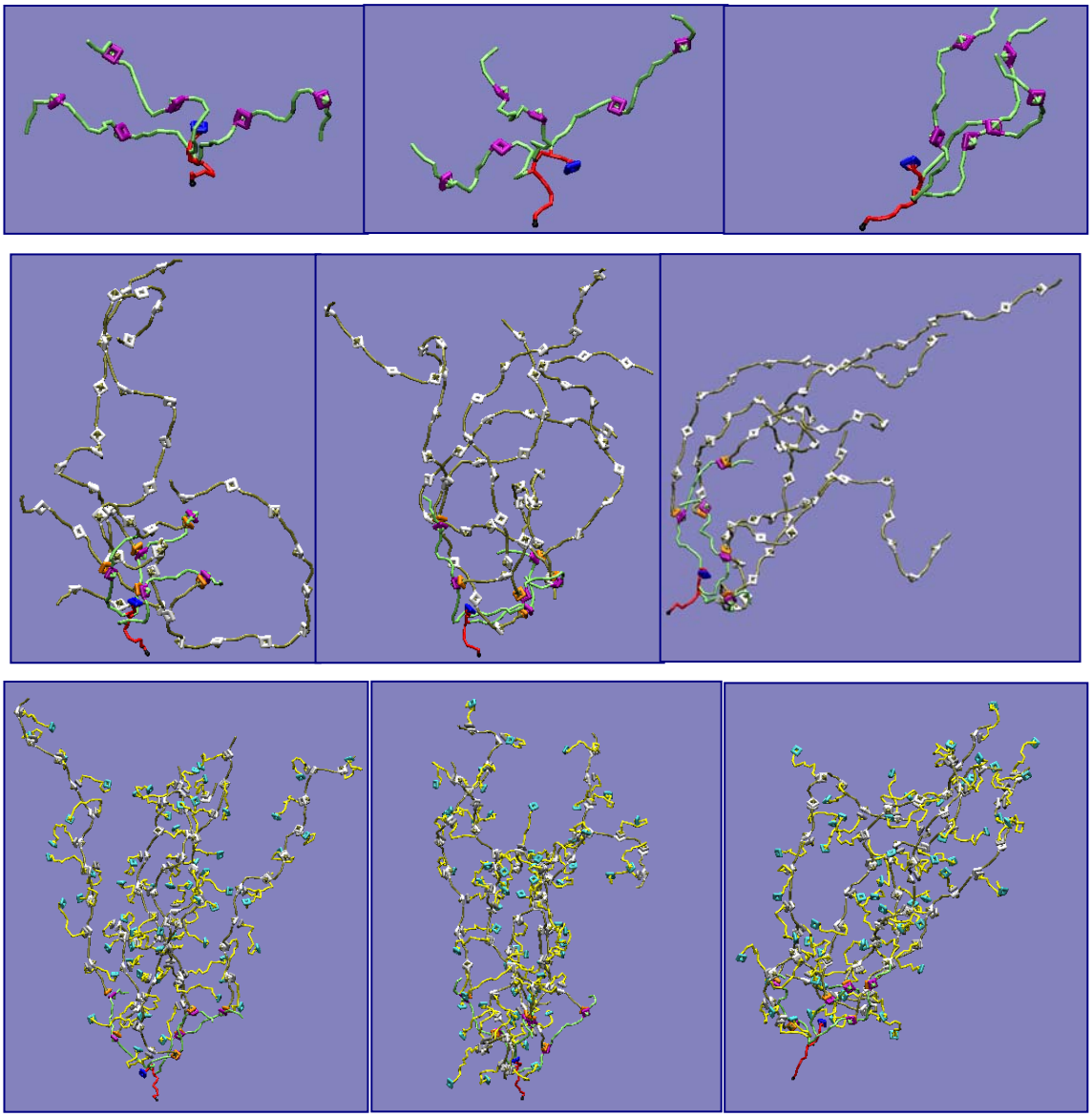

Fig. 3.12

One-tree snapshots of glycocalyx conformations: **top to bottom** – PG-only, PG+HA, full ESL; **left to right** – quiescent case, lower shear rate 0.01, higher shear rate 0.1

Apart from less vertical extension, the overall decrease in the layer thicknesses in response to shear flow can result from chain reorientation and tilting in the direction of the flow. It is useful to construct "one tree" pictures showing a single representative proteoglycan with everything attached to it (as was done previously in Fig. 2.5). The conformations of this single, isolated branched molecule can then be compared for the different applied shear flows. The next snapshots, in Fig. 3.12, are obtained in the following manner: one representative proteoglycan molecule was chosen and visualized, with all the polysaccharides attached to it, and all the plasma protein molecules attached to those polysaccharides. The reasoning for making snapshots of this kind is that, by suppressing all neighboring molecular trees, the extent of stretching and tilting can clearly be seen. Of course, the different 'trees' vary in their extent of tilting, so these snapshots are only showing representative configurations.

Overall, the data in Fig. 3.12 is consistent with the previous free end and density analysis. At lower shear rates the tree configurations are relatively symmetric in the $x-$ and $y-$directions, corresponding to no visible chain tilt for all the three glycocalyx layers. At the higher shear flow velocity there is well pronounced 'tree' orientation in the flow direction. It is more enhanced in the layers of lower overall density – the PG-only and PG+HA configurations and less pronounced in layers of higher average density. The layer density plays an important role in moderating the chain tilting mainly through inhibiting the shear flow penetration. Moreover, the stiffness of the layer components also influences their response. To illustrate this, we compare the response to strong shear flow of the PG-only layer to the response of the polysaccharide chains of the PG+HA layer. Even though the PG-only layer is much less dense than the glycocalyx with

attached hyaluronan, the overall extent of tilting of the polysaccharide chains in the PG+HA layer visibly exceeds the corresponding tilt in the proteoglycan-only configuration. Even within the PG+HA layer itself, the average tilt angle of the hyaluronan chains exceeds the corresponding average tilt angle of the syndecan side chains. The internal strain of a chain is determined by the incremental end-to-end distance for that molecule type. This information may not be obtained from the density distributions, but rather requires information about the displacement of the free ends of the various species of chains. Qualitatively, it is clear that the internal strain of the chains increases when shear flow is imposed, even though the overall thickness of the glycocalyx layer may decrease, since the overall end-to-end distances in the conditions of strong shear flow end up exceeding the corresponding ones in the quiescent case.

More quantitative information about the chain tilting can be obtained from the average end-to-end distances for all molecular types and their projections along the three coordinates for the glycocalyx layers subjected to the three wall velocities, as shown in Fig. 3.13. The three components of the end to end distance are denoted respectively by $\langle dx \rangle$, $\langle dy \rangle$ and $\langle dz \rangle$ and calculated by simply averaging the distance between the two chain ends over all molecules of the wanted type, the while the overall end-to-end distance is calculated through:

$$\langle dr \rangle = \sqrt{\langle dx \rangle^2 + \langle dy \rangle^2 + \langle dz \rangle^2} \tag{3.2}$$

The first thing to notice is that the end-to-end distances in the $x-$ and $y-$direction is statistically zero for all chain types in absence of flow. This confirms in a quantitative way the symmetry exhibited by the basic 'tree' constituents of the glycocalyx model, as was previously observed from the one-tree snapshots. Moreover, one may also conclude

from Figs. 3.12 and 3.13 that in the absence of flow the orientations of the glycocalyx sub-chains are isotropic in the $x-$ and $y-$direction, which is to be expected for relatively homogeneously grafted molecules. This mirror symmetry exists in presence of flow strictly only for the vorticity direction. The few exceptions that can be seen where the average end-to-end distance in the $y-$direction (e.g. HS end-to-end distances for PG+HA at $v=0.01$ and $v=0.1$; and HA end-to-end distances for full ESL at $v=0.01$) are probably due to small deviations from homogeneity sustained by the limited possibility of the stiffest molecular type to fill the available gaps.

The remaining information that can be taken from the figure is more or less consistent with the results in the previous section of quiescent behavior and the earlier parts of this one. Overall, the $z-$coordinate of the end-to-end distances are seen either to not be affected by flow (as in the proteoglycan core proteins) or to slightly decrease when strong shear flow is imposed. However, in all cases, the z-coordinate of the end-to-end distances increases with the layer build-up, reflecting the effect of osmotic pressure in the layer. On the other hand, the extent of the chain tilting in strong shear conditions, defined by the average end-to-end distances in the $x-$direction, exceeds by far the decrease in the end-to-end distance in the $z-$direction, confirming that the overall end-to-end distance increases with the shear rate corresponding to pronounced chain stretching in sufficiently strong flows. This effect can also be directly seen from the $\langle dr \rangle$-plots on Fig. 3.13.

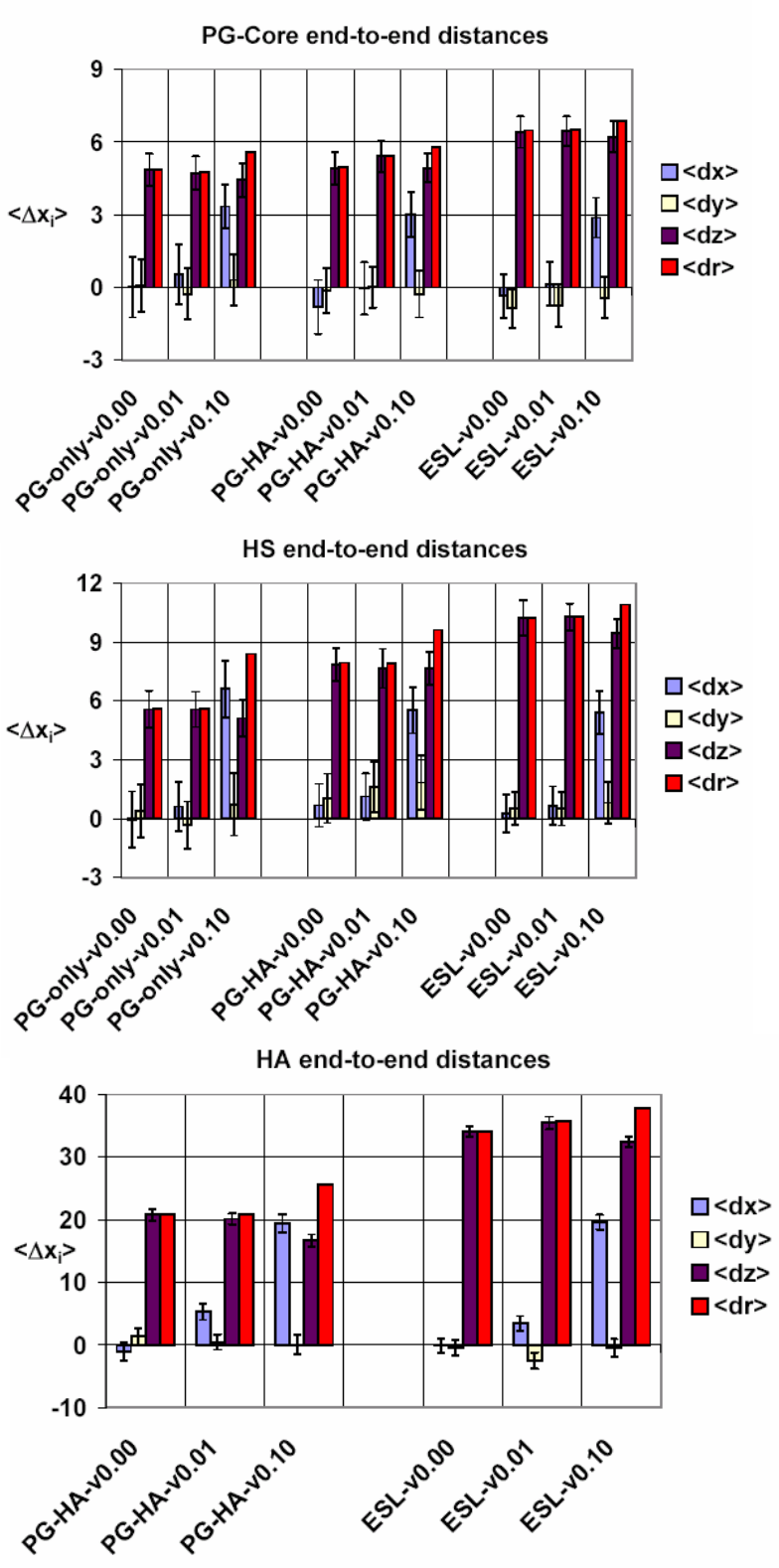

Fig. 3.13

End to end distances as a function of layer structure and shear flow velocity

3.4 Discussion

There is a fair amount of experimental data about glycocalyx reduction resulting from various enzymatic treatments that may be compared to the numerical experiment results presented here. First, the topological model as defined is broadly consistent with studies demonstrating nearly complete endothelial surface layer degradation after heparinase treatment (*van den Berg et al, 2003*). In the terms of our topological model, heparinase would act to sever the proteoglycans side chains from the surface proteoglycan core proteins, thereby stripping away all but the remnant protein cores. These remaining core proteins constitute a very small part of the overall layer density and thickness.

Treatment by hyaluronidase was shown to greatly affect the porosity of the glycocalyx and its permeability (*Henry and Duling, 1999*), while the effect on its thickness is not as drastic. In the simulations performed it was shown that the removal of the hyaluronan and the proteins associated to it would reduce the layer thickness and density to about 20% of its original values. This decrease in density is in qualitative agreement with the observations of Henry and Duling, as the density of the layer is directly related to the glycocalyx permeability.

As for hemodilution experiments, those available in the literature have been based on indirect measurements (*Long et al, 2004; Pries et al, 1998*) and have not provided a quantitative estimate of the glycocalyx structural degradation during the process. In the simulations, the endothelial surface layer thickness was shown to decrease by about 1/3 after removal of the associated plasma proteins, while its density decreased by about half. In some microscopy studies of the glycocalyx, the surface layer thickness was found to

be almost an order of magnitude smaller than in less invasive but indirect flow visualization measurements. This discrepancy may be due to the weakly associated plasma proteins being washed out during the fixation and staining protocols utilized in the microscopy studies, possible indirect evidence of a hemodilution effect. However, if the associating plasma proteins were the only component of the layer being washed out during this protocol, this would imply the proteins are the major determinant of the layer thickness, which is not the case in our topological model. Another possibility is that glycan chains also are partially removed from the glycocalyx during these relatively invasive the microscopic visualization preparations, leaving primarily the syndecans as the components of the fixed layer. This hypothesis is more consistent with the results from Vink (*van den Berg et al, 2003*) showing the glycocalyx having a fairly thick structure even in absence of plasma proteins. Our model would be more consistent with such an explanation as well.

The relative density of the glycocalyx and bead solvent in the box can give some insight into the diffuse nature of the model glycocalyx. Its relative transparency and large permeability in many experimental conditions imply a very dilute structure. Various estimates for the solid fraction of the glycocalyx range from less than one percent to several percent (*Michel and Curry, 1999*). From the density profiles obtain in the simulations, it might seem that the density of the modeled layer exceeds considerably the predictions from literature – the fully model ESL average density is around 0.12 to 0.15. When compared with the overall bead density of 0.7, this implies a glycocalyx occupying 14-20% of the volume fraction of the system. However, such an estimate is very misleading since it does not take into account the fact that the beads in the coarse-grained

simulation actually correspond to blocks or blobs of monomers and solvent molecules. Also, since the model is limited to a single fundamental bead size, it is evident that a solvent bead would contain a significantly larger number of solvent molecules compared to the number of molecules/monomers in one of the remaining glycocalyx beads (due to the fact that the molecular size of the solvents is typically smaller than the characteristic monomer size of the proteins or polysaccharides elements of the glycocalyx). Moreover, these glycocalyx blobs must also contain a significant number of solvent molecules to solvate the monomers of the proteins or polysaccharides elements. If for these reasons there is an order of magnitude difference in the total number of solvent molecules in the solvent and monomer beads compared to the total number of monomers in the remaining bead types, this would result in an effective 1.5% solid fraction of the endothelial surface layer, a value much more in agreement with the available data.

The density and free end distributions can also be compared to the results of theoretical models and simulations on linear polymer brushes (*Grest, 1999; Halperin et al, 1992*). In the absence of flow, for instance, the overall density profiles, including presence of parabolic tails in the profiles, are consistent with experimental, theoretical, and computer simulation studies of linear polymer brushes. A more detailed comparison with polymer brush models can provide some insight into glycocalyx properties and will be discussed in some detail in the final chapter of this thesis.

In contrast to the structural studies in quiescent conditions, for which there were a number of possibilities for comparison with experiments, there is much less explicit experimental data in the literature on the effects of flow on the glycocalyx. It is known for example known that the glycocalyx tends to grow well beyond its natural thickness in

conditions of ischemia, in which flow is stopped or reduced below physiological flow rates (*Mulivor and Lipowsky, 2004*). However, the results from these investigations cannot be used for comparison to the data obtained in this chapter since the effect observed cannot be attributed solely to the mechanical response of the glycocalyx to flow. Rather, available experimental evidence suggests that the response to flow has a complex biochemical and biophysical nature. For instance, plasma protein redistribution between the bulk and the endothelial surface layer can occur as a result of fluid flow decrease or discontinuance (an effect that we discuss in detail in the next chapter). A shift in the equilibrium between the endothelial cell hyaluronan production and shedding from the glycocalyx into the bulk resulting from the absence of plasma flow can also provoke the observed endothelial surface layer growth in quiescent conditions.

On the other hand, in conditions of higher than physiological shear rates there is also increased secretion of various glycocalyx constituents (*Arisaka et al, 1995*). So the modulation of the glycocalyx thickness and permeability at high shear rates cannot be attributed solely to chain tilting and deformation.

As in quiescent conditions, there are previous theoretical and computer simulations studies of polymer brush structures under shear flows that may be compared with our data. In particular, the modest decrease in the glycocalyx thickness at high shear rates is consistent with the previously observed response in polymer brushes consisting of simple linear grafted chains (*Grest, 1999*). A subsequent study of polymer brushes with different chain stiffnesses (*Danova-Okpetu et al, unpublished*) shows that the shear rate response and the extent of chain tilting under flow, in particular, is quite sensitive to the chain rigidity, with the stiffer chains being much more susceptible to deformation in flow. This

observation is also consistent with our results, if the stiffness of the different components of the endothelial surface layer is taken into account. There are also theories developed based on scaling notions which deal with the behavior of linear polymer brushes under flow. Detailed comparison of these glycocalyx simulations to appropriate polymer brush theories is deferred to the last chapter of this thesis.

Another very important issue that needs to be addressed in order to compare these simulations to experimental data is the mapping of the dimensionless variables that are used for the simulations to real values of length, time, velocities, etc. By doing so, information can be obtained regarding the physical time scales probed by the simulations, the dimensionless velocities that most closely correspond to the physiological range of microcirculation blood flow rates, and the approximate physical size of the simulation box and of the endothelial surface layer as simulated. The orders of magnitude for those parameters can be then compared to what could be realistically expected based on general knowledge about the glycocalyx.

The characteristic lengthscale, the bead size, can in principle be estimated based on the number of beads chosen for the various molecular types and data about their real dimensions and molecular weights. In the ideal case, no matter which component we choose, the same value of characteristic lengthscale would be obtained. In reality, however, the sizes of the various components of the glycocalyx differ sometimes by orders of magnitude. For example, albumin (a representative of plasma protein) has a molecular weight of 66kDa, while hyaluronan from the endothelial cells (a representative polysaccharide chains in the modeled glycocalyx layer) has a molecular weight of the order of 1000kDa. The two differ in molecular weight by more than two orders of

magnitude, while in the topological model here their length in beads differs by approximately a factor of 2.5. This discrepancy in the model was imposed by restrictions on the available computational power, which would not allow the hyaluronan molecules to be too large, and by the requirement for the characteristic plasma protein molecules to be large enough to have generic macromolecular properties. As such, the elements of our glycocalyx model are not intended to represent actual glycocalyx constituents, such as albumin. Rather, we have chosen to represent the system by generic elements that mimic the essential nature of the proteoglycan, polysaccharide, and associated plasma proteins that make up the glycocalyx and that respect the topology of the glycocalyx as a whole. Furthermore, all beads are assumed to be the same size in our model for simplicity. So, it is not an option for the beads of the different molecular types to represent different amounts of actual monomeric units. Therefore, when comparing to potential glycocalyx constituents, the inevitable inconsistencies of the size scales in the model only allow for estimation of the order of magnitude of the bead size as an average of the estimates from the different molecular types.

Another difficulty arising in the bead size determination is the fact that there are two ways of considering the configurations of the monomer units inside a bead. Usually, a polymer conformation in good solvent is like a self-avoiding walk, in which case a bead would consist of a diffuse, swollen coil of actual monomers entraining a substantial number of solvent molecules. On the other hand if the polymer chain is considered to be in the semiflexible or rigid on the scale of the bead size, then the contour length of the solvated chain of monomers might be better estimate for the bead size. Realistic situations would probably lie somewhere between these limits. Having in mind the

difference between a self-avoiding walk size and the contour size of an average polymer chain, it is clear that the two limits will give quite different results. In the glycocalyx layer model utilized in this work, there are components of various flexibility, for some of which (specifically the ones with medium flexibility) it is not explicitly clear which limit is more appropriate.

Based on the proteoglycan core protein, assuming an average size for an amino-acid to be 1nm and the approximate number of amino acids to be 250, a core protein is modeled as a chain of 13 beads, each of which contain ~20 amino-acids. The stiffness of the core protein corresponds to a somewhat semiflexible chain. Thus, the contour length of this chain of amino acids would be used to estimate the bead size, giving a value of about 20nm in diameter. Based on the proteoglycan side chains, which are known to be composed of average 50-100 disaccharide units, corresponding to average of 100-200 glucose rings with size of the order of 1nm, one bead would correspond to 40-80 glucose rings. Since the side chains are also modeled as semiflexible, the contour length is again used to estimate the bead size, which in this case is around 40-80nm. Similarly, using hyaluronan with molecular weight 500-1000kDa as basis for estimate, the value for the bead size is of the polysaccharide chains obtained is around 40-80nm, assuming semi-flexible chain conditions. Last, if the estimate is performed based on an average plasma protein (molecular weight between 20 and 100kDa) and contour length is used, the resulting characteristic lengthscale is substantially lower – of the order of 3-5nm. Thus, on average the estimate for the bead size is in the range of 4-40nm. That would correspond to real dimensions of the simulation box being between $0.18\mu m \times 0.18\mu m \times 0.4\mu m$ and $1.8\mu m \times 1.8\mu m \times 4\mu m$ and glycocalyx layer (full ESL) of

thickness between 0.2 and 2.0 microns. This value seems in reasonable agreement with indirect measurements and predictions for the endothelial surface layer thickness being of the order of a half a micron to a micron (*Pries et al, 2000*). For all the subsequent analysis though we will choose to use the lower boundary of the estimated lengthscale obtained based on the plasma proteins ($\sigma \sim 4\text{nm}$); even though it results in a glycocalyx layer which is a bit on the short side, it would correspond to more realistic characteristic timescales as can be seen next.

The estimate of the characteristic simulation timescale as the characteristic time of diffusion of a bead by its own size can be obtained using the Einstein relation:

$$\tau \sim \frac{\eta \sigma^3}{kT} \tag{3.3}$$

where η is the effective fluid viscosity of the bead solvent, σ is the characteristic bead size, k is the Boltzmann constant, and T is the absolute temperature.

The viscosity of blood $3.5 \cdot 10^{-3}\,\text{kg/m} \cdot \text{s}$ serves as a lower bound on the effective viscosity of the bead solvent. A more realistic value may be quite a bit larger than this, as the diffusion beads actually correspond to a collection of solvent molecules. Choosing a viscosity in the range $3.5 \cdot 10^{-3} < \eta < 3.5 \cdot 10^{-2}\,\text{kg/m} \cdot \text{s}$, and using the $\sigma \sim 4\text{nm}$ and $T = 300\text{K}$ in the expression above, the characteristic time obtained is in the range $5 \cdot 10^{-8} < \tau < 5 \cdot 10^{-7}\,s$. Having in mind that an average size simulation utilizes about 40 million steps, each of which is 0.005τ, i.e. 200000τ overall, that would correspond to an average simulation duration between $10^{-3}\,\text{s}$ and $10^{-2}\,\text{s}$, which is about right for numerical simulations of this scale. We note the sensitivity of τ to the choice of σ. If, for instance, we were tempted to use the estimate for the bead size coming from the proteoglycans or

polysaccharides, we would have ended up with a characteristic time of simulation that is a few orders of magnitude larger, due to the very strong dependence of the characteristic time on the bead length scale. Having estimates for the length and time scales, it is now possible to estimate the characteristic physical flow velocities imposed on the layers by relative wall motion. This characteristic velocity is simply:

$$\tilde{v} \sim \frac{\sigma}{\tau} \tag{3.4}$$

Using the characteristic lengthscale of $\sigma \sim 4\text{nm}$ and characteristic timescale of $\tau \sim 5 \cdot 10^{-8}\text{s}$, the characteristic velocity ends up being of order $\sim 0.1\text{m/s}$. Thus, the two wall velocities used for simulations roughly correspond to $\sim 10^{-2}\,\text{m/s}$ (for dimensionless velocity 0.1) and $\sim 10^{-3}\,\text{m/s}$ (for dimensionless velocity 0.01), or in terms of shear rates, $\sim 10^{4}\,\text{s}^{-1}$ and $\sim 10^{3}\,\text{s}^{-1}$, respectively.

The shear rates in the microcirculation are of the order $\sim 10^{2}\,\text{s}^{-1}$, and in the arterioles are of the order $\sim 10^{3}\,\text{s}^{-1}$ when only plasma flow and no possible vessel obstructions are taken into account (*Popel and Johnson, 2005*). Therefore it can be concluded that in such conditions in the microcirculation the glycocalyx will remain essentially not deformed. However, when red blood cells are passing through capillaries, the effective lengthscale of the plasma gap between the erythrocyte and the glycocalyx will be much smaller than the capillary size (by a factor of 10 to 100). Therefore the real velocity gradients and shear rates may differ by one-two orders of magnitude from the ones estimated from plasma-only flow. These values are closer to the larger velocity case attempted in the simulations which indicates the possibility of the glycocalyx being deformed by the shear rates imposed on it by passing red blood cells.

4. Molecular Dynamics Simulations of Self-Assembling Glycocalyx

4.1. Specifications and Parameter Values

In the next series of simulations performed the plasma protein molecules were allowed to freely dissociate and associate to the glycocalyx (rather than being irreversibly bound) and the concentration of these plasma proteins was allowed to equilibrate between the bulk solvent phase and the endothelial surface layer. The non-bonded interactions between the globular protein ends and the hyaluronan active domains were modeled as attractive Lenard-Jones potentials with cutoff distance $r_{\text{cutoff}} = 2.0$ while all the rest of the non-bonded interactions were retained as 'neutral' Lenard-Jones potentials ($\varepsilon = 1.0$; $r_{\text{cutoff}} = 1.122462$). Several values for the attractive energy of interaction were studied, namely $\varepsilon = 1.0; 1.2; 1.5$. The properties of the resulting equilibrium layers were then compared with each other and with those of the covalently bound layer investigated in the previous chapter. As a control, a 'free protein' case was studied in which the interactions between the plasma proteins and the hyaluronan molecules were kept neutral. This case was used to obtain the equilibrium distribution of the globular proteins in the absence of interactions, in which only the osmotic pressure in the glycocalyx and the entropy of mixing play an important role in the distribution of plasma proteins. The maximum value for the interaction energy used for the simulations was chosen from preliminary simulations of solutions of associating linear chains with pyramidal active domains and corresponds to the maximum energy for which only dimeric association occurred (i.e. no higher-order clusters were observed but all the associates were on a one-on-one basis).

Three types of simulations were performed on these equilibrium layers, as described in the following. In the first series, the molecular structure and total number of the different components in the layers was identical to the full ESL layer from the previous chapter. The simulations were performed using the restart files from the equilibrated covalently bound glycocalyx simulations and then modifying the bonds and angles to eliminate the covalent bonds between the plasma proteins and hyaluronan active domains. In their place, the non-bonded interactions described above were activated. This approach was used in the hope that computational resources and time may be saved as the equilibrium might be reached faster if all the plasma proteins are in the layer initially, rather than distributing the plasma protein homogeneously in the initial configuration. In this way, osmotic forces would serve to drive excess protein out of the layer, rapidly equilibrating the relative distribution of proteins inside and outside the layer. The dependence of the plasma protein distribution on the protein-hyaluronan interaction strength in quiescent flow conditions was the focus of this first set of simulations.

In the second set of simulations, the possible effect of solvent flow on the distribution of bound versus unbound plasma proteins and the potential for re-distribution of these plasma proteins in flow conditions to alter glycocalyx properties, such as layer density and reorientation and tilting of the constituent chains, was investigated. These studies were restricted to a single wall velocity, $v = 0.1$, and to interaction energies of either $\varepsilon = 1.5$ or the non-interacting case as a control. In initial configurations for these simulations were the corresponding equilibrated quiescent systems studied in the first set of simulations. All the remaining simulation parameters and protocols are identical to those used in the quiescent simulations of the self-assembling glycocalyx.

In the final set of simulations, the dependence of the relative distribution of associating plasma proteins between the glycocalyx and the bulk solvent is studied as a function of the total number of associating plasma proteins. The intention here is to clarify the effects of the partial or complete removal of macromolecular and supramolecular constituents from the plasma, on the structure of the glycocalyx. As it is not practical to introduce absorbing boundaries into the simulation box (to serve as sink for the plasma protein species), we did not directly simulate the effects of flushing the soluble plasma proteins out of the bulk fluid phase, as would occur in a typical saline perfusion experiment. Rather, we seek to mimic the progressive dilution of plasma proteins in the system by consideration of dependence of the relative distribution of associating plasma proteins on the total number in the system. This is achieved by removing a fraction of plasma proteins from a pre-equilibrated configuration, followed by re-equilibration of the system. This process is iterated to obtain the data required. For simplicity, these 'plasma depletion' simulations were carried out in quiescent conditions, since the effects of flow on protein association are found to be relatively weak.

The partial removal of the globular proteins is performed by (1) removing the bonds and angles between the corresponding plasma protein beads, and then (2) changing the bead type from the plasma protein to the solvent bead type. This procedure insures that the overall bead density in the simulation box remains unchanged. The plasma protein molecules are removed mainly from the bulk phase in the hope to save computational time, as discussed above. Two values of the hyaluronan-protein interaction energies, namely $\varepsilon = 1.0$ and $\varepsilon = 1.5$, each with the Lenard-Jones cutoff distance of $r_{\text{cutoff}} = 2.0$, were investigated for full ESL configurations with three plasma protein concentrations as

follows. The first configuration used was the full ESL system first investigated in this chapter, which included 600 plasma proteins and 600 available hyaluronan binding domains. The second configuration was obtained by removing all the proteins situated above the first half of the initial equilibrated hyaluronan layer with $\varepsilon = 1.5$, resulting in a new system with 255 proteins in the simulation box. The third configuration was obtained by removing all the proteins situated above first quarter of the initial equilibrated hyaluronan layer with $\varepsilon = 1.5$, resulting in a new system with 101 plasma proteins in the simulation box. The ESL configurations were then allowed to equilibrate before analysis of the re-distributed plasma proteins and layer conformations. The average protein bead density in the box corresponding to the investigated concentrations are $\rho_{600} = 0.0868$, $\rho_{255} = 0.0369$, and $\rho_{101} = 0.0146$ (with overall bead density still being $\rho = 0.7$).

All the simulations in this chapter were performed isothermally at room temperature $\widetilde{T} = 1.0$ maintained by a Langevin thermostat coupled to the velocity field in the $y-$direction. The time step utilized in the simulations was 0.005τ. As the systems simulated in this chapter are relatively more complex and have more degrees of freedom than those in the previous chapter, it was found that typically 40 to 60 million time steps were required for the systems to reach equilibrium, substantially more than the previous simulations. Several tests for equilibrium were utilized. First, it was required that the averaged net flux of globular proteins in the $z-$direction throughout the simulation box is approximately zero at equilibrium. Moreover, it was also verified that the average density and free end distribution profiles of all the constituents did not to evolve in time and that the distribution of plasma protein constituents in the bulk solvent phase outside of the ESL was approximately homogeneous.

4.2. Effect of Interaction Energy on ESL Assembly

Characteristic snapshots of the equilibrium configurations of the layer corresponding to four different values of the LJ interaction parameters are shown in Fig. 4.1. Apart from the overall layer height and density, the snapshots also show the relative distribution of the dynamically associating/dissociating plasma proteins between the ESL and bulk solvent phases in the simulation box. As can be observed, there is a pronounced difference in the layer thicknesses, especially between the case of neutral interactions between the binding domains of the polysaccharides and the proteins ($\varepsilon = 1.0$ and $r_{\text{cutoff}} = 1.122$) and the case of strongest binding energy between them, namely $\varepsilon = 1.5kT$. The relative distribution of the protein molecules between the endothelial surface layer and the bulk phase also obviously depends on the interaction energy, with most of the protein molecules being expelled from the glycocalyx in the neutral case (due to the osmotic pressure in the layer), and the bulk concentration of the proteins gradually decreasing with the increase of the binding energy, as the proteins absorb into the glycocalyx. The other components of the layer seem to be only weakly influenced by the dynamic equilibrium of the globular proteins, as confirmed by their density and free ends distribution profiles for different values of the association parameters. Therefore the effects of protein association on the syndecan-based inner part of the glycocalyx will not be dealt with further in this chapter.

As expected, the glycocalyx layer density also depends on the interaction energy through the amount of protein sequestered in the layer: as the association of proteins

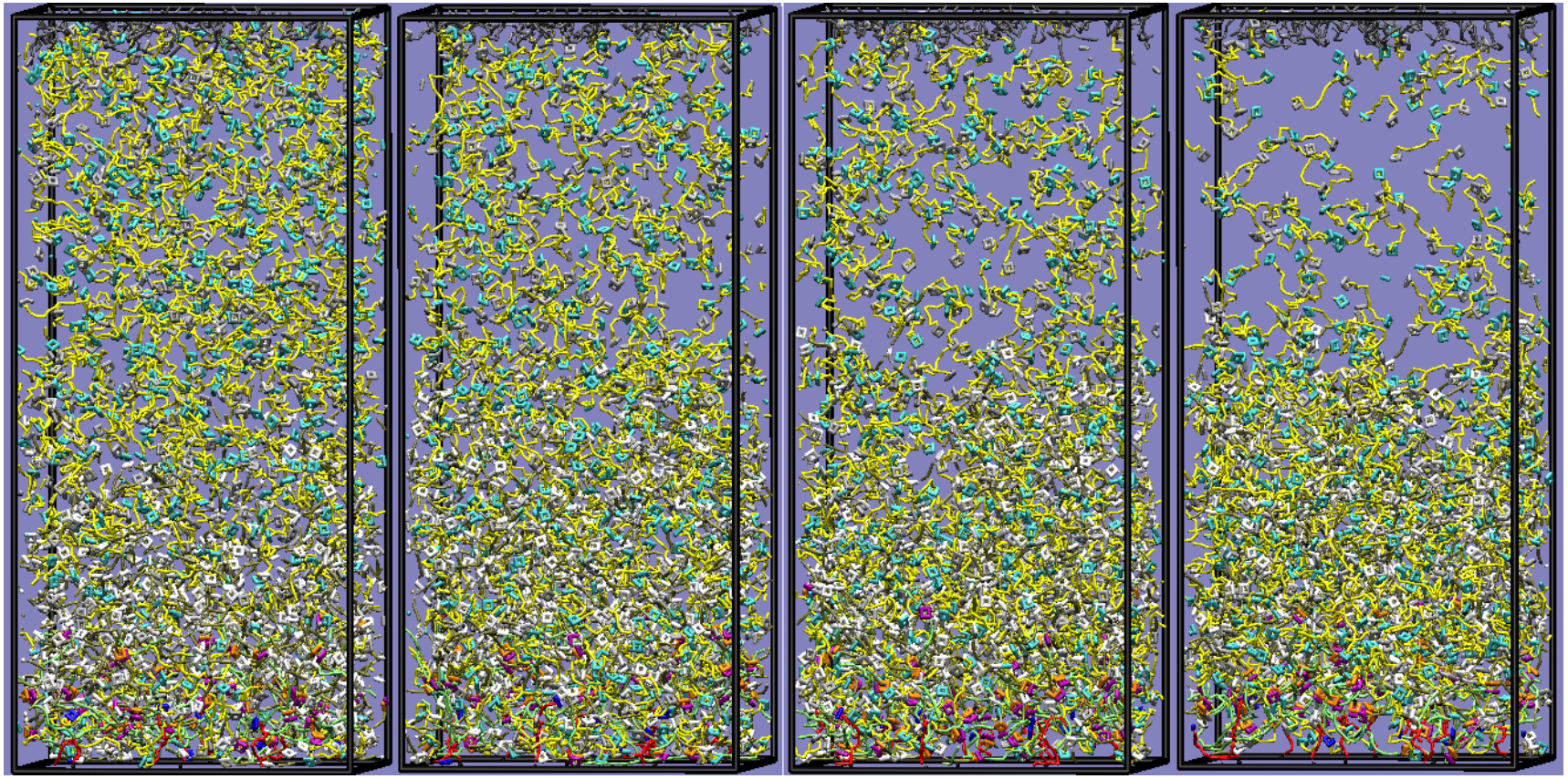

Fig. 4.1

Dynamic structure of the endothelial surface layer as a function of the plasma protein-hyaluronan energy of interaction – **from left to right** – $\varepsilon = 1.0$ and $r_{cutoff} = 1.122$; $\varepsilon = 1.0$ and $r_{cutoff} = 2.0$; $\varepsilon = 1.2$ and $r_{cutoff} = 2.0$; $\varepsilon = 1.5$ and $r_{cutoff} = 2.0$

becomes more energetically favorable, more associated proteins are found in the glycocalyx, thereby increasing the overall ESL layer density.

The density distribution profiles in Fig. 4.2 confirm in a more quantitative way the observations from the simulation snapshots. Since the plasma proteins are now present everywhere in the simulation box, the density distribution of the hyaluronan is the most reliable indicator of the overall layer thickness. As expected, the ESL thickness for the neutral protein interaction case is considerably smaller than for the other associating protein cases, and is very close (but not identical) to the case of an endothelial surface layer without plasma proteins presented in Chapter 3. At the other extreme is the covalently bound full ESL layer whose thickness significantly exceeds the corresponding height of the dynamical glycocalyx layers for all simulated interaction energies. The overall densities in the covalent and neutral layers exhibit the same trends as their respective hyaluronan densities, with the centroid of the density profile increased for the covalent layer and decreased for the neutral layer with respect to the values for the finite association energy cases. The hyaluronan conformations of the three finite energies simulated are very similar. Their degrees of extension are essentially the same with slight differences in density in the middle portion of the profiles. This peculiarity leads to unusual behavior of the plasma protein density and, as a consequence, of the overall layer density (see Fig. 4.2 bottom). The finite energy cases, as was observed, correspond to almost identical conformations of the hyaluronan but to a different extent of association of plasma proteins into the layer. Since it is the hyaluronan that the plasma proteins associate with, this results in a higher overall layer density localized in a smaller thickness than in the corresponding covalently bound layer. So, even though the

covalently bound layer contains more plasma protein than the dynamic layer with energy of interaction $\varepsilon = 1.5$, for example, the average layer density in the dynamic case ends up being larger than in the covalently bound glycocalyx. This might imply that the dynamically associated glycocalyx would be more successful in the screening of blood flow.

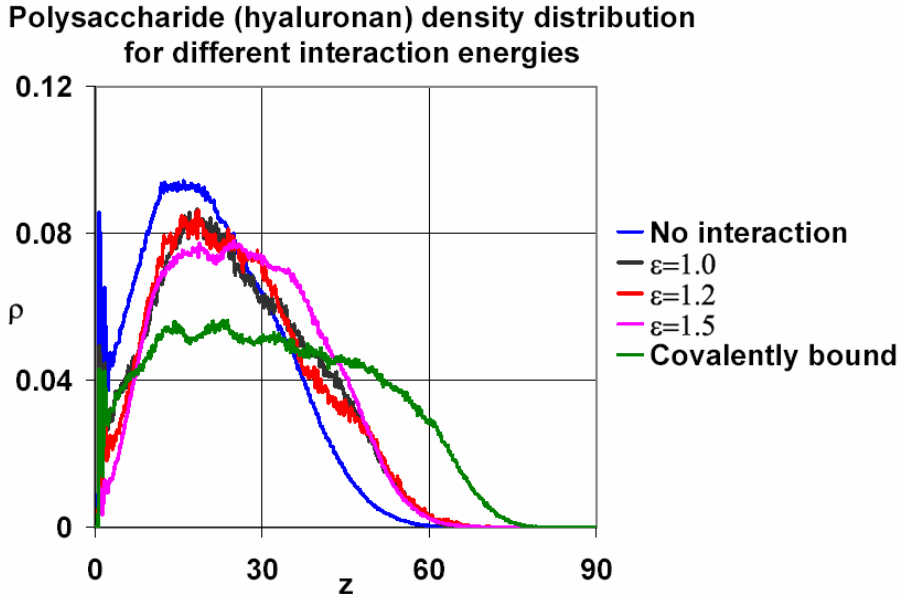

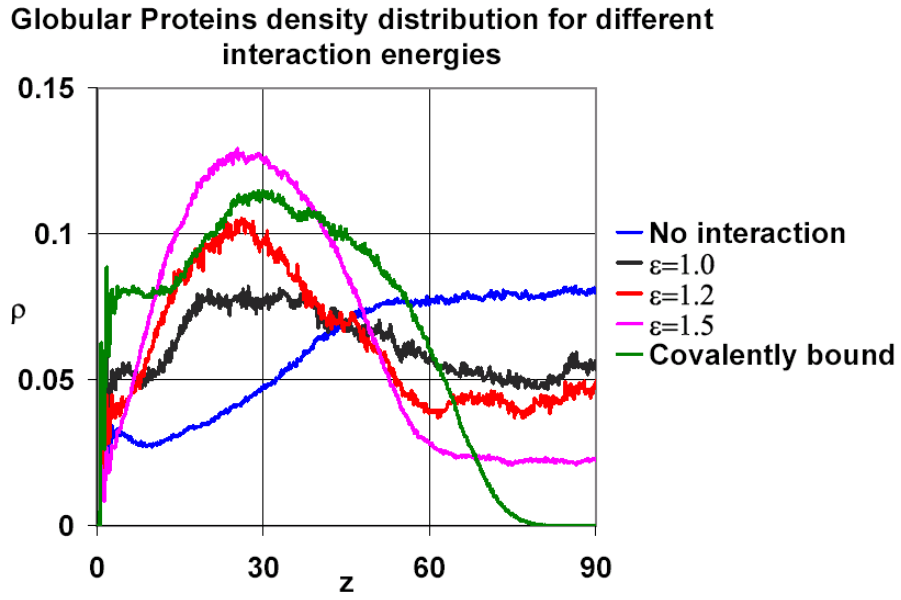

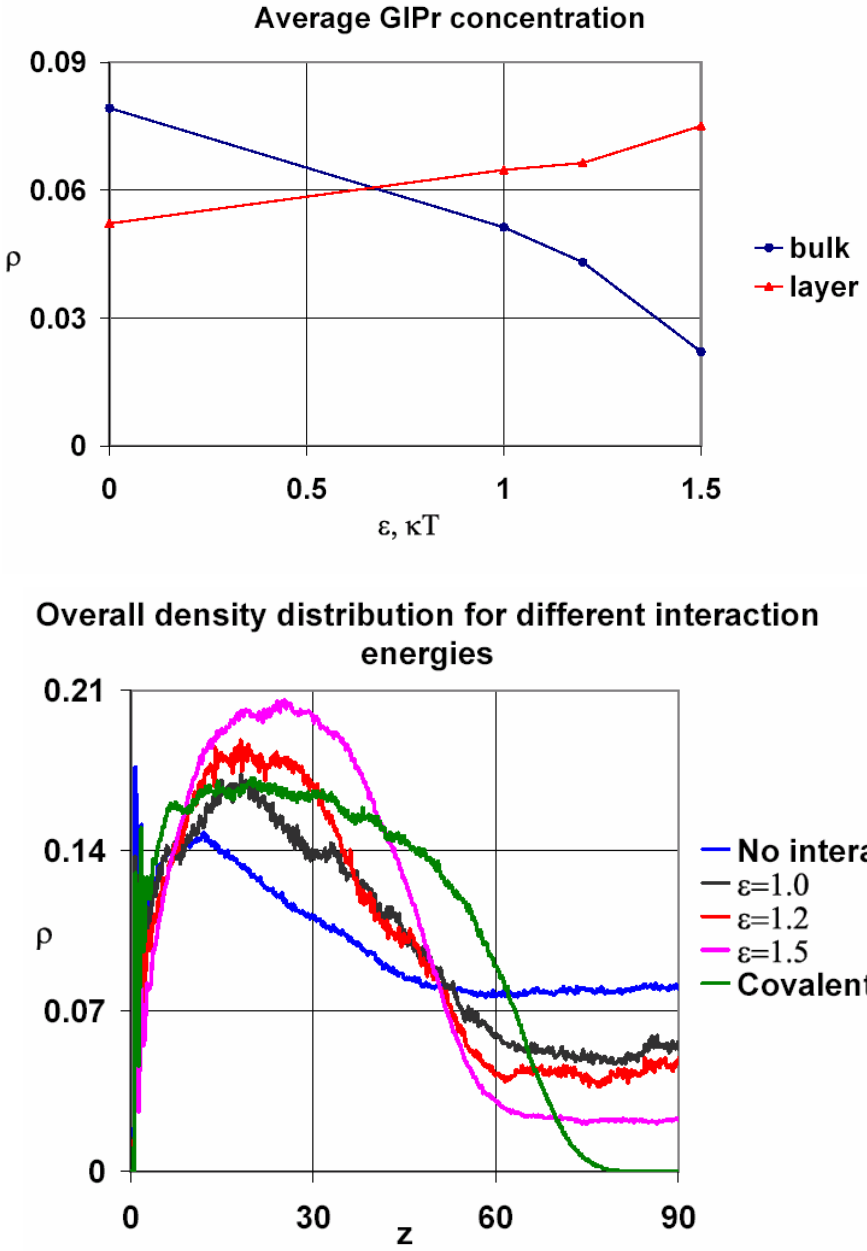

Fig. 4.2

Density distribution profiles of chosen glycocalyx components as a function of hyaluronan-protein interaction energy:
from top to bottom (including previous page)– hyaluronan density, GlPr density, average protein density in the two phases, overall ESL density.

The free end distribution profiles for the polysaccharide chains and plasma proteins generally exhibit the same trends as the density profiles (see Fig. 4.3). For the hyaluronan the three finite energies investigated give almost identical free end distributions. In contrast, the covalent and non-interacting layers are, respectively, expanded or compressed in comparison to the finite energy cases, resulting in free end distributions with relatively large or small centroid positions. On the other hand, the plasma protein

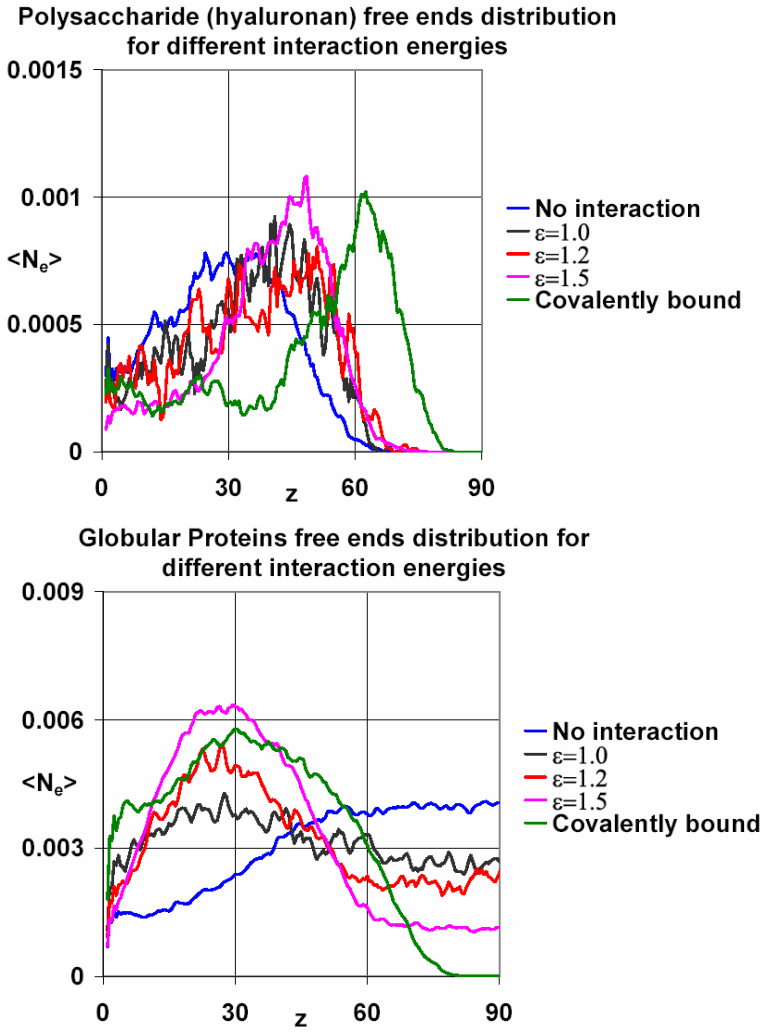

Fig 4.3

Free ends distribution of chosen ESL components as a function of hyaluronan-plasma protein interaction energy: **from top to bottom** – HA and GlPr

free ends distribution follows the same trends as its density, and provides an alternative measure of the dependence on interaction energy of the relative distribution of plasma protein inside and outside the layer. Clearly, this distribution shifts gradually, changing from the limit of a full occupied layer in the case of covalent interactions to the limit of a majority of plasma proteins osmotically excluded from the layer in the case of non-interacting plasma proteins.

Another important aspect of the layer dynamics is the transport properties of the plasma proteins in the glycocalyx. In particular, as the plasma proteins are an integral part of the dynamic layer structure, a comparison between diffusion of the proteins in the bulk and in the glycocalyx may be revealing. According to basic diffusion principles, the average diffusion coefficient for the plasma proteins within the system can be calculated by observing the mean square displacement (MSD) of all plasma proteins as a function of the time interval. For simple diffusion processes, the coefficient of proportionality is directly related to the diffusion constant, or in our case, to the dimensionless diffusion constant by the well-known expression:

$$\left\langle r^2 \right\rangle = 6Dt \tag{4.1}$$

By plotting $\left\langle r^2 \right\rangle = f(t)$ for the various interaction energies one may identify the conditions for which $\left\langle r^2 \right\rangle = f(t)$ is a linear function of time, corresponding to simple diffusion, and when appropriate estimate the average diffusion constants and how they depend on the protein-hyaluronan interaction energy. Figure 4.4 shows plots of dimensionless MSD, $\left\langle r^2 \right\rangle$, as a function of dimensionless time t for layers in the

presence of non-binding proteins, covalently bound proteins and proteins with association energies ε = 1.0, 1.2, and 1.5.

It can be seen that except for the covalently bound layer, for which the proteins are tethered to the network of fluctuating hyaluronan chains, plasma protein transport is essentially diffusive. The plasma proteins in the covalently bound layer do not exhibit pure diffusion but rather undergo excursions of a finite maximum amplitude, presumably leading to a plateau value of $\langle r^2 \rangle$ at sufficiently long times. The lack of significant

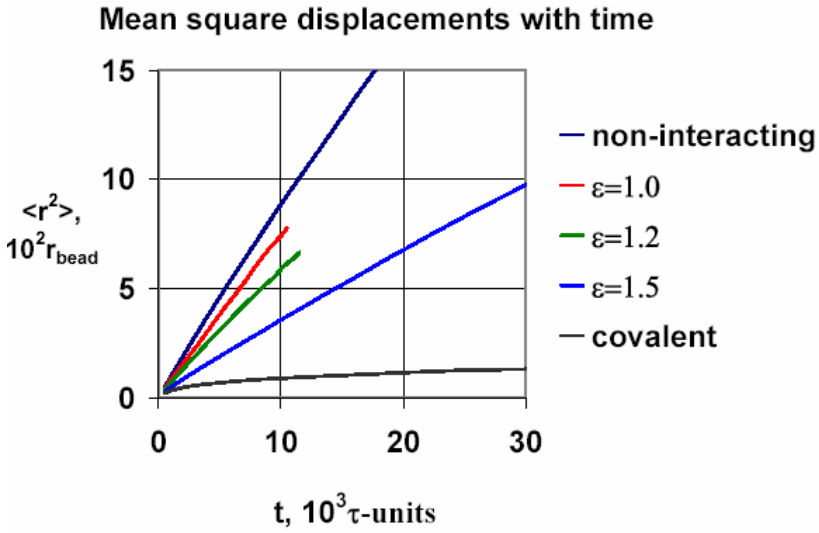

Fig. 4.4

Mean square displacements as a function of the time: linearity of the plots indicates that normal diffusion is taking place; from slopes of lines average diffusion constants can be estimated.

deviations from linearity for all cases studied of plasma protein with finite interaction energies is remarkable and leads to well-pronounced re-equilibration of the distribution of the proteins within the simulation box upon a change in binding conditions. In particular, it suggests that the association/dissociation rate is high enough to allow diffusive transport of the protein molecules to occur everywhere in the system on the

timescales probed by the simulations. The latter suggestion was subsequently investigated in more detail.

The slopes of the lines shown in Fig. 4.4 (including the covalently bound layer just for comparison) can give estimates for the corresponding dimensionless diffusion constants. Using equation (4.1), the apparent dimensionless diffusion constant for the covalently bound layer was found to be $\widetilde{D} = 3.66 \cdot 10^{-4}$, while for the non-interacting plasma proteins it was found to be $\widetilde{D} = 1.3 \cdot 10^{-2}$. For the layers with finite interaction energies $\varepsilon = 1.0$, $\varepsilon = 1.2$, and $\varepsilon = 1.5$, the apparent dimensionless diffusion constants were found to be $\widetilde{D} = 1.2 \cdot 10^{-2}$, $\widetilde{D} = 9.5 \cdot 10^{-3}$, and $\widetilde{D} = 5.0 \cdot 10^{-3}$, respectively. The range of apparent dimensionless diffusion constants for the plasma proteins spans about two orders of magnitude from the covalent to the non-interacting case. However, for the finite interaction energies studied, the dimensionless diffusion constant changes only by a factor of two. If the characteristic scaling values estimated in the previous chapter are used, it is possible to calculate at least the order of magnitude of the dimensional diffusion constants based on the present simulations. The relation between the two is simply given by $D = \sigma^2 / \tau \cdot \widetilde{D}$, where σ is the bead size and τ is the characteristic time. Such dimensional estimate will be presented in the discussion section at the end of this chapter. For the purposes of comparison with experiment, perhaps the most useful approach is to use the ratio of the diffusion constant D to its value D_0 in the bulk solvent phase: $d = D / D_0$. This method can be used for either dimensional or non-dimensional diffusion constants, thereby eliminating the need for precise estimate of characteristic dimensional quantities.

The diffusion of plasma protein as obtained from the square displacement versus time data is in principle the composite result from molecular diffusion in several different possible environments: unhindered diffusion in the bulk phase, and hindered diffusion in the endothelial surface layer. In the second case the protein diffusion can be influenced by several factors: (1) the mere presence of the endothelial surface layer hinders diffusion due to the finite permeability of the porous layer, and (2) the fact that an interacting plasma protein in the glycocalyx can undergo multiple dissociations and associations with nearby hyaluronan binding domains. Both these factors are expected to lead to an overall decrease of plasma protein diffusion within the glycocalyx compared with the bulk solvent phase.

In order to check for the existence of multiple diffusing protein populations within each simulation, MSD distributions for a selected sampling time intervals were constructed and compared for different values of the interaction energies, as shown in Fig. 4.5. If only one population of diffusing proteins is present, then the MSD distribution would have a Gaussian profile with a single peak corresponding to the apparent diffusion constant found previously. If indeed there are two or more populations of diffusion proteins, then the distribution will be generally a superposition of two or more Gaussian distributions. The sampling time interval for which the MSD distribution is built is also important. If very short times are used, then the displacement of all populations would probably show identical behavior independent of the interaction energy, since for sufficiently short times the proteins within the ESL will not move enough to feel the steric constraints imposed by the porous ESL or by the association with the hyaluronan component of the ESL. If the sampling time interval is too long, then one peak would

also be observed since an average protein would be able to explore both the bulk and the ESL phases. Thus, for very long times the information obtained should be equivalent to the averaged diffusion results depicted in Fig 4.4.

In Fig. 4.5 the MSD distributions are normalized by the sampling time interval, to facilitate comparison between data sets for the two time sampling intervals chosen.

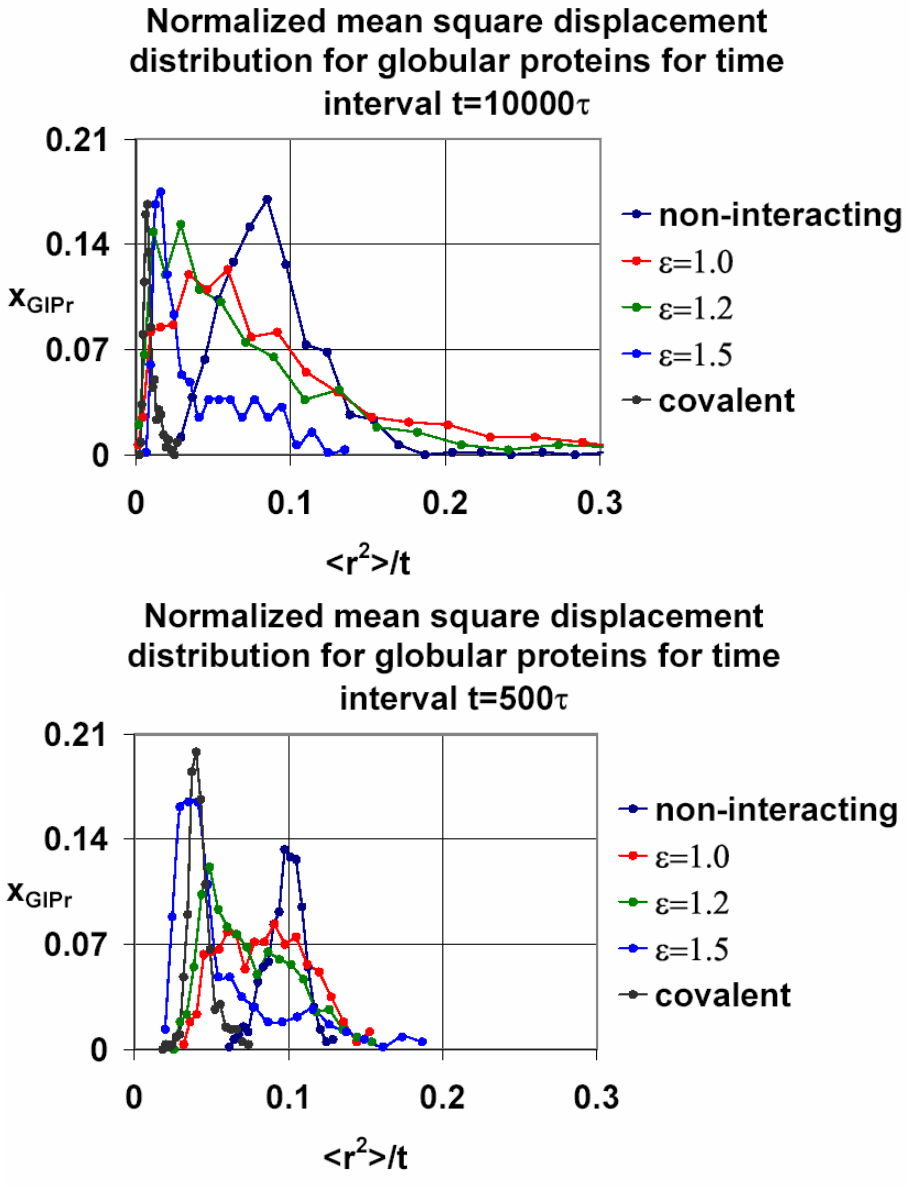

Fig. 4.5

Mean square displacement distributions for plasma proteins with different interacting energies for two different sampling time intervals.

The two extreme cases, namely the non-interacting and the covalently bound proteins, provide some insight into the diffusion inside and outside the layer, since the covalently bound layer severely restricts the protein diffusion to be strictly localized within the ESL layer, leading to a single Gaussian MSD distribution; while the non-interacting proteins are free to diffuse inside and outside the layer, leading also to a single Gaussian MSD distribution reflecting the average properties of the entire system.

The finite energy distributions are intermediate in nature between these two extremes, as expected. They are all highly non-symmetric and appear to be superpositions of pairs of MSD distributions. The ratio of two such distributions should provide a measure of the relative amount of the two populations of diffusing proteins in the system. In that sense, the relative increase of the peak amplitude corresponding to the smaller diffusion constant with increasing interaction energy ε is in agreement with the previously demonstrated effect of interaction energy on the molecular density profiles. Moreover, the positions of the distribution peaks are consistent with the averaged diffusion constants found previously (the peak positions correspond to $\left\langle \tilde{r}^2 \right\rangle / \tilde{t} = 6\tilde{D}$).

Having confirmed the existence of two populations of diffusing proteins for finite values of ε, we seek to estimate the difference in their properties. One approach to achieve this goal is the following: the simulation box is partitioned into two domains, namely the bulk and the ESL. The mean square displacements then can be measured separately for the two domains and compared to each other and to the averaged values for the full system as a function of interaction energy. This procedure is restricted to relatively short sample times and produces data with a relatively high level of noise. The reason for the former is that only molecules which do not leave the chosen domain will

be used for its characterization, and for sufficiently long sample times all diffusing proteins will have left their original domain at least once. The reason for the higher noise level in the data is the fact that the number of molecules used for averaging is considerably less than in the previous analysis method, and that this number decreases progressively as the sample time interval increases. Overall, the most difficult case for analysis is the diffusion of the protein with the highest finite interaction energy ($\varepsilon = 1.5$) in the bulk solvent region because of the relatively low number of non-associated proteins present in the bulk solvent region and the relatively higher rate of diffusion in the bulk solvent phase compared to within the glycocalyx.

In order to obtain the necessary data, additional simulations were performed where the bead coordinates were dumped into a file much more frequently than the in the dump-files used for the density and end distributions analyses.

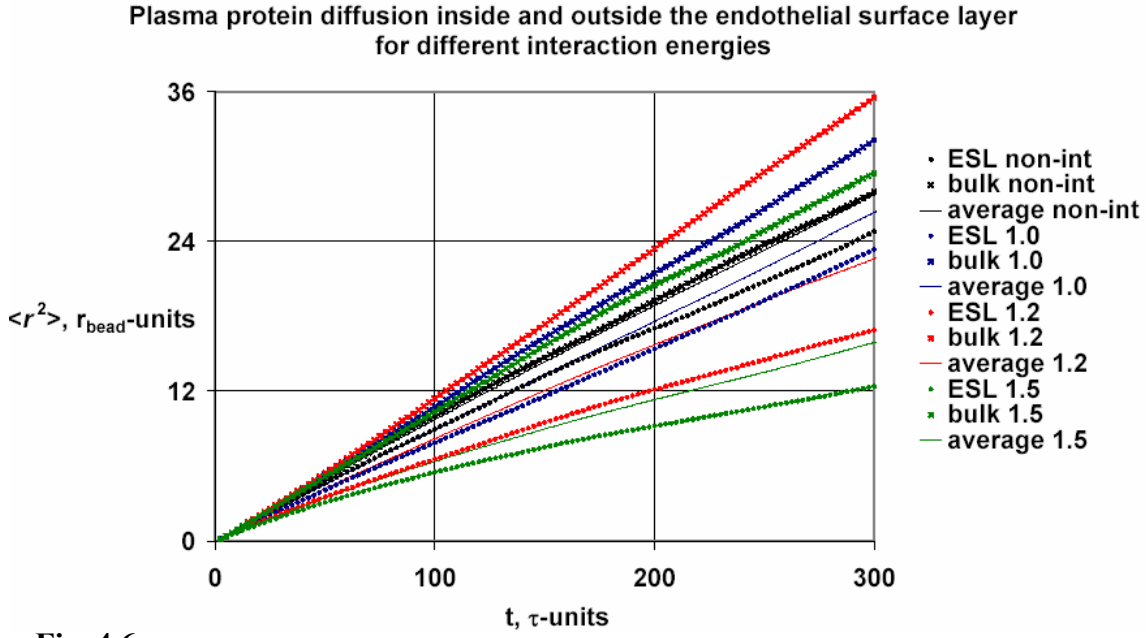

Fig. 4.6

Distinction of the two populations of plasma proteins through their MSD: ***black*** – non-interacting, ***blue*** - $\varepsilon = 1.0$, ***red*** - $\varepsilon = 1.2$, ***green*** - $\varepsilon = 1.5$; ***solid*** line – average $\langle r^2 \rangle$; ***circles*** – protein diffusion inside ESL; ***crosses*** – bulk protein diffusion.

Results from this analysis are shown in Fig. 4.6. It can be seen that indeed two populations of plasma proteins exist in the simulated systems at each time step. The difference between their properties depends on the energy of interaction ε, implying that the association/dissociation events are occurring on a timescale that is sufficiently slow to affect the protein diffusion in the ESL. The simple steric effect from the finite layer density can be estimated from the data for diffusion of the non-interacting proteins within the ESL. It was found that the steric hindrance effects were generally insignificant compared to the effects of association/dissociation events for diffusion in conditions of finite interaction energy.

The diffusion in the bulk was expected to be independent of the energy of interaction since the proteins in the bulk are diffusing freely and their concentration does not change drastically. The results, however, do show relatively weak variations of the bulk diffusivity as a function of the interaction energy. The dependence is not even monotonic – the largest diffusion constant corresponds to the energy $\varepsilon = 1.2$. Overall the dimensionless diffusion constant of the bulk protein varied in range from $1.62 \cdot 10^{-2}$ for the non-interacting case to $2.22 \cdot 10^{-2}$ for the interaction energy $\varepsilon = 1.2$. This variation in free protein diffusion constant may be a finite size effect due to the relatively small number of freely diffusing proteins and the fact that this number decreases with time. This also might be the reason that the MSD plotted in Fig. 4.6 are sub-linear functions of time at sufficiently long sample time.

The diffusion in the endothelial surface layer shows a stronger and monotonic dependence on the interaction energy ε. This can be attributed mainly to the association/dissociation processes in the layer rather than to the increased density

compared to the bulk with increasing ε. The basis for this conclusion lies in the very small difference between the bulk and ESL diffusion rates for the non-interacting case, which are generally negligible compared to the observed differences for finite ε – differences as large as a factor of 3 (see Fig. 4.6). The in-layer dimensionless diffusion constants for the different values of ε are $\widetilde{D} = 1.27 \cdot 10^{-2}$, $\widetilde{D} = 9.08 \cdot 10^{-3}$, and $\widetilde{D} = 5.72 \cdot 10^{-3}$ for $\varepsilon = 1.0; 1.2; 1.5$, respectively.

Having studied plasma protein diffusion in the ESL and bulk solvent regions, the logical next step was to characterize the properties of the transient hyaluronan-protein complexes, particularly their characteristic lifetime as a function of the interaction energy ε. In order to do that, distribution functions of complexes as a function of lifetime were obtained for each value of ε from the simulation coordinate data files as follows. At each time step, all available complexes were identified and the number of these complexes remaining for n time steps ($n = 1, 2, 3...$) was determined and used to construct a distribution. Since the coordinate files are discretized in time (i.e. the coordinates are only written every given number of time steps), there could be several possible concerns. The first one is the validity of the assumption that if a complex exists for two consecutive time steps from the coordinate file, it has existed for all the steps in between. The second concern is the possibility of a strong false one-step contribution to the distribution. If a complex only exists at one step, its validity might be put in question, more specifically whether that is a real complex or two binding partners passing by in close proximity. The second concern was eliminated through investigation of the lifetime distribution for the non-interacting endothelial surface layer. It was shown that when the cut-off distance for the complex-determining test is chosen properly (usually equal to the cutoff distance of

the corresponding Lenard Jones potential), the non-interacting case gives essentially zero complexes at each time. Thus the 'passing-by' situation rarely occurs and there is no need to worry about a false one-step contribution. The insignificance of the first concern is a bit more difficult to justify. The probability of two particular binding elements to return to the same small space in simulation box and form a complex after dissociation and subsequent diffusion was estimated and found negligible. Thus, it was possible to conclude that if two elements form a complex for two consecutive time steps in the coordinate file, they have been associated for all the intervening times.

Since the association/dissociation events do not involve crossing a potential barrier separating the bound and unbound states, it is to be expected that the lifetime distributions would have a form of an exponential. i.e.:

$$N_{\mathrm{HA\_GlPr}} \sim \exp\left(-\frac{t}{\tau}\right) \tag{4.2}$$

Thus, plots of the logarithm of the number of complexes as a function of their lifetime

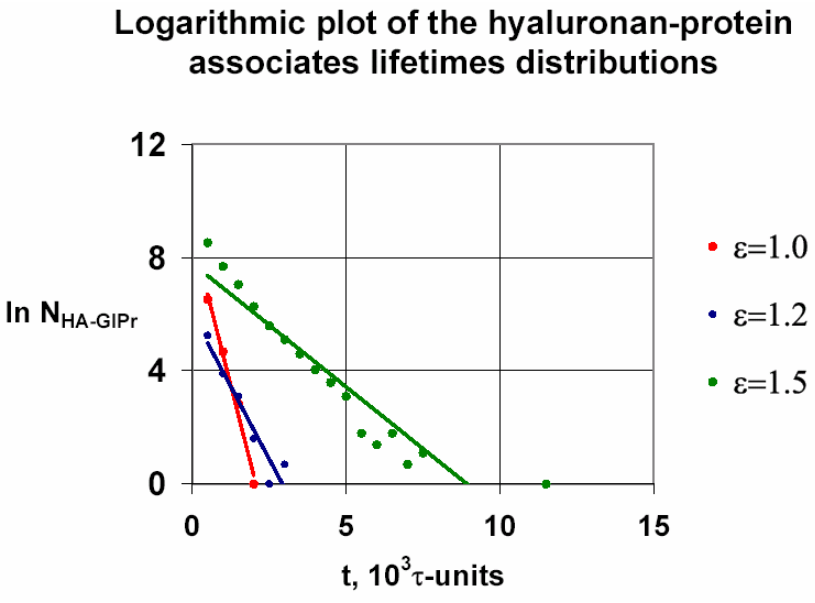

Fig. 4.7

HA-plasma protein complex lifetime distribution as a function of ε

should be linear, with their slopes providing estimates of the characteristic lifetime of the complexes. Such logarithmic plots are given in Fig. 4.7. As it can be seen from these plots, the logarithm of the number of complexes is essentially a linear function of lifetime, confirming the expected exponential distribution of the complex lifetimes. The slopes of the linear fits give the following estimates for the characteristic dimensionless lifetimes for different ε: $\widetilde{\tau}_{\text{HA-GlPr}} = 233.86\tau$ for $\varepsilon = 1.0$; $\widetilde{\tau}_{\text{HA-GlPr}} = 487.09\tau$ for $\varepsilon = 1.2$, $\widetilde{\tau}_{\text{HA-GlPr}} = 1144.2\tau$ for $\varepsilon = 1.5$, where τ is the characteristic time scale. For the value of $\tau = 10^{-8}\,\text{s}$ estimated in the previous chapter, one obtains lifetimes $\tau_{\text{HA-GlPr}} = 2.34 \cdot 10^{-6}\,\text{s}$, $\tau_{\text{HA-GlPr}} = 4.87 \cdot 10^{-6}\,\text{s}$; $\tau_{\text{HA-GlPr}} = 1.14 \cdot 10^{-5}\,\text{s}$, respectively, for $\varepsilon = 1.0; 1.2; 1.5$.

The dependence of the characteristic complex lifetime on the interaction energy is very sharp – the lifetime approximately doubles for an increase of the interaction energy by 20% and increases by a factor of 6 when the interaction energy increases by 50%. Note that the dependence of lifetime on ε is stronger than exponential. This strong dependence implies that the complex association/dissociation is not simply an ideal first-order reaction with an activation energy given by ε. This may be due to the crowded environment within the reactive ESL medium. The relatively short complex lifetimes obtained in these simulations are evidence of intensively dynamic equilibrium between the associated and dissociated states within the endothelial surface layer. Nevertheless, these short complex lifetimes do not affect the structural integrity of the ESL and its ability to efficiently retain plasma proteins in a way that achieves an even higher average layer density than the covalently bound layer. It is natural, therefore, to inquire about the sensitivity of the dynamic ESL to external forces, such as plasma flow, and to the composition of the bulk plasma phase. These are the subjects of the next two sections.

4.3 Effect of Shear Flow on ESL Assembly

Simulation snapshots for the steady-state configuration of full ESL exposed to flow of the bulk plasma phase are shown in Fig. 4.8, along with a control equilibrium snapshot in the absence of flow. Response of the ESL to a wall velocity of $v = 0$ for both interacting ($\varepsilon = 1.5$) and non-interacting plasma protein components are shown. As seen in the snapshots, imposing large shear rates on the self-assembling endothelial surface layer leads to a visible decrease in the layer thickness, similarly to the previously analyzed permanently bound glycocalyx. As with the covalent layer, the decrease in the thickness is mainly achieved by the tilting in the flow direction of the various layer constituents. This effect is present in all the snapshots, and is especially evident for the stiff hyaluronan chains components in the presence of non-interacting plasma proteins, for which there is pronounced chain orientation in the flow direction. The degree of chain extension due to the tilting cannot be estimated quantitatively from the snapshots. Therefore, investigation of the end-to-end distances was used to obtain the dependence of chain extension on flow conditions. Contrary to expectations, however, no obvious change in plasma protein concentration in either the bulk plasma or glycocalyx phases was observed between the corresponding quiescent and sheared endothelial surface layer conformations. It appears that the slight rise in the osmotic pressure difference provoked by the flow-induced increase in layer density is not sufficient to induce a visible redistribution of plasma protein between the two phases. In the case of finite ε, this suggests that the additional force applied on the plasma proteins due to the increased osmotic pressure is not sufficient to cause their dissociation from the HA binding sites.

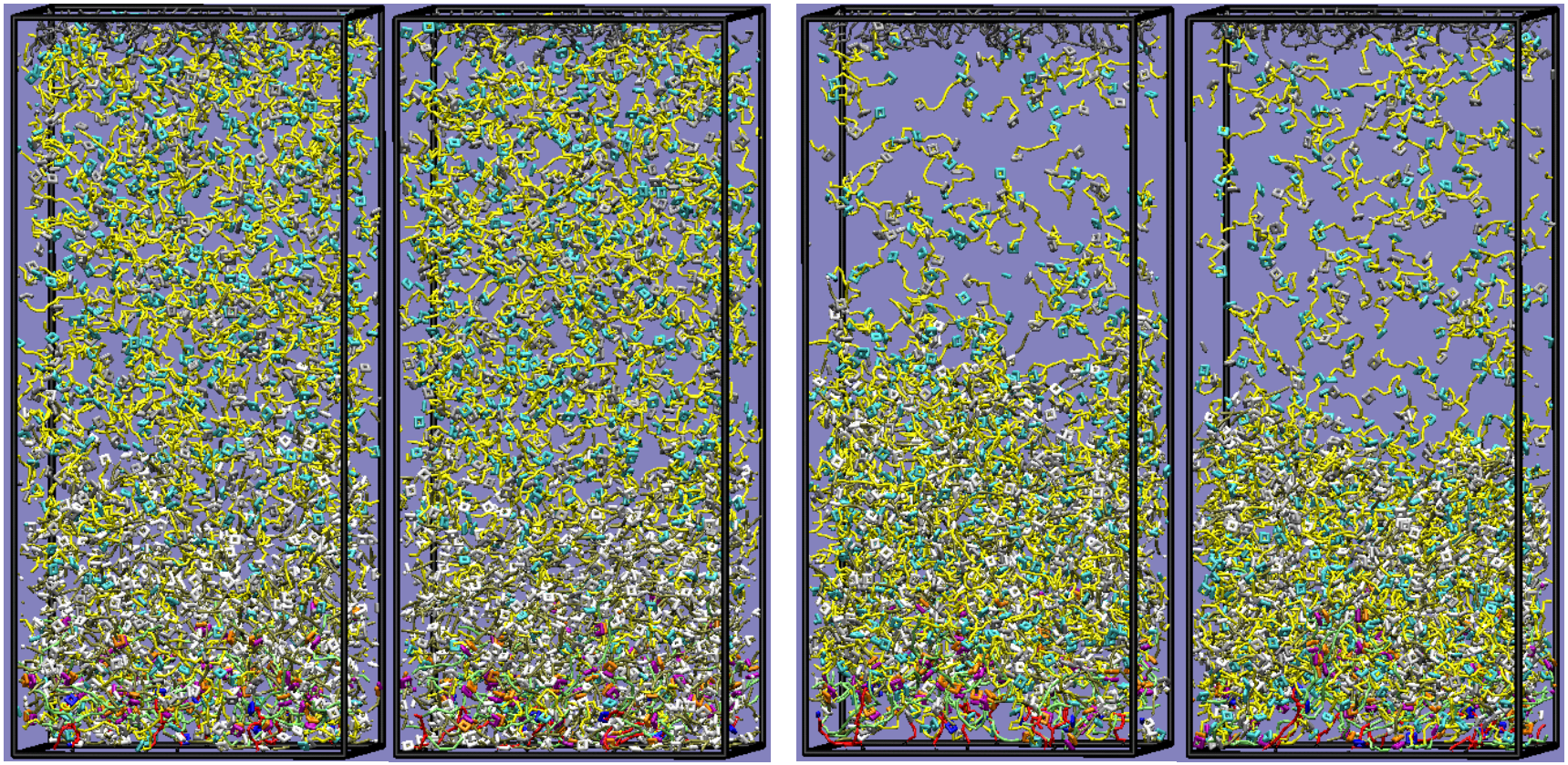

Fig. 4.8

Simulation snapshots of the self-assembling endothelial surface layer under shear flow.
from left to right – non-interacting layer at $v = 0$; non-interacting layer at $v = 0.1$; glycocalyx with hyaluronan-plasma protein interaction energy $\varepsilon = 1.5$ at $v = 0$; glycocalyx with hyaluronan- plasma protein interaction energy $\varepsilon = 1.5$ at $v = 0.1$

A more detailed analysis of the glycocalyx thickness and density is provided, as in the previous simulation attempts, by building density distributions for the various layer constituents, as shown in Fig. 4.9. Velocity profiles for the sheared cases were also constructed on the same plots – their linearity confirms once again that the hydrodynamic interactions in the system are modeled properly.

The behavior of the proteoglycan and polysaccharide components in the presence of shear flow is essentially the same as the behavior seen in the case of the covalently bound layer. The proteoglycan core proteins and heparan sulfate side chain density profiles do not experience any visible changes, even for wall velocities as high as $v = 0.1$ (as indicated by the analysis in chapter 3, this value corresponds to a flow rate that significantly exceeds physiological values in the microcirculation). The situation is different in the case of the hyaluronan density profile – mainly due to their large stiffness, the hyaluronan molecules respond visibly to the flow by tilting in its direction, and thus there is pronounced decrease in the hyaluronan thickness and a corresponding increase in its average density.

The plasma protein density profiles have two distinctly different regions – the bulk plasma region, which is uniform and invariant, and the glycocalyx region, which can be seen to weakly depend on the flow velocity. In the case of non-interacting plasma proteins in the endothelial surface layer, there is indeed a very weak decrease of the protein concentration within the layer. This is exactly compensated by the decrease in the layer thickness, so that the concentration of plasma proteins in the bulk is constant and independent of the shear flow conditions. Similarly, in the case of finite interaction energy, the endothelial surface layer loses as many plasma proteins as needed to keep the

outside concentration unchanged, while a vast majority of the plasma proteins remain in the layer even at the high shear rate. Overall, the equality of chemical potential of the plasma proteins in the bulk and in the ESL in equilibrium conditions, and the insensitivity of the chemical potential to the flow rates studied leads to the fixed value of protein concentration in the bulk plasma region.

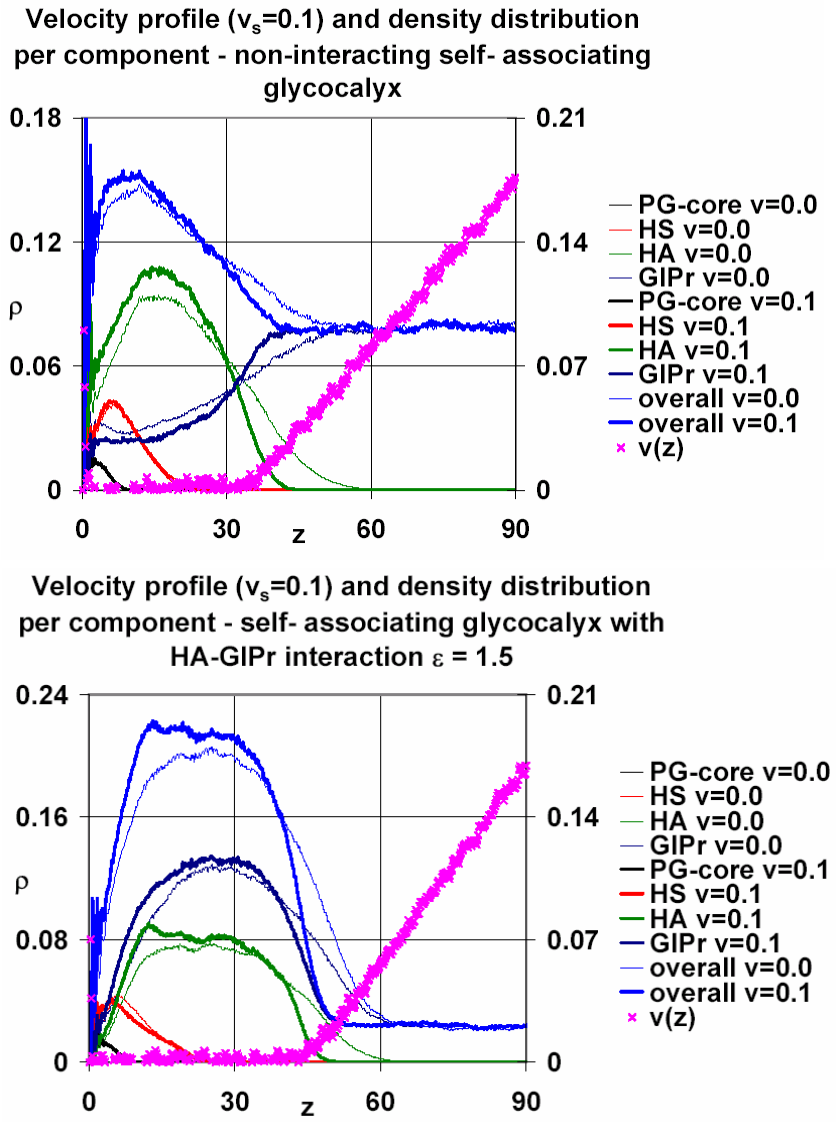

Fig 4.9

Velocity profiles (for surface velocities 0.1) and density distributions per components for the self-assembling endothelial surface layer: **top** – no hyaluronan-plasma protein interaction; **bottom** – interaction energy $\varepsilon = 1.5$

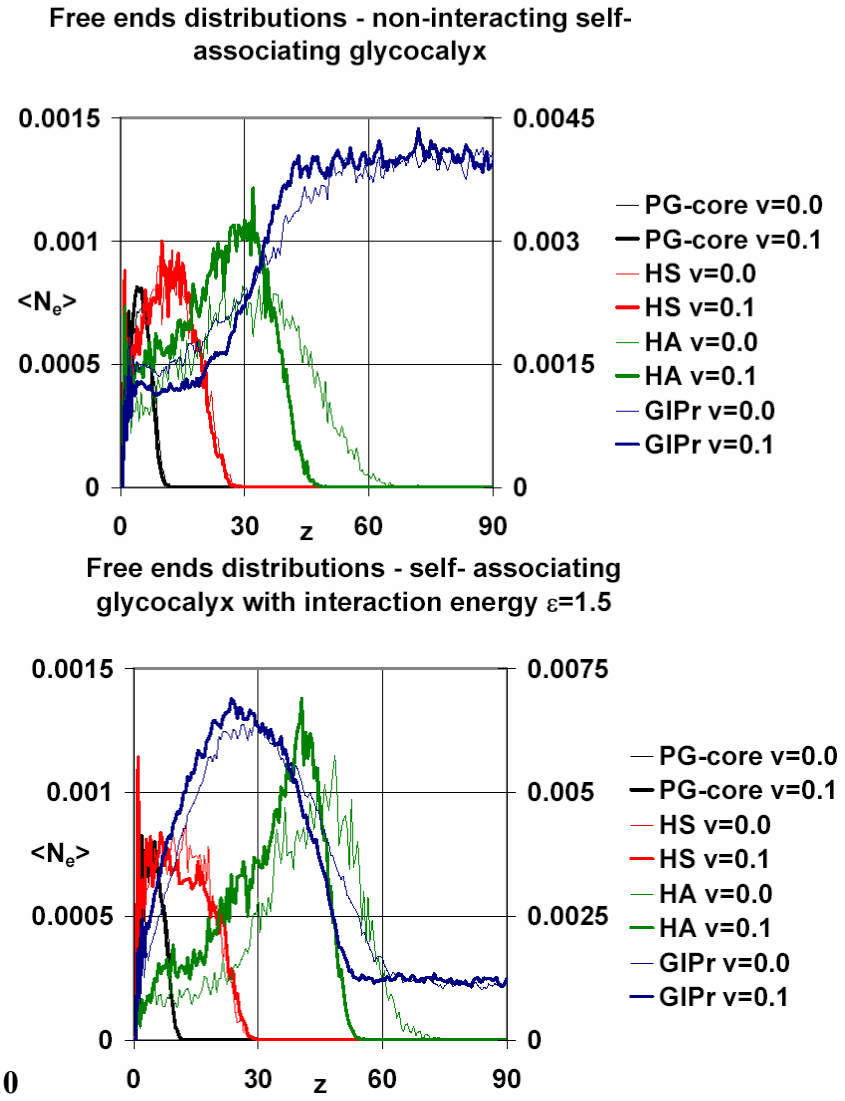

Fig. 4.10

Free ends distributions for the self-assembling endothelial surface layer: **top** – non-interacting; **bottom** – interaction energy $\varepsilon = 1.5$. Note that for the protein ends a secondary axis is used.

The free ends distributions at $v = 0$ and $v = 0.1$ for the two ESL layers (non-interacting on top and $\varepsilon = 1.5$ on the bottom) are shown in Fig. 4.10. Generally, they follow the same trends as the density distributions. In particular, the tethered proteoglycan molecules do not exhibit any changes in their free end distributions, while the hyaluronan chain ends extension in the z-direction decreases in the case of strong

flow. Accordingly, the plasma protein end distribution exhibits a very slight redistribution consistent with the overall change in conformation of the endothelial surface layer in a way that conserves the bulk concentration of plasma protein ends.

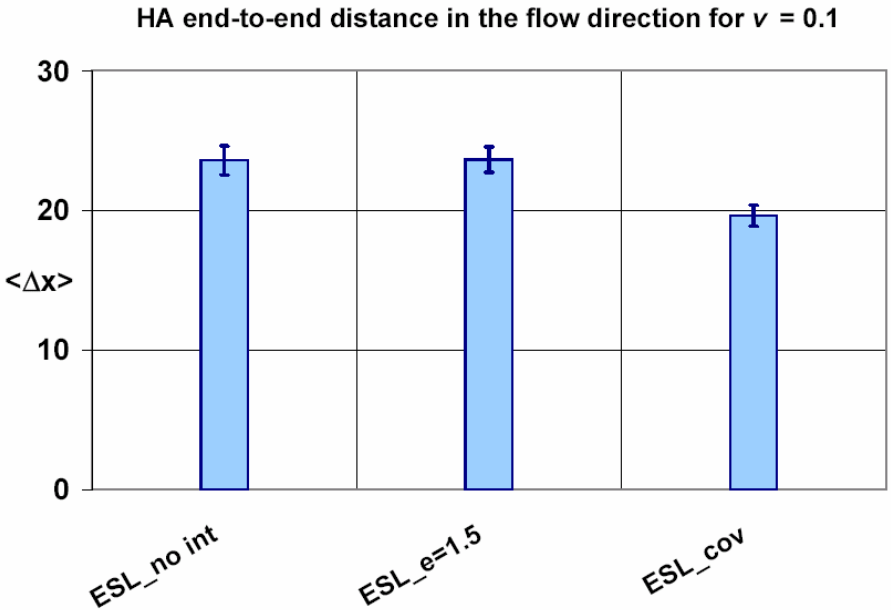

Fig. 4.11

The extent of tilting of hyaluronan molecules (measured by the end-to-end distance in the x-direction) for the high shear rate as a function of the glycocalyx conformation.

The degree of tilting of the hyaluronan chains in flow can be estimated by calculating their average end-to-end distance in the flow direction (i.e. the $x-$direction) as shown in Fig. 4.11. It is evident from the figure that the hyaluronan in the covalently bound layer tends to extend considerably less in the flow direction than in either the self-assembling layers or in the glycocalyx configuration containing no plasma proteins. The reason for this behavior may be due to the effect of plasma protein concentration on the hydrodynamic drag at the luminal surface of the ESL. On one hand, an increased concentration of bound plasma protein near the free surface of the ESL (as occurs in the covalently bound case) reduces the hydrodynamic penetration depth of solvent flow into

the ESL, thereby decreasing the total drag force per hyaluronan chain. On the other hand, the drag force on each hyaluronan chain depends on the effective viscosity of the plasma, which is an increasing function of free protein concentration in the plasma (as occurs when proteins are unbound or reversibly bound). All else being equal, these observations would imply that hyaluronan chains would feel more drag, and thereby would be stretched more in the direction of the fluid flow, (i) if submerged in a solution with more unbound plasma protein present than in a protein-depleted plasma, and (ii) if there was less protein bound to hyaluronan chains near their free ends where hydrodynamic penetration of solvent is significant.

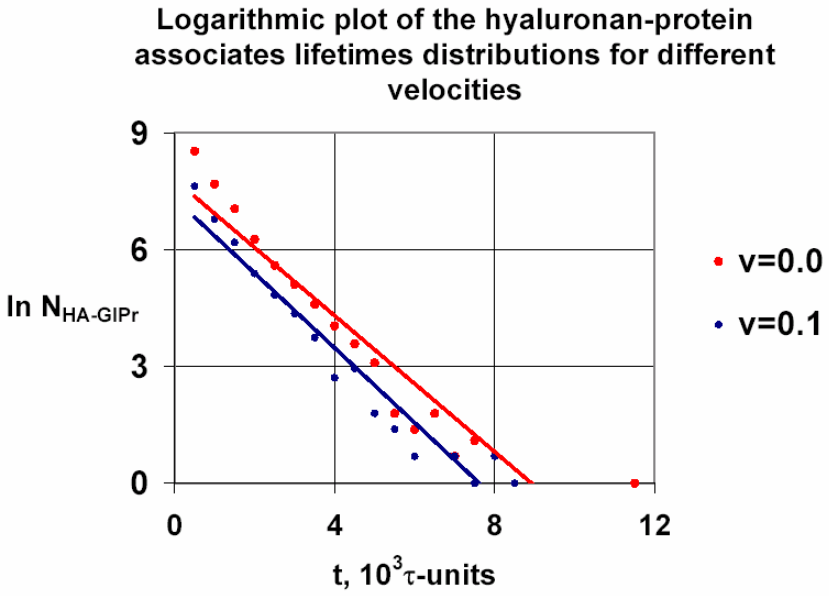

Fig 4.12

Logarithmic plot of the characteristic lifetime distributions for hyaluronan-plasma protein complexes with $\varepsilon = 1.5$ as a function of the shear flow velocity.

Another relevant ESL property to be examined is the shear rate dependence of the hyaluronan-plasma protein association/dissociation rates and the characteristic lifetimes of their complexes. Figure 4.12 shows logarithmic plots of the hyaluronan-protein complex lifetime distributions in the absence of flow, $v = 0$, and for wall velocity

$v = 0.1$. As in the previous section, the average complex lifetimes can be estimated from the slopes of these curves. The results show that the presence of the shear flow weakly decreases the characteristic complex lifetime from $1.14 \cdot 10^{-5}\,\mathrm{s}$ to about $1.04 \cdot 10^{-5}\,\mathrm{s}$. Moreover, the overall population of complexes is reduced in flow conditions. Again, since the fluid flow is screened in the most part of the endothelial surface layer, the observed decreases are mainly due to increased rates of dissociation and association close to the glycocalyx-bulk interface.

4.4 Effect of Plasma Depletion on ESL Assembly

In order to mimic the effects of plasma depletion on ESL properties, a series of ESL simulations in quiescent conditions were performed in which the overall population of plasma proteins was systematically reduced. Figure 4.13 shows simulation snapshots of the equilibrium ESL configurations for three populations of plasma proteins ($N_{\mathrm{GlPr}} = 600, 255, 101$) and two interaction energies, $\varepsilon = 1.5$ (top panel) and $\varepsilon = 1.0$ (bottom panel). As expected, visibly different equilibrium distributions of the plasma proteins were achieved in each individual case. In all the simulations the reduction of plasma protein concentration leads to a corresponding decrease in the protein amount in both the plasma and ESL regions. However, the relative distribution of plasma proteins between the two regions depends of the plasma protein-hyaluronan interaction energy. For $\varepsilon = 1.0$ the protein distribution between the glycocalyx and the bulk regions is much less polarized. Recall that the average lifetime of the protein-hyaluronan complexes is found to be by an order of magnitude smaller for $\varepsilon = 1.0$ than the corresponding lifetime for energy $\varepsilon = 1.5$. That means that the ESL much more readily gives away the plasma proteins absorbed in it when the protein concentration in the bulk is reduced. Moreover, due to the difference in the complex lifetimes, the observed equilibrium is also reached faster. As a result, for the smallest plasma protein concentration attempted, a large part of the protein molecules are effectively removed from the glycocalyx in the weak association conditions of $\varepsilon = 1.0$. On the other hand, for the case of the stronger energy of interaction, $\varepsilon = 1.5$, the distribution of the plasma proteins between the ESL and the bulk is rather inhomogeneous and is less sensitive to the overall number of plasma

proteins. The energy gain for forming the protein-hyaluronan complexes in this case exceeds the osmotic penalty paid for concentrating plasma protein within the ESL. The association energy effect is dominant to such an extent that below a certain average concentration of plasma protein molecules in the simulation box, essentially the entire protein population is found in the glycocalyx (see the top right snapshot in Fig. 4.13 which shows that all but two plasma proteins are still found in the ESL). The densities of the ESL components in these different cases are also gradually changing with the overall decrease in plasma protein concentration. The percentage decrease in the total ESL density is more pronounced in the case of the weaker protein-hyaluronan interaction energy. Therefore, this effect is most visible in the $\varepsilon = 1.0$ set of snapshots in Fig. 4.13. The configurations shown on the left and on the right sides of the bottom panel indicate that the ESL with most total plasma protein has a significantly larger density than the layer with the least protein, for which the overall density comes mainly from the covalently bound constituents – proteoglycans and polysaccharides. On the other hand, the relative density decrease in the strong interaction energy case (top panel of Fig. 4.13) seems to be less with decreasing total number of plasma proteins, even though intuitively it corresponds to a larger absolute number of proteins removed from the ESL. In contrast, the ESL thickness does not seem to be affected by a drop in overall protein concentration in the case of the weaker interaction energy $\varepsilon = 1.0$, implying that ESL thickness in this case is mainly determined by the hyaluronan chain configurations. However, in the case of interaction energy $\varepsilon = 1.5$ there is a visible ESL thickness difference between the highest protein concentration case and the others, implying that a critical number of associated plasma proteins is required to swell the ESL.

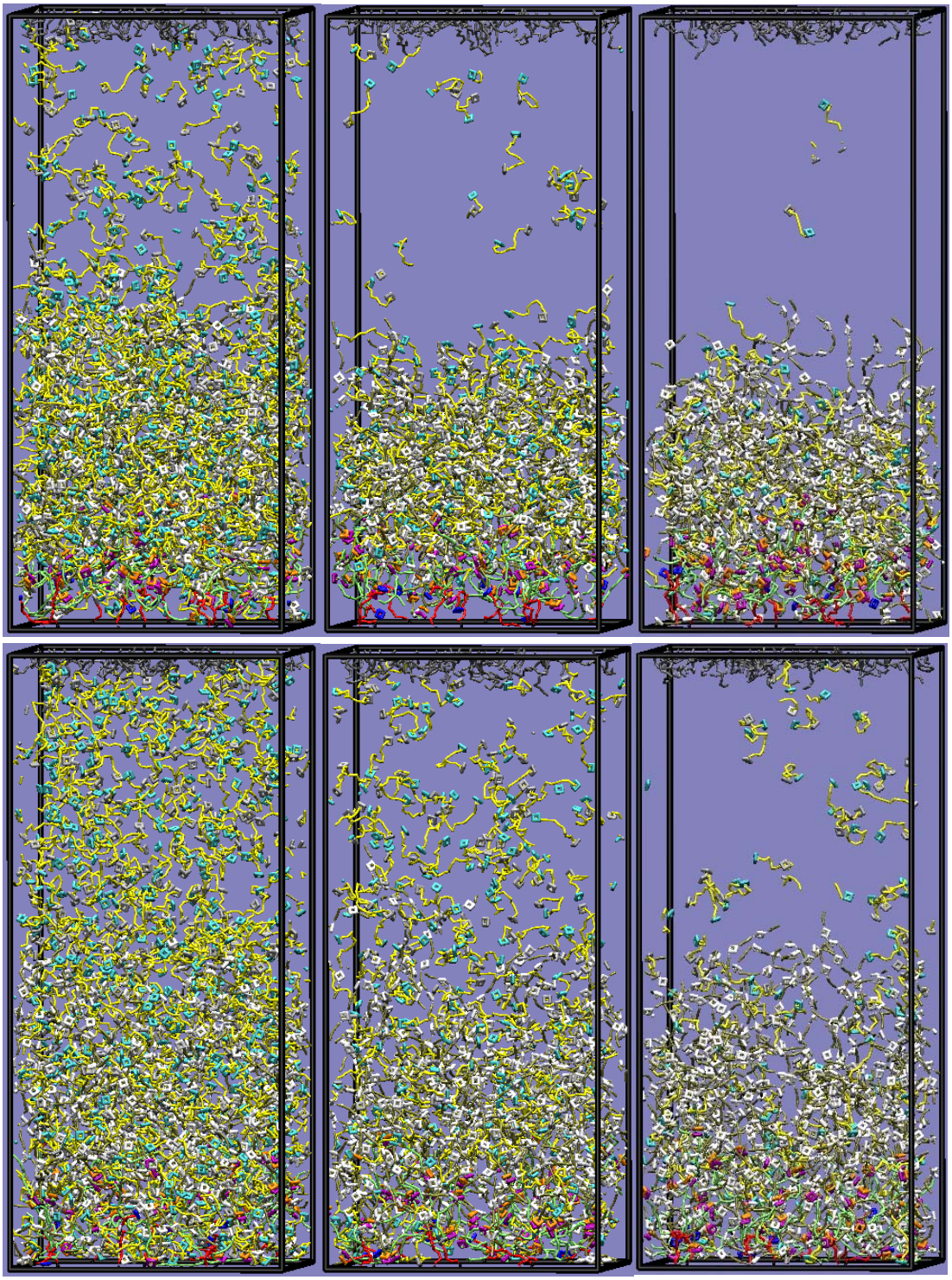

Fig. 4.13

Simulation snapshots of the self-assembling endothelial surface layer in hemodilution: **top** three – interaction energy $\varepsilon = 1.5$; **bottom** three - $\varepsilon = 1.0$; on each level **from left to right** - $N_{\mathrm{GlPr}} = 600$; $N_{\mathrm{GlPr}} = 255$; $N_{\mathrm{GlPr}} = 101$

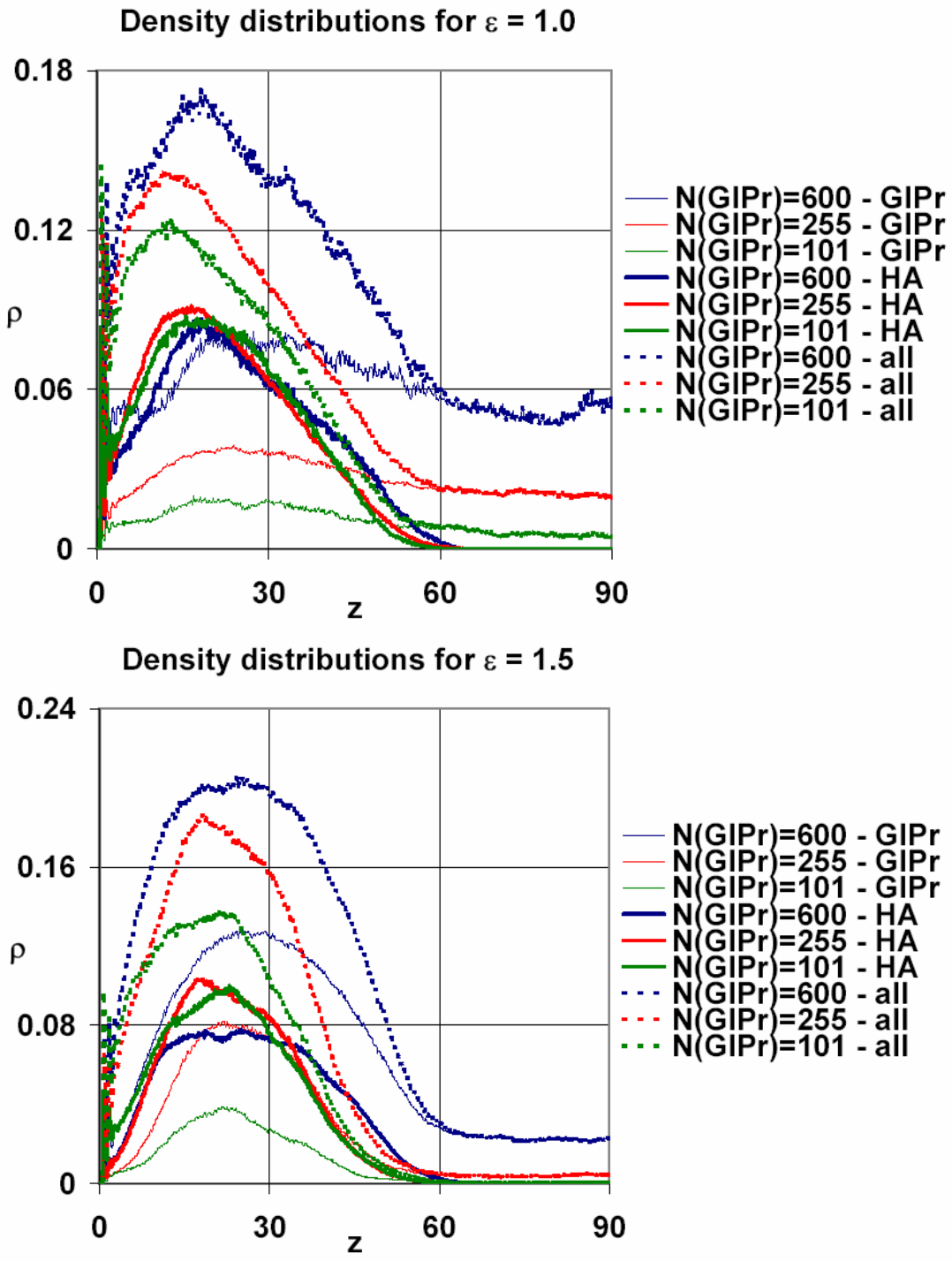

Fig. 4.14

Density distributions by components (proteoglycan densities not included): **top** – interaction energy $\varepsilon = 1.0$; **bottom** - interaction energy $\varepsilon = 1.5$.

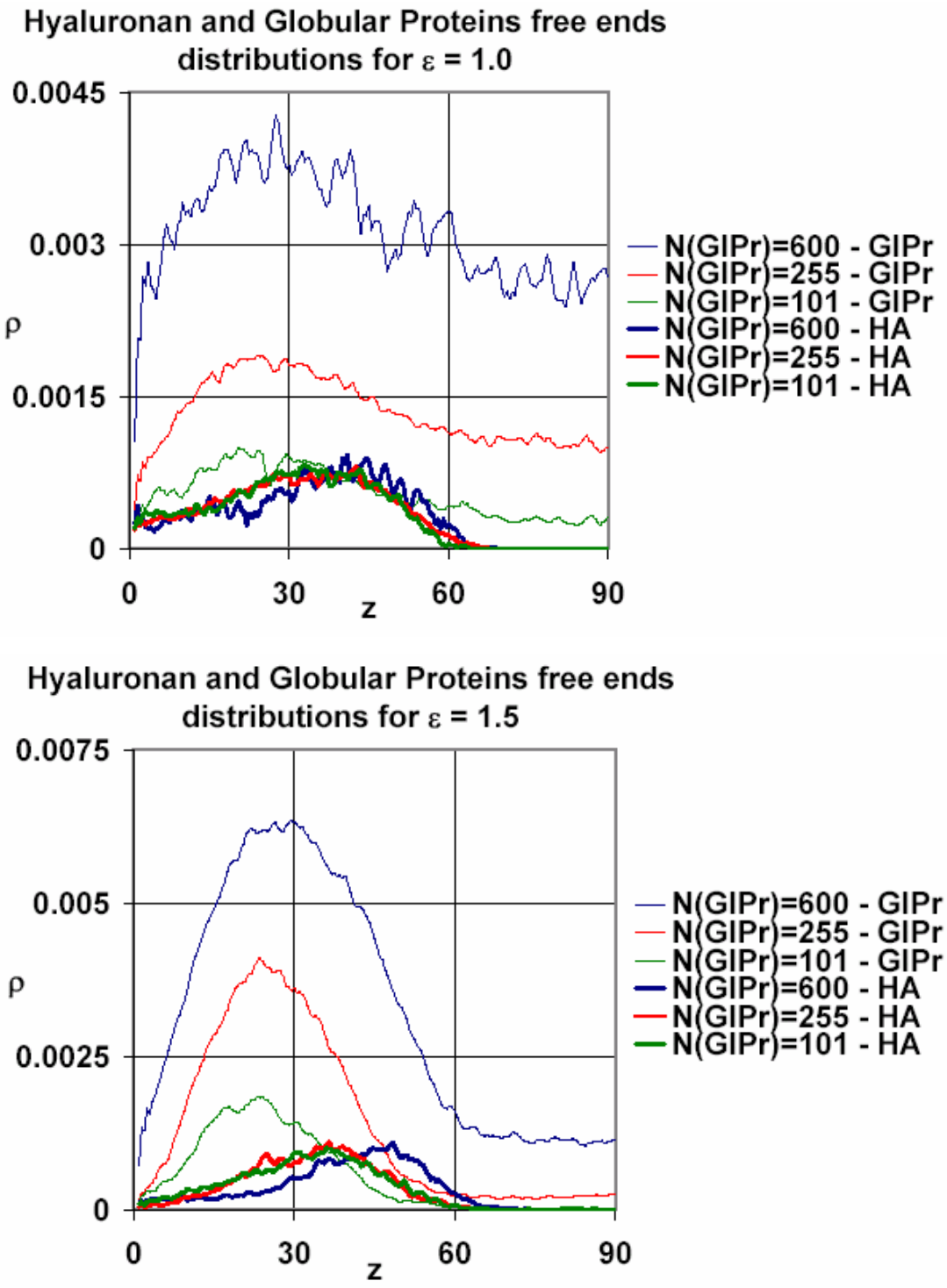

Fig. 4.15

Free end distributions by components (with proteoglycan free ends not included): **top** – interaction energy $\varepsilon = 1.0$; **bottom** - interaction energy $\varepsilon = 1.5$.

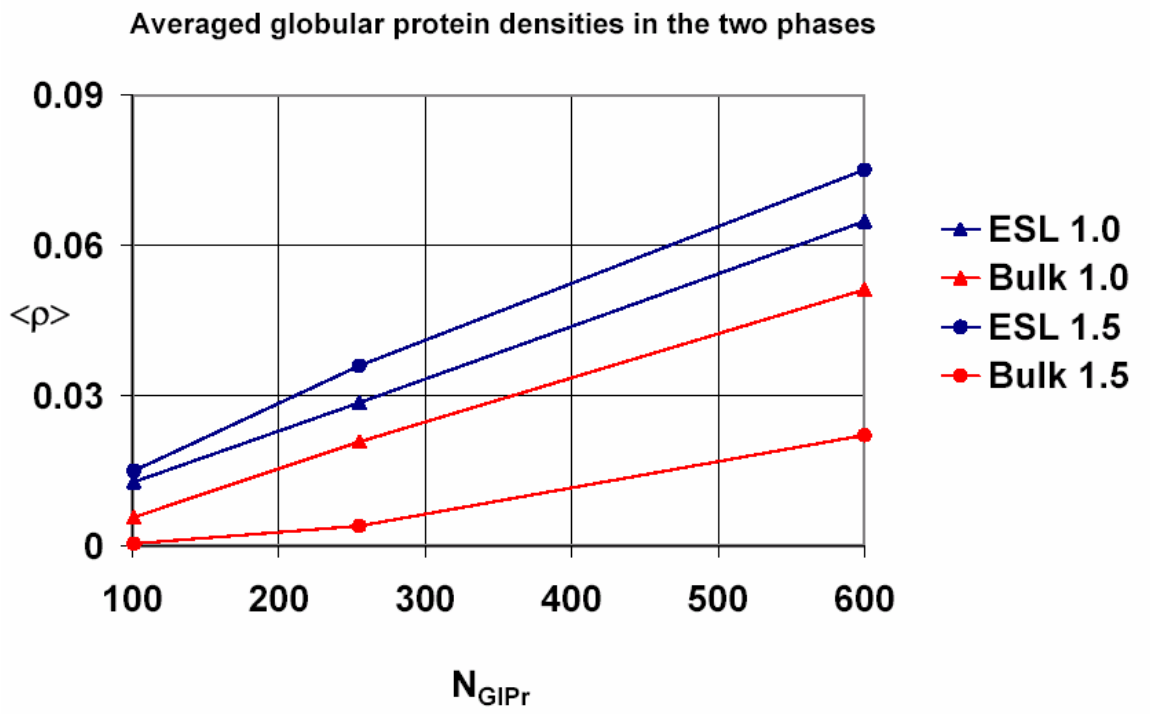

Fig. 4.16

Plasma protein density averaged over the entire bulk/ESL regions as a function of the total number of plasma proteins.

A more quantitative data analysis for the concentration dependence of the relative distribution of plasma proteins can be obtained from density and free end distributions, as was done in the previous chapters and shown in Figs. 4.14, 4.15 and 4.16. The first observation from the density and free ends profiles is that the plasma protein density and concentration of free ends outside the layer is approximately constant, which is an indication that indeed the conformations observed have reached their equilibrium state. From the hyaluronan density and free end distributions for the two energies, the effect of the overall plasma protein concentration on the ESL thickness can be estimated. In the case of the weaker hyaluronan-plasma protein interaction energy $\varepsilon = 1.0$, the change in the layer thickness is relatively insignificant even over a six-fold decrease of plasma protein concentration, a result consistent with the snapshots in Fig. 4.13. The height

dependence on the plasma protein concentration in the case of energy $\varepsilon = 1.5$ is more pronounced, but again not as strong an effect as seen in the snapshot observations. The difference can be accounted for by the fact that the uppermost part of the glycocalyx in that case contains mainly plasma proteins.

On the other hand, the effect of the plasma proteins removal on the overall layer density is significant for both interaction energies studied. In the case of $\varepsilon = 1.0$ the endothelial surface layer density decreases by about 40% in response to the six-fold decrease of the plasma protein concentration, while in the case of $\varepsilon = 1.5$, the corresponding decrease is 50%. Such a decrease would certainly affect the glycocalyx permeability for macromolecules and hydrodynamic penetration for shear flow, even if it does not significantly change the effective thickness of the ESL. If the ratio between the glycocalyx and bulk concentration is characterized for the different concentration regimes, very different behavior is observed for the two energies investigated. In the case of $\varepsilon = 1.0$, the ratio between the number of plasma proteins situated in the layer and in the bulk plasma changes very little as the total concentration of plasma proteins decreases from 1.26 (the case of 600 proteins) to 2.24 (the case of 101 proteins). On the contrary, when the energy of interaction is strong ($\varepsilon = 1.5$) the corresponding ratio increases dramatically with the decrease in total plasma protein concentration. Particularly for the lowest plasma protein concentration case, the density of plasma proteins inside the layer is about 34.1 times larger than the corresponding bulk concentration (compared with 3.4 times for the highest plasma protein concentration). This shows an important difference between the two energy cases investigated. Even though in the long run both of the glycocalyx layers would probably lose all their plasma proteins when the bulk phase

above is protein-depleted plasma, the time scale over which that phenomenon would be observed is very different between the two interaction energies. Exact calculations of those time scales cannot be performed in this work because of the difficulty to create a simulation setup that properly models an experimental saline perfusion scenario. However, it can be speculated that for the weaker interaction energy investigated, the time over which the endothelial surface layer would effectively lose its plasma protein content during saline perfusion would be comparable to the characteristic time over which the present simulations were performed. In these particular cases the average simulation time of 30-40 million steps of time 0.005τ, with τ estimated in chapter 3 being of the order of 10^{-8}-10^{-7} s, corresponds to a fairly short timescale of the order of milliseconds for plasma protein removal from the glycocalyx. In the case of strongly binding plasma proteins, this timescale is expected to be several orders of magnitude larger than the timescales of the present simulations. This is only speculation, since a proper estimate cannot be made based on the available data. However, it is apparent that for large enough values of the interaction energy, the ESL is still able to retain the vast majority of plasma proteins, even when the bulk plasma protein concentrations are negligible. Thus, there is even a possibility that during plasma depletion, if the interaction energy between the hyaluronan molecules and the plasma proteins is large enough the plasma proteins would not be entirely removed from the endothelial surface layer in physiological timescales.

Another interesting feature of these results is the apparent need for some minimal threshold amount of plasma protein molecules in the endothelial surface layer in order for additional extension of the hyaluronan chains and the resulting increase of the ESL

thickness to occur. From the simulation results obtained, that threshold seems to be reached only at fairly high interaction energy levels and high plasma protein concentrations. Having in mind the macromolecular nature of the layer constituents, this feature is expected – this threshold value of the plasma concentration in the layer would correspond to the limit where the additional osmotic pressure in the glycocalyx exceeds the entropy-originated elastic forces that govern the extension of tethered hyaluronan molecules. A proper model based on scaling polymer ideas, to be introduced in the next chapter, will provide more quantitative information about that threshold concentration and the subsequent behavior of the layer after it is reached, and will be compared to the results obtained here.

4.5 Discussion

The simulations of the associating ESL model reveal a very dynamic structure with considerable rates of association and dissociation of the plasma protein-hyaluronan complexes and correspondingly low values for the characteristic complex lifetime. In spite of this very dynamic nature, the presence of attractive protein-hyaluronan interactions leads to the assembly of a robust ESL layer within which the diffusion of the mobile associating elements is strongly influenced with respect to diffusion in the bulk phase. Moreover, the effects of steric hindrance due to finite layer density were shown to be insignificant in comparison to the contribution of the association/dissociation events to plasma protein transport within the layer.

The simulations performed also showed that the distribution of the plasma protein molecules between the bulk plasma and ESL phases is fairly sensitive to the magnitude of the energy of interaction between the hyaluronan and the associating protein species. The pronounced sensitivity comes mainly from the way the binding sites are modeled as 'pyramidal' ligand-receptor pairs. Through the use of these pyramidal binding sites, the achieved sensitivity provides the means for fine adjustment of the association behavior and the potential for mapping onto experimental association parameters when available.

To our knowledge, there is no published data available concerning the average lifetimes of the hyaluronan-protein complexes. Unpublished results from Ralph Colby's at Penn State University on studies of hyaluronan-albumin interactions in synovial fluid indicate that the interactions are indeed very dynamic with estimated lifetimes for the complexes of the order of microseconds (*R.H. Colby, private communication)*. Such

predictions are in surprising agreement with the results obtained in the present work. Experimental studies of tagged albumin diffusion in the ESL *(Osterloh, et al, 2002)* also found that transport of albumin within the layer was only moderately hindered by the presence of the ESL, in qualitative accord with our findings. Direct quantitative comparison of our results with experimental diffusion data is problematic, due to the simplistic nature of our coarse-grained model and its lack of an appropriate range of characteristic length and time scales separating small molecule solvent and macromolecular properties. However, it may be possible to make indirect comparisons by comparing the *ratios* of hindered and free diffusion of plasma proteins in experiments with those in our simulations. Specifically, using such an approach one would be able to compare the ratio of our dimensionless diffusion coefficients from the simulation of generic plasma protein transport to the ratio of physical, dimensional diffusion constants from appropriate experiments (i.e. the unknown dimensional scaling does not enter into the comparison).

The rapid association/dissociation dynamics of the hyaluronan-plasma protein complexes and the correspondingly high diffusivity of the plasma proteins in the ESL might be expected to imply a significant susceptibility of the ESL to external perturbations such as plasma flow or rapid changes in plasma composition. For the case of the ESL in shear flow, however, the simulations results indicated somewhat weaker response than expected. Rather weak plasma protein redistribution was observed, adequate to compensate the weak brush thickness decrease due to chain tilting, but the bulk concentration of plasma protein remained the same for all shear rates studied. Moreover, the dynamic ESL response was comparable to that observed in the case of an

ESL with covalently bound constituents – a weak decrease in height and a weak increase in density with no significant redistribution of the free ends of glycocalyx components.

On the other hand, the results from this chapter are in definite disagreement with recent experimental results (*Ueda et al, 2004*) reporting that increased shear rates lead to an increase in the glycocalyx thickness and elevated uptake of albumin, which implies an increased permeability of the layer. This permeability increase could correspond to a decrease in the endothelial surface layer density, which is again the opposite of what was observed during the simulations. This disagreement is probably due to factors not accounted for in the present model. One relevant phenomenon is the observed increase of cellular production of hyaluronan in conditions of elevated shear stress. This secreted hyaluronan can then incorporate itself into the glycocalyx and thereby recruit additional albumin to associate with the new unoccupied hyaluronan binding domains, thus leading to an overall increase in the layer thickness as experimentally observed.

The redistribution of plasma proteins between the bulk plasma and ESL regions in response to plasma protein dilution was shown in this work to depend sensitively to the strength of the hyaluronan-plasma protein interaction energy ε. For a relatively large value ($\varepsilon = 1.5$), the reduction of the total number of plasma proteins led to a progressively large relative protein concentration in the ESL (i.e. the ESL acted as a sink for proteins at low concentrations). On the other hand, for a relatively small value ($\varepsilon = 1.0$), the ESL became relatively depleted of plasma protein with the reduction of the total number of plasma proteins in the system - a phenomenon reminiscent of the effect seen in certain perfusion experiments. There are two possible major experimental approaches to characterizing the glycocalyx during perfusion of saline or another plasma

substitute that can be used for reference and comparison with our simulation results. Both of these are indirect methods of inferring changes in the glycocalyx, either *in vivo* or *in vitro*, from measurements of blood flow properties. In one such study (*Pries et al, 1998*) the blood flow resistance in the rat mesentery *in vivo* was measured during hemodilution or saline perfusion with or without heparinase pretreatment. The results from the experiment were consistent with the removal of a 1.5 micron thick layer of ESL. The simulation results on the simple three-component ESL model cannot predict such extensive dissolution of the ESL by depletion of macromolecules from the plasma. This is due to the fact that the only reversibly assembling constituent of the model in its present form is the plasma protein; the hyaluronan-like component in the full ESL representation is irreversibly bound to the syndecan species, which in turn is permanently grafted to the lower surface. In reality, all components are transiently bound into the ESL assembly. Moreover, the underlying endothelial cells are likely to shed their components in response to changes in plasma composition, a feature also not built into our model.

Plasma depletion is also able to significantly increase the glycocalyx permeability to flow, which may be an alternative mechanism for the flow resistance change in absence of plasma proteins observed in experiments. Another experimental work (*Long et al, 2004*) inferred the glycocalyx modifications during hemodilution by accounting for alterations in blood viscosity and shear rate profiles in hemodilution conditions. The results of this study were interpreted in terms of changes in layer thickness with a conserved hydraulic conductivity. However, the alternative mechanism of permeability change due to a decrease of ELS layer density at fixed ESL thickness, as suggested by the simulations, may also be used to interpret the experimental results.

5. Theoretical Modeling of the Self-Assembling Glycocalyx Based on Polymer Scaling Principles

5.1. The Model Description

The outer portion of the endothelial surface layer, consisting of relatively stiff polysaccharide chains and the globular plasma proteins associated with them, was shown to constitute a considerable part of the overall glycocalyx structure and be decisive for the overall layer thickness, density and other related properties. Therefore it might be acceptable while modeling the endothelial surface layer to neglect the contribution of the inner proteoglycan part.

In this chapter a theoretical model is developed that takes into account only the outer part of the endothelial surface layer. The glycocalyx is treated as a polymer brush *(Halperin et al, 1992)* of end-tethered semiflexible linear chains submerged in good solvent. The chains have a certain number of binding sites evenly distributed along their length, to which short side chains can be associated by their ends. Polymer brushes formed from 'comb polymers', flexible main chains decorated with covalently attached side chains, have been studied previously (*Zhulina and Vilgis, 1995; Birshtein et al, 1987*) using scaling arguments. In addition, the properties of free self-assembling comb polymers in solution have also been studied as a model for surfactant association to long flexible polymer chains (*Fredrickson, 1993*). The model presented in this chapter is similar to the one introduced by Fredrickson, but extended for the case of tethered,

semiflexible polymer chains in the brush regime, which is much more relevant for the glycocalyx description.

A sketch of the model system in question is shown in Fig. 5.1. The polymer brush consists of semiflexible chains with degree of polymerization N made up of monomers of size a. The chains are grafted on a planar surface with an average distance between two neighboring chains d which corresponds to a dimensionless grafting density $\sigma = (d/a)^{-2}$. In general, in order for the polymers to be considered in brush regime the polymer coil radius in the unrestricted state, which for good solvent conditions is known to be $R_{N,0} \approx aN^{3/5}$, should significantly exceed the average distance between two chains, i.e. $d << aN^{3/5}$ or $\sigma >> N^{-6/5}$ (otherwise, the polymers on the grafting surface do not significantly interact among each other and therefore do not adopt extended conformations).

Since the grafted chains are considered semiflexible in this model, a characteristic lengthscale has to be introduced over which the chain generally remembers its direction.

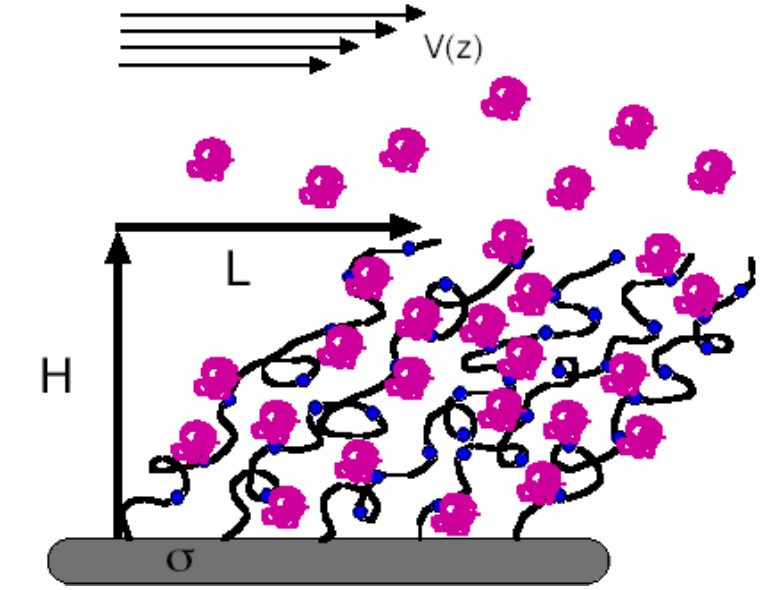

Fig. 5.1

Sketch of a decorated polymer brush.

This lengthscale is expressed by the persistence length L_p, which for semiflexible chains is larger than the monomer size but less than the contour length of the polymer. A stiffness parameter can also be introduced, which is a dimensionless ratio defined as $l_p = L_p / a$.

The polymer coils that associate with the main chains comprising the polymer brush (the pink coils in Fig. 5.1) are assumed for simplicity to have the same size monomer unit, namely a, and consist of M monomer units each. Depending on the number of coils attached to each chain there can be several regimes of chain behavior. If the average distance between two attached coils exceeds their unperturbed size i.e. $R_M \sim aM^{3/5}$, then one may simplify the model by neglecting the effect of coil-coil interactions on the coil conformations. The opposite limit, when the coils are associated close enough to each other that their conformations are also perturbed, is often referred to as 'bottle brush'. The situation most relevant for modeling of the ESL is closer to the first limit described. Thus, in the analysis that follows will assume that

$$P << NM^{-3/5} \qquad \text{or} \qquad P/N << M^{-3/5} \tag{5.1}$$

where P is the number of coils associated to a given chain of the polymer brush.

The equilibrium height of a chain decorated by coils will depend on various factors. Among those is the chain molecular weight and degree of polymerization, the grafting density, the number of attached coils and their size. When shear flow is also imposed on the system, the equilibrium conformation of the chains in the polymer brush may be modified – the chains can deform, mainly by stretching or/and tilting. Therefore, in this case the brush height will in principle depend on the shear flow as well.

We will denote the magnitude of the shear force applied per chain by $f_{\|}$. This shear force is mainly due to the drag from the solvent on the free surface of the polymer brush. It is typically of the order of $f_{\|} \approx \eta V(H) l_{\mathrm{H}}$, where η is the kinematic viscosity of the solvent, $V(H)$ is the fluid velocity at the edge of the brush and $l_{\mathrm{H}} \sim V(H)/V'(H)$ is the characteristic penetration depth of the solvent flow into the polymer brush. The applied force may change the height compared to quiescent conditions and may also induce a lateral displacement of the chain ends. In the following, we will denote the brush height by H, the lateral displacement by L, and the overall end-to-end distance of a chain by $S = \sqrt{H^2 + L^2}$. In the analysis, we adopt the De Gennes ansatz that all chains in the brush behave identically (*Halperin et al, 1992*). This approximation implies that all chain ends would be found at the same height from the grafting surface, near the free surface of the brush. This well-established assumption gives the correct scaling behavior of polymer brushes, and simplifies the analysis considerably by allowing one to model the behavior of each chain as surrounded by identical neighbors.

The free energy of such a chain will have several major contributions. The first, F_{el}, is of purely entropic origin and would account for the elastic stretching of the chain compared to its unconstrained conformation. It is usually given as a ratio between the squares of the perturbed and unperturbed conformations, but in this case a finite extensibility term will be added (*Kuznetsov and Chen, 1998*) to give:

$$F_{\mathrm{el}} = \alpha_1 \frac{S^2}{NaL_{\mathrm{p}}} \left(1 - \frac{S}{Na}\right)^{-1} \tag{5.2}$$

where α_1 is a constant of order of unity.

Another contribution to the free energy, F_{int}, would result from excluded-volume interactions with the chain neighbors, with a term separately accounting for the interactions of the main chains and a term for the interactions between associated coils. Both terms are obtained through a virial expansion with the inclusion of only two-body interactions:

$$\frac{F_{\text{int}}}{kT} = \alpha_2 v a^3 \frac{N^2}{Hd^2} + \alpha_3 w R_{\text{M}}^3 \frac{P^2}{Hd^2} \tag{5.3}$$

where v and w are, respectively, the dimensionless second virial coefficients for the main chain monomer-monomer interactions and the side chain coil-coil interactions and α_2 and α_3 are constants of order of unity. In the following, we will set $v = w = 1$, for simplicity.

The total free energy per chain can be non-dimensionalized for simplicity in the subsequent analysis. The characteristic lengthscale is chosen to be Na, the contour length of a linear polymer chain *(Halperin et al, 1992)*. Therefore, the corresponding dimensionless brush height, lateral displacement and end-to-end distance will be:

$$h = \frac{H}{Na}; \quad l = \frac{L}{Na}; \qquad s = \frac{S}{Na} \tag{5.4}$$

Using the dimensionless variables above, it is possible to express the equation for the free energy per chain in the following manner:

$$\frac{F}{NkT} = \alpha_1 \frac{s^2}{l_{\text{p}}}(1-s)^{-1} + \alpha_2 \frac{\sigma}{h} + \alpha_3 M^{9/5} \frac{\sigma}{h}\left(\frac{P}{N}\right)^2 \tag{5.5}$$

If the numerical constants α_{i} (unknown but of order unity) are set to $\alpha_{\text{i}} = 1$, then by introducing the function $\zeta(N, M, P) = 1 + M^{9/5}(P/N)^2$ the chain free energy becomes:

$$\frac{F}{NkT} = \frac{s^2}{l_p(1-s)} + \frac{\sigma}{h}\zeta(N,M,P) \tag{5.6}$$

Using Eq. (5.6), one may obtain an expression for the osmotic pressure in the brush using the relation *(Rubinstein and Colby, 2004)*

$$\Pi = -\frac{\partial F_{\text{int}}}{\partial V} \tag{5.7}$$

where V is the volume occupied by a single decorated chain. If the dimensionless osmotic pressure is defined as $\pi = a^3\Pi/kT$, then from Eq. (5.7) and the relation between the chain volume and dimensionless height it follows that:

$$\pi = \frac{\sigma^2}{h^2}\zeta(N,M,P) \tag{5.8}$$

The expression for the dimensionless osmotic pressure defined in this manner is valid for both quiescent and sheared brush cases. The dependence on the shear flow comes into the osmotic pressure indirectly through the dimensionless height and also through the function $\zeta(N,M,P)$. The second dependence comes from the possibility of redistribution of coils due to the shear flow, and as a result a different number of coils per chain P, which would also change the value of $\zeta(N,M,P)$.

The analysis so far has only dealt with the conformation of a chain containing P associated coils. However, the equilibrium distribution of the associating coils within the system has not yet been determined. In general, numerous states of association may occur, leading to the formation of various types of decorated chains differing from each other by the number of globular coils associated with them. When thermodynamic equilibrium is established in the whole system, there is a certain distribution of the decorated chains in coexistence with free coils in solution, with each type of decorated

chain having a certain volume fraction, denoted ϕ_{P} for a chain decorated by P coils. In this notation ϕ_0 signifies the volume fraction of non-decorated chains in the brush. The equilibrium volume fraction of the free coils is denoted ϕ_{coil}, and the corresponding solvent volume fraction is constrained by:

$$\phi_{\mathrm{s}} = 1 - \phi_{\mathrm{coil}} - \sum_{P=0}^{P_{\max}} \phi_{\mathrm{P}} \tag{5.9}$$

where $P_{\max}$ is the maximum possible number of coils that can attach to a single polymer chain; i.e. the number of binding domains along the chain.

Adapting the same approach used previously for the description of block copolymers (*Goldstein, 1986*) and surfactant association on polymers (*Fredrickson, 1993*), a law of mass action can be derived for our system as well:

$$\phi_{\mathrm{P}} = \frac{\phi_{\mathrm{coil}}^{P} \phi_{\mathrm{Pol}} \exp\left(-\Delta_{\mathrm{P}}/kT\right)}{N \sum_{P=0}^{P_{\max}} \phi_{\mathrm{coil}}^{P} \left(N + PM\right)^{-1} \exp\left(-\Delta_{\mathrm{P}}/kT\right)} \tag{5.10}$$

where $\phi_{\mathrm{Pol}} = \sum_{P=0}^{P_{\max}} \phi_{\mathrm{P}}$ is the overall volume fraction of polymer chains in all their possible forms, decorated or non-decorated, and the variable Δ_{P} is related to the free energy of a chain as follows (the expression is written in the same dimensionless manner as the free energy):

$$\frac{\Delta_{\mathrm{P}}}{NkT} = \frac{1}{N} - \frac{P}{N} - \varepsilon \frac{P}{N} + \frac{\left[F(P) - F(0)\right]}{NkT} \tag{5.11}$$

where $-\varepsilon kT$ is the energy of association of one coil to a polymer chain binding domain. This binding energy is a local quantity that is assumed to not depend on the number of coils attached to a given chain.

From the volume fractions equations (5.10) and (5.11), it is possible to evaluate the mean coil aggregation number for the chains as the following sum (*Fredrickson, 1993*):

$$\langle P \rangle = \frac{\sum_{n=0}^{P_{\max}} P \phi_{\text{coil}}^{P} \left(N + PM\right)^{-1} \exp\left(-\Delta_{\text{P}}/kT\right)}{\sum_{P=0}^{P_{\max}} \phi_{\text{coil}}^{P} \left(N + PM\right)^{-1} \exp\left(-\Delta_{\text{P}}/kT\right)} \tag{5.12}$$

In an explicit, dimensionless form this becomes:

$$\frac{\langle P \rangle}{N} = \frac{\sum_{n=0}^{P_{\max}} \frac{P/N}{1+(P/N)M} \phi_{\text{coil}}^{N(P/N)} \exp\left(-N\left(\frac{1}{N} - \frac{P}{N} - \varepsilon\frac{P}{N} + \frac{\left[F(P)-F(0)\right]}{NkT}\right)\right)}{\sum_{P=0}^{P_{\max}} \left(1+(P/N)M\right)^{-1} \phi_{\text{coil}}^{N(P/N)} \exp\left(-N\left(\frac{1}{N} - \frac{P}{N} - \varepsilon\frac{P}{N} + \frac{\left[F(P)-F(0)\right]}{NkT}\right)\right)} \tag{5.13}$$

The approach developed above is also valid in cases when shear flow is imposed on the system, for which the effects of shear are implicit in the free energies, *F(P)* and *F(0)*. Using the expressions obtained for the free energy components, it is possible now to evaluate the degree to which the coils would partition into the brush and associate with it as a function of different system conditions including in the presence of the shear flow. It is also possible to calculate the equilibrium height of the brush as a function of the shear flow, the volume fraction of coils in the system, and other system parameters.

Since the system modeled mimics upper portions of the self-assembling layers studied by simulations in the previous chapters (i.e. with the proteoglycans taking a passive role as a grafting mechanism), it is interesting to qualitatively compare the simulation results (namely the ESL brush conformation dependence on factors like energy of interaction between the binding elements, flow velocity and plasma protein concentration) to the results obtained from the theoretical model. This will be done in the discussion section of the present chapter.

5.2. The Glycocalyx Model Analysis in Quiescent Conditions

The first case we will investigate is when the brush is found in **quiescent conditions**. In the absence of flow, there is no average lateral displacement of the chains, so that we may set $s = h$. The free energy per chain from Eq, (5.6) then becomes:

$$\frac{F}{NkT} = \frac{h^2}{l_p(1-h)} + \frac{\sigma}{h}\zeta(N,M,P) \tag{5.14}$$

The equilibrium value of h is the one that minimizes this free energy. Solving $\partial F/dh = 0$ gives the following expression for h:

$$h^4 - 2h^3 + (1-h)^2 l_p \sigma\zeta(N,M,P) = 0 \tag{5.15}$$

If we compare the solutions of the above equation to the result for a Gaussian chain, it can be seen that, due to the finite extensibility term included in the elastic free energy contribution, the equilibrium height ends up being relatively smaller for Gaussian chains with or without associated globular coils. The Gaussian chain and the finite-extensibility chain models only converge for the cases of very long chains or very low densities: $N \to \infty$ or $\sigma \to 0$.

In Fig. 5.2 the equilibrium polymer height is shown as a function of the grafting density and persistence length for three cases – a brush of decorated ($P/N = 0.01$) semiflexible chains of finite extensibility, a bare polymer brush of the same kind, and a brush of bare Gaussian chains, for comparison. As shown in the top plot, the bare Gaussian chain brush height significantly exceeds both the bare and decorated finite extensibility brushes. The decorated brush is expectedly thicker than its bare counterpart,

and the dependence of the heights on the persistence length is slightly different, with the Gaussian chain height not exceeding the height of the decorated chains.

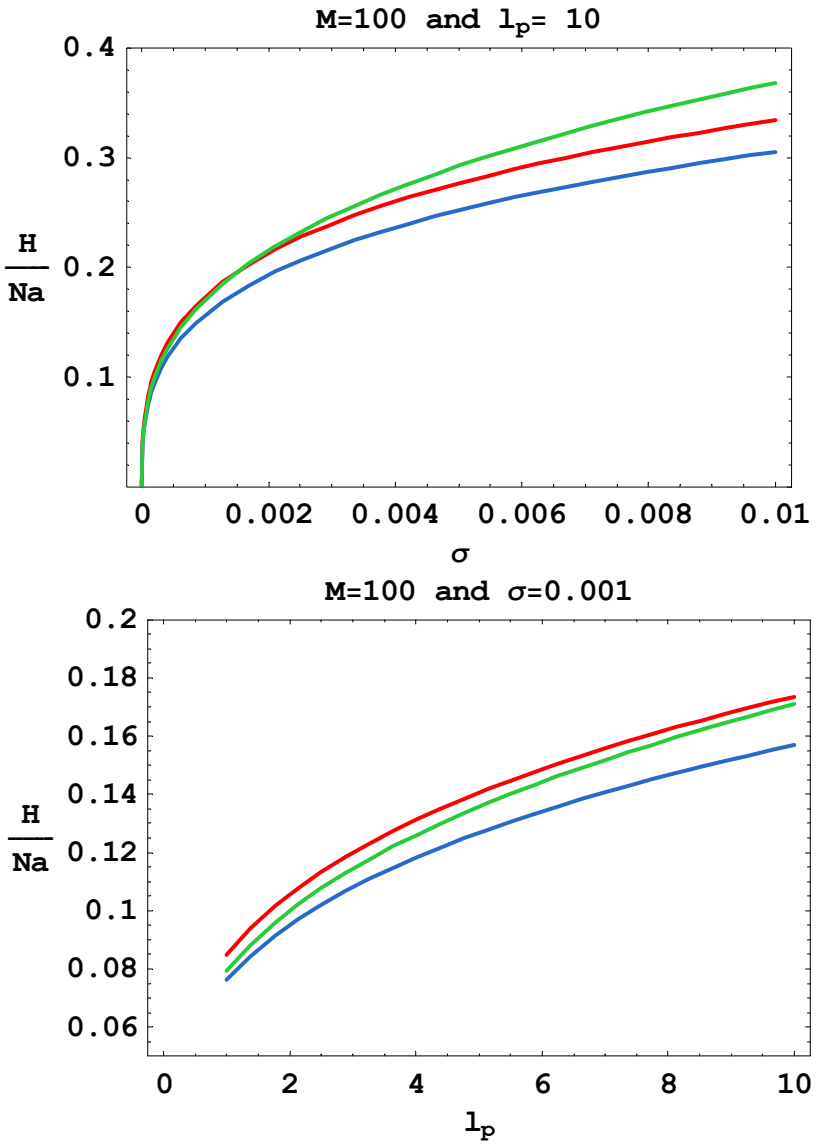

Fig. 5.2

Polymer brush height as a function of the grafting density (**top** plot) and the persistence length (**bottom** plot) for finite extensibility chains with and without associated coils versus Gaussian chains: ***red*** lines – decorated chains with $P/N = 0.01$; ***green*** lines – Gaussian bare chains; ***blue*** lines – finite extensibility chains with no associated coils.

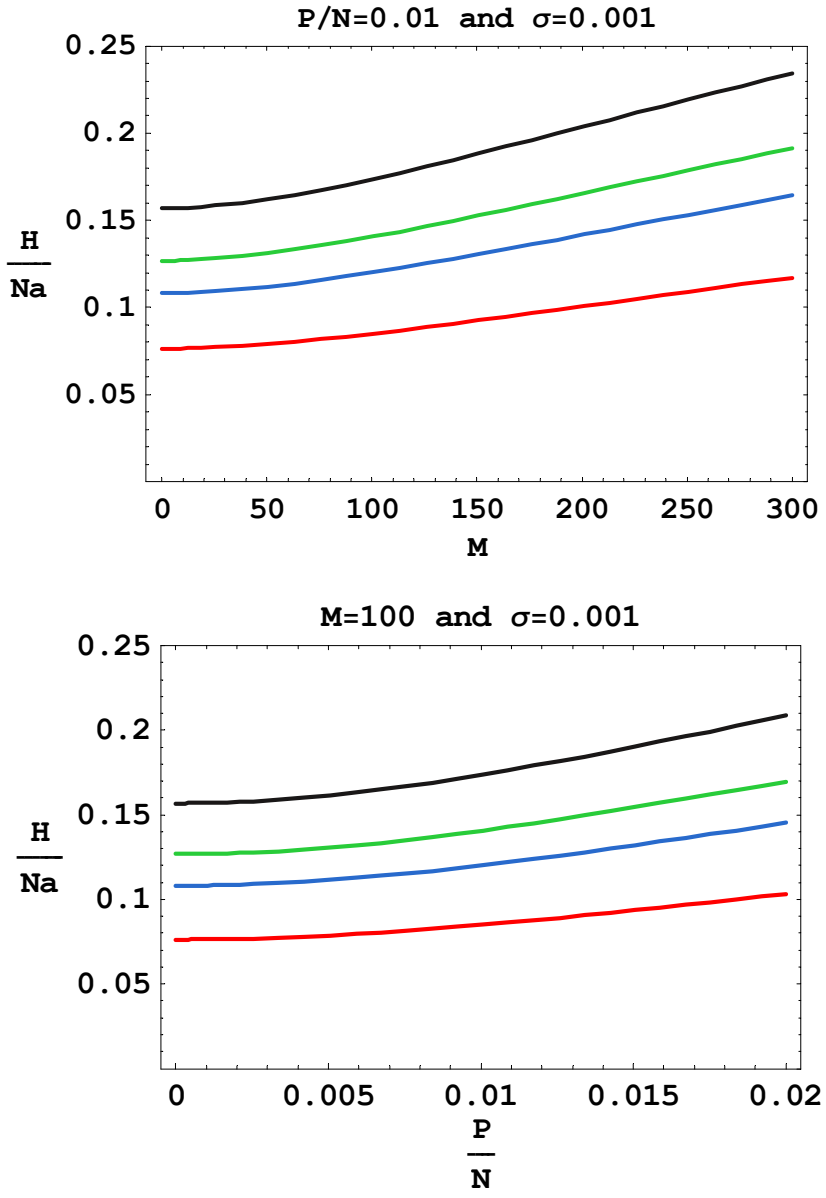

Fig. 5.3

Brush height as a function of coil degree of polymerization M (**top** plot) and the fraction of the chain decorated P/N (**bottom** plot). The different colored lines correspond to: ***red*** - $l_p = 1$; ***blue*** - $l_p = 3$; ***green*** - $l_p = 5$; ***black*** - $l_p = 10$.

In Fig. 5.3 the dependence of the brush height is shown as a function of associating coil size (parameterized by its degree of polymerization M) and the number of coils associated per chain (parameterized by the occupancy fraction P/N of the main chains). The dependence on the persistence length is also included by plotting the heights for several values of l_p on each plot. The trends shown in the plots are a monotonic and non-linear increase of the brush heights with the increase of the coil size or the occupancy fraction. The chains in the brush naturally also tend to become more extended as the persistence length increases. In the case of constant coil size (bottom plot in Fig. 5.3) a change of the persistence length by an order of magnitude results in increase of the brush height by about a factor of 2. Note that all the plots are restricted to the sparsely decorated regime which corresponds to $M < 2000$ for the first plot and $P/N < 0.06$ for the second plot. For values outside of that range the coils are too strongly interacting for the current model to be valid without modification.

Based on the calculated height of the polymer brush in different conditions, it is also possible now, by simply inserting the solution of (5.15) into (5.6) and (5.8), to calculate the dimensionless free energy per chain and the dimensionless osmotic pressure at the constrained equilibrium height. The corresponding plot is shown in Fig. 5.4, where the dimensionless free energy is plotted against the occupancy fraction for a given persistence length (top graph) in order to compare the finite extensibility regime to a Gaussian chain, and then for a set of persistence lengths (middle graph). The dimensionless osmotic pressure is plotted for a set of persistence lengths in the bottom graph of Fig. 5.4.

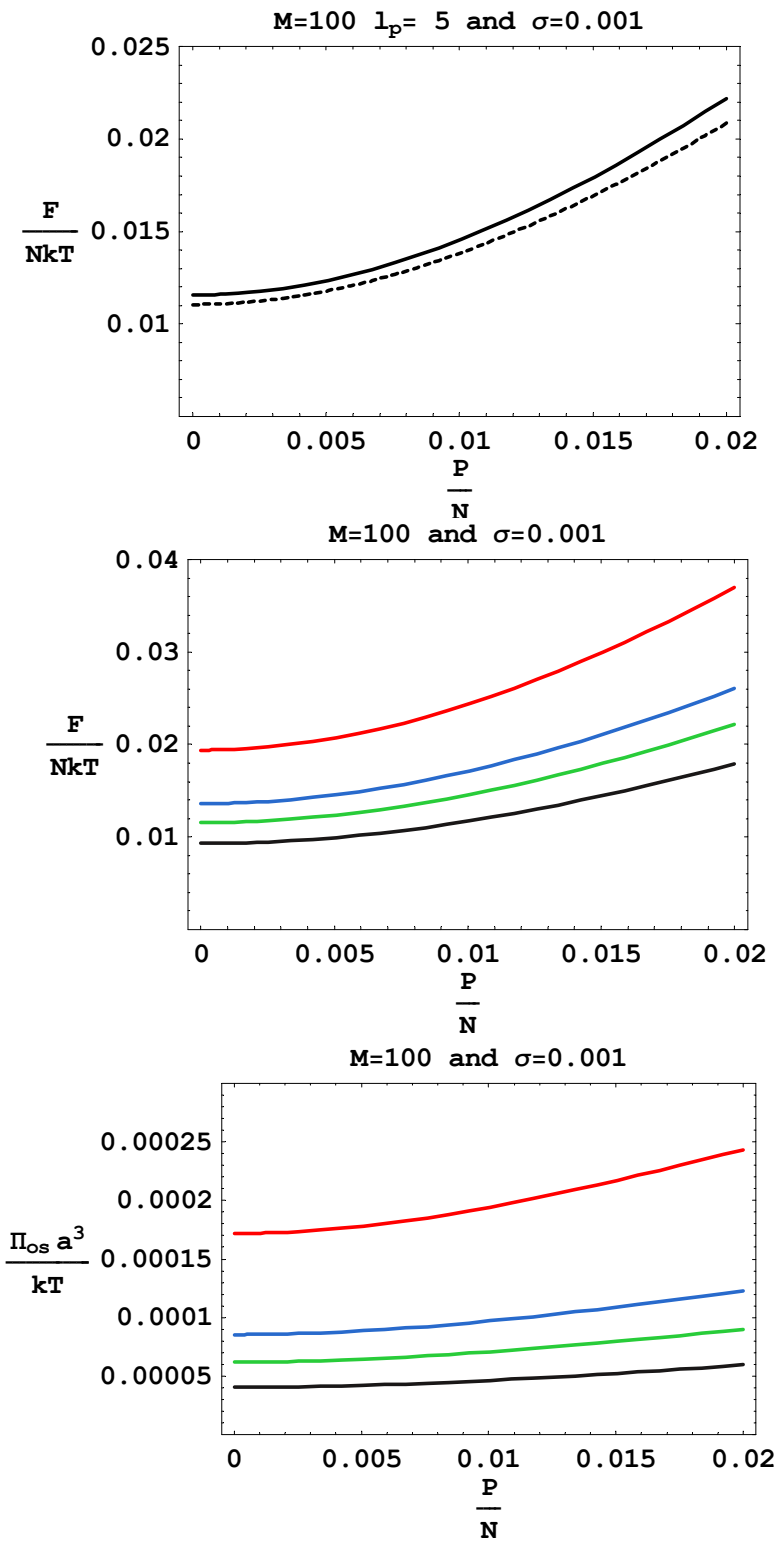

Fig. 5.4

Free energy and osmotic pressure dependence on the occupancy fraction P/N. **Top** plot: ***dashed*** – Gaussian chain; ***solid*** – FE chain. **bottom** two plots: ***red*** - $l_p = 1$; ***blue*** - $l_p = 3$; ***green*** - $l_p = 5$; ***black*** - $l_p = 10$.

Note that the free energy of a Gaussian chain is actually slightly lower than for the finite extensibility chain even though, as the estimation of the brush heights showed, the Gaussian chain is more stretched than the chain with finite extensibility. The reason for this result is in the extra-term for finite extensibility which increases the elastic free energy at any given chain extension relative to the Gaussian case. As for the dependence of the free energy and osmotic pressure on the occupancy fraction, they are shown to increase monotonically as the amount of associated coils per chain increases. For any given occupancy, the osmotic pressure decreases with increasing persistence length. This is expected since increasing persistence length increases the height of the brush, leading to decrease in the brush density, which is the main determining parameter for the osmotic pressure. As for the free energy, the dependence upon the persistence length might seem a bit counterintuitive since the most stretched chains corresponding to the highest values of l_p end up having the lowest free energy at equilibrium. The result can be explained by the fact that the elastic free energy is an entropic term that is inversely proportional to the persistence length, the unit length of steps in the chain conformation.

Having investigated the polymer brush properties for a constrained degree of associating coil occupancy, we now determine brush properties self-consistently with the average degree of occupancy $\langle P \rangle$ by solving the thermodynamic equilibrium expression for the average number of coils per chain (Eq. 5.13) as a function of the energy of interaction between the coils and the binding sites of the chains, and the contents of the system (i.e. volume fractions of the different constituents). Having determined equilibrium values of $\langle P \rangle$, we can use these to obtain brush properties, such as the brush thickness, as a function of the system composition and interaction energy.

In Fig. 5.5 the dependence of the average occupancy fraction <*P*>/N calculated using Eq. (5.13) is shown as a function of the overall coil volume fraction ϕ_{coil} in the system for two grafting densities. The sigmoidal shape of the low grafting density curve (red) indicates that in some conditions the number of associating coils rapidly increases with ϕ_{coil} above some characteristic threshold value, followed by a saturation of association at large volume fraction. The appearance of such a threshold volume fraction is indicative of the requirement for a sufficient amount of polymer in the bulk solution to be able to overcome the osmotic pressure in the brush and allow coil penetration into the polymer brush in significant numbers. For the higher grafting density case (blue curve), the monotonic and non-sigmoidal increase in <*P*>/N with ϕ_{coil} may reflect the effects of both increased osmotic pressure in the brush and the onset of steric hindrance on coil partitioning at this higher grafting density. For both cases plotted in Fig. 5.5, the polymer brush is significantly below its saturated state (which for these conditions would correspond to $\langle P \rangle / N = 0.01$).

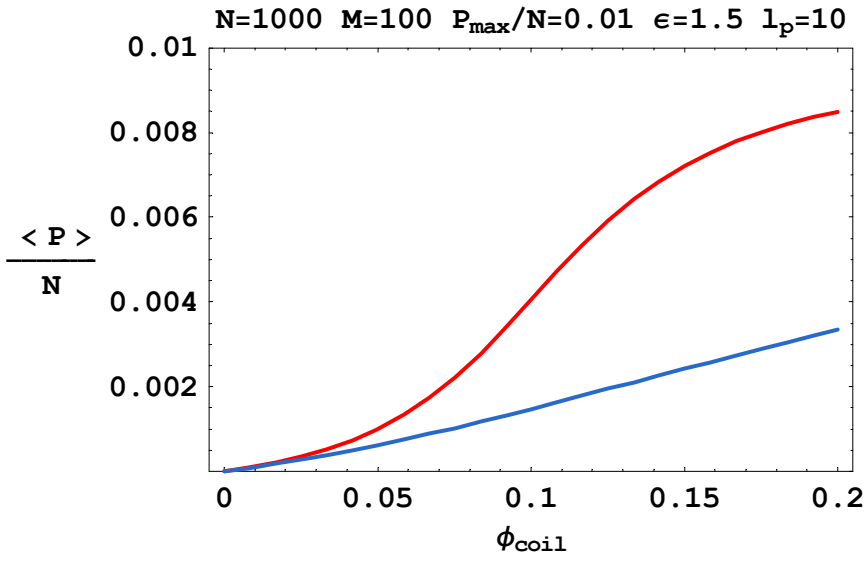

Fig. 5.5

Dependence of the mean occupancy fraction from the overall volume fraction of available coils for two grafting densities: ***red*** - $\sigma = 0.001$; ***blue*** - $\sigma = 0.01$

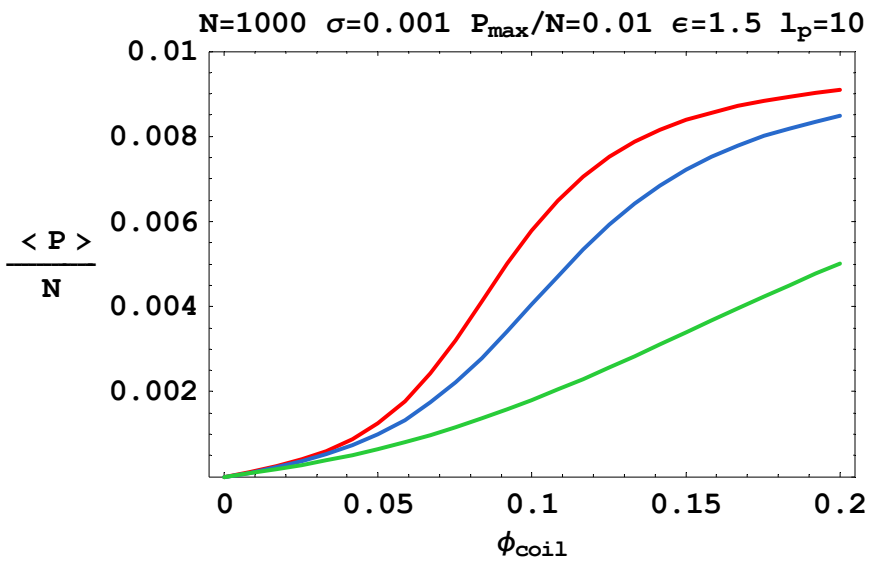

Fig. 5.6

Mean occupancy fraction dependence on coil volume fraction for three coil degrees of polymerization: ***red*** - $M = 50$; ***blue*** - $M = 100$; ***green*** - $M = 200$

In Fig. 5.6 the dependence of the mean occupancy fraction is shown for several different degrees of polymerization of the associating coils. This result shows a significant decrease of the amount of coils associated in the brush as the coil size increases. For the smaller two coil sizes the polymer brush approaches the saturated state (which for main chains with degree of polymerization 1000 corresponds to P=10) when the volume fraction of coils becomes close to $\phi_{\text{coil}} = 0.2$, while for $M = 200$ the amount of associated coils in the brush is substantially less, even at $\phi_{\text{coil}} = 0.2$. The results obtained in the plot above are consistent with the expected effects of steric hindrance in the brush. The permeability of a polymer brush for macromolecules depends on the grafting density and the size of the coils entering the brush. If the coil is smaller than the average distance between neighboring chains in the brush, it must only overcome osmotic pressure to enter the brush. However, if the coil is larger than this characteristic value, it experiences an additional barrier to entry for purely steric reasons.

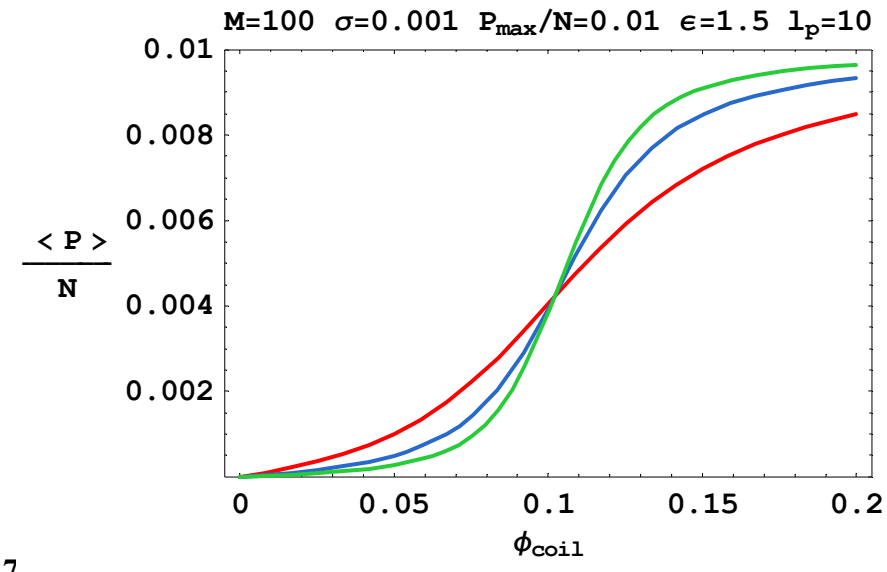

Fig. 5.7

Mean occupancy fraction as a function of average coil volume fraction in the system for several chain lengths: ***red*** - $N = 1000$; ***blue*** - $N = 2500$; ***green*** - $N = 5000$

In the next set of plots, the behavior of main chains with different degrees of polymerization is investigated (see Fig. 5.7). Generally, a fairly weak effect on the maximum occupation of associating coils is seen over the 5-fold increase of the degree of polymerization (from 1000 to 5000). However, a significant sharpening of the transition between the associated and unassociated states occurs with increasing N, leading to an increasingly well-defined threshold concentration. The reason for the observed behavior is that longer chains naturally form a much more extended brush (at fixed grafting density). In order to reach a certain occupancy fraction, the coils must therefore penetrate deeper into the polymer brush against a larger osmotic pressure than in the case of shorter chains.

The average occupancy per chain also strongly depends on the binding energy between the coils and the chains in the polymer brush (see Fig. 5.8). Apart from the amount of coils absorbed into the brush, which changes drastically over a 3-fold change

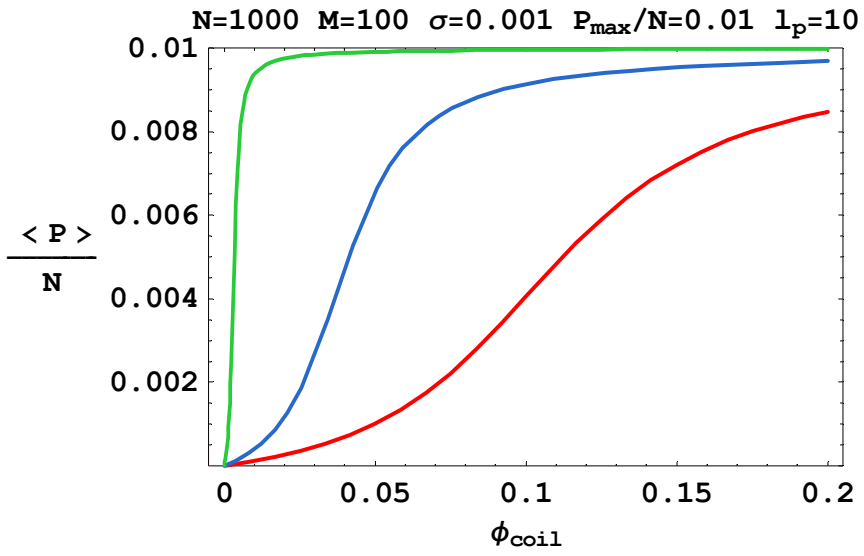

Fig. 5.8

Mean occupancy fraction as a function of average coil volume fraction for a set of several interaction energies: ***red*** - $\varepsilon = 1.5$; ***blue*** - $N = 2.5$; ***green*** - $N = 5.0$

of the binding energy, especially for low-to-moderate coil concentrations, the threshold coil volume fraction is also sensitive to the changes in the binding energy, when all other parameters are unchanged. In fact, if the interaction energy is high enough, the threshold concentration can decrease to practically zero (see green line on Fig. 5.8 corresponding to binding energy $\varepsilon = 5$), and the transition between bare and decorated main chains becomes nearly discontinuous. This result is consistent with what we saw from the plasma depletion simulations of the highly associative proteins, where at the lowest attempted concentrations practically all the available globular proteins were found associated in the endothelial surface layer. Another thing interesting to notice is that even for the lowest energy attempted in the plots of Fig. 5.8, at the highest volume fraction of coils, the chains in the polymer brush were relatively close to being saturated.

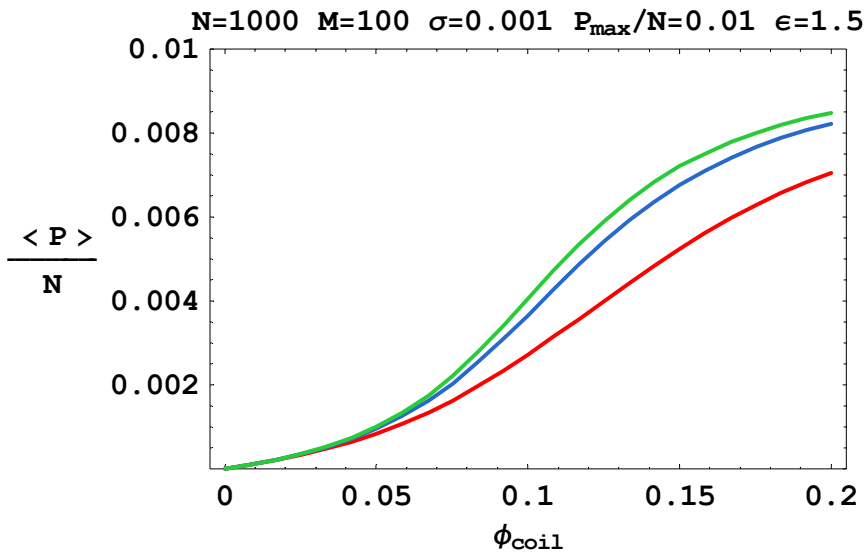

Fig. 5.9

Mean occupancy fraction as a function of average coil volume fraction for a set of several persistence lengths: ***red*** - $l_P = 1$; ***blue*** - $l_P = 5$; ***green*** - $l_P = 10$

Finally, the influence of the persistence length of the polymer brush chains on the mean occupancy fraction of the coils was investigated. As shown by the plots in Fig. 5.9, an increase of the persistence length leads to a relatively weak increase in the mean occupancy number. This effect is due to the fact that the higher persistence length brushes are more extended compared to identical brushes of more flexible chains and therefore less dense, which has the effect of both increasing brush permeability and decreasing brush osmotic pressure. As a result, the resistance to the coils penetrating the brush and associating with the main chain binding domains is reduced, which in turn results in a higher fraction of occupied sites for the stiffer polymer brushes.

It would be interesting as a next step to link the average coil concentration directly to the brush height and the osmotic pressure through the equilibrium mean occupancy number <P>. For the sake of brevity, we will focus on a restricted set of relevant parameters for this analysis.

In Fig. 5.10 the brush height dependence on the average coil volume fraction is shown. In the top plot, three coil sizes are compared, namely M = 50, 100, and 200. First of all, the two regimes of coil absorption that were observed in the average occupancy plots (Fig. 5.6) are also seen here. There is an apparent threshold coil concentration for effective association into the brush to occur. That threshold value does not seem to depend upon the coil size, whereas the amount of coils absorbed above the threshold depends on the coil size in a non-monotonic way, with the most rapid rise in height with ϕ_{coil} occurring for the intermediate coil size. This non-monotonic behavior may be related to the enhanced steric hindrance experienced by the largest coils at this grafting density, leading to a diminished association of these coils inside the brush (see Fig. 5.6).

The middle plot of the same figure shows equilibrium brush heights for three different interaction energies. In this case, there is clear dependence of the threshold coil concentration on the interaction energy. For the lowest energy plotted, the threshold is relatively high ($\phi_{coil} \sim 0.1$), whereas for the highest energy it is very small. Another noticeable feature is sharp transition from very low occupancy to near saturation binding as the threshold ϕ_{coil} is crossed for $\varepsilon = 5$. These results are qualitatively consistent with the observations from the simulations (more details about this comparison will be given in the discussion section).

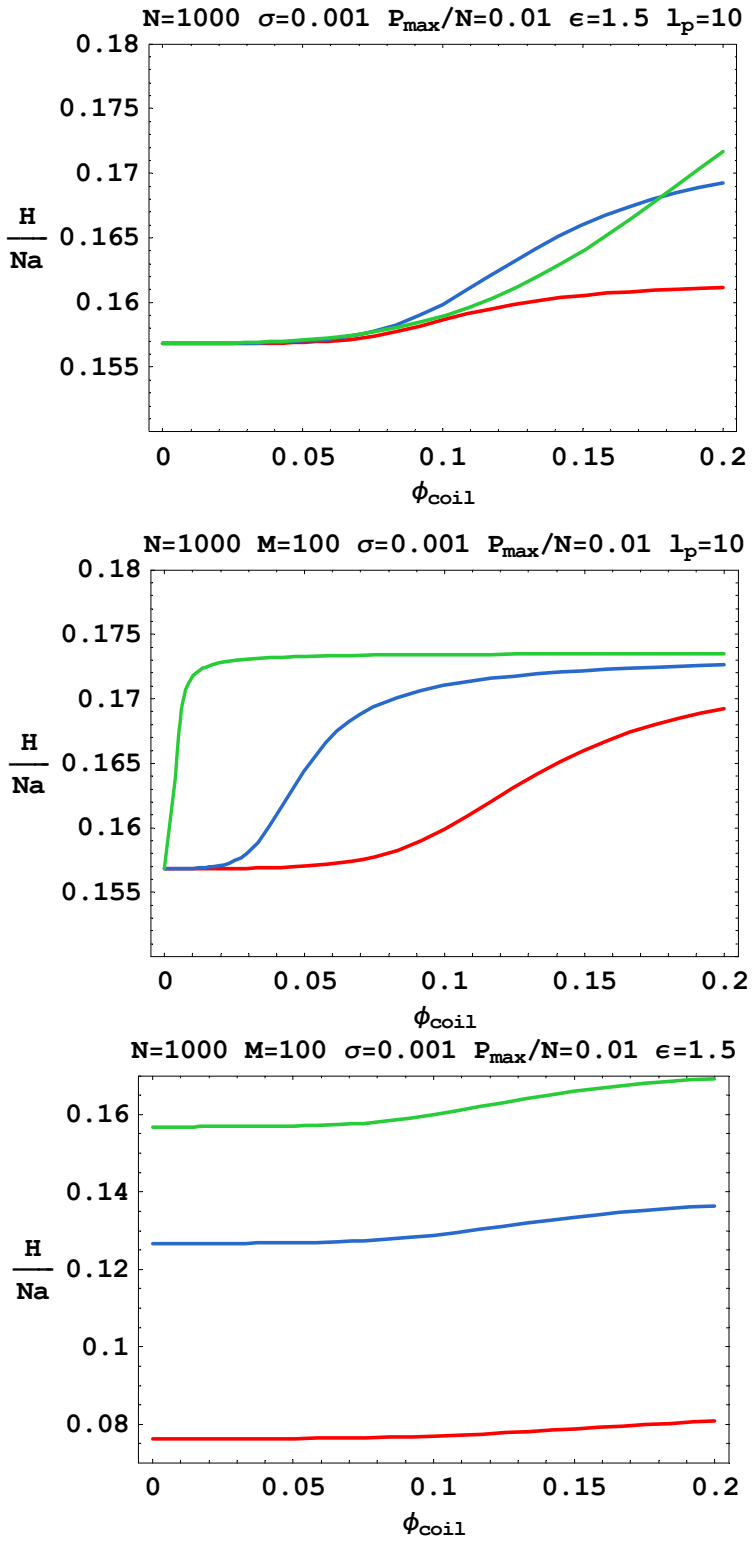

Fig. 5.10

Polymer brush height dependence on coil volume fraction: **top** – for three coil sizes (***red*** – $M = 50$; ***blue*** – $M = 100$; ***green*** – $M = 200$); **middle** – for three interaction energies (***red*** – $\varepsilon = 1.5$; ***blue*** – $\varepsilon = 2.5$; ***green*** – $\varepsilon = 5.0$); **top** – three persistence lengths (***red*** – $l_p = 1$; ***blue*** – $l_p = 5$; ***green*** - $l_p = 10$)

In the bottom plot of Fig. 5.10, the influence of the persistence length is shown. Contrary to the previous plots where the brush height was not drastically changing, here the heights for the different persistence length differ up to a factor of 2, which is expected since the persistence length plays a major role in determining chain extension in a polymer brush. The dependence on the coil volume fraction is as expected (the height increases after a threshold concentration is reached), however this increase is observed to be much weaker than the persistence length dependence and becomes more pronounced for stiffer chains.

Similarly in Fig. 5.11, the osmotic pressure of the brush is shown as a function of the coil volume fraction for three coil sizes (top plot), three interaction energies (middle plot) and three persistence lengths (bottom plot). The information obtained from these plots is consistent with the previous figure. As the coil size changes, this only weakly influences the threshold coil concentration but does significantly influence the osmotic pressure due to the variation in incorporation of associating coils into the brush and the induced brush swelling. The interaction energy influences the osmotic pressure in a similar way as the brush height. The threshold concentration decreases drastically to almost zero as the energy goes from 1.5 to 5 and the plateau region indicates that in the case of strong binding energy the brush binding sites are saturated with coils even at fairly small bulk concentrations. Finally, the persistence length decreases the brush height, resulting in a diminished osmotic pressure in the brush with increasing persistence length more or less independently of the weak coil volume fraction effects.

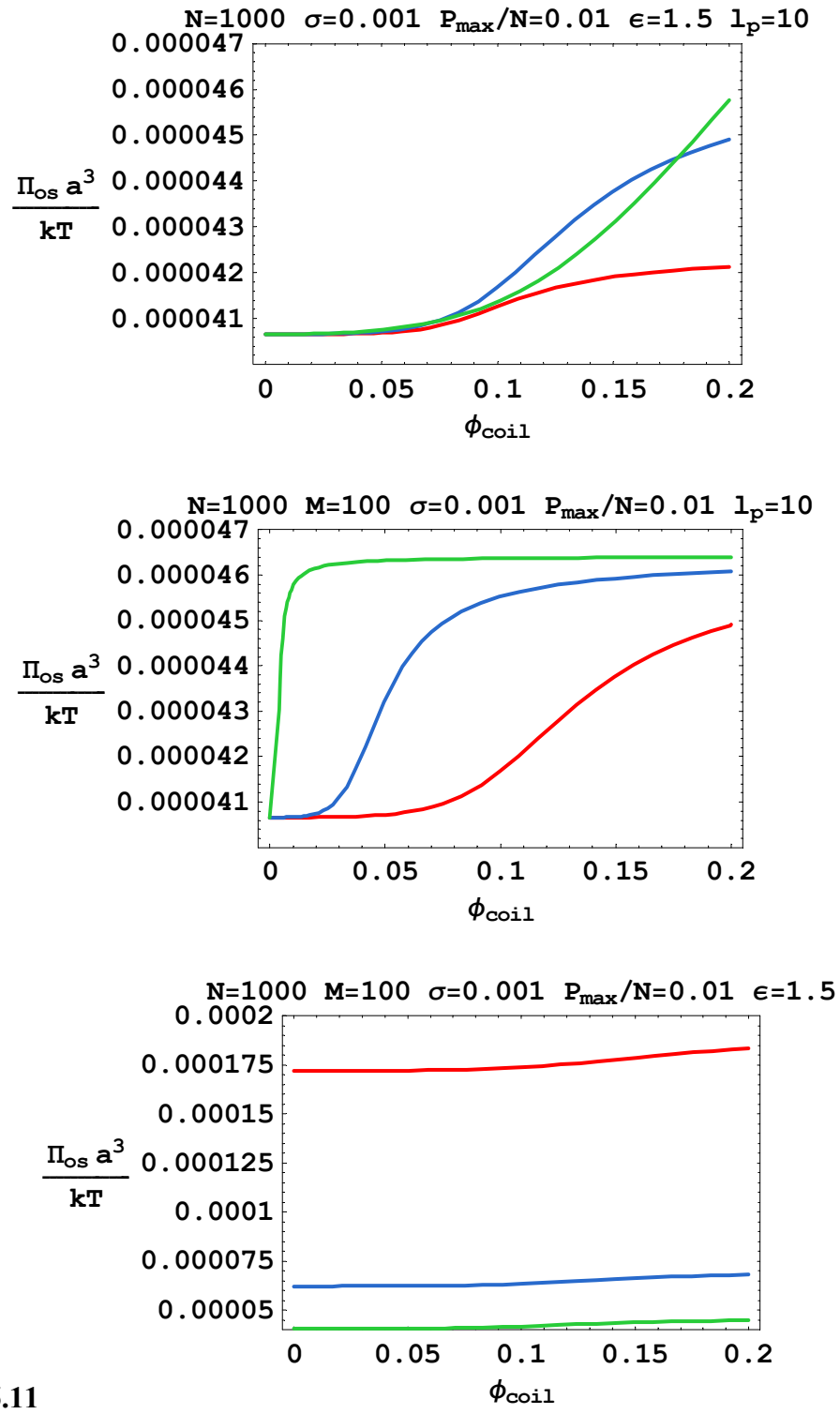

Fig. 5.11

Polymer brush osmotic pressure dependence on coil volume fraction: **top** – for three coil sizes (***red*** – $M = 50$; ***blue*** – $M = 100$; ***green*** – $M = 200$); **middle** – for three interaction energies (***red*** – $\varepsilon = 1.5$; ***blue*** – $\varepsilon = 2.5$; ***green*** – $\varepsilon = 5.0$); **top** – three persistence lengths (***red*** – $l_p = 1$; ***blue*** – $l_p = 5$; ***green*** - $l_p = 10$)

5.3 Glycocalyx model analysis in shear flow

In the presence of shear flow there will be both lateral and vertical displacement of the brush so that both $\Delta H \neq 0$ and $\langle L \rangle \neq 0$. Thus, the chain free energy depends on the perturbations in both directions. Using the same non-dimensionalization as defined in the first section of this chapter, the equilibrium values for the lateral displacement and the height can be found from a mechanical force balance:

$$\frac{\partial}{\partial h}\left(\frac{F}{NkT}\right)=0 \qquad \text{and} \qquad \frac{\partial}{\partial l}\left(\frac{F}{NkT}\right)=\frac{af_{\parallel}}{kT} \tag{5.16}$$

where as defined earlier $f_{\parallel} \approx \eta V(H) l_{\mathrm{H}}$ is the shear force parallel to the free surface of the polymer brush due to the hydrodynamic drag of the flowing plasma, and where the external normal force is assumed to vanish. Using Eq. (5.6), the two equations in (5.16) give the following expressions for the two components of the free end displacements:

$$l=\frac{\lambda h^3}{\zeta(N,M,P)}, \text{ where } \lambda=\frac{af_{\parallel}}{\sigma kT} \tag{5.17a}$$

$$2h^3-h^4\sqrt{1+\frac{\lambda^2 h^4}{\zeta^2}}-l_{\mathrm{p}}\zeta\sigma\left(1-h\sqrt{1+\frac{\lambda^2 h^4}{\zeta^2}}\right)^2=0 \tag{5.17b}$$

The problem is now closed and numerically solvable for a given set of parameters. Once the displacements of the chain ends are known, from (5.6) and (5.8) we can estimate, respectively, the free energy and the osmotic pressure in the polymer brush, and plot them as functions of the applied shear flow. As a final step, the thermodynamic equilibrium of the brush with its associating coils in the presence of the shear flow will be studied.

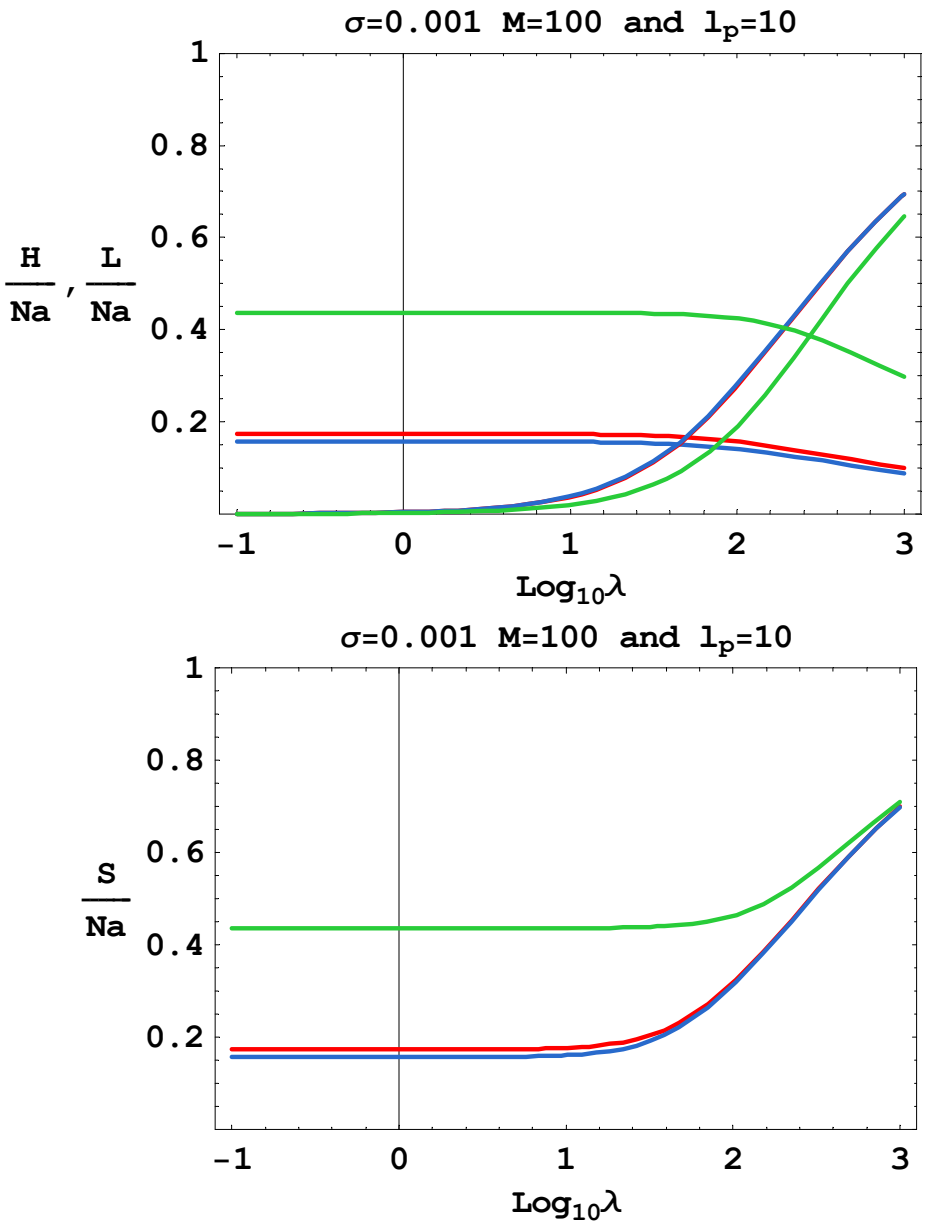

Fig. 5.12

Top plot: Height and lateral displacement for sheared finite extensibility chains decorated with fraction $P/N = 0.01$ (***red*** lines), $P/N = 0.10$ (***green*** lines) and bare (***blue*** lines) as a function of the logarithm of the characteristic dimensionless shear force λ. The decreasing lines are the heights and the increasing lines are the lateral displacements. Remaining parameters: $\sigma = 0.001$; $M = 100$; $l_p = 10$.

Bottom plot: overall chain end-to-end distance as a function of the logarithm of the dimensionless shear force for decorated chains with fraction $P/N = 0.01$ (***red*** lines), $P/N = 0.10$ (***green*** lines) and bare (***blue*** lines) finite extensibility chains. Remaining parameters are the same as in top plot.

Figure 5.12 shows semi-logarithmic plots of the components of the chain end-to-end distances (top plot) and the overall end-to-end distance (bottom plot) as a function of the dimensionless shear force as defined in (5.17a). The figure includes plots for both bare and decorated finite extensibility chains (with binding site fraction $P/N = 0.01$ and $P/N = 0.10$). The set of parameters used for the two plots is the same and corresponds to a grafting density of $\sigma = 0.001$, coil degree of polymerization $M = 100$ and persistence length $l_p = 10$. For both the bare and the decorated chains, the height of the polymer brush is shown to stay approximately constant for relatively low values of λ (up to about $\lambda = 10$) and to slowly decrease for stronger shear flows, corresponding to brush thinning. The lateral displacement as expected starts from approximately zero for small shear forces and grows in a pronouncedly non-linear way as the shear flow increases. The behavior for the two chain types (bare and decorated) is shown to be very similar. In the bottom plot, the overall end-to-end length of the chains is observed for different shear flows – it is shown to considerably increase in a nonlinear fashion for values of $\lambda > 10$. In the case of bare and less decorated chains, the increase is about a factor of 3, while for the more decorated chains it is less pronounced. This is primarily due to the fact that brush thickness of the heavily decorated chains is already larger by a factor of approximately 2 in the absence of flow than that of the bare chain brushes. Hence, the incremental stretching achieved by shear flow is relatively smaller, by about 75%, than that of the corresponding bare chain brushes under shear flow. Note that $\lambda = 10^3$ corresponds to extremely strong shear flows and leads to extreme values of the lateral displacement and the overall end-to-end distance. For instance, the value of about 0.7 exhibited for the dimensionless chain end-to-end distance at $Log_{10}\lambda = 3$ on the bottom

plot corresponds to a chain whose length is stretched to 70% of its maximum contour length.

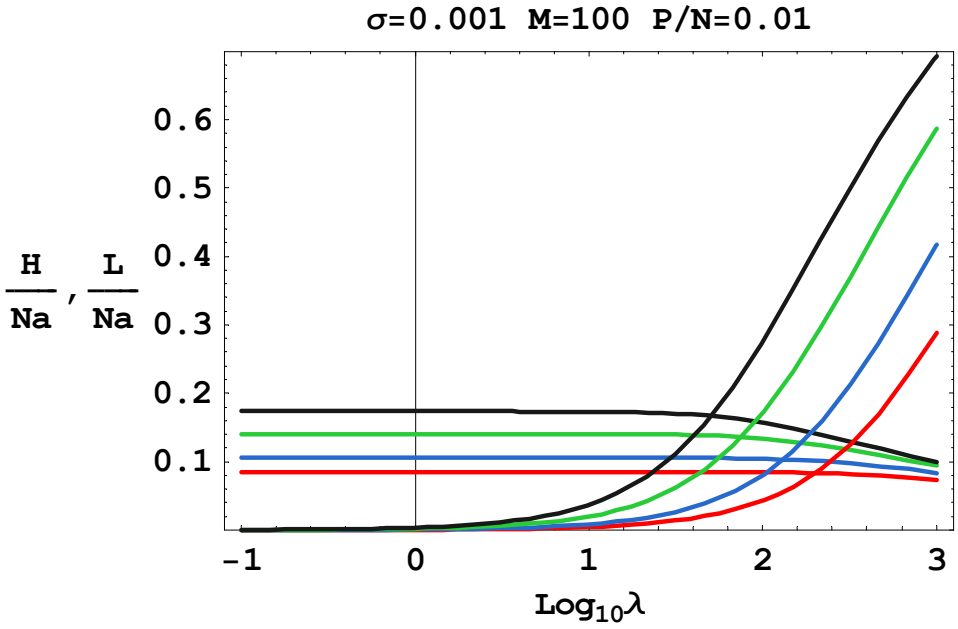

Fig. 5.13

Height and lateral displacement for sheared finite extensibility chains as a function of the logarithm of the characteristic dimensionless shear force λ for several persistence lengths: ***red*** - $l_p = 1$; ***blue*** - $l_p = 2$; ***green*** - $l_p = 5$; ***black*** - $l_p = 10$. The decreasing lines are the heights and the increasing lines are the lateral displacements. Remaining parameters: $\sigma = 0.001$; $M = 100$; $P/N = 0.01$.

Next the shear flow dependence of the height and lateral displacement is shown for a set of different persistence lengths of the polymer chains (see Fig. 5.13). The result indicates that the effect of shear flow on the chain conformations in the brush is more pronounced for larger persistence lengths. The height decrease for the most flexible chains observed ($l_p = 1$) is 2-3 times less than the corresponding decrease in the case of the stiffest chains plotted ($l_p = 10$). In the limit of very strong flows, the heights of the different stiff brushes asymptotically approach each other. Similarly, the lateral displacement is also most pronounced for the stiffest chains, being around factor of 2

larger than the most flexible case. Both effects are roughly monotonic with the persistence length change.

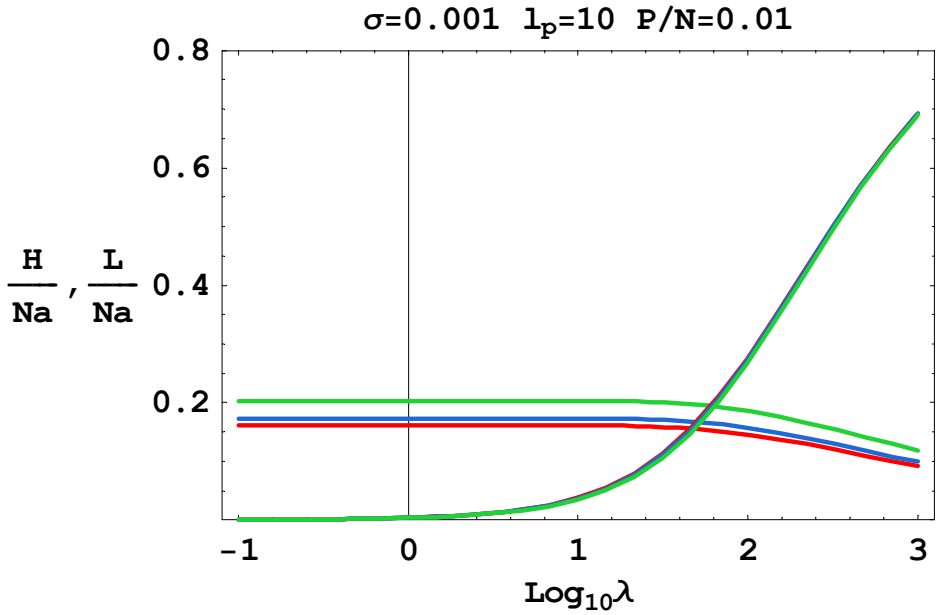

Fig. 5.14

Height and lateral displacement for sheared finite extensibility chains as a function of the logarithm of the characteristic dimensionless shear force λ for several coil sizes: ***red*** - $M = 50$; ***blue*** - $M = 100$; ***green*** - $M = 200$. The decreasing lines are the heights and the increasing lines are the lateral displacements. Other parameters: $\sigma = 0.001$; $l_p = 10$; $P/N = 0.01$.

Next the influence of the coil size on the behavior of the polymer brush under shear flow is investigated (see Fig. 5.14). As already seen in the quiescent case analysis, the brush height increases for larger coils when all other parameters are kept constant, even though the effect here is rather weak due to the comparatively low coil occupation of the brush for larger coils, as previously discussed. The behavior of the lateral displacement as a function of the shear flow depends extremely weakly on the coil size. For 4-fold increase of M the behavior of the lateral displacement remains practically the same. Other than that, the lateral displacement shows the expected behavior of non-linear growth with the increase of the dimensionless shear force. Another weak effect that can

be seen is that the brush starts showing thinning effects at slightly lower shear flows for the smaller coil sizes than for larger coils.

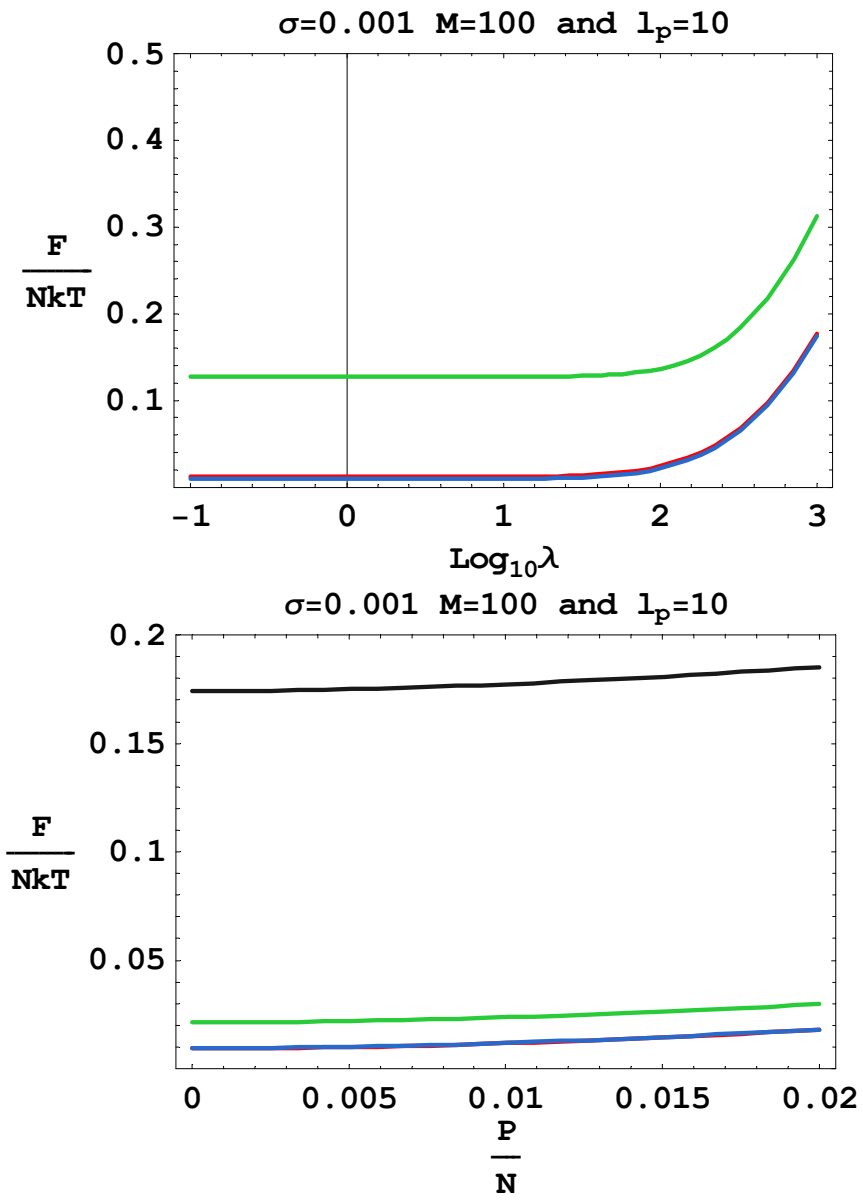

Fig. 5.15

Dimensionless free energy as a function of the logarithm of the characteristic dimensionless shear force λ and occupancy fraction: **top** plot – for bare (***blue***) and decorated with fraction $P/N = 0.01$ (***red***) and $P/N = 0.1$ (***green***) chains; **bottom** plot - $\lambda \approx 0$ (***red***); $\lambda = 10$ (***blue***); $\lambda = 100$ (***green***); $\lambda = 1000$ (***black***). Remaining parameters: $M = 100$; $l_p = 10$; $\sigma = 0.001$

As in the preceding quiescent case investigation, from the height and lateral displacement in the shear flow dependent equilibrium state, it is possible to calculate the chain free energy and osmotic pressure and observe their dependence on the shear flow for various combinations of the remaining parameters.

In Fig. 5.15 and Fig. 5.16, respectively, the free energy and the osmotic pressure are shown as functions of the shear flow for bare and decorated chains for comparison (top plots) and as functions of the occupancy fraction for several different shear rates (bottom plots). It can be observed that for shear flows below $\lambda \approx 10$, both the free energy and the osmotic pressure are approximately constant. For higher values of the shear flow, both for the bare and decorated chains, the osmotic pressure and free energy increase in a nonlinear manner. The effect on the free energy of bare and decorated chains is qualitatively similar but differs in relative magnitude (about an order of magnitude for bare and low-coverage chains versus 2-fold for the high coverage). In contrast, the highly-decorated chains show a more pronounced increase in the osmotic pressure at high shear rates relative to bar or low-coverage chains. The bottom plots of Figs. 5.15 and 5.16 confirm the tendency of the free energy and osmotic pressure to increase with the shear flow. These plots include the free energy and osmotic pressure dependence on the occupancy fraction for three shear flows, corresponding namely to $\lambda = 10^{-10} \approx 0$ (essentially a no-flow condition), $\lambda = 10$, and $\lambda = 100$. The difference between the first two flow rates is very small, in accordance with the top plots of 5.15 and 5.16. The largest λ, corresponding to a relatively strong shear flow, stands out with an osmotic pressure exceeding the others by about 25% and a free energy which is about 2 times higher than the others.

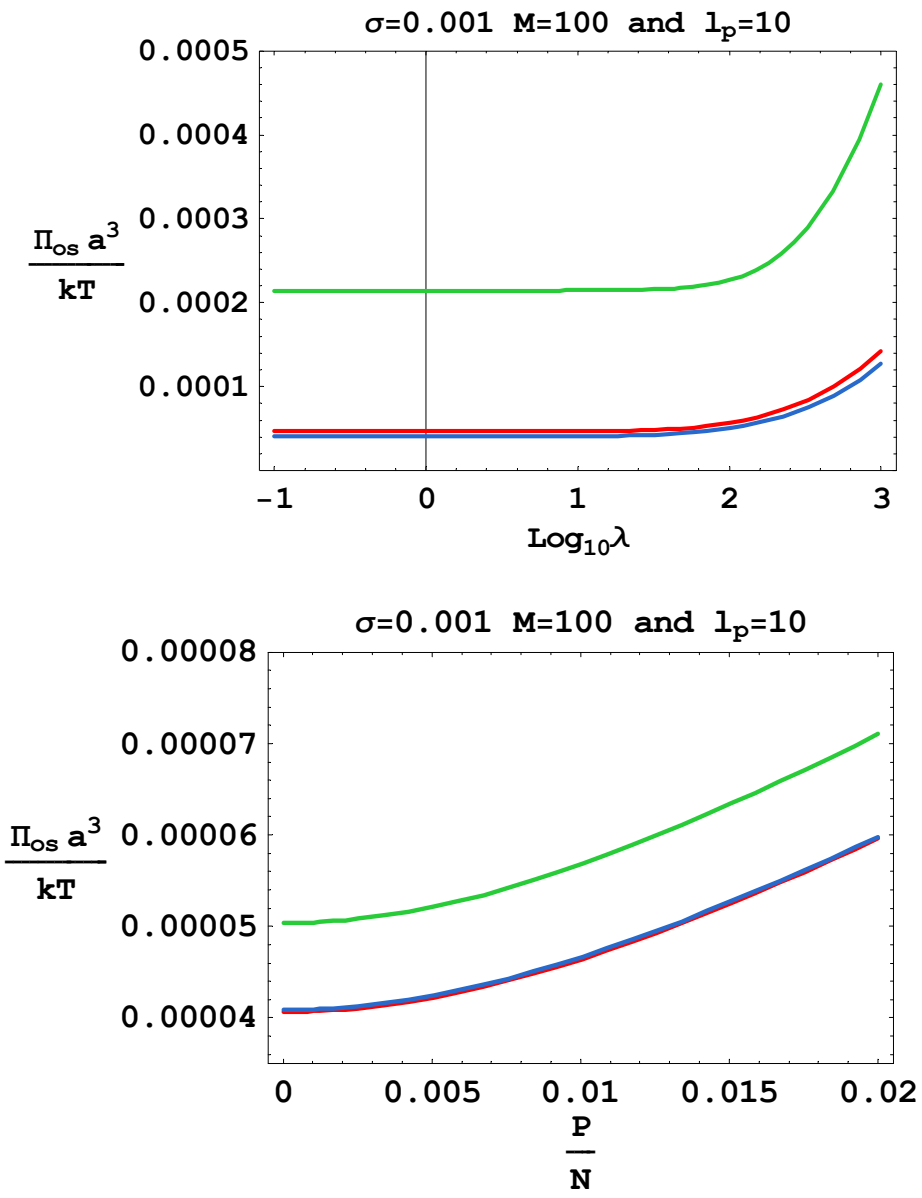

Fig. 5.16

Dimensionless osmotic pressure as a function of the logarithm of the characteristic dimensionless shear force λ and occupancy fraction: **top** plot – for bare (***blue***) and decorated with fraction $P/N = 0.01$ (***red***) and $P/N = 0.1$ (***green***) chains; **bottom** plot - $\lambda \approx 0$ (***red***); $\lambda = 10$ (***blue***); $\lambda = 100$ (***green***). Remaining parameters: $M = 100$; $l_p = 10$; $\sigma = 0.001$

As in the quiescent case, since there is equilibrium between the bound and unbound state of the coils, there will be various degrees of association within the brush. The average number of coils per chain $\langle P \rangle$ strongly depends on all the parameters in the system, as we have already seen in the previous part of this chapter. In the following, the dependence of the mean occupancy number on the shear flow will be the focus.

In Fig. 5.17 a typical dependence of the average occupancy fraction on the shear flow is shown. It has three characteristic regions. For low enough shear rates the mean occupancy fraction of the chains in the polymer brush is not affected by the flow. After exceeding a certain dimensionless shear force (in this particular plot corresponding to around λ=10) there is a very slight increase in the amount of coils absorbed into the layer (in this plot consisting of 1-2%) followed by a sharp decrease in the mean occupancy as

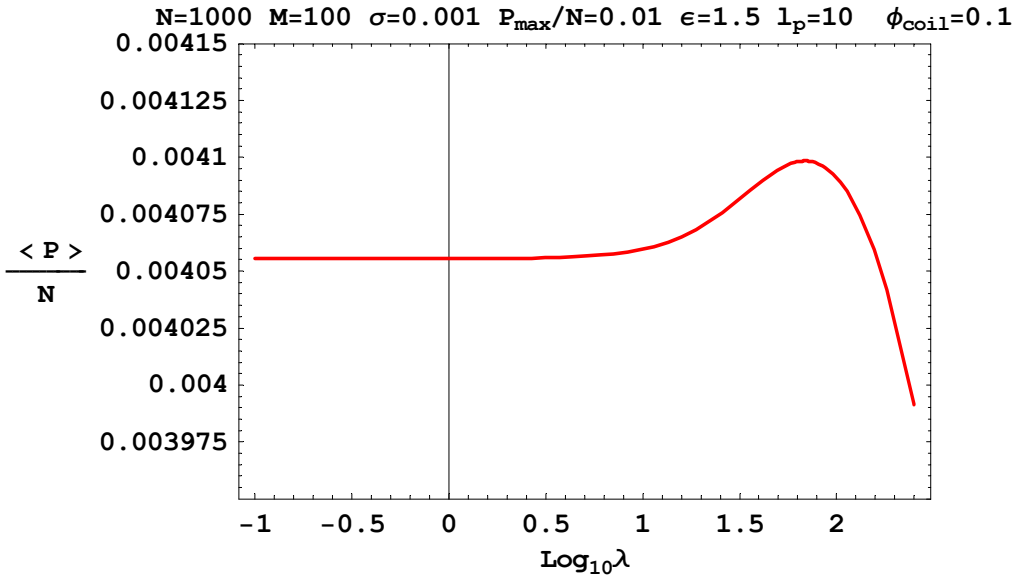

Fig. 5.17

Average occupancy fraction as a function of the dimensionless shear force for a set of parameters as follows: $N = 1000$; $M = 100$; $P_{\max}/N = 0.01$; $\varepsilon = 1.5$; $l_p = 10$; $\phi_{\text{coil}} = 0.1$; $\sigma = 0.001$

the shear rates increase further. The decrease in the occupancy fraction at strong shear flows can be explained by what we already know from the previous part of this chapter, i.e. that polymer brushes (both bare and decorated) tend to decrease their heights at strong enough shear flows (see Fig. 5.12-5.14). That effect leads to an increase of the osmotic pressure inside of the brush (see Fig. 5.16) and can be regarded as an additional force that would eventually suppress association of coils into the brush. The peak in the occupancy number preceding the drop is a very weak effect that could result from a number of delicate balances. One possibility is that it could correspond to a shear rate at which the lateral chain extension is increasing more rapidly than the layer thickness is decreasing, leading to a slightly lower incremental energy cost of adding a few coils to the brush. Another possibility is that the slight increase in average occupancy $\langle P \rangle$ reflects a subtle perturbation of the shape of the distribution function for coil association. In any event, the apparent peak in $\langle P \rangle$ as a function of λ is such a weak effect that it is unlikely to have any measurable consequences.

In Fig. 5.18 the dependence of the mean occupancy fraction on the shear flow is shown for two values of the grafting density, namely $\sigma = 0.001$ and $\sigma = 0.005$. Since the relative magnitude of the peak and subsequent drop in the occupancy fraction is much less than the difference between the low-shear plateau values for the two observed grafting densities, they are hardly noticeable on the top plot, and only become apparent in the bottom plots showing $\langle P \rangle$ relative to the corresponding values without shear flow.

The overall impression from the plots is that the grafting density influences mainly the position of the peak and subsequent drop off, which occurs earlier for higher grafting density – there is about an order of magnitude difference in the shear flow required for

initial change in the brush mean occupancy number between the grafting density $\sigma = 0.001$ and $\sigma = 0.005$. This effect indicates the sensitivity of coil association to the effective density of main chain polymer in the brush. The fact that the average occupancy number is considerably less for the grafting density $\sigma = 0.005$ compared to $\sigma = 0.001$ at any observed shear rate is as expected. Moreover, the effect of sufficiently high shear rates is to reduce brush height, thereby further increasing the effective brush density and

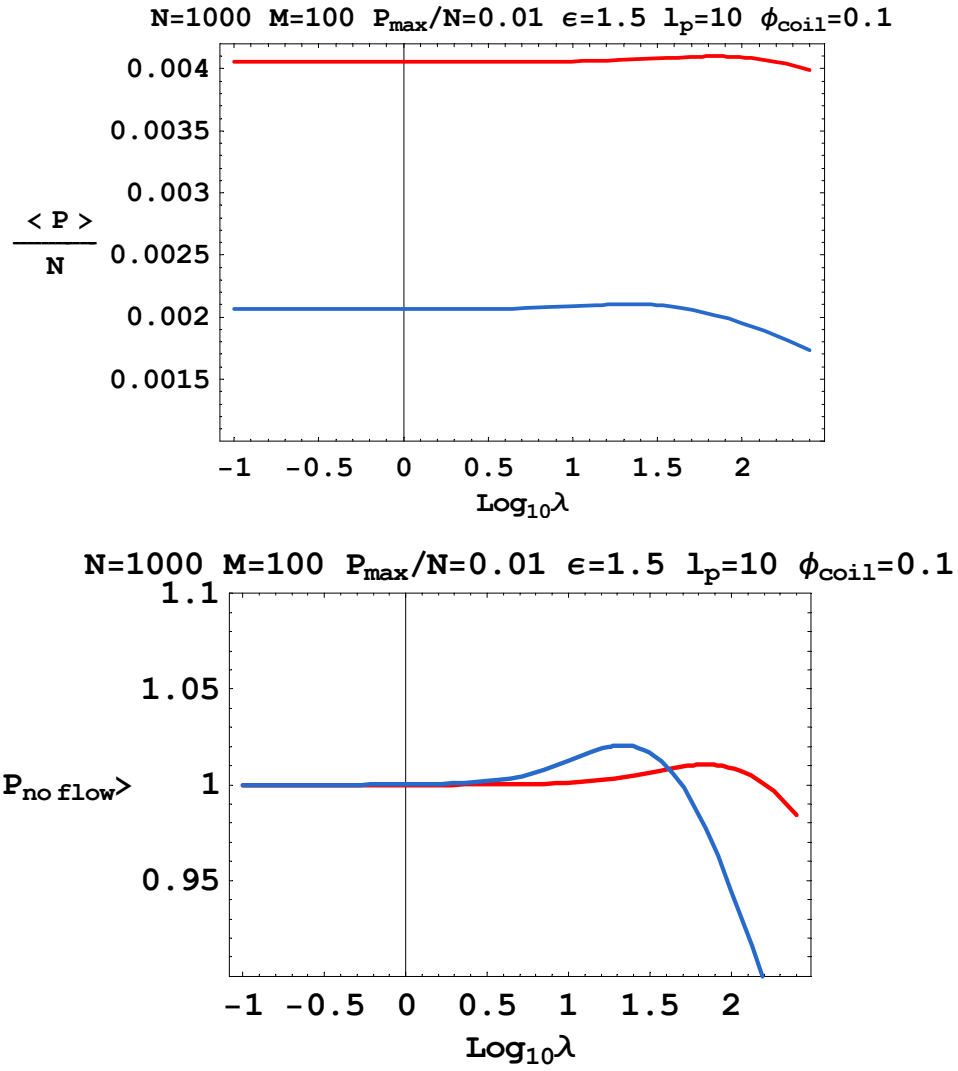

Fig. 5.18

Average occupancy fraction as a function of the dimensionless shear force for two grafting densities: ***red*** - $\sigma = 0.001$; ***blue*** - $\sigma = 0.005$; remaining parameters are: $N = 1000$; $M = 100$; $P_{\max}/N = 0.01$; $\varepsilon = 1.5$; $l_p = 10$; $\phi_{\text{coil}} = 0.1$

consequently reducing the occupancy of associating coils. Note that the ratio of the two occupancy numbers remains approximately constant, with small fluctuations for strong shear flows.

In Fig. 5.19, the dependence of the mean occupancy fraction on the shear flow is shown for a set of three different coil sizes. As with the previous figure, a supplementary finer-scale plot is added so that the relative change in the occupancy number resulting from the shear flow is more clearly seen. Overall, the dependence on the shear flow is qualitatively similar for the three coil sizes. The peaks are found at similar magnitudes of the shear flow and have an increasing intensity with an increase of the coil size (for $M = 200$ the peak is about 10 times more pronounced than for $M = 50$). For strong shear flows, the decrease in the mean occupancy is also more pronounced for the larger coils – the difference between the largest and smaller coil size observed is about a factor of 2. The non-monotonic effects shown in this supplementary figure are quite weak. The most pronounced peak (for $M = 200$) has a maximum value that is only about 2% above the no-flow mean occupancy fraction. For the coil size $M = 50$ this enhancement is much less than 1%. The decrease in the occupancy fraction occurring at higher shear rates is also not appreciable (for the range observed), showing a maximum decrease of 2-3%, although it is assumed that outside of the observed range of shear flows the occupation fraction continues to decrease monotonically. The absolute values of the mean occupancies are such that they correspond to about 60% chain saturation in the case of $M = 50$, which decreases to about 20% when the coil size becomes as large as $M = 200$. The same effect was seen in the quiescent case plots, and in comparison to it, the incremental effect from the shear flow for the range of λ studied is negligible.

In Fig. 5.20 the mean occupancy dependence is shown for several main chain degrees of polymerization. The magnitude of the mean occupancies is very close in this case so one plot was sufficient to provide all the information needed. Apart from the relatively small difference in the absolute value of the occupancies, which increases by about 5%

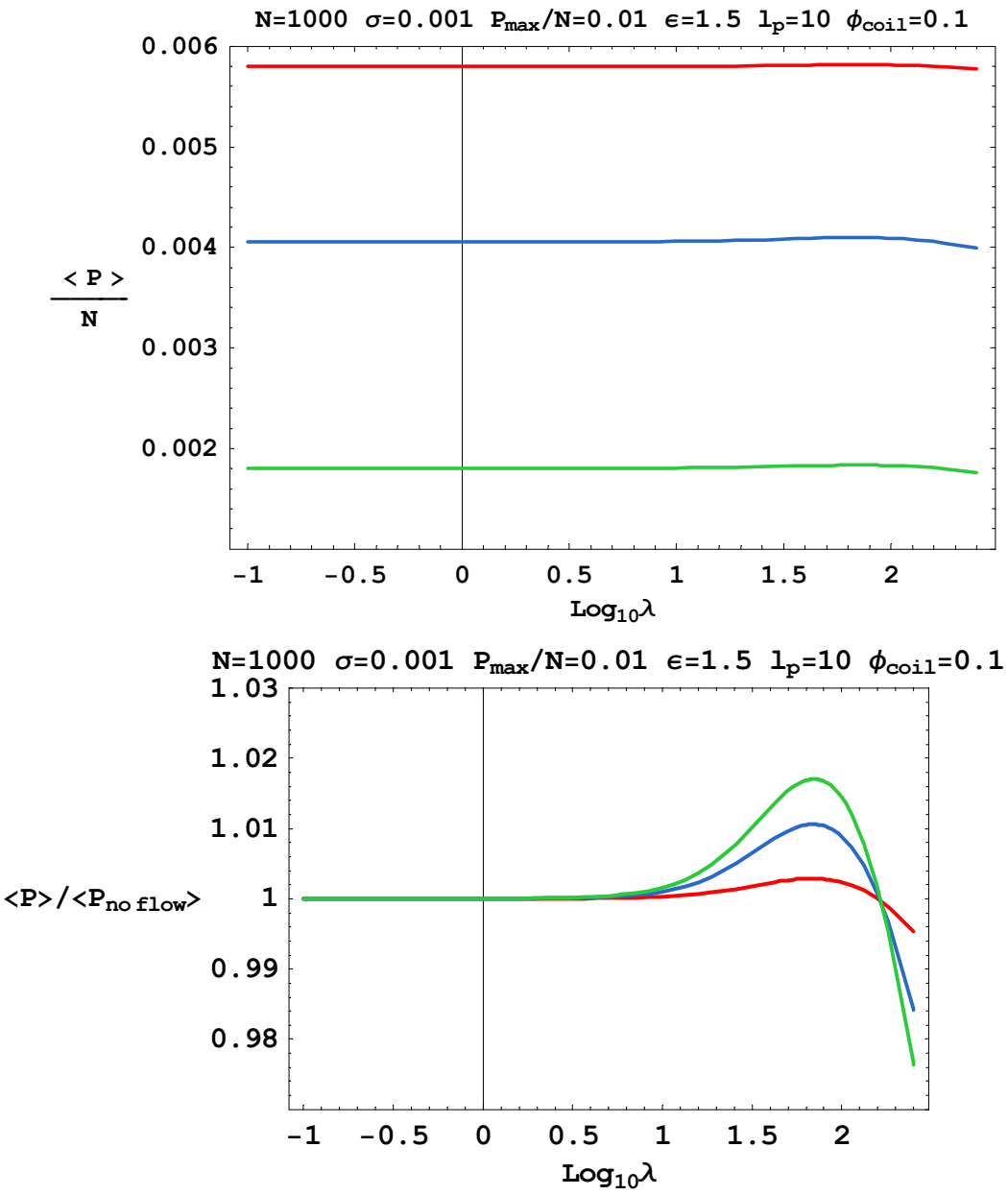

Fig. 5.19

Average occupancy fraction as a function of the dimensionless shear force for three coil sizes: ***red*** - $M = 50$; ***blue*** - $M = 100$; ***green*** - $M = 200$; remaining parameters are: $N = 1000$; $\sigma = 0.001$; $P_{\max}/N = 0.01$; $\varepsilon = 1.5$; $l_{\mathrm{P}} = 10$; $\phi_{\mathrm{coil}} = 0.1$

with a 5-fold increase of the polymer chain degree of polymerization, the dependence on shear flow is very similar. The peaks are situated at nearly the same shear flow value corresponding to about $\lambda = 100$ (note that this is very strong shear rate). They have similar intensity, increasing weakly with the increase of the polymer chain lengths, and the behavior at shear flows greater than $Log_{10}\lambda \sim 2$ (particularly the slope of the dependence) is also comparable for all the three degrees of polymerizations studied.

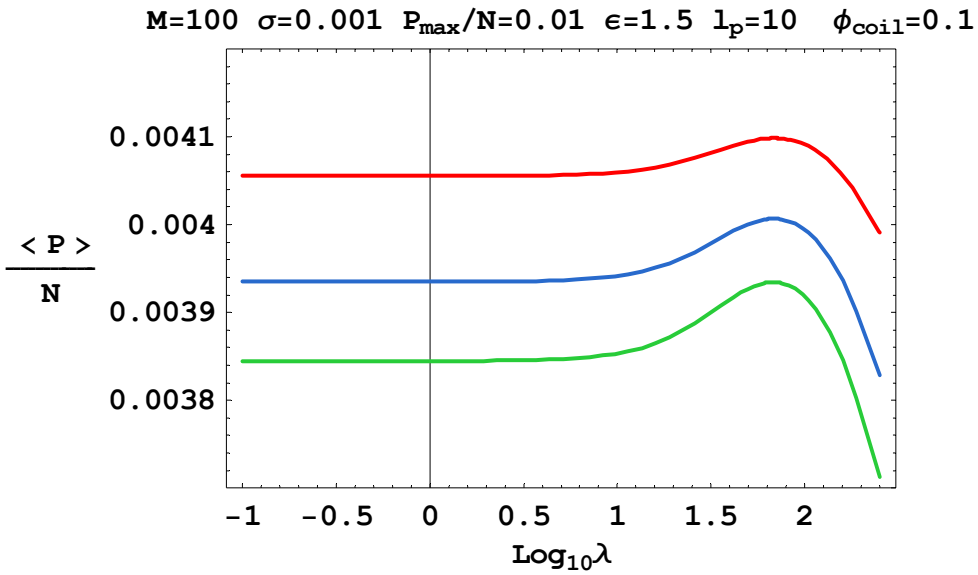

Fig. 5.20

Mean occupancy as a function of the dimensionless shear force for three main chain sizes: ***red*** - $N = 1000$; ***blue*** - $N = 2500$; ***green*** - $N = 5000$; remaining parameters: $M = 100$; $\sigma = 0.001$; $P_{\max}/N = 0.01$; $\varepsilon = 1.5$; $l_p = 10$; $\phi_{\text{coil}} = 0.1$

In Fig. 5.21 the mean occupancy fraction is shown for a set of interaction energies, again in two plots for the absolute and relative-to-quiescent values. From the top plot it can be seen that the absolute values of the occupancy show a much stronger effect on the interaction energy (occupancies ranging from 40% for $\varepsilon = 1.5$ to totally saturated chains at $\varepsilon = 5.0$) compared to the effect from the shear flow, which are entirely negligible in the top plot. The bottom plot confirms that the strongest effect of shear is seen in the case

of weakest energy of interaction, amounting to a 1-2% effect. Whereas, the effect of shear on the occupancy fraction in the case of large ε is practically zero.

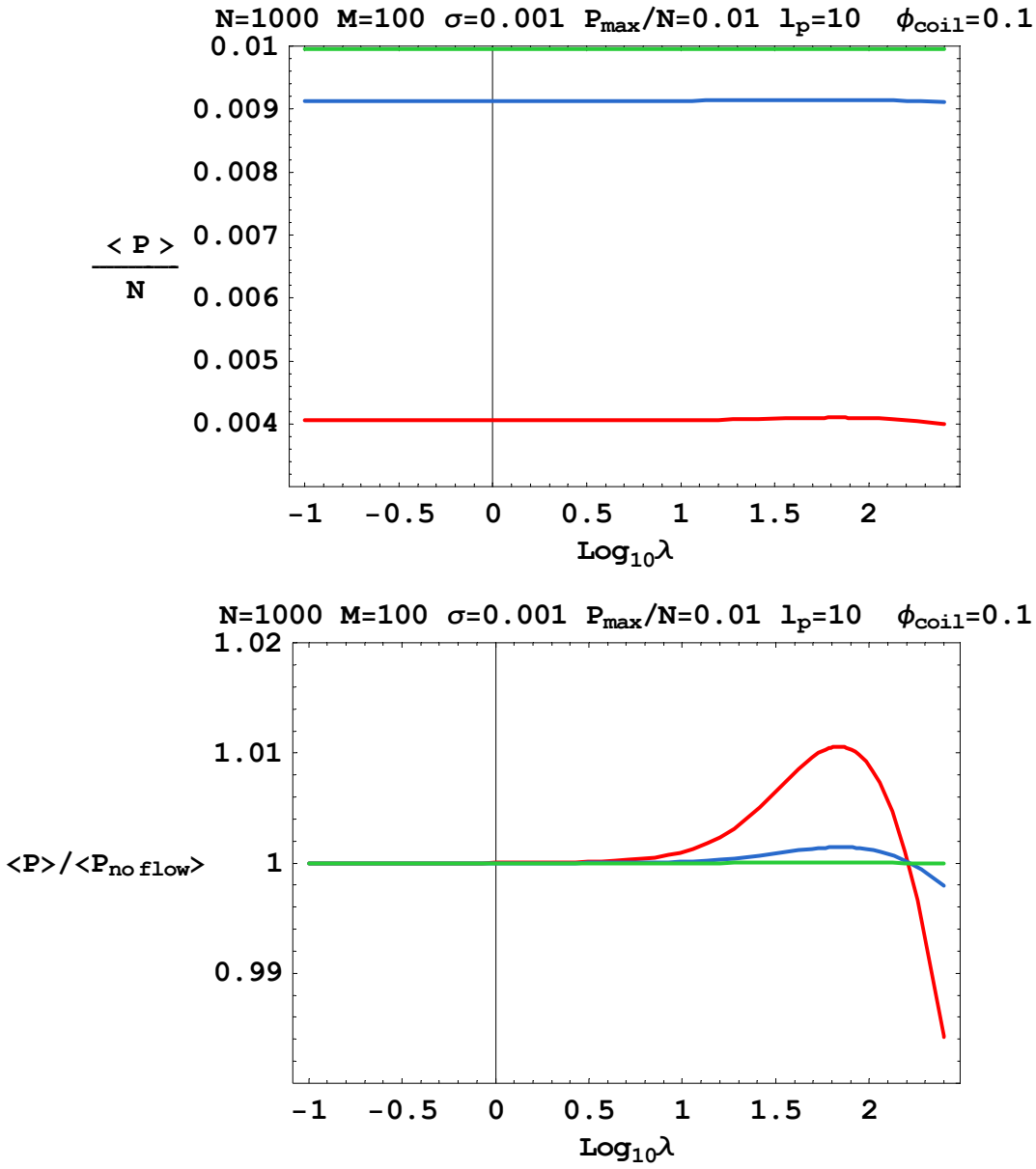

Fig. 5.21

Mean occupancy as a function of the dimensionless shear force for three interaction energies: ***red*** - $\varepsilon = 1.5$; ***blue*** - $\varepsilon = 2.5$; ***green*** - $\varepsilon = 5.0$; remaining parameters: $N = 1000$ $M = 100$; $\sigma = 0.001$; $P_{\max}/N = 0.01$; $l_{\mathrm{P}} = 10$; $\phi_{\mathrm{coil}} = 0.1$

In Fig. 5.21 the mean occupancy fraction is shown for a set of interaction energies, again in two plots for the absolute and relative-to-quiescent values. From the top plot it can be seen that the absolute values of the occupancy show a much stronger effect on the interaction energy (occupancies ranging from 40% for $\varepsilon = 1.5$ to totally saturated chains at $\varepsilon = 5.0$) compared to the effect from the shear flow, which are entirely negligible in the top plot. The bottom plot confirms that the strongest effect of shear is seen in the case of weakest energy of interaction, amounting to a 1-2% effect. Whereas, the effect of shear on the occupancy fraction in the case of large ε is practically zero.

The dependence of the shear flow on main chains with different persistence lengths l_{p} is shown in the next figure (Fig. 5.22). As in all the previous cases, the dependence on the shear flow is much weaker (from the bottom plot – up to 2%) than the absolute difference of the occupancy numbers among the different persistence lengths. Upon a 5-fold increase of the persistence length, the average occupancy increased by about 50%, which is expected since the stiffer brushes are more extended, therefore have lower osmotic pressure and more readily accept coils for association.

The dependence of the occupancy number in flows normalized by the one in quiescent conditions for the same set of persistence lengths is presented in the bottom plot of Fig. 5.22. The peak position is observed to depend on the persistence length – for stiffer chains it is moves toward lower shear forces, and for the most flexible chains observed the peak is actually outside of the range plotted. The peak intensity doesn't seem to change over a 5-fold increase of the persistence length. Moreover, the slope of the terminal decrease for shear flows stronger than the 'peak' shear flow is essentially the same for the cases of $l_{\mathrm{p}} = 5$, $l_{\mathrm{p}} = 10$ and presumably for $l_{\mathrm{p}} = 1$ as well.

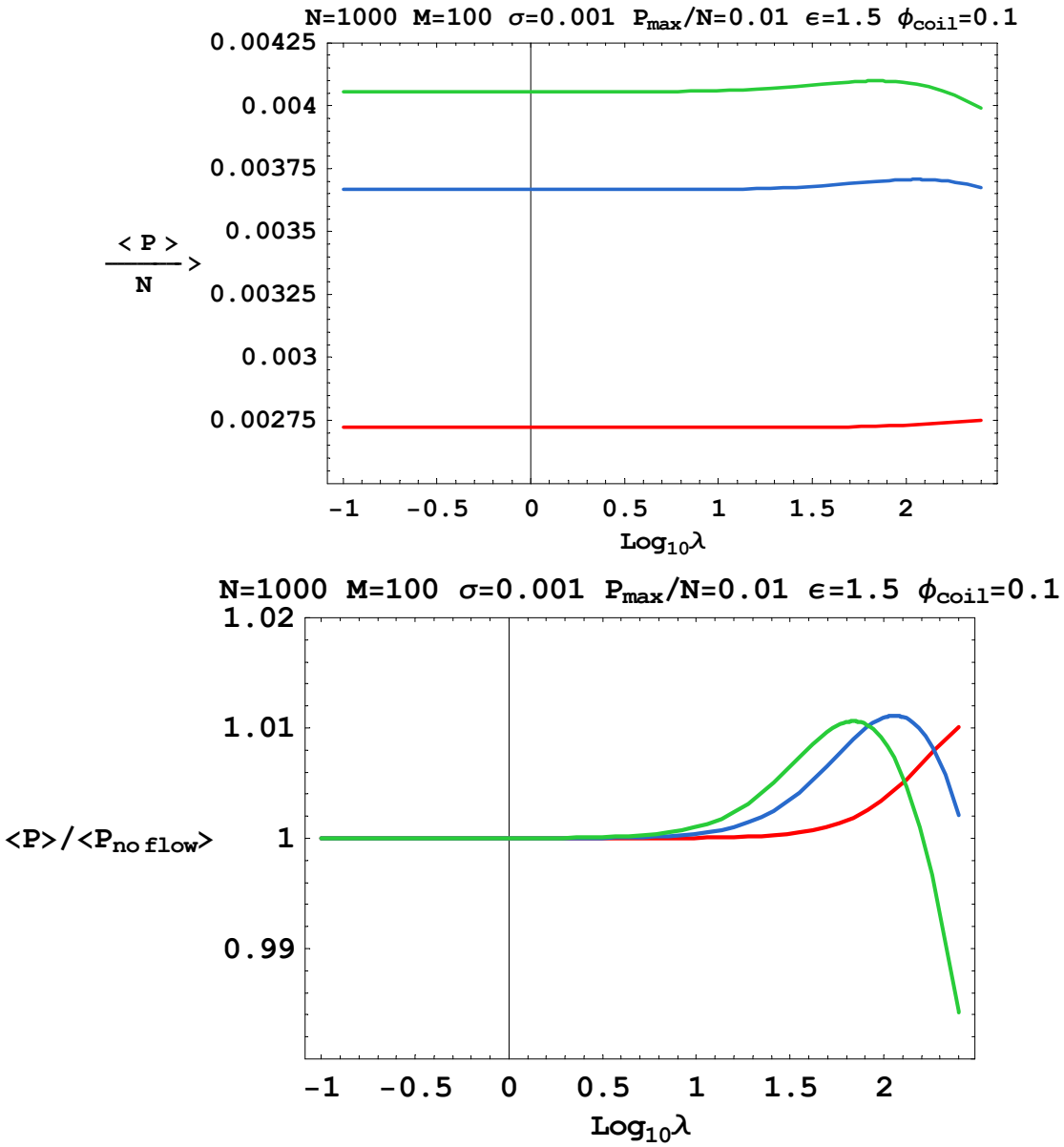

Fig. 5.22

Mean occupancy as a function of the dimensionless shear force for three persistence lengths: ***red*** - $l_p = 1$; ***blue*** - $l_p = 5$; ***green*** - $l_p = 10$; remaining parameters: $N = 1000$ $M = 100$; $\sigma = 0.001$; $P_{max}/N = 0.01$; $\varepsilon = 1.5$; $\phi_{coil} = 0.1$

The last analysis to be presented is the connection between the mean occupancy number and the brush deformation and osmotic pressure in flow conditions. Here we present the brush thickness, lateral displacement, and osmotic pressure directly as a function of the shear flow for a given total volume fraction of coils. For this part of the

investigation we choose to work with a higher maximal occupancy number, in order to enhance the difference between decorated chains and the corresponding bare chains. However, if we want to work in the low coverage regime, according to (5.1), the maximal occupancy may not exceed $M^{-3/5}$ which for $M = 100$ gives around $P_{\max}/N \approx 0.06$, which we have chosen as the maximal occupancy in the remaining analysis.

In Fig. 5.23, the dependence on the shear flow of the height and lateral displacement calculated based on fixed total coil volume fraction (rather than fixed average occupancy number) is shown. The top plot, where three coil sizes are compared, shows that for the set of parameters chosen, the coil size does not significantly affect the height or the displacement of the brush at any flow rate. This independence is probably due to the fact that the analysis here is restricted to cases where the maximum occupancy is sufficiently low that the chains are saturated with associating coils at all flow rates. For cases where the maximal occupancy and the volume fraction of the coils allow for a larger extent of association, both the height and the lateral displacement of the polymer chains in the brush will be imminently affected. The middle plot of Fig. 5.23 compares the height dependence on shear flow for three interaction energies. The lateral displacement shows only a slight decrease with increasing ε for energies varying by more than a factor of 3. The height, however, is very much affected by ε; it doubles as the energy goes from $\varepsilon = 1.5$ to $\varepsilon = 5$. This is in agreement with the previous plots showing that for strong interaction energies the polymer brush binding domains become saturated with coils at very low coil volume fractions. The brush height starts responding to the shear flow at $Log_{10}\lambda \sim 1.5$ for all three energies of interaction, after which there is a weak decay of the height that is more pronounced for stronger coil-brush interactions.

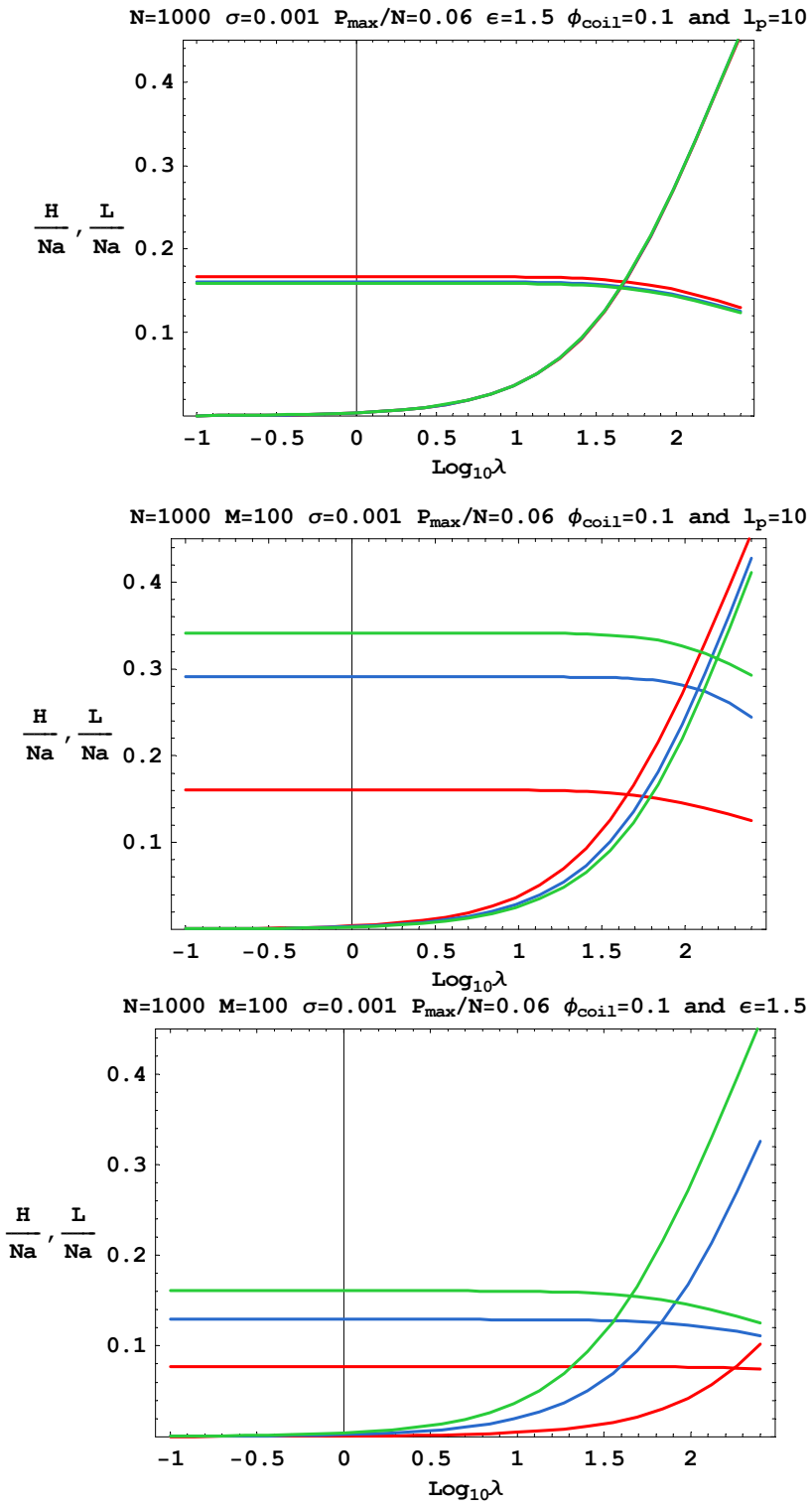

Fig. 5.23

Brush height and lateral displacement dependence on shear flow: **top** -for three coil sizes (***red*** - $M = 50$; ***blue*** - $M = 100$; ***green*** - $M = 200$); **middle** – for three interaction energies (***red*** - $\varepsilon = 1.5$; ***blue*** - $\varepsilon = 2.5$; ***green*** - $\varepsilon = 5$); bottom – for three persistence lengths (***red*** - $l_P = 1$; ***blue*** - $l_P = 5$; ***green*** - $l_P = 10$)

The bottom plots of Fig. 5.23 compare cases of different persistence lengths. Here, there is a pronounced difference in the lateral displacement which increases by more than a factor of 5 from the stiffest ($l_p = 10$) to the most flexible ($l_p = 1$) chains observed. In contrast, the heights behave in a similar way – they remain approximately constant up to $Log_{10}\lambda \sim 1.5$ and then show a slight decrease, which is much more pronounced for the stiffest chains than for the brush of flexible chains.

The osmotic pressure dependence on the shear flow, when the osmotic pressure is calculated with fixed total coil volume fraction, is shown in Fig. 5.24. The top plot compares data for three coil sizes, as in the previous figure. The curves corresponding to the different coil sizes are close but distinguishable contrary to the heights shown in the top of Fig. 5.23. This behavior is expected since for brushes with a given thickness, the ones with bigger coils associated to them will exhibit the larger osmotic pressure in the brush. Since the amount of coils associated to the brush for the parameters used is quite low, the effect is not pronounced and the pressures differ by some 5%.

For shear flows larger than $Log_{10}\lambda \sim 1$, the osmotic pressure shows considerable growth for all the coil sizes observed, up to 40% at $Log_{10}\lambda \sim 2.5$ compared to the corresponding quiescent osmotic pressure. The observed behavior is consistent with the data obtained previously for the height and amount of coils in the brush. Since overall the height decrease is more pronounced than the effect of coils leaving the brush at high shear flows, this would naturally lead to an increase in the osmotic pressure.

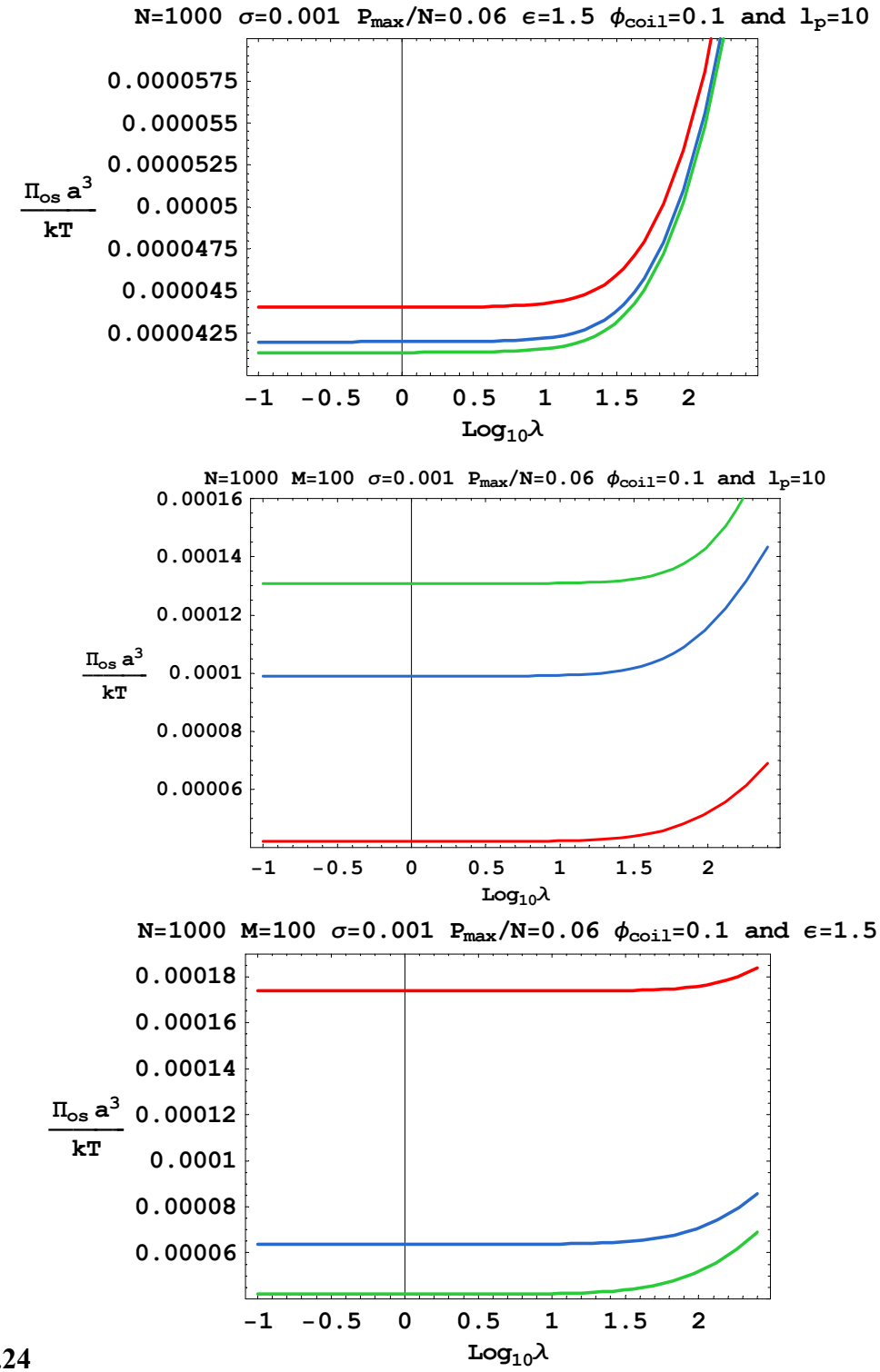

Fig. 5.24

Dimensionless osmotic pressure dependence on shear flow: **top** -for three coil sizes (***red*** - $M = 50$; ***blue*** - $M = 100$; ***green*** - $M = 200$); **middle** – for three interaction energies (***red*** - $\varepsilon = 1.5$; ***blue*** - $\varepsilon = 2.5$; ***green*** - $\varepsilon = 5$); bottom – for three persistence lengths (***red*** - $l_P = 1$; ***blue*** - $l_P = 5$; ***green*** - $l_P = 10$)

In the middle plots of Fig. 5.24, the influence of interaction energy is shown. As expected, the osmotic pressure for the different energies differs strongly, by about an order of magnitude between $\varepsilon = 1.5$ and $\varepsilon = 5$. This is again related to the different occupancy of the main chain binding sites for different interaction energies, varying from relatively low association at $\varepsilon = 1.5$ to complete saturation even for low coil volume fractions at $\varepsilon = 5$. The effect of the interaction energy on the brush height apparently is not enough to balance the effect from the increase of associated coils, which results in increased osmotic pressure. Apart from that, the three curves presented on the plot behave in a very similar way as a function of the applied shear flow.

The bottom plots of Fig. 5.24 show results for different persistence lengths. The behavior of the curves with flow is similar. There is a slight difference (of approximately a factor of five) between the characteristic shear flows at which the osmotic pressure starts responding to the shear flow, showing a trend of increased resistance to flow with increasing chain flexibility. The response of the brush at strong shear flows also varies; it becomes more pronounced for brushes made up of stiffer chains. The pronounced decrease of the absolute value of the osmotic pressure with the chain stiffness shows that the height increase effect is again predominant over the increase in the mean occupancy fraction of the brush chains.

8.3 Discussion

The theoretical model developed for the description of the endothelial surface layer can be qualitatively compared to data available from various sources, including our simulation results described in the previous chapters of this thesis work, and experimental results on the glycocalyx behavior in different conditions. In this discussion we will focus on the former and at the end comment briefly on the latter. As for comparison with our simulation results, both the covalently-bound and the self-assembling layers can be compared to the results of the scaling model presented in this chapter. In order to compare the model analysis to the covalently-bound glycocalyx simulations, we can use the results obtained for the brush height, lateral displacement, etc. at fixed occupancy fraction of coils in the brush. Alternatively, for comparison with the self-assembling glycocalyx simulations, the thermodynamic equilibrium analysis is used in which the brush parameters are calculated based on the average coil occupancy as determined by the total coil volume fraction in the system.

The covalently-bound layer simulations can be qualitatively compared to our model by the influence of two parameters, namely the occupancy fraction and shear flow. The occupancy fraction dependence will be estimated by comparing the HA+PG layer where the occupancy of the HA chains with coils or plasma proteins is zero, and with the full ESL layer containing a fixed fraction of coils irreversibly associated with the polymer brush. The qualitative effect of shear flow will be estimated by simply comparing the data for the quiescent and sheared layers both with and without attached plasma proteins.

Before starting the comparison, an estimate is needed for the values of the free parameters included in the theoretical model, namely the persistence length, grafting density, degree of polymerization for both main chains and coils, fraction of binding sites in the polymer chains (i.e. maximum occupancy fraction), energy of interaction and coil volume fraction (the last two parameters are only needed for the dynamic case).

Due to the coarse-grained nature of the simulation model, the parameters from the simulation must be properly mapped onto those of the scaling theory. First of all, all the macromolecules in the simulations consist of beads that represent a cluster of monomers. As a result, the degree of polymerization (DP) of chains in the simulations (e.g. ~55 for the effective DP of hyaluronan) corresponds to much larger DP for an explicit polymeric chain of monomer units. Moreover, the theoretical model utilized here is based on scaling principles, which are only valid for macromolecules with sufficiently large DP. Therefore, in order to compare simulation and theory, we must scale-up the simulation parameters in such a manner that the DPs of the components are large enough for treatment using the scaling approach while preserving the relative length scales present in the simulated system. If we base the scale-up on target value for the DP of the main chains being $N = 1000$ (i.e. an increase by about an order of magnitude over the simulated DP), then corresponding scaling gives values for the coil DP of around $M \sim 100$. The occupancy fraction of the polymer chains also needs to be rescaled, so that the same number of coils is allowed to attach to the brush. In the simulations there were 10, therefore the occupancy we will in the scaling model is $P/N = 0.01$ (that will also be the value used for the maximal occupancy in the comparison with dynamically associating glycocalyx). The grafting density used in the simulations corresponded to

roughly 0.03 for the polysaccharide chains (that is $\sigma = 0.005$ for the proteoglycan cores, each with six tethered polysaccharides). Since in the model the non-dimensionalization of the heights was done using the chains degree of polymerization and the dimensionless grafting density did not include it, this implies that we need to rescale the grafting density as well, namely decrease it by about an order of magnitude. For this particular comparison we will use $\sigma = 0.001$. The persistence length of the polysaccharide chains was calculated based on their radii of gyration to be between 5 and 10, so here we will use the value of $l_{\mathrm{p}} = 10$.

For the dynamically associating layer, the coil volume fraction and the interaction energy will also be needed. In the simulations, 600 protein molecules each with 20 beads in length occupying a box containing 140000 total beads. This corresponds to about 8% volume fraction of proteins in the simulation box. In this comparison we are mainly interested in the order of magnitude of the parameters and so we will use $\phi_{\mathrm{coil}} = 0.1$. The energy of interaction between the coils and the chains was varied between non-interacting and an energy of interaction of 1.5kT. Keeping in mind the pyramidal geometry of the complexes, this monomer-monomer interaction energy needs to be multiplied by roughly a factor of 4 to obtain the effective interaction energy of a single complex, since the existence of every complex implies the cooperative association of all four of the pyramidal binding sites. Therefore, the strongest interacting energy from the simulations can be roughly taken as being equivalent to $\varepsilon = 5$ in the model. Overall, the parameters chosen roughly correspond to these in the simulation data, and are, by construction, among those used in the scaling model analysis presented in the previous parts of this chapter.

In Chapter 3 we compared the glycocalyx conformation and properties in quiescent conditions with and without the presence of the absorbed proteins; it was observed that the addition of proteins resulted in height, density and subsequent osmotic pressure increase (Figs. 3.1, 3.3, 3.4 bottom). Qualitatively, the same effects were predicted by the scaling model (Figs. 5.2 and 5.4 bottom). As the amount of coils associated in the brush grows, that was shown to lead to brush height and osmotic pressure increase. Quantitatively, however, the effects observed in the model using the parameters chosen, namely less than a 20% increase for the height and a similar one for the osmotic pressure, were significantly weaker than the effects observed during the simulations, which was as much as a factor of two for the height and an even more pronounced increase for the osmotic pressure.

The effect of the shear flow on the properties of the covalently bound glycocalyx was shown to be non-existent for weak and medium shear flows. In case of strong shear flows there was pronounced brush thinning (Fig. 3.9) which was comparable in magnitude between the bare brush (PG+HA layer) and decorated brush (full ESL). Apart from that, considerable lateral displacement was observed both for bare and decorated brushes (Fig. 3.13); the effect was also comparable in magnitude for the two systems. The osmotic pressure was observed to increase slightly for strong shear flows and to remain constant for weak and moderate shear (Fig. 3.10). Those effects are also qualitatively consistent with the predictions from the scaling model, showing lack of effect for the height and osmotic pressure and an absence of lateral displacement for weak shear flows; and slow decrease of the height, increase of the osmotic pressure and build-up of lateral chain extension for strong shear (Figs. 5.12, 5.16). As in the previous comparison, the

magnitude of the effects predicted by the model is substantially less than what was observed in the simulations.

In the case of dynamically assembling glycocalyx, simulated in Chapter 4, there are even more possibilities for comparison. We can use the data we have on glycocalyx behavior for different interacting energies between the hyaluronan and the plasma proteins for comparison with the predictions of the theoretical model about the role of the energy of interactions on the brush properties. We can also compare the effect of the shear flow on the dynamic equilibrium and the layer properties qualitatively to the model predictions. Finally, using the results from the numerical experiments for different protein concentrations, the effect from the coil volume fraction can be compared to model predictions.

The interaction energy between the hyaluronan and plasma proteins in the simulations was shown to be a major factor in the establishment of the equilibrium distribution between the bulk and endothelial surface layer proteins – for lower interaction energies the amount of coils inside the layer was substantially less, and for the maximal energy of interaction attempted a vast of majority of the coils were found in the layer (Fig. 4.1). That is directly related to the amount of plasma proteins that are actually associated in the glycocalyx. The trends observed during the simulations are in agreement with the predictions of the model. For the interaction energy corresponding to the maximum value studied in the simulations, $\varepsilon=5$, the model predicts an essentially saturated brush even at low coil volume fractions (Fig. 5.8). In the limit of low interaction energy, only a small fraction of the coils were found associated, as was also observed in the simulations of the non-interacting and weakly interacting glycocalyx layers. The influence of binding

energy on the equilibrium glycocalyx height was also estimated during the simulations, where it was shown to increase very weakly with the increase of the interaction energy. These observations are qualitatively in agreement with the scaling model, which also shows an increase in the equilibrium height of the brush with the increase of the interaction energy (Fig. 5.10). Quantitatively, however, the effect predicted from the model is stronger than what was observed in the simulations.

The simulations of the dynamically self-assembling glycocalyx subjected to shear flow showed thickness decrease and lateral displacement comparable to the covalent case (Figs. 4.9 and 4.11). However, even for strong shear flows there was no redistribution of proteins between the bulk and the layer, implying that the layer deformation is due only to shear-provoked chain deformations. The theoretical model predictions for this situation are very much in agreement with the simulations. The changes of the average occupancy number with the flow were shown to be extremely weak for all values of the energy of interaction (Figs. 5.17, 5.21). The height change with the shear flow seem in the scaling model was also shown to be due to flow-induced chain deformation, the same conclusion that was drawn from the simulation results. As for the absolute values of the height changes and lateral displacement due to flow, the predictions are qualitatively the same as in the covalent case. However, the quantitatively the effect of the interaction energy on the height is strongly overestimated in the scaling model.

The last comparison to be made is the influence of the total volume fraction of plasma protein coils on the glycocalyx behavior in quiescent conditions, explored in the plasma depletion simulations of Ch. 4.4. According to the simulations, the decrease of overall plasma protein concentration was accompanied by weak decrease in the brush thickness,

an obvious decrease of protein concentration in both the ESL and plasma phases, and increased polarization between the two phases in the case of strong binding energy (Figs. 4.13, 4.14). The same qualitative effects are seen in the model predictions (Figs. 5.10 and 5.8). As the coil volume fraction decreases, the brush height decreases as well, in a less sharp way for weak interaction energies but in a very abrupt way for strongly associating coil. Quantitatively, the effects on the height predicted by the theoretical model are considerably larger than what is observed in the simulations. In the case of large interaction energy, one may infer an increased polarization between the coils in the bound and unbound states (Fig. 5.8). That conclusion is based on the fact that even for low concentrations of coils, the chains in the brush will attempt to keep their fully saturated state provided the binding energy is high enough. This is in good agreement with the simulation results for interaction energy 1.5 at low protein concentration, where practically all the proteins were found associated to the endothelial surface layer (Fig. 4.13).

Overall, even though the model presented is relatively crude and based on scaling principles that are only able to provide rough order of magnitude predictions for the effects of various parameters and conditions on the endothelial surface layer behavior, the model shows a surprising qualitative agreement with basically all the effects observed in the simulations. In the previous chapters, the simulation results were compared to and found to be generally consistent with previously reported results from hemodilution and saline perfusion experiments and the effects from various enzymatic treatments of the ESL. Therefore, the simple model presented here may be useful for gaining insight into the physical behavior of the ESL.

6. Conclusions

In this thesis, theoretical studies were made to clarify the dynamic structure and properties of the endothelial surface layer based on two alternative methods – non-equilibrium Molecular Dynamics simulations and theoretical modeling based on polymer scaling principles. For both approaches, a simple layer topology representation was used consisting of two (model) or three (simulations) basic building elements of macromolecular nature. Even though the ESL representation and the subsequent simulations and modeling are rather simplified, they still present a much higher level of detail than previous modeling studies, which have mostly treated the endothelial surface layer in a purely mechanical manner as a continuous media. In fact, the present thesis is the first macromolecular study of the endothelial surface layer accounting for its multi-component nature and dynamic structure.

In large part, the simulations and modeling results are consistent with each other and are in qualitative agreement with phenomena observed in available experiments. The simulations predict large variations in the glycocalyx properties with alterations of the layer composition and show that a full ESL including all the components from the topological model is required for proper flow screening and macromolecular permeability of the glycocalyx. On the contrary, layers containing only proteoglycan components were observed to lead to considerable flow penetration into the layer reaching all the way to the cell surface. Moreover, glycocalyx lacking associated plasma proteins was shown to have considerably lower osmotic pressure and higher permeability compared to the complete ESL. The results obtained are in qualitative agreement with experimental data

on reduced glycocalyx function after various enzyme treatments (*van den Berg et al., 2003; Hendy and Duling, 1999; Vogel et al., 2000; Desjardins and Duling, 1990; Hecker et al, 1993*). When the glycocalyx is subjected to shear flow, very high rates were required for the layer to deform in response to the flow – the deformation was seen in both the thinning of the glycocalyx and the pronounced lateral extension and tilting of its constituents in the flow direction.

In the case of the self-assembling glycocalyx, the interaction energy between the associating elements was found to play a crucial role for the equilibrium distribution of the dynamically bound plasma protein species. The protein diffusion inside the glycocalyx and outside in the plasma fluid with their characteristic diffusion constants was evaluated. The glycocalyx was found to be sufficiently diffuse that it only moderately perturbs the protein diffusion, in agreement with recent experimental results (*Osterloh et al, 2002*). On the other hand, the association and dissociation events are found to affect the partition of plasma protein between the glycocalyx and plasma fluid, so that there are two distinct equilibrium protein populations in the system. The short characteristic lifetime of the protein-hyaluronan complexes, found from the simulation results to be of the order of a microsecond, corresponds to a very dynamic behavior of the glycocalyx and suggests that its properties might be easily influenced by external physical stimuli, as indirectly indicated by experiments (*Arisaka et al, 1995; Ueda et al, 2004*). However, simulations of sheared self-assembling ESL revealed that the response of the glycocalyx to the shear flow is comparable to the previously analyzed irreversibly assembled layer and is characterized at all flow rates by tethered chain deformation without any observed redistribution of the associating plasma proteins. The last results

are not in agreement with recent experimental results reporting glycocalyx growth from increased albumin uptake at strong shear flows (*Ueda et al., 2004*), but the observed discrepancy can be easily explained by the model limitations which will be discussed later in this chapter. The influence of plasma composition on the glycocalyx was also investigated through the simulation of a range of total plasma protein concentrations and the analysis of the equilibrium distribution at different concentrations and interaction energies. It was observed that for strong enough interaction energies, there is a residual amount of proteins in the glycocalyx even for extremely low bulk concentrations of proteins, while the moderate and low interactions are characterized by less polarized protein distributions and the possibility of substantial removal of plasma proteins from the layer during plasma depletion.

The theoretical model developed shows the same qualitative responses of the endothelial surface layer for the various physico-chemical factors. Among the model predictions are layer thinning and considerable lateral chain displacement in strong shear flows (both for irreversibly assembled and self-assembled glycocalyx), the increase in the layer height with the increase of the interaction energy or the overall associating coil concentration, and the slight change of the coil content in the glycocalyx in response to flow.

The challenges and uncertainties in the approaches used in this thesis come from several different sources. First, due to lack of detailed structural information about the glycocalyx components, most importantly their connectivity and macromolecular properties, many of the parameters needed for the simulations were chosen in an ad hoc manner, based only on general knowledge of the chemical nature of the subunits of

various classes of likely ESL constituents (proteins, proteoglycans, and polysaccharides). For example, there is no explicit data about the relative persistence lengths of the proteoglycan protein cores versus their heparan sulfate side branches. There is also no data available for the strength of interaction between the different constituents. The immediate surface interactions of the various components are also important for the behavior of the layer in close proximity to the cell surface, where the shear stress is transported through the membrane. However, there is little useful information about cell membrane-ESL interactions, so in all the simulations it was simply assumed that all system components (including the solvent beads) interact with the grafting wall in a completely identical and inert manner.

Another possible source of inaccuracy is the potential oversimplification of the glycocalyx topology. In the present work, the model only has three different molecular species, two of which are irreversibly bound in a fixed configuration, and is intended as a minimalist model of the ESL. Obviously, such a simple model cannot account for the immense molecular diversity on the endothelial cell surface. The possibility of molecule generation or removal during the simulations was also entirely neglected, although there is abundant evidence that some glycocalyx constituents (e.g. hyaluronan and the syndecan proteoglycans) are constantly produced by the cells, incorporated into the glycocalyx, and possibly shed into the plasma. So the concentration of many ESL components in the layer is partially regulated by the dynamic equilibrium between the rate of production and shedding. Moreover, the shedding of proteoglycans from the cell membrane also eliminates anchoring sites for the ESL on the cell surface, a feature not accounted for in the topology model and the simulations.

Oversimplification of the molecular connectivity within the glycocalyx topology model is another possible concern. However, data regarding the association behavior of potential ESL constituents is scarce and rather indirect. Thus, the topology of the layer must be considered as a plausible hypothesis, although a change in the connectivity of the layer would probably have a qualitative influence on its overall behavior.

Difficulties in the interpretation of the simulation results can also arise from the way the different components in the glycocalyx are scaled, in particular the use of a single lengthscale (the bead size) as the fundamental subunit for all molecular species. As discussed in Chapter 3, the computational resources available do not allow an entirely consistent simulation study of molecules differing in their molecular weights by more than two orders of magnitude. Therefore, the chosen relative lengths for the different molecules in our studies do not accurately reflect the relative sizes of the actual glycocalyx constituents, which can also result in inaccuracies in the results.

The theoretical model developed also includes some of the same sources of inaccuracy. As constructed, the scaling model does not incorporate dynamic shedding of all the polymer brush constituents, and it also involves a number of parameters that must to be assigned using very general guidelines, since concrete information is lacking. Other generalizations of the model include the De Gennes ansatz of a single type of chain conformation in the brush, which simplifies the problem immensely but strictly speaking is not correct. This was clearly seen by the simulations which exhibited a distribution of different chain conformations, some of which were buried well inside the polymer brush. The theoretical model is also restricted to the case when the associating coils in the layer are in regime of low coverage, an assumption largely validated by the simulations.

Future directions and extensions of this research may include a range of additions and alternative methods of glycocalyx investigation. First, more elaborate topology models can be created. These may include the presence of additional free hyaluronan in the bulk that is able to connect to other surface-bound hyaluronan molecules via plasma proteins. Such a construct may result in a build-up of a network consisting of multiple hyaluronan -based layers built upon the proteoglycan base, in a manner similar to the associative-polymer experiment described in the introduction chapter (*Huang and Santore, 2002*). If shear stress transmission needs to be evaluated accurately for different conditions, it would be necessary to change the scaling of the system so that the proteoglycan molecules are described in more molecular detail than in the present work (where they consisted of oligomeric chains with some 10-20 beads each, which cannot be expected to statistically behave like real polymers). In a larger scale model of the proteoglycans, various macromolecular approaches can be used to evaluate the free energy of deformation of the proteoglycans in flow, and based on those estimates the tension transmission can be evaluated for different conditions. Other new phenomena can also be analyzed using the present topology model or a more elaborate one. One possible example is a more detailed observation of the protein transport inside the endothelial surface layer, its dependence on the size of the protein molecule and perhaps even its charge, since charge is known to be important for macromolecular transport in the glycocalyx.

Finally, since the simulation methods used in the present work are not amenable to the modeling of open systems with changing concentrations of ESL constituents, alternative approaches may be successfully applied to clarify the role of production and

shedding of various components in the dynamic glycocalyx. Two possible approaches allowing the introduction of sources and sinks of glycocalyx components are Brownian Dynamics and Dissipative Particle Dynamics. Additional theoretical modeling based on associating polymer principles may also provide new insights into the multi-scale nature and properties of the endothelial surface layer.

References:

1. Adamson R. H., "Permeability of frog mesenteric capillaries after partial pronase digestion of the endothelial glycocalyx", *Journal of Physiology*, **428**, p.1 (1990)
2. Adamson R. H., Clough G., "Plasma proteins modify the endothelial glycocalyx of frog mesenteric microvessels", *Journal of Physiology*, **445**, p.473 (1992)
3. Albrecht K. H., Gaehtgens P., Pries A., Heuser M., "The Fahraeus effect in narrow capillaries (3.3 to 11.0μm)", *Microvascular Research*, **18**, p.33 (1979)
4. Alexander S., "Adsorption of chain molecules with a polar head: a scaling description", *Le Journal de Physique*, **38**, p.983 (1977)
5. Arisaka T., Mitsumata M., Kawasumi M., Tohjima T., Hirose S., Yoshida Y. "Effects of shear stress o glycosaminoglycan synthesis in vascular endothelial cells", *Annals of the NY Academy of Sciences*, **748**, p.543 (1995)
6. Balazs E. A., "Physical chemistry of hyaluronic acid", *Federation Proceedings*, **17**, p.1086 (1958)
7. Barrat J.-L., "A possible mechanism for swelling of polymer brushes under shear", *Macromolecules*, **25**, p.832 (1992)
8. Beauvais D. M., Rapraeger A. C. "Syndecans in tumor cell adhesion and signaling", *Reproductive Biology and Endocrinology*, **2**, p.3 (2004)
9. Berne R. B., Levy M. N., "Physiology", 3rd Edition, *Mosby-Year Book Inc* (1993)
10. Bernfield M., Gotte M., Park P. W., Reizes O., Fitzgerald M. L., Lincecum J., Zako M., "Functions of cell surface heparan sulfate proteoglycans", *Annual Reviews of Biochemistry*, **68**, p.729 (1999)

11. Bernfield M., Kokenyesi R., Kato M., Hinkes M., Spring J., Gallo R. L., Lose E. J., "Biology of the syndecans: a family of transmembrane heparan sulfate proteoglycans", *Annual Review of Cell Biology*, **8**, p.365 (1992)

12. Bettelheim F. A., Philpott D. E., "Electron microscopic studies of hyaluronic acid-protein gels", *Biochimica et Biophysica Acta*, **34**, p.124 (1959)

13. Birshtein T. M., Borisov O. V., Zhulina Y. B., Khokhlov A. R., Yurasova T. A., "Conformations of comb-like macromolecules", *Polymer Science USSR*, **29**, p.1293 (1987)

14. Bright J. N., Woolf T. B., Hoh J. H., "Predicting properties of intrinsically unstructured proteins", *Progress In Biophysics And Molecular Biology*, **76**, p.131 (2001)

15. Brown M. D., Egginton S., Hudlicka O., Zhou A. L., "Appearance of the capillary endothelial glycocalyx in chronically stimulated rat skeletal muscles in relation to angiogenesis", *Experimental Physiology*, **81**, p1043 (1992)

16. Buonassisi V., Colburn P., "Biological significance of heparan sulfate proteoglycans", *Annals of NY Academy of Sciences,* **401**, p76 (1982)

17. Carey D. J., "Syndecans: multifunctional cell-surface co-receptors", *Biochemical Journal*, **327**, p.1 (1997)

18. Chambers R., Zweifach B. W., "Intercellular cement and capillary permeability", *Physiology Reviews*, **27**, p.436 (1947)

19. Chen B., Fu B. M. "An electrodiffusion-filtration model for effects of endothelial surface glycocalyx on microvessel permeability to macromolecules", *Journal of Biomechanical Engineering*, **126**, p.614 (2004)

20. Clough G., Michel C. C., "Quantitative comparisons of hydraulic permeability and endothelial intercellular cleft dimensions in single frog capillaries", *Journal of Physiology (London)*, **405**, p.563 (1988)

21. Constantinescu A. A., Spaan J. A. E., Vink H., "Transcapillary chylomicron leakage at sites of degraded glycocalyx in hyperlipidemic mice" *(submitted for publication)*

22. Constantinescu A. A., Vink H., Spaan J. A. E., "Elevated capillary tube hematocrit reflects degradation of endothelial cell glycocalyx by oxidized LDL", *American Journal Of Physiology: Heart Circulation and Physiology*, **280**, p.H1051 (2001)

23. Constantinescu, A. A., Vink H., Spaan J. A. E., "Endothelial cell glycocalyx modulates immobilization of leukocytes at the endothelial surface", *Arteriosclerosis and Thrombosis Vascular Biology*, **23**, p.1541 (2003)

24. Copley A. L., "Non-Newtonian behavior of surface layers of human plasma protein systems and a new concept of the initiation of thrombosis", *Biorheology*, **8**, p.79 (1971)

25. Copley A. L., Scott Blair G. W. "Comparative observations on adherence and consistency of various blood systems in living and artificial capillaries", *Rheologica Acta*, **1**, p.170 (1958)

26. Copley A. L., Staple P. H., "Hemorheological studies on the plasmatic zone in the microcirculation of the cheek pouch of Chinese and Syrian hamsters", *Biorheology*, **1**, p.3 (1962)

27. Copley A., "Hemorheological aspects of the endothelium-plasma interface", *Microvascular Research*, **8**, p.192 (1974)

28. Copley A., "The endothelial fibrin lining as the crucial barrier and the role of fibrin(ogen) gels in controlling transcapillary transport", *Biorheology*, **21**, p.135 (1984)

29. Cowman M. K., Li M., Balazs E. A. "Tapping mode atomic force microscopy of hyaluronan: extended and intramolecularly interacting chains", *Biophysical Journal*, **75**, p.2030 (1998)

30. Curry F. E., Michel C. C. "A fiber matrix model of capillary permeability", *Microvascular Research*, **20**, p.96 (1980)

31. Damiano E. R., "The effect of the endothelial-cell glycocalyx on the motion of the red blood cells through capillaries", *Microvascular Research*, **55**, p.77 (1998)

32. Damiano E. R., Duling B. R., Ley K., Skalak T. C., "Axisymmetric pressure-driven flow of rigid pellets through a cylindrical tube lined with a deformable porous wall layer", *Journal of Fluid Mechanics*, **314**, p163 (1996)

33. Damiano E. R., Stace T. M. "Flow and deformation of the capillary glycocalyx in the wake of a leukocyte", *Physics of Fluids*, **17**, #031509 (2005)

34. Damiano E. R., Stace T. M., "A mechano-electrochemical model of radial deformation of the capillary glycocalyx", *Biophysical Journal*, **82**, p.1153 (2002)

35. Danielli J. F. "Capillary permeability and edema in the perfused frog", *A*, **98**, p.109 (1940)

36. Danova-Okpetu D., Grest G. S., Harden J. L., "Non-equilibrium molecular dynamics simulations of grafted semi-flexible polymers in shear flow conditions", (*unpublished*)

37. De Gennes P. G., "Scaling theory of polymer adsorption", *Le Journal de Physique*, **37**, p.1445 (1976)

38. Delvos U., Preissner K. T., Muller-Berghaus G. "Binding of fibrinogen to cultured bovine endothelial cells", *Thrombosis and Haemostasis*, **53**, p.26 (1985)

39. Desjardins C., Duling B. R. "Microvessel hematocrit: measurement and implications for capillary oxygen transport", *American Journal of Physiology: Heart and Circulatory Physiology*, **252**, p.H494 (1987)

40. Desjardins C., Duling B., "Heparinase treatment suggests a role for the endothelial cell glycocalyx in regulation of capillary hematocrit", *American Journal Of Physiology: Heart And Circulatory Physiology*, **258**, p.H647 (1990)

41. Fahraeus R., "The suspension stability of the blood", *Physiological Reviews*, **9**, p.241 (1929)

42. Filmus J., Selleck S. B. "Glypicans: proteoglycans with a surprise", *Journal of Clinical Investigation*, **108**, p.497 (2001)

43. Florey H. W., Poole J., Meek G., "Endothelial cells and 'cement' lines", *J Pathol Bacteriol,* **77***,* p625 (1959)

44. Florian J. A., Kosky J. R., Ainslie K., Pang Z., Dull R. O., Tarbell J. M., "Heparan sulfate proteoglycan is a mechanosensor on endothelial cells", *Circulation Research*, **93**, p.e136 (2003)

45. Fouissac E., Milas M., Rinaudo M., Borsali R., "Influence of the ionic strength on the dimensions of sodium hyaluronate", *Macromolecules*, **25**, p.5613 (1992)

46. Fransson L.-A. "Glypicans", *International Journal of Biochemistry and Cell Biology*, **35**, p.125 (2003)

47. Fredrickson G. H., "Surfactant-induced lyotropic behavior of flexible polymer solutions", *Macromolecules*, **26**, p.2825 (1993)

48. Fu B. M., Chen B., Chen W. "An electrodiffusion model for effects of surface glycocalyx layer on microvessel permeability",*American Journal Of Physiology: Heart And Circulatory Physiology*, **284**, p.H1240 (2003)

49. Goldsmith H. L., Cokelet G. R., Gaehtgens P., "Robin Fahraeus: evolution of his concepts in cardiovascular physiology", *American Journal of Physiology: Heart and Circulatory Physiology*, **281**, p.H1005 (1989)

50. Goldstein R. E., "Model for phase equilibria in micellar solution of nonionic surfactants", *Journal of Chemical Physics*, **84**, p.3367 (1986)

51. Gouverneur M., Spaan J. A. E., Vink H., "Fluid shear stress is a critical stimulus for endothelial synthesis of glycocalyx hyaluronan", *American Journal of Physiology: Heart and Circulatory Physiology***, 289**, H592 (2005)

52. Grest G. S., "Normal and shear forces between polymer brushes", *Advances in Polymer Science*, **138**, p.149 (1999)

53. Guo Z., Thilumalai D., "Kinetics and thermodynamics of folding of a de novo designed four-helix bundle protein", *Journal of Molecular Biology*, **263**, p.323 (1996)

54. Haldenby K. A., Chappell D. C., Winlove C. P., Parker K. H., Firth J. A., "Focal and regional variations in the composition of the glycocalyx of large vessel endothelium", *Journal of Vascular Research*, **31**, p2 (1994)

55. Halperin A., Tirrell M., Lodge T. P., "Tethered chains in polymer microstructures", *Advances in Polymer Science*, **100**, p.31 (1992)

56. Harden J. L., Borisov O. V., Cates M. E., "Deformation of polyelectrolyte brushes in strong flows: good solvent regime", *Macromolecules*, **30**, p.1179 (1997)

57. Harden J. L., Cates M. E., "Deformation of grafted polymer layers in strong shear flows", *Physical Review E*, **53** (4), p.3782 (1996)

58. Harden J. L., Long D., Ajdari A., "Influence of end-grafted polyelectrolytes on electro-osmosis along charged surfaces", *Langmuir*, **17**, p.705 (2001)

59. Hecker M., Mulsch A., Bassenge E., Busse R., "Vasoconstruction and increased flow: two principal mechanisms of shear stress-dependent endothelial autacoid release", *American Journal of Physiology: Heart and Circulatory Physiology*, **265**, p.H828 (1993)

60. Heine D., Grest G., Danova-Okpetu D., Harden J., "Dynamical and Mechanical Behavior of Reversible Protein Hydrogels", Center for Integrated Nanotechnologies Workshop, Albuquerque, NM, January 19-21, 2005

61. Henry C. B. S., Duling B. R., "Permeation of the luminal capillary glycocalyx is determined by hyaluronan", *American Journal Of Physiology: Heart And Circulatory Physiology*, **277**, p.H508 (1999)

62. Huang Y., Santore M. M., "Dynamics in adsorbed layers of associative polymers in the limit of strong backbone – surface attractions", *Langmuir*, **18** (6), p.2158 (2002)

63. Huxley V. H., Williams D. A., "Role of glycocalyx on coronary arteriole permeability to proteins: evidence from enzyme treatments", *American Journal Of Physiology: Heart And Circulatory Physiology*, **278**, p.H1177 (2000)

64. Khorramian B. A., Stivala S. S. "Small-angle x-ray scattering of high- and low-affinity heparin", *Archives of biochemistry and biophysics*, **247**, 384 (1986)

65. Klitzman B., Duling B. R., "Microvascular hematocrit and red cell flow in resting and contracting striated muscle", *American Journal of Physiology: Heart and Circulatory Physiology*, **237** (4), p.H481 (1979)

66. Kuznetsov D. V., Chen Z. Yu, "Semiflexible polymer brushes: a scaling theory", *Journal of Chemical Physics*, **109** (16), p.7017 (1998)

67. Lapcik Jr. L., Lapcik L., De Smedt S., Demeester J., Chabrecek P., "Hyaluronan: preparation, structure, properties and applications", *Chemical Reviews*, **98**, p.2663 (1998)

68. Laurent T. C., Fraser J. R. E., "Hyaluronan", *FASEB Journal*, **6**, p.2397 (1992)

69. Lindahl U., Kusche-Gullberg M., Kjellen L., "Regulated diversity of heparan sulfate", *Journal Of Biological Chemistry*, **273** (39), p.24979 (1998)

70. Long D. S., Smith M. L., Pries A. R., Ley K., Damiano E. R. "Microviscometry reveals reduced blood viscosity and altered shear rate and shear stress profiles in microvessels after hemodillution", *Proceedings of the National Academy of Sciences US*, **101**, p.10060 (2004)

71. Loudon M. F., Michel C. C., White I. F., "The labeling of vesicles in frog endothelial cells with ferritin", *Journal of Physiology (London)*, **296**, p.97 (1979)

72. Luft J. H. "Fine structure of capillary and endocapillary layer as revealed by ruthenium red", *Federation Proceedings*, **25**, p.1773 (1966)

73. Mason J. C., Curry F. E., Michel C. C., "The effects of proteins upon the filtration coefficient of individually perfused frog mesenteric capillaries", *Microvascular research*, **13**, p.185 (1977)

74. Mendichi R., Soltes L., Schieroni A. G., "Evaluation of radius of gyration and intrinsic viscosity molar mass dependence and stiffness of hyaluronan", *Biomacromolecules*, **4**, p.1805 (2003)

75. Mertens G., Cassiman J.-J., Van den Berghe H., Vermylen J., David G., "Cell surface heparan sulfate proteoglycans from human vascular endothelial cells: core protein characterization and antithrombin III binding properties", *The Journal of Biological Chemistry*, **267** (28), p.20435 (1992)

76. Michel C., "The investigation of capillary permeability in single vessels", *Acta Physiologica Scandinavica Suppl.*, **463**, p67 (1979)

77. Michel C.C., Curry F. E., "Microvascular permeability", *Physiological Reviews*, **79**(3), p703 (1999)

78. Mochizuki S., Vink H., Hiramatsu O., Kajita T., Shigeto F., Spaan J. A. E., Kajiya F., "Role of hyaluronic acid glycosaminoglycans in shear-induced endothelium-derived nitric oxide release", *American Journal of Physiology: Heart and Circulatory Physiology*, **285**, p.H722 (2003)

79. Mulivor A. W., Lipowsky H. H., "Inflammation- and ischemia-induced shedding of venular glycocalyx", *American Journal of Physiology: Heart and Circulatory Physiology*, **286**, p.H1672 (2004)

80. Mulivor A. W., Lipowsky H. H., "The role of the glycocalyx in leukocyte-endothelial cell adhesion", *American Journal Of Physiology: Heart And Circulatory Physiology*, **283**, p.H1282 (2002)

81. Osterloh K., Ewert U., Pries A. R., "Interaction of albumin with the endothelial cell surface", *American Journal Of Physiology: Heart Circulation and Physiology*, **283**, p.H398 (2002)

82. Padding J. T., Briels W. J. "Time and length scales of polymer melts studies by coarse-grained molecular dynamics simulations", *Journal of Chemical Physics*, **117**, p.925 (2002)

83. Pigman W., Gramling E., Holley H. L., "Interactions of hyaluronic acid with serum albumin", *Biochimica et Biophysica Acta*, **46**, p.100 (1961)

84. Poiseuille J. L. M., "Recherches sur les causes du movement du sang dans les vaisseaux capillaires", Comptes Rendus de l'Academie des Sciences, **1**, p554 (1835)

85. Popel A. S., Johnson P. C., "Microcirculation and hemorheology", *Annual Review in Fluid Mechanics*, **37**, p43 (2005)

86. Pries A. R., Ley K., Gaehtgens P. "Generalization of the Fahraeus principle for microvessel networks", *American Journal of Physiology: Heart and Circulatory Physiology*, **251**, p.H1324 (1986)

87. Pries A. R., Schonfeld D., Gaehtgens P., Kiani M. F., Cokelet G. R., "Diameter variability and microvascular flow resistance", *American Journal of Physiology: Heart and Circulatory Physiology*, **272**, p.H2716 (1997a)

88. Pries A. R., Secomb T. W., Gaehtgens P., "The endothelial surface layer", *Pflügers Archiv European Journal of Physiology*, **440**, p.653 (2000)

89. Pries A. R., Secomb T. W., Gessner T., Sperandio M. B., Gross J. F., Gaehtgens P., "Resistance to blood flow in microvessels in vivo", *Circulation Research*, **75**, p.904 (1994)

90. Pries A. R., Secomb T. W., Jacobs H., Sperandio M., Osterloh K., Gaehtgens P., "Microvascular blood flow resistance: role of endothelial surface layer", *American Journal Of Physiology: Heart And Circulatory Physiology*, **273**, p.H2272 (1997b)

91. Pries A.R., Secomb T.W., Speranido M., Gaehtgens P., "Blood flow resistance during hemodillution: effect of plasma composition", *Cardiovascular Research*, **37**, p225 (1998)

92. Rabin Y., Alexander S., "Stretching of grafted polymer layers", *Europhysics Letters*, **13** (1), p.49 (1990)

93. Risau W., "Differentiation of endothelium", *FASEB Journal*, **9**, p.926 (1995)

94. Rostgaard J., Qvortrup K. "Electron microscopic demonstrations of filamentous molecular sieve plugs in capillary fenestrae", *Microvascular Research*, **53**, p.1 (1997)

95. Rubinstein M., Colby R. H., "Polymer Physics", *Oxford University Press* (2004)

96. Rubinstein M., Dobryinin V., "Solutions of associative polymers", *TRIP*, **5**, p.181 (1997)

97. Schnitzer J. E., Pinney E., "Quantitation of specific binding of orosomucoid to cultured microvascular endothelium: role in capillary permeability", *American Journal of Physiology: Heart and Circulatory Physiology*, **263**, p.H48 (1992)

98. Schriver Z., Liu D., Sasisekaran R. "Emerging views of heparan sulfate glycosaminoglycan structure/activity relationships modulating dynamic biological functions", *Trends in Cardiovascular Medicine*, **12**, p.71 (2002)

99. Secomb T. W., Hsu R., Pries A. R., "A model for red blood cell motion in glycocalyx-lined capillaries", *American Journal Of Physiology: Heart And Circulatory Physiology*, **274**, p.H1016 (1998)

100. Secomb T. W., Hsu R., Pries A. R., "Blood flow and red blood cell deformation in nonuniform capillaries: effects of the endothelial surface layer", *Microcirculation*, **9**, p.189 (2002)

101. Secomb T. W., Hsu R., Pries A. R., "Effect of the endothelial surface layer on transmission of fluid shear stress to endothelial cells", *Biorheology*, **38**, p.143 (2001a)

102. Secomb T. W., Hsu R., Pries A. R., "Motion of red blood cells in a capillary with an endothelial surface layer: effect of flow velocity", *American Journal Of Physiology: Heart And Circulatory Physiology*, **281**, p.H629 (2001b)

103. Sevick E. M., "Shear swelling of polymer brushes grafted onto convex and concave surfaces", *Macromolecules*, **29**, p.6952 (1996)

104. Simionescu M., Simionescu N., "Functions of the endothelial cell surface", *Annual Reviews of Physiology*, **48**, p.279 (1986)

105. Sorensson J., Matejka G. L., Ohlson M., Haraldsson B. "Human endothelial cells produce orosomucoid, an important component of the capillary barrier", *American Journal of Physiology: Heart and Circulatory Physiology*, **276**, p.H530 (1999)

106. Squire J. M., Chew M., Nneji G., Neal C., Barry J., Michel C., "Quasi-periodic substructure in the microvessel endothelial glycocalyx: a possible explanation for molecular filtering", *Journal Of Structural Biology*, **136**, p.239 (2001)

107. Srinivas G., Klein M. L. "Coarse-grain molecular dynamics simulations of diblock copolymer surfactants interacting with a lipid bilayer", *Molecular Physics*, **102**, p.883 (2004)

108. Srinivas G., Shelley J. C., Nielsen S. O., Discher D. E., Klein M. L. "Simulation of diblock copolymer self-assembly using a coarse-grain model", *Journal of Physical Chemistry B*, **108**, p.8153 (2004)

109. Stace T. M., Damiano E. R., "An electrochemical model of the transport of charged molecules through the capillary glycocalyx", *Biophysical Journal*, **80**, p.1670 (2001)

110. Stehbens W. E., "Endothelial cement in the frog", *Quarterly Journal of Experimental Physiology*, **48**, p324 (1963)

111. Stehbens W. E., Florey H., "The behavior of intravenously injected particles observed in chambers in rabbits' ears", *Quarterly Journal of Experimental Physiology*, **45**, p252 (1960)

112. Stringer S. E., Gallagher J. T., "Heparan sulfate", *International Journal of Biochemistry And Cellular Biology*, **29** (5), p.709 (1997)

113. Thi M., Tarbell J. M., Weinbaum S., Spray D. C., "The role of the glycocalyx in reorganization of the actin cytoskeleton under fluid shear stress: a "bumper car" model", *Proceedings of the National Academy of Sciences US*, **101**, p.16483 (2004)

114. Toole B. P., Wight T. N., Tammi M. I., "Hyaluronan-cell interactions in cancer and vascular disease", *The Journal of Biological Chemistry*, **277**, p.4593 (2002)

115. Turley E. A., Noble P. W., Bourguignon L. Y. W., "Signaling properties of hyaluronan receptors", *The Journal of Biological Chemistry*, **277**, p.4589 (2002)

116. Ueda A., Shimomura M., Ikeda M., Yamaguchi R., Tanishita K., "Effect of glycocalyx on shear-dependent albumin uptake in endothelial cells", *American Journal of Physiology: Heart and Circulatory Physiology* , **287**, p.H2287 (2004)

117. Van den Berg B. M., Vink H., Spaan J. A. E., "The endothelial glycocalyx protects against myocardial edema", *Circulation Research*, **92**, p.592 (2003)

118. Vink H, Constantinescu A. A., Spaan J. A. E., "Oxidized lipoproteins degrade the endothelial surface layer: implications for platelet-endothelial cell adhesion", *Circulation*, **101**, p1500 (2000)

119. Vink H, Nieuwdorp M., "Perturbation of a large vascular glycocalyx marks atherogenic vulnerability in type 1 diabetes" (*submitted for publication*)

120. Vink H., Duling B. R., "Identification of distinct luminal domains for macromolecules, erythrocytes and leukocytes within mammalian capillaries", *Circulation Research*, **79**, p.581 (1996)

121. Vink H., Spaan J. A. E., Duling B. R. "Mechanical properties of the endothelial surface layer", *FASEB Journal*, **13**, p.A11 (1999)

122. Vogel J., Sperandio M., Pries A. R., Linderkamp O., Gaehtgens P., Kuschinsky W. "Influence of the endothelial glycocalyx on cerebral blood flow in mice", *Journal of Cerebral flow and Metabolism*, **20**, p.1571 (2000)

123. Vogel S. M., Minshall R. D., Pilipovic M., Tiruppathi C., Malik A. B. "Albumin uptare and transcytosis in endothelial cells in vivo induced by albumin-binding protein", *American Journal of Physiology: Lung Cellular and Molecular Physiology*, **281**, p.L1512 (2001)

124. Warnke K. C., Skalak T. C. "The effects of leukocytes on blood flow in a model skeletal muscle capillary network", *Microvascular Research*, **40**, p.118 (1990)

125. Weinbaum S., Zhang X., Han Y., Vink H., Cowin S. C., "Mechanotransduction and flow across the endothelial glycocalyx", *Proceedings of the National Academy of Sciences US*, **100**, p.7988 (2003)

126. Winnik M. A., Yekta A., "Associative polymers in aqueous solution", *Current Opinions in Colloid and Interface Science*, **2**, p.424 (1997)

127. Witte S., "The endothelial lining as studies by a fluorescent labeling technique in situ", *Thrombosis Research*, **29 sup.2**, p.93 (1983)

128. Yevdokimova N. Y., "High glucose-induced alterations of extracellular matrix of human skin fibroblasts are not dependent onTSP-1-TGFβ1 pathway", *Journal of Diabetes and Its Complications*, **17**, p.355 (2003)

129. Zhou Y., Karplus M., "Interpreting the folding kinetics of helical proteins", *Nature*, **401**, p.400 (1999)

130. Zhulina E. B., Vilgis T. A., "Scaling theory of planar brushes formed by branched polymers", *Macromolecules*, **28**, p.1008 (1995)

131. Zimmermann P., David G., "The syndecans, tuners of transmembrane signaling", *The FASEB Journal*, **13**, p.S91 (1999)

Curriculum Vita

Darina Danova-Okpetu was born in Kharkiv, Ukraine on January 21, 1978 as the eldest child of Tatyana Danova and Krasimir Danov. After graduating from the French Language High School in Sofia in 1996, she started her undergraduate studies in Chemistry at the Sofia University "Kliment Ohridski" later in 1996, where she completed her Bachelor degree in Chemistry and Masters degree in Chemical Engineering by 2001. During her studies she also worked for several months as a research assistant in the Laboratory of Chemical Physics and Engineering in the Faculty of Chemistry at Sofia University. Later in 2001, she was admitted as a graduate student to the Chemical Engineering Program at Johns Hopkins University and was awarded the Robert H. Roy Fellowship for 2001. Since then she worked with Prof. James Harden on multi-scale modeling of endothelial surface layer. During her graduate studies, she participated in the NATO Advanced Study Institute "Computer Simulations of Surfaces and Interfaces" in Varna, Bulgaria in September, 2002 and worked for several months doing summer research at Sandia National Laboratories, Albuquerque, New Mexico. After the completion of her Ph.D. in October 2005, she will be working as a post doctoral fellow with Prof. Frederick Mackintosh at the Department of Physics, Vrije Universiteit in Amsterdam, Netherlands.